Electrode–skin Impedance Compensation for Improved Bioelectrical Signal Acquisition

Benjamin C. Fortune

Doctor of Philosophy

Mechanical Engineering

Supervised by

Associate Professor Chris Pretty

Centre for Bioengineering

University of Canterbury

Christchurch

New Zealand

November

2020

Acknowledgements

To my supervisors, thank you for your endless support. A special thanks goes to my primary supervisor, Chris Pretty, for your invaluable guidance and ability to always discuss, provide advice on and review my work. Also, for further supporting my research with a Mechanical Engineering Doctoral scholarship. Michael Hayes, thank you for sharing your broad knowledge on electrical theory and signal processing, and providing valuable feedback on my work. Stefanie Gutschmidt, thank you for your knowledge and support in the early stages of my research, prior to changing my thesis topic.

To Scott Lloyd and Julian Murphy, thank you sharing your invaluable technical experience, which assisted in developing the hardware used to produce this thesis.

To my fellow office mates, thank you for the office outings and providing me with technical and emotional support throughout our shared struggle.

Finally, to Mum and Dad, thank you for your eternal support and guidance through my life's endeavours. Lauren, thank you for your unconditional support, and encouragement and understanding when times were tough. And God, thank you for providing me with the strength and ability to overcome the challenges that were bestowed upon me during this research.

Publications

Over the course of this research, a number of papers have been published. The research demonstrated in these papers is based on the work presented in this thesis. The co-authorship forms, related to publications in this thesis, are in Appendix O.

Journal Papers

- **Fortune, B. C.**, Cameron, C. J., Pretty, C. G., Hayes, M. P. "Modelling the Impedance of Electrode-Skin Interfaces in a Bipolar Electrode Configuration", BioMedical Engineering OnLine [Submitted]. *Forming the contents of Chapter 6.*

- **Fortune, B. C.**, Pretty, C. G., Cameron, C. J., McKenzie, L. R., Chatfield, L. T., Hayes, M. P. "Electrode–skin impedance imbalance measured in the frequency domain." Biomedical Signal Processing and Control, 63, 102202. *Forming the contents of Chapter 5.*

- **Fortune, B. C.**, Pretty, C. G., Chatfield, L. T., McKenzie, L. R., Hayes, M. P. "Data captured using low-cost active electromyography." Data in Brief, 29, (2020), 105239. *Contributing to the contents of Chapter 3.*

- **Fortune, B. C.**, Pretty, C. G., Chatfield, L. T., McKenzie, L. R., Hayes, M. P. "Low-cost active electromyography." HardwareX, 6 (2019): e00085. *Contributing to the contents of Chapter 3.*

Conference Papers

- **Fortune, B. C.**, McKenzie, L. R., Chatfield, L. T., Pretty, C. G. "Electrode-Skin Impedance Component Estimation in the Time-domain". 15th ASME/IEEE International Conference on Mechatronic and Embedded Systems and Applications (MESA 2019). *Forming the contents of Chapter 4.*

- **Fortune, B. C.**, McKenzie, L. R., Chatfield, L. T., Pretty, C. G. "Crosstalk Removal in Stimulus-evoked Forearm Electromyography". 10th IFAC Symposium on Biological and Medical systems, (BMS 2018).

- **Fortune, B. C.**, McKenzie, L. R., Chatfield, L. T., Pretty, C. G. "Crosstalk Removal in Forearm electromyography During Static Gripping". 14th ASME/IEEE International Conference on Mechatronic and embedded Systems and Applications (MESA 2018).

- **Fortune, B. C.**, Stewart, A., Hansenne, E., McKenzie, L., Chatfield, L., Pretty, C. G. "Design and testing of a low-cost electromyogram that uses a right leg driver circuit". 24th IEEE International Conference on Mechatronics and Machine Vision in Practice (M2VIP 2017).

Abstract

Stroke is the third leading cause of disability worldwide, commonly removing a subject's independence. However, physical therapy can assist a subject in regaining their lost functionality. Modern physical therapy is incorporating assistive robotic devices, allowing more intensive and repetitive training while reducing therapy cost.

The incorporation of surface electromyography (sEMG) into assistive robotics can enable patient-driven intention-based control, leading to increased patient interaction and a more natural, unconscious interface. sEMG is the non-invasive technique of measuring the bioelectrical activity of the skeletal muscle at the skin surface. The bioelectrical signal is bipolar with an amplitude of $\leq 10\,\mathrm{mV_{pk-pk}}$, a frequency spectrum of 0–500 Hz and is typically measured using two recording electrodes and a single reference electrode. However, electrical interference and bioelectrical crosstalk limit the efficacy of bioelectrical feedback for assistive robotic control.

In built-up environments, the human body is capacitively coupled to the mains power supply and ground, leading to interference potentials which are a function of the impedance imbalance between recording electrodes. The current methods of reducing electrical interference either removes a portion of the signal of interest; can have limited affect, resulting in large interference potentials; or can be time consuming with the potential to lead to skin irritation.

Bioelectrical crosstalk, detected with sEMG, is the phenomenon of one muscle's signal influencing the recording of another. Crosstalk can lead to misrepresentation of the target signal, increasing the difficulty to provide accurate biofeedback. The tripolar electrode configuration is commonly used to reduce crosstalk. However, using three electrodes increases the possibility of impedance imbalances between recording electrodes.

Previous research has focused on balancing the common-mode input impedance of the bioelectrical instrumentation device with the impedance of the electrode-skin interface. The common-mode interference potential was used as an indicator to control the required common-mode input impedance. However, without measuring the electrode-skin impedance, the unique transfer function of each electrode-skin interface will be unknown, reducing the ability to use the frequency spectrum of the bioelectrical signal for biofeedback. Therefore, there is a need to balance the impedance between electrode-skin interfaces and determine the resulting transfer function between the electrode-skin interface and the bioelectrical instrumentation device.

Commercial, research-level sEMG devices do not have an open source signal processing architecture. Therefore, to quantify the impact of balancing the impedance of multiple electrode-skin interfaces, a high quality near-raw signal output sEMG device was developed. The device has a resolution of 298 nV, a baseline noise of less than 5.2 μV_{rms} (when abrasive skin preparation is applied), a signal bandwidth of 21.2–433 Hz, a sampling rate of 1 kHz and built in 1 x 10 mm Ag bar electrodes.

Characterising the behaviour of the electrode-skin interface provides quantitative insight into optimising a compensatory system to balance the impedance between multiple electrode-skin interfaces. A method to model the step response of the electrode-skin interface was developed using simulation and physical, passive circuitry, resulting in a mean error per modelled component of 0.076% and 3.49% for simulation and passive circuitry, respectively.

However, the method was unsuccessful in modelling the electrode-skin interface of a human subject. The method relied on the system reaching steady state, which did not occur with the human subject during the 500 s recording period. This is thought to be due to an oversimplified model, and the step voltage changing the chemistry of the electrodes, causing ions to be removed from one electrode and attached to the other. To produce a method that could be used in real-time, frequency dependent stimulation and spectral analysis was used.

The impedance imbalance between electrode-skin interfaces at mains frequency (50 Hz) has been reported to have a typical range of 10–20 kΩ when using Ag/AgCl electrodes. In this work, a trial was conducted on ten subjects, where the electrode-skin impedance imbalance between two electrode-skin interfaces was recorded over a frequency range of 1 Hz–100 kHz, resulting in a mean impedance imbalance of (37.6 ± 47.1) kΩ and (15.0 ± 18.3) degrees using Ag/AgCl electrodes without skin preparation; (4.52 ± 7.65) kΩ and (4.6 ± 6.9) degrees using Ag/AgCl electrodes with abrasive skin preparation; and (36.2 ± 45.1) kΩ and (3.4 ± 3.6) degrees using Ag bar electrodes with abrasive skin preparation. These results indicate that the impedance imbalance between electrode-skin interfaces is larger than originally anticipated, and highlights the need to balance the impedance between electrode-skin interfaces.

The measured impedance data was used to characterise the electrode-skin interface using a seven-parameter model, consisting of resistive and constant-phase elements. A normalised root mean square error was used to quantify the model fit for the bioelectrical signal range (1–500 Hz), resulting in a mean error and standard deviation of (12.5 ± 14.7) % for the magnitude and (4.5 ± 4.9) % for the phase using Ag/AgCl electrodes without skin preparation, (3.2 ± 1.7) % for the magnitude and (6.2 ± 8.9) % for the phase using the Ag/AgCl electrodes with abrasive skin preparation, and (15.5 ± 17.9) % for the magnitude and (4.4 ± 1.8) % for the phase using the Ag bar electrodes with abrasive skin preparation.

A large contribution to the modelling error is thought to be due to noise in the raw data and the temporal relationship of the electrode-skin interface.

A novel system was developed to digitally measure and control the common-mode input impedance of the bioelectrical instrumentation device, with the aim of balancing the resulting transfer functions formed by each electrode-skin interface in series with the bioelectrical instrumentation device. The methods used to measure and model the electrode-skin interfaces were the foundation of estimating the required common-mode input impedance, and the developed sEMG device was used to measure the impact of the compensatory system. Another trial was conducted on ten subjects, where the bioelectrical signal from the biceps brachii was measured using a bipolar and tripolar electrode configuration, and the bioelectrical signal from the triceps brachii was simultaneously measured using a bipolar electrode configuration. The compensatory system was implemented on the tripolar electrode configuration, resulting in a mean reduction of electrical interference of $(43.9 \pm 49.2)\%$ at the mains supply frequency (50 Hz) and $(69.4 \pm 36.2)\%$ at the second harmonic of the mains supply frequency (100 Hz). There was no crosstalk detected for any of the subjects. Therefore, the efficacy of the tripolar electrode configuration for crosstalk reduction could not be verified.

Overall, this thesis developed and validated a method of measuring the impedance of multiple individual electrode-skin interfaces, wideband modelling of the electrode-skin interface for multiple electrode configurations, and a method to balance and measure the transfer functions formed by each electrode-skin interface in series with the bioelectrical instrumentation device. The resulting system reduces electrical interference produced by capacitive coupling of the human body to the mains supply, with the possibility of increasing the efficacy of bioelectrical feedback for assistive robotic control.

Contents

List of Figures

List of Tables

List of Abbreviations

ADL activities of daily living

ARV average rectified value

BSS blind signal separation

CIA custom impedance analyser

CPE constant phase element

DTFT discrete-time Fourier transform

DUT device under test

FFC flat flexible cable

FFT fast Fourier transform

FIR finite impulse response

KIA Keysight Technologies E4990A impedance analyser

NLLS non-linear least squares

NRMSE normalised root mean square error

ODR output data rate

PSD power spectral density

RMS root mean square

RMSE root mean square error

SNR signal-to-noise ratio

Neuromuscular Abbreviations

ACh acetylcholine

ADP adenosine diphosphate

ATP adenosine triphosphate

MUAP motor unit action potential

MUAPT motor unit action potential train

Bioelectrical Abbreviations

Ag silver

Ag/AgCl silver-silver chloride

BE branched electrode

DD double differential

ECG electrocardiography

EEG electroencephalography

EMG electromyography

RLD right leg driver

sEMG surface electromyography

Electrical Abbreviations

AC alternating current

ADC analogue-to-digital converter

CMRR common-mode rejection ratio

DC direct current

EMF electromotive force

ESD electrostatic discharge

CHAPTER 1

Introduction

1.1 Stroke and Rehabilitation

Stroke is the third leading cause of disability (Feigin et al., 2014) and the fifth most common cause of death worldwide (Benjamin et al., 2017). It is common for stroke to impair a subject's ability to perform activities of daily living, removing a subject's independence. However, physical therapy can enable a subject to regain their lost functionalities (Dam et al., 1993; Smith et al., 1981). Traditional rehabilitation is time consuming and labour intensive, potentially resulting in a costly rehabilitation. With the age of the population and life expectancy increasing, there is demand for an improved quality of life for the elderly and disabled, therefore, research focused on producing affordable and more widely accessible assistive robotic devices to aid rehabilitation is predicted to increase (Gelderblom, Wilt, Cremers, & Rensma, 2009). Assistive robotic devices can reduce the time and physical exertion required from a therapist, allowing more intensive repetitive training while reducing the cost of therapy (Díaz, Gil, & Sánchez, 2011).

Surface electromyography (sEMG) can be incorporated into assistive robotics to enable patient-driven intention-based control. sEMG is the non-invasive technique of measuring the bioelectrical activity of the skeletal muscle at the skin surface (Basmajian & De Luca, 1979). Generally, bioelectrical instrumentation measures a differential potential between recording electrodes with respect to a reference electrode. Specifically for sEMG, the bipolar electrode configuration is commonly used, requiring two recording electrodes and one reference electrode. The recording electrodes are placed above the muscle of interest, and the reference electrode is best placed above electrically neutral tissue (De Luca, 2002).

Surface electromyography incorporated with assistive robotic devices can increase patient interaction compared to standard kinematic and kinetic sensors alone (Kawamoto & Sankai, 2002) and support a more natural unconscious interface compared to manual controllers, such as a joystick (Sankai, 2010). The bioelectrical signals occur 2–3 ms before a muscle contraction (Basmajian & De Luca, 1979), allowing synchronous device and subject motion (Kawamoto, Lee, Kanbe, & Sankai, 2003). However, electrical interference and bioelectrical crosstalk limit the practical ability to use bioelectrical signals for assistive robotic control.

1.1.1 Electrical Interference

Bioelectrical signals can be contaminated by mains supply interference, limiting the signal-to-noise ratio (SNR) of the recorded signal. In built-up environments, the human body is capacitively coupled to the mains power supply and ground, causing conduction currents to flow through the human body (Huhta & Webster, 1973; Metting van Rijn, Peper, & Grimbergen, 1990; Webster, 2009). The conduction currents result in a common-mode potential at the recording electrodes. Each electrode in contact with the skin has a high impedance electrode-skin interface, which has the potential to distort the common-mode signal into a differential-mode signal due to the potential divider effect (Huhta & Webster, 1973; Metting van Rijn et al., 1990; Pacela, 1967).

In addition, electrode leads are typically used to transmit the bioelectrical signal from the recording electrodes to the bioelectrical instrumentation device. The electrode leads are also capacitively coupled to the mains supply (Huhta & Webster, 1973; Metting van Rijn et al., 1990; Webster, 2009). Since the input impedance of the bioelectrical instrumentation device is orders of magnitude larger than the electrode-skin impedance, the capacitive coupling causes conduction currents to flow into the electrode leads and to ground. The conduction currents produce a differential-mode potential as a function of the conduction current and the electrode-skin impedance imbalance.

There are methods of reducing this interference, but the efficacy of these techniques are limited. The capacitive coupling between the electrode leads and the mains power supply can be reduced using shielded electrode leads, but the distributed capacitance of the shielded cable reduces the input impedance of the bioelectrical instrumentation device, increasing the differential-mode interference produced due to the potential divider effect (Betts & Brown, 1976; Huhta & Webster, 1973; Metting van Rijn et al., 1990; Webster, 2009). The high impedance path to ground through the electrode-skin interface in which the coupled conduction currents flow, can be reduced by implementing active electrodes. Active electrodes couple the recording electrodes with low output impedance operational amplifiers on the same module, limiting the resulting differential-mode potential due to the flow of conduction currents (Huhta & Webster, 1973). Active electrodes are not always used as they have fixed interelectrode distances, limiting their use between different muscle sites and recording techniques.

The interference current caused by capacitive coupling of the subject to the mains supply can be reduced using a right leg driver (RLD). The RLD reduces the effective reference electrode impedance (Winter & Webster, 1983a), reducing common-mode interference, and limiting the impact of the potential divider effect. The RLD reduces common-mode interference by driving the reference electrode to the inverted common-mode interference

potential. However, while effective at reducing electrical interference, the RLD does not eliminate it.

Skin preparation reduces the electrode-skin impedance, reducing the maximum possible electrode-skin impedance imbalance (Searle & Kirkup, 2000). Skin preparation is achieved by methods ranging from cleaning the skin with alcohol, to abrading the skin surface with sand paper (Betts & Brown, 1976). However, skin preparation can be time consuming, lead to skin irritation and large interference potentials when performed incorrectly.

Filtering methods are commonly used to reduce the remaining differential-mode interference. Typically, an analogue notch filter (Hardalaç & Canal, 2004), or digital filtering is applied (Supuk, Skelin, & Cic, 2014; Youn & Kim, 2009). However, as the differential interference is within the frequencies of interest, the filtering also attenuates the signal of interest.

1.1.2 Crosstalk

Bioelectrical crosstalk, detected with sEMG, is the phenomenon of one muscle's signal influencing the recording of another. Crosstalk contamination makes it difficult to measure the bioelectrical signal from a single muscle, which can lead to misrepresentation of the target signal, making it difficult to provide accurate biofeedback. Crosstalk is due to spatially overlapping fibre territories, tissue volume conduction (Kilner, Baker, & Lemon, 2002) and the extinction of the action potentials at the tendons (Basmajian & De Luca, 1979; De Luca, 1997; Farina, Merletti, Indino, Nazzaro, & Pozzo, 2002). The skin tissue acts as a low pass filter with the cut-off frequency decreasing as the distance from the signal source to the skin surface increases. Since crosstalk signals typically originate further from the skin surface than target muscles, crosstalk can be low frequency and appear as common-mode voltage (Basmajian & De Luca, 1979; Broman, Bilotto, & Luca, 1985; De Luca & Merletti, 1988). However, human tissue is anisotropic and inhomogeneous, introducing

a phase shift into the volume conducted signal components. This phase shift distorts the crosstalk signals, resulting in voltage gradients (Broman et al., 1985).

A common crosstalk reduction method, the tripolar electrode-configuration, records the average potential of two flanking electrodes with respect to a centre electrode. The configuration was developed to reject voltage gradients that are situated along the axis of the recording electrodes. The tripolar electrode configuration permits the distinction of a distant source producing a voltage gradient, and a local bioelectrical signal from the desired muscle. The tripolar electrode configuration can be superior to the bipolar electrode configuration (De Luca, Kuznetsov, Gilmore, & Roy, 2012; Koh & Grabiner, 1993; Van Vugt & Van Dijk, 2001). Therefore, balancing the impedance of three electrode-skin interfaces may reduce electrical interference and crosstalk contamination simultaneously, with the potential to improve bioelectrical signal acquisition.

1.1.3 Balancing the Impedance of Electrode-skin Interfaces

Previous research has been conducted on balancing the impedance between two electrode-skin interfaces by adding some form of compensation, but there are limitations in these studies. Compensation has been applied to an electrode pair submerged in a saline solution (zero contact with the human body), removing the variability associated with the human body (Nag, Sikdar, Thakor, Rao, & Sharma, 2015). Therefore, this method cannot be applied to balance electrode-skin interfaces produced by electrodes in contact with the human skin. Tuning compensatory impedance to minimise common-mode interference has been implemented. This was achieved using manual tuning (Adli & Yamamoto, 1998), and in-phase and quadrature component signal techniques (Parente et al., 2018). The common-mode interference potential was used as an indicator to control the common-mode input impedance of the bioelectrical instrumentation device. However, without measuring the electrode-skin impedance, the unique transfer function produced by each electrode-skin interface in series with the compensatory impedance will be unknown. Therefore, the

frequency spectrum of the bioelectrical signal will be attenuated by an unknown frequency dependent gain, limiting the ability to use the frequency content of the bioelectrical signal for biofeedback.

1.2 Preface

The aim of this thesis is to develop a novel real-time electrode-skin impedance balancing system to improve bioelectrical signal capture, particularly for sEMG. A trial will be conducted to quantify the electrode-skin impedance imbalance over a number of subjects and different electrode configurations. This data will permit modelling the electrode-skin interface, which will provide valuable insight to the electrode-skin interface. Using the experimental data, a non-linear electrode-skin impedance compensatory system will be developed. A second trial will be conducted to quantify the reduction of electrical interference and crosstalk contamination using the novel electrode-skin impedance compensation system.

This work involves hardware development to measure and balance the electrode-skin interface, involving the production of an sEMG device; an electrode-skin impedance measurement system that can record the impedance imbalance between electrode-skin interfaces; and a novel electrode-skin impedance compensatory system. This work also involves software development to control the hardware, model the electrode-skin impedance and optimise the compensatory system used to balance multiple electrode-skin interfaces.

1.2.1 Contributions to the Field

The novelty of this work is the development of a real-time system that simultaneously measures and balances the impedance of three electrode-skin interfaces for electrical interference and crosstalk contamination reduction, with the ability of quantifying the improvement of sEMG signal acquisition. This removes the limitations of existing systems which do not apply electrode-skin impedance imbalance compensation, or produce unknown frequency

dependent attenuation due to their compensatory system.

To my knowledge, there has not been a study on how adding compensatory impedance to balance multiple electrode-skin interfaces affects bioelectrical signal recording quality in the presence of crosstalk contamination. Reducing electrical interference and crosstalk contamination has the potential to increase bioelectrical signal acquisition, permitting a more accurate assistive robotic device control based on voluntary muscle contractions, increasing the efficacy of stroke rehabilitation.

1.2.2 Overview

An overview of this thesis is outlined below:

Chapters 1 and 2 provide background information and context for the content of this thesis.
Chapter 1 introduces the challenges associated with sEMG.
Chapter 2 provides detailed background knowledge and context about assistive robotic devices in stroke rehabilitation, the origin of the bioelectrical signal, sources of electrical interference and crosstalk contamination, and existing methods to improve bioelectrical signal acquisition. This detailed background allows a better understanding of the limitations and current methods used to improve the signal quality of sEMG.

Chapter 3 outlines the hardware design, developed as an open source bipolar active electrode sEMG device. The data from testing the device on three subjects is also outlined in this chapter. The basis of this design is used to assist in quantifying the impact of balancing multiple electrode-skin interfaces (results presented in Chapter 8).

Chapter 4 presents the method used to model the electrode-skin interface in the time domain. It was determined that measuring and modelling the electrode-skin interface is more effective in the frequency domain.

Chapter 5 describes the process used to measure the impedance of the electrode-skin interface in the frequency domain. A trial was conducted on ten subjects, where the impedance of the electrode-skin interface for the ten subjects was measured using three electrode configurations. This chapter highlights the extent of the electrode-skin impedance imbalance, confirming the need to balance electrode-skin interfaces.

Chapter 6 develops a model for the electrode-skin interface using the data from Chapter 5. It was verified that purely capacitive elements could not produce an accurate fit for the three electrode configurations, therefore, constant phase elements (CPEs) were employed. The resulting model contained seven-parameters, consisting of resistive and constant-phase elements.

Chapter 7 describes the novel electrode-skin impedance compensation method. The input impedance of the bioelectrical instrumentation device was balanced with the impedance of the electrode-skin interface. This was simultaneously performed for three electrodes in a tripolar electrode configuration. The method was achieved by measuring the impedance of the electrode-skin interfaces, characterising the electrode-skin interfaces using a resistive-capacitive model, and applying resistive-capacitive compensation to minimise the imbalance between the transfer functions of the electrode-skin interface and the bioelectrical instrumentation device.

Chapter 8 presents the results from applying the compensatory system to ten subjects. It was verified that the compensatory system was effective in reducing electrical interference. However, crosstalk was not present in any of the subjects during the trial. Therefore, only the reduction in electrical interference could be quantified.

Chapters 9 and 10 provide a summary of this thesis and highlights possible avenues to extend and complement the work presented in this thesis.

CHAPTER 2

Literature Review

2.1 Assistive Robotics in Stroke Rehabilitation

Stroke is the third leading cause of disability (Feigin et al., 2014) and the fifth most common cause of death worldwide (Benjamin et al., 2017). It is common for stroke to lead to paralysis of one side of the body: this neurological impairment is known as hemiplegia. Hemiplegia drastically impairs a subject's ability to perform activities of daily living (ADL), such as bathing, eating and transferring. Not being able to perform ADL removes a subject's independence. However, physical therapy can enable a subject to regain their lost functionalities, allowing them to once again perform ADL (Dam et al., 1993; Smith et al., 1981).

Without rehabilitation, a subject with stroke will suffer deterioration of muscle strength, which can lead to spastic, uncontrollable movements; lessened sensory awareness on their affected side; or unnatural, compensatory joint movements to perform a given task. Performing functional activities during rehabilitation is required for a fast and successful re-

covery. It has been shown that the brain can produce new neural pathways needed for the relearning of ambulation and upper extremity motion (Dam et al., 1993).

The field of assistive robotic devices is expanding due to multiple factors: traditional stroke rehabilitation is labour intensive and the need for care is increasing with the increasing age of the population. Traditional rehabilitation is time consuming and labour intensive, especially the rehabilitation of a subject's gait. Typically, at least three therapists are required to manually manipulate a subject's torso and lower extremities to enable the subject to produce ambulation. This process can result in a costly rehabilitation. With the age of the population increasing, and the demand for an improved quality of life for the elderly and disabled, the expected shortage of health care professionals is predicted to increase the research efforts into producing affordable and more widely available assistive robotic devices (Gelderblom et al., 2009).

Assistive robotic devices can reduce the time and physical exertion required for a therapist, allowing more intensive, repetitive training while reducing the therapy cost. Robotic devices can also provide quantitative motor level recovery measurements and ambulation patterns, permitting an easier measure of subject recovery (Díaz et al., 2011).

Electromyography (EMG) can be incorporated into assistive robotic devices to enable patient-driven intention-based control. EMG is the technique applied to measure the bioelectrical signal produced from a subject's volitional muscle contraction (Basmajian & De Luca, 1979). When EMG is incorporated with assistive robotic control, patient interaction can increase (Kawamoto & Sankai, 2002) and support a more natural unconscious interface (Sankai, 2010). The bioelectrical signals occur 2–3 ms before a muscle contraction (Basmajian & De Luca, 1979), allowing synchronous device and subject motion (Kawamoto et al., 2003).

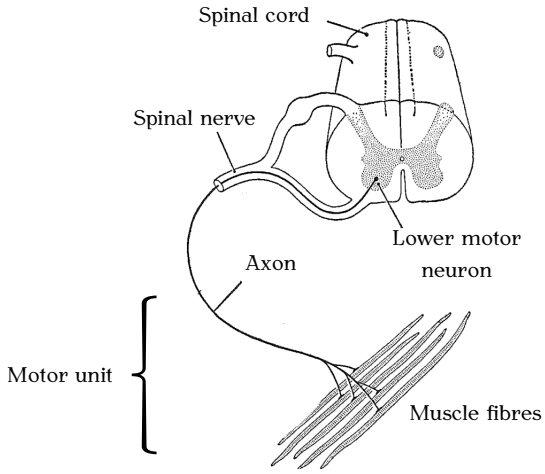

Figure 2.1: The motor unit, consisting of several muscle fibres innervated by a single axon, and its associated alpha motor system (Basmajian & Szatmari, 1955).

2.2 Neuromuscular System

The neuromuscular system is comprised of muscles and the associated innervating nerves. This system establishes the link between brain activity and movement produced by muscle contraction.

2.2.1 Motor Units and the Nerve Action Potential

The motor unit and its associated alpha motor system are the basic level of the nervous system organisation of the muscle (Patton & Thibodeau, 2010; Reece et al., 2011). This system consists of the lower motor neuron, its axon and the various muscle fibres it innervates, Figure 2.1. The number of muscle fibres innervated by a single motor unit can range from 100, in the hand, to 2000, in the lower limb (Buchthal & Schmalbruch, 1980). When a muscle contracts, initially the smallest motor units are recruited, but as the exertional demand increases, the synaptic drive and excitatory potential firing rates increase, resulting in the recruitment of larger motor units and increased contraction strength (Cram, 1998).

When the spatial and temporal summation of excitatory potentials received by the neuron is above its threshold, cell body depolarisation is initiated, triggering the production of a

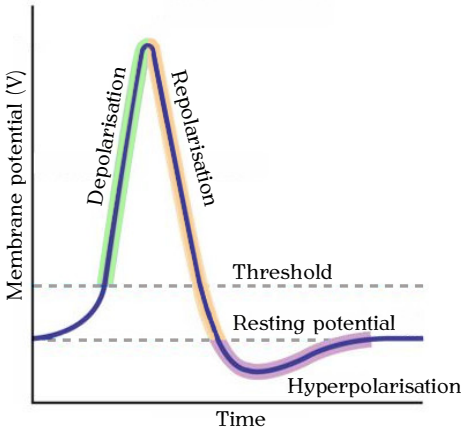

Figure 2.2: Nerve action potential due to excitatory potential summation above the neuron's threshold. Based on figure from (Patton & Thibodeau, 2010).

nerve action potential, Figure 2.2. Voltage gated ion channels located in the axon control the flow of nearby ions, where the state of the ion channel (open or closed) is controlled by its electric potential. Depolarisation of the cell body opens the sodium ion voltage gated channels, resulting in an inrush of sodium ions due to electrical and diffusion forces. This causes a chain reaction, opening the next closest sodium ion voltage gated channel. The same spatial and temporal summation of excitatory potentials that opened the sodium ion voltage gated channel, also cause potassium ion voltage gated channels to open. However, these channels have a slower response time than the sodium ion channels. The potassium ions in the membrane get driven out of the cell due to electrical and diffusion forces, hyperpolarising the membrane potential. This process of depolarisation and hyperpolarisation produces the nerve action potential.

The axon connects to multiple muscle fibres, creating neuromuscular synapses. When the nerve action potential reaches a synapse, the neurotransmitter, acetylcholine (ACh), is released into the junction. The release of ACh causes a charge to travel along the cell membrane. Transverse tubules extend into the cell membrane, allowing the charge to penetrate the cell membrane and open the pores of the sarcoplasmic reticulum, releasing calcium ions (Ca^{++}), Figure 2.3. The branched axons vary in length and diameter, affecting the time required for the nerve action potential to reach the neuromuscular synapses.

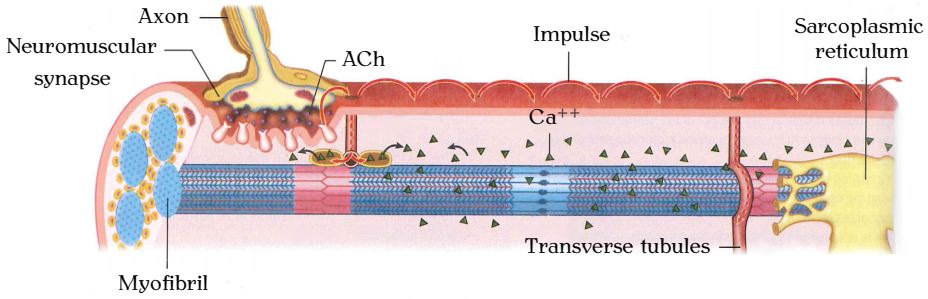

Figure 2.3: A nerve action potential causing the release of acetylcholine (ACh) at the neuromuscular junction, resulting in the sarcoplasmic reticulum releasing calcium ions (Ca^{++}) to initiate a muscle contraction. Modified from (Patton & Thibodeau, 2010).

The varied transmission periods result in asynchronous activation of the muscle fibres, producing smooth muscle contractions.

2.2.2 Muscle Composition

Skeletal muscles are comprised of a series of small compartments known as muscle fascicles, which are situated along the same direction, separated and protected by connective tissue, (Andersen, Schjerling, & Saltin, 2000; Patton & Thibodeau, 2010; Reece et al., 2011). Each muscle fascicle contains a series of muscle cells (muscle fibres), which are made up from clusters of myofibril, Figure 2.4. Each myofibril contains segments called sarcomeres, which are made up of overlapping myosin and actin filaments. The myosin and actin filaments produce the movement to create the muscle contraction. This layout is the basic structure of every skeletal muscle.

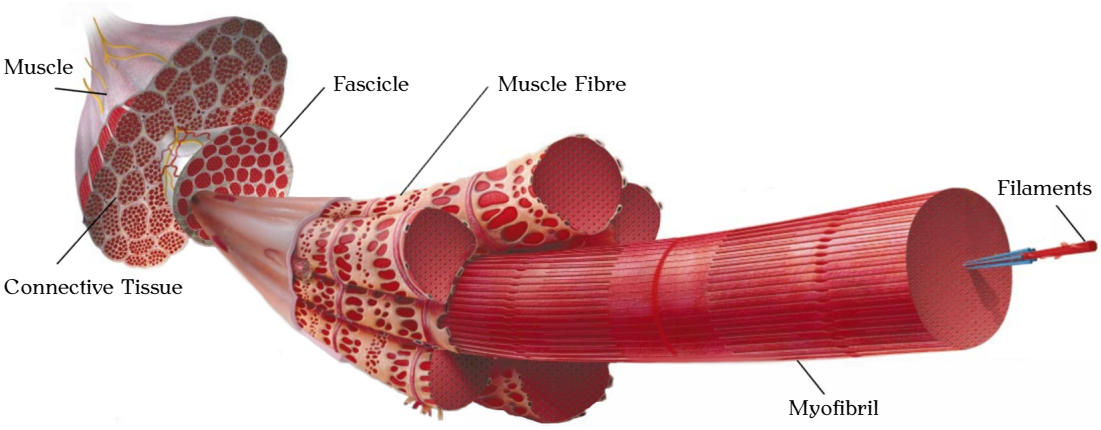

Figure 2.4: Muscle composition showing the series of components which make up a skeletal muscle. Modified from (Andersen et al., 2000).

Myosin is a thick filament containing molecules with globular heads, and actin is a thin filament composed of two molecules which spiral around each other, Figure 2.5. The myosin heads attach to binding sites located on the actin to produce a contraction force. This phenomenon is characterised by the sliding filament model (Hodgkin & Huxley, 1952; Huxley & Niedergerke, 1954). When the muscles are not contracting, the actin-myosin binding sites are covered by tropomyosin, a protein that is spiralled around the actin. The tropomyosin have regulatory proteins, troponin, that trigger muscular contractions when the calcium ions bind to them.

The myosin and actin filaments are negatively charged, mutually repelling each other. The myosin heads have a single adenosine triphosphate (ATP) molecule attached to it. When calcium attaches to the troponin, the tropomyosin changes shape, revealing the actin-myosin binding sites. The strong positive charge of the bonded calcium ions attract the negatively charged myosin filament. This chemically induced electromagnetic attraction forces the two filaments against each other, flattening out the myosin head and producing the ratcheting effect of the sliding filament model. The erection of the myosin depletes the ATP, resulting in adenosine diphosphate (ADP). To maintain the ratcheting effect, increasing the muscles fibres contraction strength, another ATP molecule binds to the myosin head and the process of flattening the myosin head against the actin-myosin binding site continues. Once the calcium ions have been freed from the troponin, the tropomyosin changes back to its original shape, blocking the actin-myosin binding sites and stopping the muscle contraction. This results in both filaments becoming negatively charged and repealing each other once again.

2.2.3 Motor Unit Action Potential

The release of ACh at the neuromuscular synapse produces a motor unit action potential (MUAP). Repeated firing of the motor unit results in the repeated release of ACh, resulting in a motor unit action potential train (MUAPT). EMG records the spatial summation of

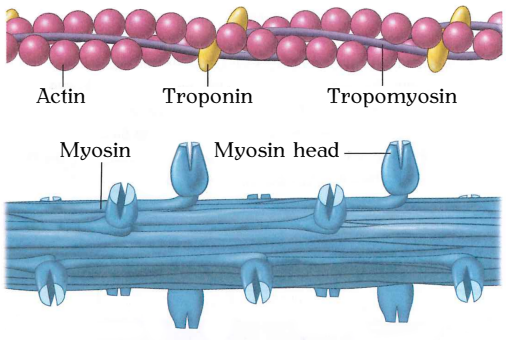

Figure 2.5: The myosin and actin filaments (Patton & Thibodeau, 2010).

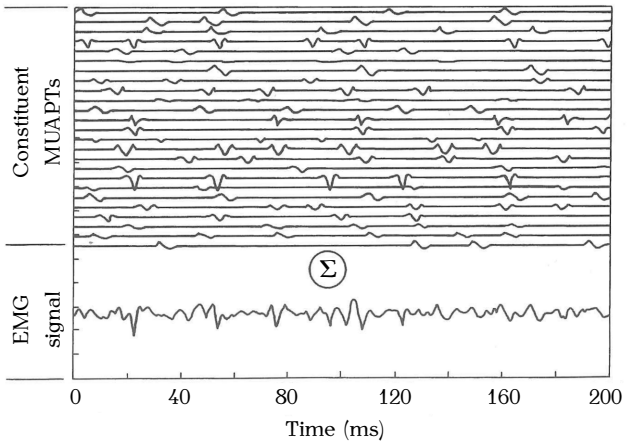

Figure 2.6: Summation of motor unit action potential trains (MUAPTs) to produce the bioelectric signal measured using an EMG device (Cram, 1998).

continuous MUAPTs (Basmajian & De Luca, 1979), Figure 2.6. A MUAP from a single muscle fibre is difficult to record, since motor units typically overlap their fibre territories spatially. The cross-sectional area of the muscle fibre is 10–30 times smaller than the cross sectional area of the motor unit territory (Brandstater & Lambert, 1973; Buchthal, Erminio, & Rosenfalck, 1959). Therefore, a single MUAPT can only be measured during very weak muscle contractions, when very few fibres are recruited (Basmajian & De Luca, 1979). The amplitude of the bioelectrical signal detected at the skin surface using EMG ranges from microvolts to millivolts (Basmajian & De Luca, 1979; De Luca, 2002), and is a function of the adipose tissue, muscle tissue, muscle fibre diameter, and the distance between the muscle fibre and the electrode recording site.

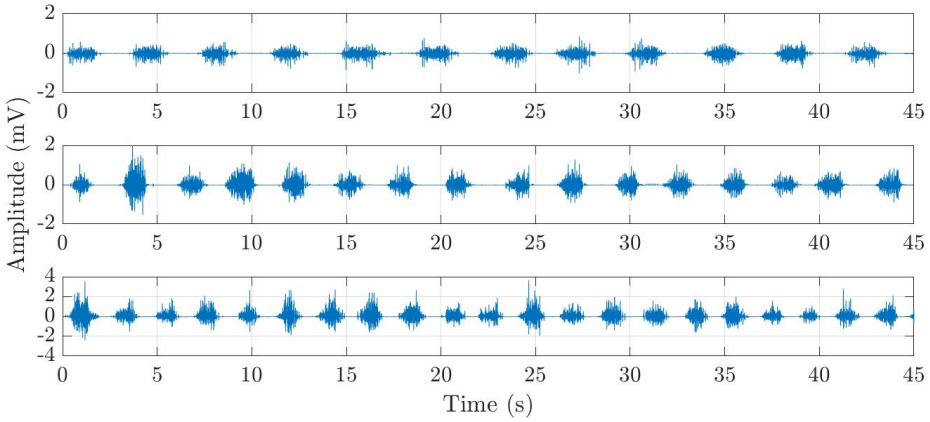

Figure 2.7: Raw sEMG captured from three able-body subjects performing multiple contractions of the biceps brachii. Note the difference in the vertical axis scales.

2.3 Surface Electromyography (sEMG)

Surface electromyography (sEMG) is the non-invasive technique of measuring the bioelectrical activity of the skeletal muscle at the skin surface, Figure 2.7. Bioelectrical instrumentation measures a differential potential between the recording electrodes with respect to a reference electrode. The most common electrode configuration in sEMG, the bipolar electrode configuration, uses two recording electrodes and the reference electrode. The recording electrodes are placed above the muscle of interest, and the reference electrode is best placed above an electrically neutral site on the subject (providing a more stable reference potential) for example, over a bony prominence (De Luca, 2002).

An electrode in contact with a human produces an electrode-electrolyte interface, resulting in a direct current (DC) offset known as a half-cell potential (Thakor, 2015). The magnitude of the half-cell potential is dependent on the electrode material and the electrolyte medium. Typically, adhesive electrodes with an electrolyte medium (wet electrodes) are used for sEMG. The most commonly used wet electrode is silver-silver chloride (Ag/AgCl), since its chemical composition is less sensitive to electrolyte concentration and has a low half-cell potential (Pacela, 1967). However, wet electrodes have their limitations: they are single use, need to be replaced every few days during long term monitoring, and have

large adhesive surfaces. Therefore, wet electrodes can be expensive, and they typically necessitate large interelectrode distances ($\geq$ 20 mm), resulting in less sensitive recordings. Dry electrodes consist of conductive material without an electrolyte medium. Dry electrodes are becoming more popular due to being multi-use, having the ability of being used for long-term monitoring, and they can have small interelectrode distances. However, the trade off with dry electrodes is an increased electrode-skin impedance and a less stable half-cell potential resulting from naturally occurring electrolytes, such as sweat.

Surface electromyography has been used for subject intention estimation, force estimation, limb angle estimation and determining the level of muscle activation (Chandrapal, 2012; Sankai, 2010). However, the challenges associated with sEMG must be well understood to produce a device capable of performing usable biofeedback. The two main challenges with sEMG are electrical noise and bioelectrical crosstalk.

2.3.1 Electrical Noise

Electrical interference recorded during sEMG due to changing external electrical and magnetic fields is typically attributed to magnetic induction, and capacitive coupling of the subject and electrode leads to the mains supply (Huhta & Webster, 1973; Metting van Rijn et al., 1990; Webster, 2009; Winter & Webster, 1983b).

Magnetic induction

Magnetic induction produces an electromotive force (EMF) around a conduction loop when a changing magnetic flux density passes through the loop (Huhta & Webster, 1973). A conduction loop is formed between the bioelectrical recording device, electrode leads and human subject, Figure 2.8. Assuming a constant loop orientation and magnetic field frequency, the peak induced EMF is proportional to the magnitude of the flux density, and loop area,

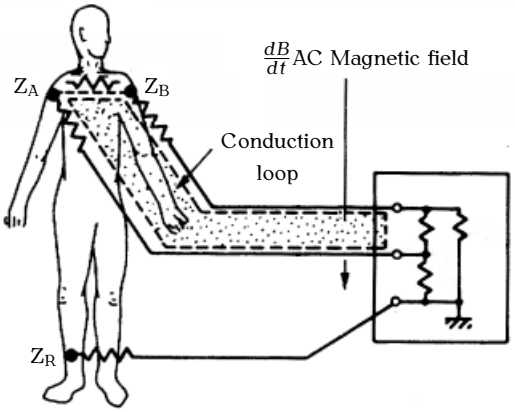

Figure 2.8: Conduction loop formed with the recording device, electrode leads and human subject. Modified from (Huhta & Webster, 1973).

$$\mathrm{EMF}_{\mathrm{peak}} = K \cdot B_M \cdot A\,, \tag{2.1}$$

where B_M is the magnetic flux density caused by the alternating current (AC) of the mains supply; A is the loop area produced by the recording device, electrodes and human subject; and K is a proportionality constant that is a function of conduction loop orientation and magnetic field frequency.

To limit the interference associated with magnetic induction, the magnetic flux density or the loop area must be reduced. To minimise magnetic flux density, magnetic shielding must be implemented for the entire conduction loop area. As this is impractical, the conduction loop area is reduced by using twisted electrode leads, Figure 2.9.

Capacitive coupling of the human body

In built-up environments, the human body is capacitively coupled to the mains power supply and ground, causing the flow of displacement and conduction currents, resulting in interference potentials (Huhta & Webster, 1973; Metting van Rijn et al., 1990; Webster, 2009), Figure 2.10, where V_{mains} is the 240 V 50 Hz mains supply, V_{AB} is the total differential-mode

interference, C_{pow} is the capacitive coupling between the subject and mains supply, C_{body} is the capacitive coupling between the subject and ground, C_A is the capacitive coupling between electrode lead A and the mains supply, C_B is the capacitive coupling between electrode lead B and the mains supply, C_{ISO} is the stray capacitance of the bioelectrical instrumentation device when it is isolated from mains ground (which is typically a larger impedance than that caused by C_{body} (Winter & Webster, 1983a)), I_{body} is the conduction current flowing into the subject's body, I_{lead_A} is the conduction current flowing through electrode lead A, I_{lead_B} is the conduction current flowing through electrode lead B, Z_A is the impedance of recording electrode A, Z_B is the impedance of recording electrode B, Z_R is the impedance of reference electrode, Z_{IA} and Z_{IB} are the common-mode input impedances of the bioelectrical instrumentation device.

Typical values for C_{pow} and C_{body} are 3 pF and 300 pF, respectively (Huhta & Webster, 1973; Winter & Webster, 1983b). This causes typical interference currents of $0.3\,\mu A_{pk-pk}$ to flow through the body. However, the size of the interference current is determined by how close the subject is to power sources and grounded objects (Winter & Webster, 1983b).

The interference current flowing through the subcutaneous skin layer causes differential-mode and common-mode interference potentials. The resistance of the subcutaneous layer

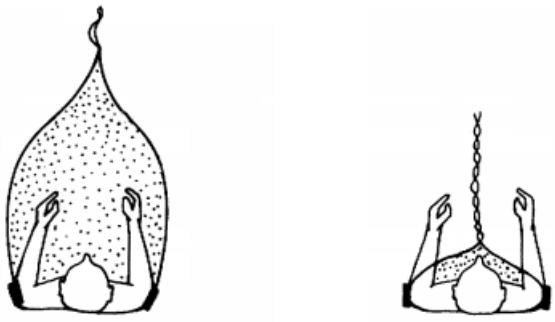

(a) Large conduction loop area.

(b) Reduced conduction loop area.

Figure 2.9: Conduction loop area reduction due to implementing twisted electrode leads. Modified from (Huhta & Webster, 1973).

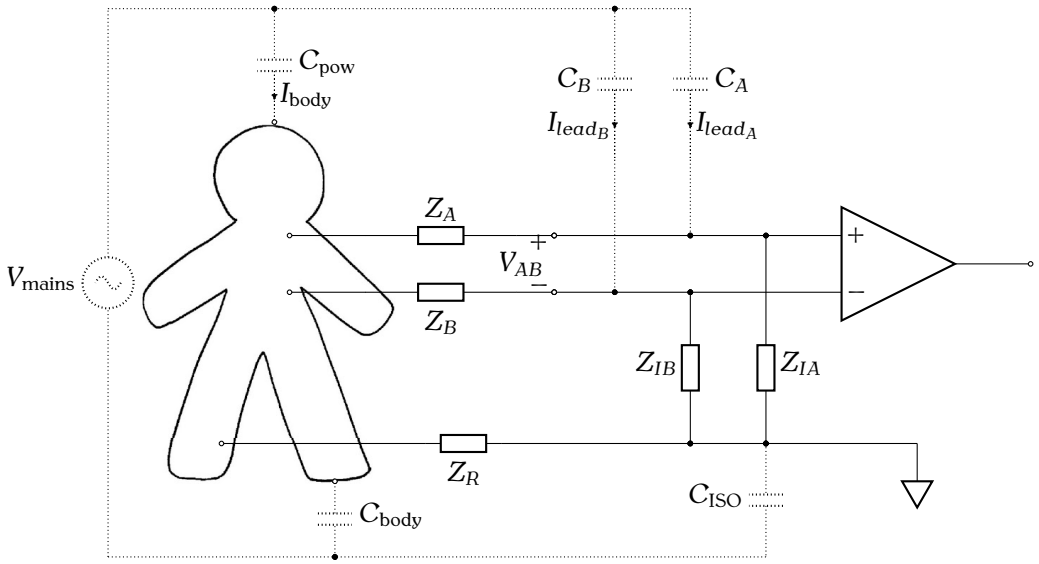

Figure 2.10: Bioelectrical instrumentation input source interference.

ranges from 20 Ω throughout the torso, to 400 Ω through the arm, therefore, interference currents entering the body through various locations produce different potentials throughout the body (Huhta & Webster, 1973).

The differential-mode interference potential is detected at the recording electrodes and amplified by the bioelectrical instrumentation. The differential-mode interference potential is a function of the differential subcutaneous resistance between the recording electrodes, ΔZ_S (which is dependent on the interelectrode distance and recording site), and the interference current,

$$V_{AB_{\text{BODY}}} = I_{\text{body}} \cdot \Delta Z_S \,. \tag{2.2}$$

A common-mode voltage is also produced from the displacement current flowing through the body. When the interelectrode distance is small, ΔZ_S is negligible in comparison to the reference electrode impedance. Therefore, the common-mode potential is quantified as,

$$V_{CM_{\text{BODY}}} = I_{\text{body}} \cdot Z_R \,. \tag{2.3}$$

A typical displacement current of $0.3\,\mu A_{pk-pk}$, an approximate differential subcutaneous resistance of $25\,\Omega$ (Rosell, Colominas, Riu, Pallas-Areny, & Webster, 1988) and a reference electrode impedance at mains frequency of $100\,\text{k}\Omega$ results in $7.5\,\mu\text{V}_{\text{pk-pk}}$ and $30\,\text{mV}_{\text{pk-pk}}$ differential- and common-mode interference potentials, respectively,

$$V_{AB_{\text{BODY}}} = 0.3\times10^{-6} \times 25 = 7.5\,\mu\text{V}_{\text{pk-pk}}\,, \tag{2.4}$$

$$V_{CM_{\text{BODY}}} = 0.3\times10^{-6} \times 100\times10^{3} = 30\,\text{mV}_{\text{pk-pk}}\,. \tag{2.5}$$

Depending on the many factors that dictate the amplitude of the bioelectrical signal, this level of differential-mode interference can result in a low signal-to-noise ratio (SNR), reducing the efficacy of bioelectrical signals being used for many uses, such as control.

This level of common-mode interference is low. However, a portion of common-mode interference is typically transformed into differential-mode interference due to the non ideal properties of the bioelectrical instrumentation device, increasing the differential-mode interference (Winter & Webster, 1983b). Large variations of C_{pow} and C_{body} are common, resulting in coupling capacitances up to three times larger (Huhta & Webster, 1973; Metting van Rijn et al., 1990), leading to proportionally larger interference potentials.

Capacitive coupling of the electrode leads

Electrode leads transmit the bioelectrical signal from the recording electrodes to the bioelectrical instrumentation device. The electrode leads are capacitively coupled to the mains supply (Huhta & Webster, 1973; Metting van Rijn et al., 1990; Webster, 2009), Figure 2.10. Since the input impedance of the bioelectrical instrumentation device is orders of magnitude larger than the electrode-skin impedance, the capacitive coupling causes conduction currents ($I_{\text{lead}_{A,B}}$) to flow into the electrode leads and to ground through C_{body} and Z_R in series with C_{ISO}. The conduction currents produce a potential on each electrode lead,

$$V_{\text{lead}_A} = Z_A \times I_{\text{lead}_A} + (I_{\text{lead}_A} + I_{\text{lead}_B})\, Z_R\,, \tag{2.6}$$

$$V_{\text{lead}_B} = Z_B \times I_{\text{lead}_B} + (I_{\text{lead}_A} + I_{\text{lead}_B})\, Z_R\,. \tag{2.7}$$

Typically, sEMG electrode leads are the same length and twisted together, therefore, it is assumed the conduction currents are equal, $I_{\text{lead}_A} = I_{\text{lead}_B} = I_{\text{lead}}$. Using this assumption, the differential- and common-mode interference potentials due to capacitive coupling of the electrode leads to mains supply can be estimated,

$$V_{AB_{\text{LEAD}}} = (Z_A - Z_B)\, I_{\text{lead}}\,, \tag{2.8}$$

$$V_{CM_{\text{LEAD}}} = \frac{(Z_A + Z_B)\, I_{\text{lead}}}{2} + 2 \cdot I_{\text{lead}} \cdot Z_R\,. \tag{2.9}$$

Huhta and Webster (1973) measured displacement currents caused by capacitive coupling of electrode leads to the mains supply, "In a typical experiment, a single 3-m length of number 20 [0.81 mm] unshielded wire picked up 6 nA (1 nA = 10^{-9} A) of displacement current under poor recording conditions (ac cords and equipment nearby)". Therefore, a 6 nA_{pk-pk} conduction current will be used for I_{lead}.

Electrode-skin impedance can range from 1 kΩ up to 100 kΩ at mains frequency when wet electrodes are used (Huhta & Webster, 1973), leading to typical electrode-skin impedance imbalances of 10–20 kΩ (Grimnes, 1983; Huhta & Webster, 1973; Metting van Rijn et al., 1990). However, impedance imbalances as large as 58 kΩ can occur (Olson, Schmincke, & Henley, 1979). Using Equation 2.8 with an electrode-skin impedance imbalance of 20 kΩ and a conduction current of 6 nA_{pk-pk}, a differential-mode interference of 120 $\mu V_{\text{pk-pk}}$ is produced (Metting van Rijn et al., 1990; Webster, 2009),

$$V_{AB_{\text{LEAD}}} = 20\times10^{3} \times 6\times10^{-9} = 120\,\mu V_{\text{pk-pk}}\,. \tag{2.10}$$

Using Equation 2.9 with recording and reference electrode-skin impedances of 100 kΩ in the presence of a 6 nA_{pk-pk} conduction current will produce a common-mode interference of 2 $mV_{\text{pk-pk}}$,

$$V_{CM_{\text{LEAD}}} = \frac{\left(100\times10^{3} + 100\times10^{3}\right) \times 6\times10^{-9}}{2} + 2\cdot6\times10^{-9}\cdot100\times10^{3} = 2\,mV_{\text{pk-pk}}\,. \tag{2.11}$$

Capacitive coupling of the electrode leads to the mains supply is a large source of differential-mode interference. Typically, electrode leads are shorter than 3 m, decreasing the con-

duction current through the electrode leads. However, electrode-skin impedance imbalances as high as 58 kΩ can be present when using wet electrodes, increasing the resulting differential-mode interference potential.

It is becoming popular to use dry electrodes, resulting in electrode-skin impedances up to 2 MΩ at 57 Hz (Searle & Kirkup, 2000). A larger electrode-skin impedance can result in larger electrode-skin impedance imbalances, leading to increased differential-mode interference. Although the differential-mode interference is large, the associated common-mode interference is small.

Half-cell potential

Bioelectrical instrumentation produce a differential recording between multiple electrodes. However, the half-cell potential produced by each electrode-skin interface is typically a different magnitude (Pallas-Areny, Colominas, & Rosell, 1989), resulting in a differential-mode DC offset that can be larger than the bioelectrical signal. A large DC potential requires a lower differential gain, which is further limited for low voltage systems (Spinelli, Pallas-Areny, & Mayosky, 2003). A low differential gain limits the common-mode rejection ratio (CMRR), and therefore, the SNR.

Potential divider effect

An imbalanced source or input impedance can result in common-mode interference being converted to differential-mode interference. This phenomenon is known as the potential divider effect (Huhta & Webster, 1973; Metting van Rijn et al., 1990; Pacela, 1967). The interference potential at each recording electrode due to the potential divider effect is,

$$V_{A_{\mathrm{COM}}} = V_{CM}\left[\frac{Z_{IA}}{Z_{IA} + Z_A}\right], \tag{2.12}$$

$$V_{B_{\mathrm{COM}}} = V_{CM}\left[\frac{Z_{IB}}{Z_{IB}+Z_B}\right] . \tag{2.13}$$

The amount of differential-mode interference caused by the potential divider effect, $V_{AB_{\mathrm{COM}}}$, can be estimated. Two assumptions are applied: bioelectrical instrumentation common-mode input impedance is balanced ($Z_{IA} = Z_{IB} = Z_I$) and the electrode-skin impedances are far less than the bioelectrical instrumentation input impedance. Applying these assumptions, the differential-mode interference caused by the potential divider effect is,

$$V_{AB_{\mathrm{COM}}} = V_{CM} \times Z_I\left[\frac{Z_B - Z_A}{Z_A \times Z_B + Z_I\left(Z_A + Z_B\right) + Z_I^2}\right] , \tag{2.14}$$

$$V_{AB_{\mathrm{COM}}} = V_{CM}\left[\frac{Z_B - Z_A}{Z_I}\right] \qquad \left(Z_{A,B} \ll Z_I\right) , \tag{2.15}$$

where V_{CM} is the sum of the common-mode interference potentials produced from capacitive coupling of the human body (Equation 2.5) and the electrode leads to the mains supply (Equation 2.11),

$$V_{CM} = V_{CM_{BODY}} + V_{CM_{LEAD}} = 32\,\mathrm{mV_{pk-pk}} . \tag{2.16}$$

Typically, the bioelectrical instrumentation device uses an instrumentation amplifier, with a typical common-mode input impedance of $R_i||C_i = 100\,\mathrm{G\Omega}\,||\,9\,\mathrm{pF}$ (Texas Instruments, 2018). A typical electrode-skin impedance imbalance of $20\,\mathrm{k\Omega}$ at $50\,\mathrm{Hz}$, in the presence of a common-mode interference potential of $32\,\mathrm{mV_{pk-pk}}$, results in a differential-mode

interference of $1.8\,\mu V_{\mathrm{pk-pk}}$ due to the potential divider effect,

$$V_{AB_{\mathrm{COM}}} = 32\times10^{-3}\left[\frac{20\times10^{3}}{350\times10^{6}}\right] = 1.8\,\mu V_{pk-pk}\,, \tag{2.17}$$

where the input impedance magnitude at 50 Hz is,

$$|Z_i| = |R_i \,||\, C_i| = \left|\left[\frac{1}{R_i} + \frac{1}{Z_{C_i}}\right]^{-1}\right| = \frac{1}{\sqrt{\frac{1}{R^2} + (2\pi fc)^2}} = 350\,\mathrm{M\Omega}\,. \tag{2.18}$$

The differential-mode interference produced by the potential divider effect is lower than the differential-mode interference caused by capacitive coupling. However, larger electrode-skin impedances will increase common-mode interference and result in larger impedance imbalances. These two factors increase the impact of the potential divider effect, reducing the SNR and the ability to use sEMG for assistive device control.

Interference reduction

The total differential-mode interference due to capacitive coupling and the potential divider effect is approximately $130\,\mu V_{pk-pk}$. This is calculated using,

$$\begin{aligned} V_{AB} &= V_{AB_{BODY}} + V_{AB_{LEAD}} + V_{AB_{\mathrm{COM}}}\,, \\ &= 7.5\times10^{-6} + 120\times10^{-6} + 1.8\times10^{-6}\,, \\ &= 130\,\mu V_{pk-pk}\,. \end{aligned} \tag{2.19}$$

Since the bioelectrical signal amplitude ranges from microvolts to millivolts, this level of

interference can be larger than the bioelectrical signal. However, there are methods of reducing this interference: shielded electrode leads, active electrodes, skin preparation, filtering, right leg driver (RLD) and impedance bootstrapping.

The capacitive coupling between the electrode leads and the mains power supply can be reduced. Shielded electrode leads reduce the coupling capacitance between the leads and the power supply, reducing the coupled displacement current. However, the distributed capacitance of the shielded cable reduces the input impedance of the bioelectrical instrumentation device, increasing the differential-mode interference produced through the potential divider effect (Betts & Brown, 1976; Huhta & Webster, 1973; Metting van Rijn et al., 1990; Webster, 2009).

The high impedance path to ground through the electrode-skin impedance that the coupled conduction currents flow, can be reduced by implementing active electrodes. Active electrodes have the recording electrodes and the bioelectrical differential amplification stage designed into the same module. Therefore, the bioelectrical differential amplification stage is attached directly above the muscle. Since the output impedance of the active electrode is low, there is negligible interference produced from conduction currents in the single-ended electrode lead (Huhta & Webster, 1973). However, active electrodes are not always used as they are more expensive (Laszlo, Ruiz-Blondet, Khalifian, Chu, & Jin, 2014) and typically have fixed interelectrode distances, limiting their use between different muscle sites and recording techniques.

The interference current caused by capacitive coupling of the subject and electrode leads to the mains supply can be reduced, limiting the resulting interference. Implementing a grounded equipotential surface close to the AC source can be used to distort the electric field, reducing the displacement currents by up to 90% (Huhta & Webster, 1973). However, implementing a grounded equipotential surface is not practical in every recording

environment. Grounding the subject would provide the best common-mode interference immunity. However, this can result in dangerous currents to flow through the subject. The RLD was developed to reduce the effective reference electrode impedance, reducing the amount of common-mode interference and limiting the impact of the potential divider effect, while ensuring safe current flow through the subject (Winter & Webster, 1983a). The RLD reduces common-mode interference by driving the reference electrode to the inverted common-mode interference potential. However, a non-optimised design can limit the amount of effective reference electrode impedance reduction.

The interference caused by electrode leads and the potential divider effect are a function of the electrode-skin impedance and its imbalance. Skin preparation reduces the electrode-skin impedance, reducing the maximum possible electrode-skin impedance imbalance (Searle & Kirkup, 2000). Skin preparation is achieved with methods ranging from cleaning the skin with alcohol, to abrading the skin surface with sand paper (Betts & Brown, 1976). However, incorrectly or inconsistently performed skin preparation can increase the impedance imbalance between electrode-skin interfaces, leading to large interference potentials. Skin preparation can also be time consuming and lead to skin irritation (Betts & Brown, 1976).

Due to the half-cell potential, the bioelectrical signal requires AC-coupling to mitigate the DC offset. This process is typically performed post-differential amplification stage, since implementating AC-coupling prior the differential amplification stage can degrade the common-mode input impedance, increasing the interference due to the potential divider effect (Spinelli et al., 2003). However, correct design of pre-differential amplification AC-coupling can lead to higher differential gains, and therefore, a higher CMRR.

Increasing the common-mode input impedance of the bioelectrical instrumentation reduces the impact of the potential divider effect. Impedance bootstrapping is used to increase

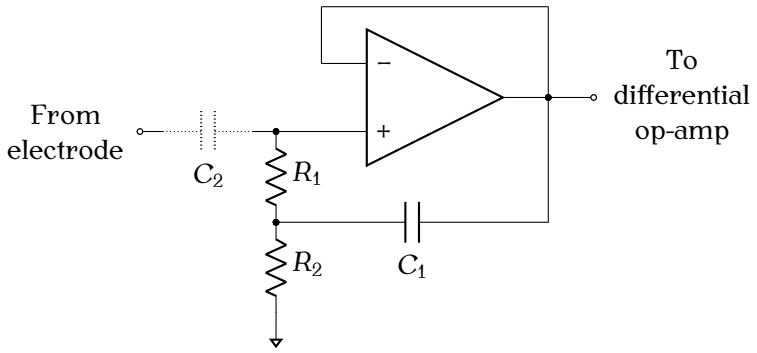

Figure 2.11: Impedance bootstrapped front end with series input capacitance (C_2) for AC-coupling.

the effective input impedance without affecting the transfer function of the bioelectrical instrumentation. Impedance bootstrapping is achieved using positive feedback (Betts & Brown, 1976; Dobrev & Neycheva, 2011; Pallas-Areny et al., 1989; Pallás-Areny & Webster, 1990; Thakor & Webster, 1980), Figure 2.11. The addition of a series input capacitor can be used to produce an AC-coupled bioelectrical instrumentation front-end (Pallas-Areny et al., 1989; Pallás-Areny & Webster, 1990). Although the input impedance of bioelectrical instrumentation can be increased using impedance bootstrapping, large impedances and impedance imbalances of dry electrodes can still result in differential-mode interference.

Filtering is commonly used to reduce the remaining differential-mode interference. Typically, an analogue notch filter (Hardalaç & Canal, 2004), or post-processing is applied (Supuk et al., 2014; Youn & Kim, 2009). However, filtering of mains and its harmonics also attenuates the bioelectrical signal. Post-processing can increase processing power requirements and decrease throughput rate, with the potential to impact real-time use.

Bioelectrical noise summary

The two main sources of bioelectrical interference are due to capacitive coupling of the human body and recording electrode leads to the mains power supply and ground. There are multiple techniques used to reduce this bioelectrical interference: active electrodes reduce the interference potential caused by coupled electrode leads, a RLD reduces the effective reference electrode impedance, skin preparation reduces the electrode-skin impedance

and its imbalance, and impedance bootstrapping can increase the bioelectrical instrumentation input impedance. Each source of interference, and method of reduction, has a range of impact, especially as not all interference reduction methods can be applied to all bioelectrical applications. Therefore, it is difficult to accurately quantify the level of interference expected in the bioelectrical signal. Although there are multiple interference reduction methods, impedance imbalances between electrode-skin interfaces still leads to interference potentials being detected, and amplified by the bioelectrical instrumentation (Searle & Kirkup, 2000). Therefore, to reduce the amount of interference in the bioelectrical signal, the electrode-skin impedance should be balanced.

2.3.2 Crosstalk

Bioelectrical crosstalk detected with EMG is the phenomenon of one muscle's signal (crosstalk muscle) influencing the recording of another (muscle of interest). Crosstalk is due to the spatially overlapping fibre territories, tissue volume conduction (Kilner et al., 2002) and the extinction of the action potentials at the tendons (Basmajian & De Luca, 1979; De Luca, 1997; Farina et al., 2002). This phenomenon is greatest when muscles are close together. Therefore, crosstalk in the forearm is expected to be more significant than that in the leg (Kong, Hallbeck, & Jung, 2010). However, crosstalk is a still concern in gait studies as it can lead to misinterpretation of the contraction force and activation timing for muscles of interest (De Luca et al., 2012). Since intramuscular electrodes are more sensitive to electrical activity in close proximity to the electrode site, surface electrodes are expected to encounter larger crosstalk amplitudes than intramuscular electrodes (Cardillo, Dresden, & Solem, 1998). However intramuscular electrodes are not a viable crosstalk reduction method due to the added difficulty of their use (Selvanayagam, Riek, & Carroll, 2012). Therefore, it is difficult to separate the components of the bioelectrical signal into crosstalk and signal of interest. Therefore, crosstalk interference is superimposed with the target bioelectrical signal, producing the need for crosstalk reduction methods.

Human tissue acts as a low pass filter, with the cut-off frequency decreasing as the distance from the signal source to the skin surface increases. Bioelectrical crosstalk signals typically originate further from the skin surface than target muscles. Therefore, crosstalk can be low frequency and appear as common voltage (Basmajian & De Luca, 1979; Broman et al., 1985; De Luca & Merletti, 1988). However, human tissue is anisotropic and inhomogeneous, introducing a phase shift into the volume conducted signal components. This phase shift distorts crosstalk signals, resulting in voltage gradients (Broman et al., 1985). These voltage gradients due to crosstalk signal distortion need to be reduced.

Crosstalk contamination

There are two common methods used in literature to quantify crosstalk and its reduction: correlation-based index and amplitude-based index. Correlation-based indices use a correlation coefficient obtained from simultaneously measured target muscle and crosstalk muscle (Kong et al., 2010; Mogk & Keir, 2003; Selvanayagam et al., 2012). Due to not needing an uncontaminated signal without crosstalk, the correlation-based index is easier to use (Kong et al., 2010). However, there is controversy as to whether a correlation-based index can reliably quantify crosstalk (De Luca & Merletti, 1988; Farina et al., 2002). The phase shift introduced to the volume conducted signal components may affect the ability to use the correlation coefficient for quantifying crosstalk.

There are three commonly used amplitude-based indices for quantifying crosstalk: normalised peak-to-peak amplitude, normalised average rectified value (ARV) and normalised root mean square (RMS) (De Luca & Merletti, 1988; Farina et al., 2002; Van Vugt & Van Dijk, 2001). Amplitude-based metrics require an uncontaminated bioelectrical signal without crosstalk for the normalisation process. This is typically achieved by measuring agonist and antagonist muscles (Van Vugt & Van Dijk, 2001) or targeting particular muscles using electrical stimulation (Selvanayagam et al., 2012).

Crosstalk studies have measured large quantities and ranges of crosstalk contamination, ranging from 4–60%. For crosstalk studies on the forearm, all muscles of interest detected contamination. Crosstalk contamination of 11–25% was detected for digit-dedicated flexors using the normalised RMS amplitude index. However, there was only 4% crosstalk contamination when using a correlation-based index (Kong et al., 2010). A similar discrepancy was also found in the wrist-dedicated extensors, 32–50% and 22% of crosstalk detected on the muscles of interest for normalised RMS and correlation-based indices, respectively. Similar levels of crosstalk contamination have been detected in other studies: 60% for flexor muscles and 50% for wrist-dedicated extensor muscles using a correlation-based index (Mogk & Keir, 2003) and 20–39.4% using a correlation-based index (Selvanayagam et al., 2012). These studies highlight the potential inconsistencies that can arise using a correlation-based index for quantifying crosstalk contamination. Two crosstalk studies on the lower limb have shown less crosstalk contamination and more consistency between the amplitude-based indices. Crosstalk contamination detected on three muscles of the quadriceps ranged from 12.8–25.9% and 12.2–30.6% using a normalised peak-to-peak amplitude and normalised ARV, receptively (Farina et al., 2002). Similarly, crosstalk detected on three sites on the lower shank ranged from 5.0–19.4%, 5.4–19.9% and 5.0–18.4% for normalised peak-to-peak amplitude, normalised ARV and normalised RMS, respectively (De Luca & Merletti, 1988). These studies highlight the interchangeability of the amplitude-based indices, and outline the severity of crosstalk contamination, which may lead to misinterpretation of contraction force and activation timing for muscles of interest.

Crosstalk reduction

Crosstalk detection methods are relatively common; however, reduction techniques are less applied and more complex. Due to the phase shift in the volume conducted signals, the frequency content cannot provide any indication of crosstalk, therefore, temporal high-pass filtering cannot be used for crosstalk reduction (Farina et al., 2002). The blind signal separation (BSS) algorithm (first proposed by Chan (1997)) removes noise when the

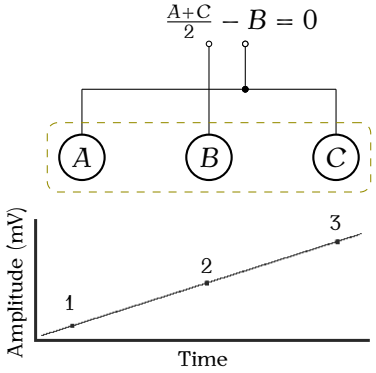

Figure 2.12: High level schematic illustrating how the tripolar electrode configuration removes voltage gradients. Dashed lines highlight electrodes A, B and C, which are measuring 1, 2 and 3 mV, respectively. Taking the difference between electrodes A and C with respect to electrode B results in zero amplitude.

interference source is unknown. The BSS algorithm cannot be applied directly, as the bioelectrical signals are not independent (Kilner et al., 2002). The weak synchronisation that often occurs between motor units from different muscles voids this criterion. However, applying third-order mathematical differentiation achieves independent bioelectrical signals. Unfortunately, the BSS algorithm only guarantees two recordings do not contain common activity. Therefore, crosstalk contamination from unrecorded muscles cannot be removed, leading to an increased number of recording electrodes which is undesirable in some recording applications.

Another method of crosstalk reduction is the tripolar electrode configuration. The tripolar electrode configuration uses three electrodes: one centre and two flanking. The configuration is designed to reject voltage gradients that are orientated along the axis of the recording electrodes. A tripolar electrode records the average potential of the two flanking electrodes with respect to the centre electrode. When a voltage gradient is recorded, the average potential of the flanking electrodes should be the same as the centre electrode. Therefore, the output of the bioelectrical instrumentation should have an amplitude of zero, Figure 2.12. However, if a bioelectrical signal was detected at any single electrode, the signal would propagate through the bioelectrical instrumentation without the voltage gradient (Loeb & Gans, 1986).

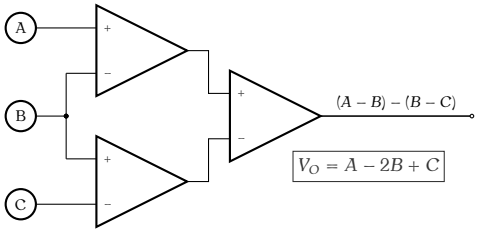

(a) Double differential electrode configuration.

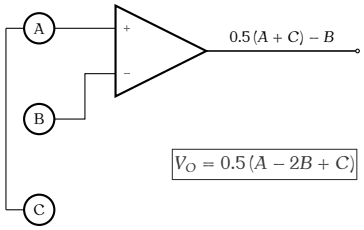

(b) Branched electrode configuration.

Figure 2.13: Two common tripolar electrode configurations used for crosstalk reduction (Van Vugt & Van Dijk, 2001).

Tripolar electrode configurations can be superior to bipolar electrode configurations (De Luca et al., 2012; Koh & Grabiner, 1993; Van Vugt & Van Dijk, 2001). With a bipolar electrode configuration, it is difficult to deduce whether the bioelectrical signal is a result of a local source producing a higher potential at one electrode or a distant source producing a voltage gradient. Introducing the third electrode makes it possible to distinguish the difference between these cases. However, tripolar electrode configurations have limitations.

There are two common types of tripolar electrode configurations: the double differential (DD) and the branched electrode (BE). The two electrode configurations vary in the way they are connected to the bioelectrical instrumentation, Figure 2.13. The DD electrode configuration requires two extra instrumentation amplifiers than a conventional bioelectrical instrumentation device. Initially, the configuration was designed to assist in estimating the propagation speed of the MUAP (Broman et al., 1985). Due to non-delayed signals (crosstalk) being present, it was difficult to determine two distinct measuring points within the bioelectrical signal, resulting in abnormally large propagation speeds. The DD electrode configuration permitted estimating MUAP propagation speeds that agreed with values stated in literature, highlighting the performance of the DD electrode configuration.

The BE configuration uses the same bioelectrical instrumentation as the bipolar electrode configuration. However, the flanking electrodes are directly connected (shorted) together. When the BE configuration has twice the applied gain as the DD electrode configuration,

they are mathematically identical and interchangeable (Koh & Grabiner, 1993; Van Vugt & Van Dijk, 2001). The BE configuration is advantageous as it requires only a single instrumentation amplifier, therefore, it can be used with conventional bioelectrical instrumentation.

The centre electrode of the DD electrode configuration connects to two instrumentation amplifiers. Therefore, the effective common-mode input impedance seen by the centre electrode is half the common-mode input impedance seen by the flanking electrodes. The flanking electrodes of the BE configuration are shorted together, halving the effective electrode-skin impedance of the flanking electrodes. To not introduce an impedance imbalance between the three electrode-skin interfaces, the centre electrode of both the DD and BE configurations needs to have an impedance that is half that of the flanking electrodes. As the electrode-skin impedance has an inverse relationship with electrode area (Burns, 1950), the centre electrode needs to have a contact area twice that of the flanking electrodes. However, impedance imbalances between the three electrode-skin interfaces will still be present, where the potential divider effect will convert common-mode interference into differential-mode interference.

Crosstalk reduction is difficult to quantify. The BSS algorithm can only guarantee the resulting signals have no common activity. There is controversy about whether a correlation-based index can be used, and the amplitude-based indices require an uncontaminated signal. The BSS algorithm has been used for crosstalk reduction in the forearm (Kilner et al., 2002; Kong et al., 2010), where only five muscles were measured in both studies. Although there was no common crosstalk signals within the forearm flexors (Kong et al., 2010), there are 39 muscles in the forearm, each with the possibility of producing crosstalk (Kilner et al., 2002). The DD electrode configuration has been used to obtain the "uncontaminated" signals required for the amplitude-based index (De Luca & Merletti, 1988). However, tripolar electrode configurations do not completely remove crosstalk. This limitation is believed to

be due to the different paths that the crosstalk signals travel to the three different recording electrodes, introducing attenuation and phase lag, resulting in voltage gradients with non-constant slopes. The DD electrode configuration resulted in 4.7–22.5% and 6.6–25.9% residual crosstalk for normalised peak-to-peak amplitude and normalised ARV, respectively (Farina et al., 2002).

The effects of interelectrode distance

Crosstalk contamination is a function of the interelectrode distance (De Luca et al., 2012; Farina et al., 2002). Studies have shown that increasing the interelectrode distance of a tripolar electrode configuration from 10 mm to 20 mm can double the crosstalk contamination (Farina et al., 2002). Although decreasing the interelectrode distance reduces crosstalk contamination, the bioelectrical signal also decreases, impacting the SNR. Studies have shown that a 10 mm interelectrode distance is optimal for reducing crosstalk contamination while maintaining a high bioelectrical SNR. However, the relationship between crosstalk and interelectrode distance for the bipolar electrode configuration differs. An increase in interelectrode distance from 12 mm to 20 mm has been shown to have no impact on crosstalk contamination (Koh & Grabiner, 1993), and an increase in interelectrode distance from 10 mm to 40 mm has been shown to result in a mean increase of crosstalk contamination by 2% (Farina et al., 2002).

Crosstalk summary

Crosstalk contamination of EMG is the phenomenon of one muscle's signal (crosstalk muscle) influencing the recording of another (muscle of interest). Crosstalk contamination has been recorded on many areas of the body, where up to 60% of the crosstalk muscle's signal can be detected on the muscle of interest. There are two common crosstalk reduction methods, the BSS algorithm and tripolar electrode configuration. The limitation of the BSS algorithm is the need to simultaneously measure all sources of crosstalk for a complete removal of contamination. The tripolar electrode configuration can reduce crosstalk

without measuring the source of the crosstalk. However, the DD electrode configuration only reduced the maximum mean crosstalk from 30.6% to 25.9% using the ARV amplitude index.

2.4 Electrode-skin Interface

Electrical interference detected within bioelectrical signals is a function of the impedance imbalance between multiple electrode-skin interfaces. The electrode-skin interface is an electrochemical transducer with characteristics that exhibit non-linear frequency, temporal and current-density characteristics that are dominated by the large and variable impedance of the skin itself (Olson et al., 1979). However, an impedance imbalance of the electrode-skin interface can be caused by both physiological changes in the subject and imperfections related to the electrodes. This variation is often unpredictable (Grimnes, 1983; Olson et al., 1979).

The physiological variability related to the subject can be due to perspiration, sweat glands and ducts, the epidermis layer of the skin (Webster, 2009) or local changes in temperature at the electrode site (Nag et al., 2015). The variability of the electrode can be due to the fabrication process, resulting in electrodes with different surface properties and non-homogeneous electrolyte medium (Nag et al., 2015).

Between applying the electrodes to a subject, and recording the bioelectrical signals, the impedance of each electrode-skin interface changes and can continue to change, with controversy about whether this alters the electrode-skin impedance imbalance (Grimnes, 1983; Pacela, 1967), or not (Olson et al., 1979). The electrode-skin impedance has an inverse temporal and frequency relationship, except with heavily abraded skin, which exhibits an increase in impedance over time. The temporal relationship is thought to be due to the electrolyte medium seeping through the skin surface, shunting the skin impedance (Olson et al., 1979). This theory explains why different electrolyte media result in different tempo-

ral relationships. Therefore, repeated, simultaneous measurements of the electrode-skin interface impedance is the most reliable and effective method to understand the impedance behaviour (Grimnes, 1983).

2.4.1 Measuring the Electrode-skin Impedance

To measure the electrode-skin impedance, the magnitude and phase of the voltage across the electrode-skin interface must be measured during the simultaneous application of an excitation current. A minimum of three electrodes is required to measure the impedance imbalance of a bipolar electrode configuration. There are two common methods used to measure the electrode-skin impedance imbalance. The methods use either one or three excitation paths. The triple excitation path method is accomplished by performing three separate excitations (Almasi & Schmitt, 1970; Olson et al., 1979), producing three dependent impedances, Figure 2.14,

$$Z_{AR} = Z_{A_C} + R_{AR} + Z_{R_C} , \tag{2.20}$$

$$Z_{AB} = Z_{A_C} + R_{AB} + Z_{B_C} , \tag{2.21}$$

$$Z_{BR} = Z_{B_C} + R_{BR} + Z_{R_C} , \tag{2.22}$$

where Z_{AR}, Z_{AB} and Z_{BR} are the combined electrode-skin impedances between electrode A and the reference electrode, electrodes A and B, and electrode B and the reference electrode, respectively; Z_{A_C}, Z_{B_C}, Z_{R_C} are the contact impedances of electrodes A, B, and the reference electrode, respectively; and R_{AR}, R_{AB} and R_{BR} are the combined subcuta-

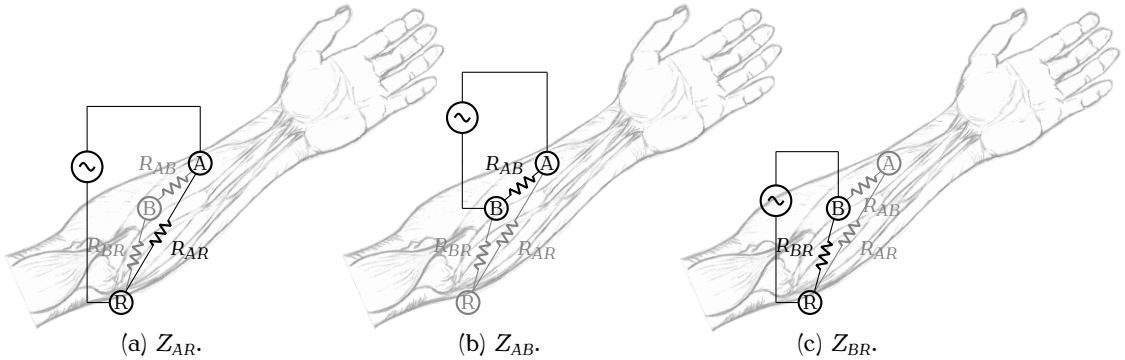

(a) Z_{AR}. (b) Z_{AB}. (c) Z_{BR}.

Figure 2.14: Three excitation paths used to produce three dependent electrode-skin impedance measurements.

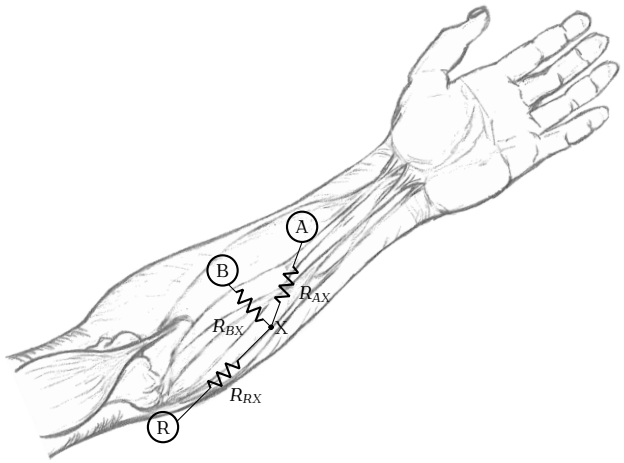

Figure 2.15: Electrode-skin interface impedances obtained using three excitation paths and a delta-wye transform.

neous resistances between electrode A and the reference electrode, electrode A and B, and electrode B and the reference electrode, respectively.

As the subcutaneous resistance is orders of magnitude smaller than the electrode-skin impedance, the imbalance associated with the subcutaneous resistance is assumed to be negligible. Therefore, the impedance of each electrode-skin interface, Z_A, Z_B and Z_R, Figure 2.15, is calculated using a delta-wye transform by inverting the matrix form of the of the three dependent impedances,

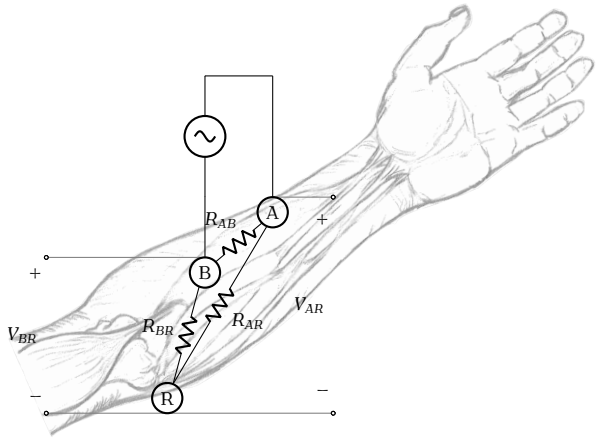

Figure 2.16: Electrode-skin interface impedances obtained using a single excitation path and measuring the voltage across each recording electrode with respect to the reference electrode.

$$\begin{bmatrix} Z_{AR} \\ Z_{AB} \\ Z_{BR} \end{bmatrix} = \begin{bmatrix} 1 & 0 & 1 \\ 1 & 1 & 0 \\ 0 & 1 & 1 \end{bmatrix} \begin{bmatrix} Z_{A_C} + R_{AX} \\ Z_{B_C} + R_{BX} \\ Z_{R_C} + R_{RX} \end{bmatrix}, \tag{2.23}$$

$$\begin{bmatrix} Z_A \\ Z_B \\ Z_R \end{bmatrix} = \begin{bmatrix} Z_{A_C} + R_{AX} \\ Z_{B_C} + R_{BX} \\ Z_{R_C} + R_{RX} \end{bmatrix} = 0.5 \cdot \begin{bmatrix} 1 & -1 & 1 \\ 1 & 1 & -1 \\ -1 & 1 & 1 \end{bmatrix} \begin{bmatrix} Z_{AR} \\ Z_{AB} \\ Z_{BR} \end{bmatrix}. \tag{2.24}$$

The single excitation path method stimulates the recording electrodes while measuring the voltage across each recording electrode with respect to the reference electrode, Figure 2.16. As negligible current flows through the reference electrode due to a high impedance measurement device, the recorded electrode-skin impedance is independent to the reference electrode. The single-excitation method has the advantage of only requiring a single excitation path. However, high input impedance custom hardware is required in addition to an impedance analyser.

Although an impedance imbalance between the recording electrodes results in electrical

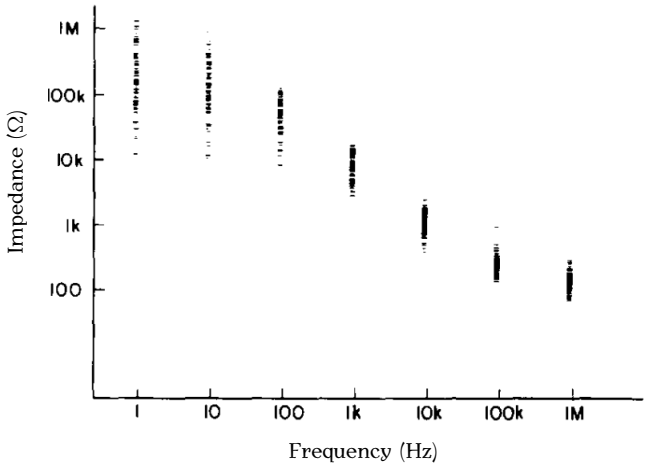

Figure 2.17: Electrode-skin impedance measured for ten subjects at ten locations on the body (Rosell et al., 1988).

interference, there is limited research investigating the electrode-skin impedance imbalance. The electrode-skin impedance is typically measured using an excitation frequency sweep. The excitation frequency range is typically between 1–1000 Hz (Casal & Mura, 2016; Grimnes, 1983; Olson et al., 1979), with some researchers measuring up to 1 MHz (Rosell et al., 1988). However, the study that investigated higher excitation frequencies did not measure the electrode-skin impedance imbalance, but the electrode-skin impedance of one electrode at ten sites over the human body. The electrode-skin impedance varies up to 1 MHz, and can have impedance values up to 1 MΩ at 1 Hz for wet electrodes, Figure 2.17, and double this for dry electrode pairs at mains frequency (Searle & Kirkup, 2000). The excitation current used in measuring the electrode-skin impedance must be low to ensure a linear response (Schwan, 1968). Excitation currents of 1 nA (Grimnes, 1983) to 25 μA (Almasi & Schmitt, 1970), and 100 μA for frequencies above 10 kHz (Rosell et al., 1988) have been used.

2.4.2 Modelling the Electrode-skin Interface

Modelling the impedance of the electrode-skin interface provides an understanding of the impedance imbalance between multiple electrode-skin interfaces. The electrode-skin interface was modelled as early as 1950 (Burns, 1950). However, there is still controversy about what model to use. Two common models are the summed exponential and single

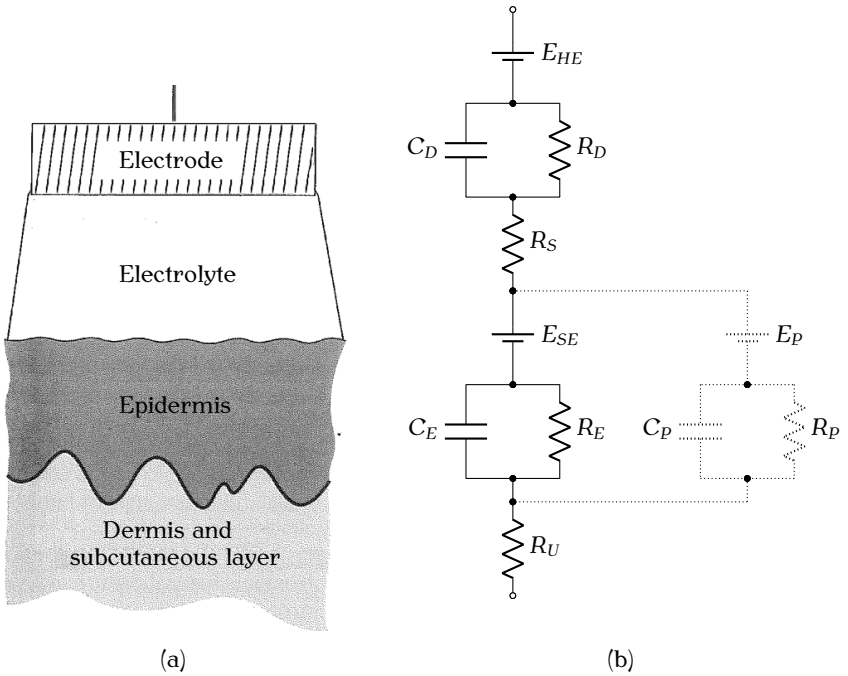

Figure 2.18: Schematic of the electrode-skin interface (a), characterised by the summed exponential model (b). The dashed segment is additional to the summed exponential model, and used to characterise the sweat glands and ducts for modelling the electrodermal response. Modified from (Webster, 2009).

exponential. These models are expected to characterise both wet and dry electrodes. However, the parameter values used to characterise the electrodes will differ (Assambo, Baba, Dozio, & Burke, 2007).

Summed exponential model

The summed exponential model is based on the physiological understanding of the human body and characterises the non-linear frequency behaviour of the electrode-skin interface (Webster, 2009). The summed exponential model is comprised of two repeated four-element segments, resulting in an eight-parameter model, Figure 2.18. Each segment contains a DC potential, a series resistance and a parallel capacitive-resistive portion.

The first segment of the summed exponential model characterises the electrode and electrolyte medium, where E_{HE} represents the half-cell potential produced by the contact between the electrode and electrolyte medium; C_D and R_D characterise the impedance associated with the electrode-electrolyte interface and polarisation effects. C_D also captures the

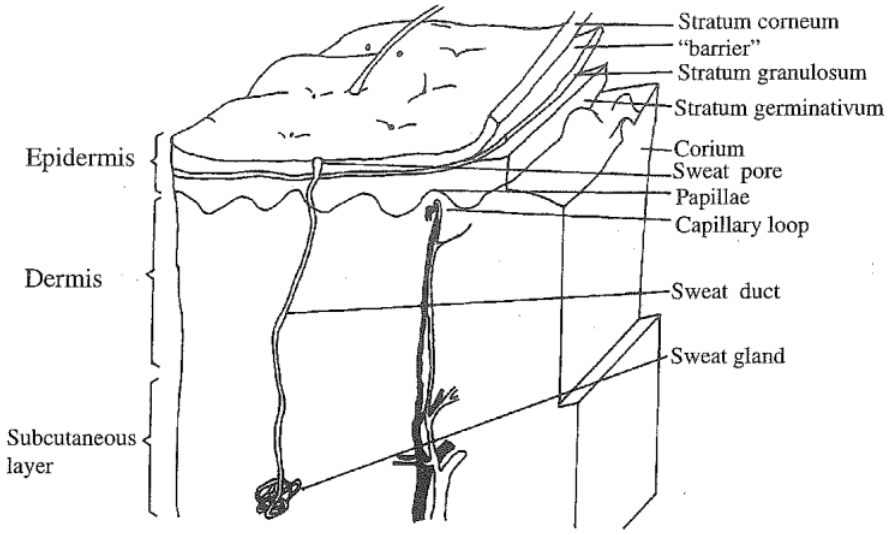

Figure 2.19: Cross-section of the human skin layers (Webster, 2009).

effects associated with the distribution of ionic charge at the electrode-electrolyte interface, which is considered a double layer of charge; R_S represents the resistance associated with the electrolyte and its interference effects.

The second segment of the summed exponential model characterises the skin interface. The skin interface, Figure 2.19, is more complicated than the electrode-electrolyte interface. However it can be characterised using the same elements. The epidermis is the outermost layer of the skin, and is comprised of three sublayers: the stratum corneum, stratum granulosum and the stratum germinativum. The epidermis is constantly rebuilding itself. Cells divide and grow within the stratum germinativum. As the cells grow, they are displaced into the stratum granulosum. The cells begin to degrade, losing their nuclear material as they pass through the stratum granulosum. The stratum corneum is formed by these degenerating cells, producing the horny layer of dead material at the skin surface.

A differential ionic concentration across the semipermeable membrane of the epidermis produces a potential difference, represented by E_{SE}. The impedance of the epidermis is characterised by the parallel network C_E and R_E. The resistance associated with the dermis and subcutaneous layers is represented by the series resistance R_U. An additional

capacitive-resistive network can be used to characterise the sweat glands and ducts, E_P, C_P and R_P in Figure 2.18. However, these components are usually only included when considering electrodermal response (Webster, 2009).

Single exponential model

Removing the capacitive-resistive portion associated with the impedance of the epidermis, C_E and R_E, results in the single exponential model. This process is biologically achieved through skin preparation, reducing the affect of the stratum corneum (Webster, 2009). However, attempts to model experimental data using the single exponential model have not be successful (Assambo et al., 2007; Kaczmarek & Webster, 1989).

Constant phase element (CPE)

Capacitors cannot represent the frequency dependence of the electrode-skin interface (Burns, 1950). Therefore, to achieve a more realistic behaviour, the constant phase element (CPE) replaces the capacitor in the aforementioned models (Richardot & McAdams, 2002). However, it is more complex and used less frequently. The impedance of the CPE, Figure 2.20, is defined as,

$$Z_{\mathrm{CPE}}(\omega) = \frac{1}{Q_0 \times (j\omega)^{\beta}}\,, \tag{2.25}$$

where β is a dimensionless parameter, ranging from 0–1, that dictates the phase of the CPE, $\phi_{\mathrm{CPE}} = (-90 \cdot \beta)^{\circ}$. When $\beta = 1$, the CPE characterises a purely capacitive element, when $\beta = 0$, the CPE characterises a purely resistive element. Q_0 is referred to as the

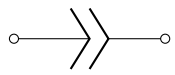

Figure 2.20: Electrical symbol for the constant phase element (CPE).

magnitude of the CPE, and is numerically equivalent to the admittance of the CPE at $\omega = 1\,\text{rad/s}$, otherwise it has a unit of $S \cdot s^{\beta}$.

Modelling limitations

Modelling the impedance of the electrode-skin interface is a challenging task. Despite skin preparation reducing the impedance of the stratum corneum, the single exponential model cannot truly capture the characteristics of the electrode-skin interface (Assambo et al., 2007; Kaczmarek & Webster, 1989), and ideal capacitors cannot capture the frequency dependence of the electrode-skin interface (Burns, 1950). However, applying these assumptions produces a simple model that can assist in the early stages of modelling the interface. The impedance of the electrode-skin interface can vary over the range of 1 Hz to 1 MHz, with impedances ranging from 100 Ω to 1 MΩ for wet electrodes (Rosell et al., 1988). This results in an interface with a large frequency and impedance span, increasing the difficulty to accurately measure the electrode-skin impedance.

Electrode-skin impedance compensation

To be able to reduce electrical interference, the electrode-skin impedance should be balanced using compensatory impedance. A single exponential model-driven method, using resistive compensation has been developed (Nag et al., 2015). The compensation was applied to an electrode-electrolyte interface submerged in a saline solution. The exhaustive search method was also implemented for resistive compensation on simulated data (Silva, Naviner, & Freire, 2006). As the impedance of the electrode-skin interface is non-linear with respect to frequency, the efficacy of resistive compensation is limited, and performing compensation on simulated data, or an electrode-electrolyte interface removes the difficulty inherent with biological interfaces, and cannot be used to balance the electrode-skin interface. The exhaustive search method has also been used to balance a pair of electrodes used during electrocardiography (ECG) measurements (Adli & Yamamoto, 1998). Initially the electrical interference detected in the bioelectrical recording was approximately 11%

of the signal, which was reduced to approximately 1% after balancing the electrodes. This process was achieved by adding compensatory resistive-capacitive networks in series with each electrode, where the resistors were manually tuned to limit the electrical interference. Although this approach did reduce electrical interference detected in the bioelectrical signal, to produce a real-time system that is adaptable to changing environments, automatic tuning of both resistive and capacitive portions is required

Electrode-skin impedance compensation can be performed using the common-mode interference. This can be achieved by balancing the input impedance of the bioelectrical instrumentation device with each electrode-skin interface (Parente et al., 2018; Yonce, 2005). This method of compensation requires the decomposition of the bioelectrical signal, producing in-phase and quadrature components. The in-phase component is obtained by multiplying the bioelectrical signal with the common-mode interference, and the quadrature component is obtained using the same method, but the common-mode interference is negated and shifted by 90 degrees. The two components are low pass filtered and integrated, producing in-phase and quadrature DC components. The in-phase component controls resistive compensation, and the quadrature component controls capacitive compensation. The compensation signals have been used to control the gain of voltage controlled amplifiers (Yonce, 2005) and analogue multipliers (Parente et al., 2018), permitting the effective input impedance to be manipulated.

These electrode-skin impedance compensation methods have limitations. As one technique was published as a patent, (Yonce, 2005), the efficacy of the compensation was not published. The other technique also implemented a 50 Hz notch filter (Parente et al., 2018). This makes it difficult to verify the reduction in electrical interference due to electrode-skin impedance balancing. However, this study emulated an impedance imbalance by temporarily reducing the contact area of one electrode. This caused a large disturbance artefact, which is typical of intermittent electrode connection loss. The amplitude of the disturbance reduced with

time, indicating the success of the compensation network.

These compensatory methods manipulate the transfer function (voltage divider) between the electrode-skin impedance and the bioelectrical instrumentation device. Manipulating the impedance of the bioelectrical instrumentation device has the potential to alter this transfer function. Since the electrode-skin impedance is unknown, the resulting transfer function is also unknown, particularly for dry electrodes that realise large electrode-skin impedances. Therefore, the frequency spectrum of the bioelectrical signals utilising these methods can be attenuated by an unknown frequency dependent gain, limiting the ability to use the frequency content of the bioelectrical signal for biofeedback. There is a need for a system that measures the electrode-skin interface, compensates for the impedance-imbalance between electrode-skin interfaces and determines the frequency dependent attenuation applied to the bioelectrical signal. Combing this compensatory system with a tripolar electrode configuration, may produce a bioelectrical device that can reduce electrical interference and crosstalk contamination, resulting in improved bioelectrical signal acquisition.

2.5 Summary

The limitations associated with EMG must be well understood to improve on current bioelectrical instrumentation. There are many limitations that affect both short- and long-term stability, where the main causes are crosstalk contamination and electrical interference. Crosstalk is the phenomenon of one muscle's signal influencing the recording of another. This is due to spatially overlapping fibre territories, volume conduction and the extinction of the action potential at the tendons. Tripolar electrode configurations are a common method applied in the attempt to reduce crosstalk. Electrical interference is due to displacement currents caused by capacitive coupling of the human body and electrode leads to the mains supply. There are multiple techniques used to reduce bioelectrical interference: active electrodes, RLD, skin preparation, and impedance bootstrapping. However,

each cause of interference and method of reduction has a large range of impact, especially as not all interference reduction methods can be applied to all bioelectrical applications. Therefore, there is a need for a system that can further reduce electrical interference in bioelectrical signals, while simultaneously implementing crosstalk reduction techniques.

Since electrical interference is a function of the electrode-skin impedance imbalance, balancing the electrode-skin impedance has the potential to increase bioelectrical signal quality and specificity. This research aims to reduce the affect of impedance imbalances between electrode-skin interfaces, by developing a system that can measure and characterise the impedance of multiple electrode-skin interfaces, and applying a novel, non-linear compensatory network, in real-time, to balance the electrode-skin interfaces. The efficacy of the compensation network will be validated by the means of crosstalk and electrical interference reduction, with the attempt to verify that having balanced electrode-skin interfaces results in higher bioelectrical signal quality. Therefore, three recording electrodes will be used and balanced. Successful implementation would add to the existing body of work, enhancing the capabilities of physiotherapy and rehabilitation.

To my knowledge, there has not been a study on how adding compensatory impedance to balance multiple electrode-skin interfaces affects bioelectrical signal recording quality in the presence of crosstalk contamination.

CHAPTER 3

Open Source Bipolar Electromyography Design

Bioelectrical instrumentation is used to measure weak bioelectrical signals. However, these signals can be contaminated by several forms of interference: mains supply (common-mode) interference, mains supply (differential-mode) interference due to common-mode conversion, and crosstalk from endogenous sources in close proximity. The severity of the electrical interference is a function of the impedance imbalance between electrode-skin interfaces. To improve bioelectrical signal acquisition, the impedance between electrodes should be balanced, and used to implement a tripolar electrode configuration. Although electrode-skin impedance imbalance impacts many bioelectrical recording techniques, for example, electromyography (EMG), electroencephalography (EEG) and electrocardiography (ECG), this chapter focuses on the application to surface electromyography (sEMG).

Surface electromyography is the non-invasive technique applied to measure the bioelectrical signal produced by a contracting skeletal muscle. The bioelectrical signal is bipolar

with an amplitude of $\leq 10\,\text{mV}$ pk-pk, which contains its useful energy within the frequency range of 0–500 Hz.

Commercial, research-level sEMG devices can be expensive, and are not open source hardware, resulting in a device that must be treated as a black box, as it is difficult to determine the applied signal processing. To be able to quantify the impact of balancing multiple electrode-skin interfaces, the signal processing architecture of the bioelectrical instrumentation used to record the bioelectrical signals must be understood. Therefore, there is a need for a high quality near-raw signal output, open signal processing architecture sEMG device.

This chapter presents a low-cost, USD $112, open source active electrode sEMG design. Although the device was designed to permit quantifying the impact of balancing multiple electrode-skin interfaces, the open source device may also provide researchers access to a raw bioelectrical signal, while saving time and money on sEMG device development. However, the cost of production of the sEMG device is not comparable to commercial devices, which have addition production, labour, and distribution costs.

3.1 Design Considerations

The sEMG device outlined in this chapter, Figure 3.1, consists of two silver bar electrodes, a reference electrode, a pre-amplification stage, a low-pass filter, a high-pass filter in the form of an AC-coupler, a right leg driver (RLD) to reduce common-mode noise, and an analogue-to-digital converter (ADC). A high level schematic is outlined in Figure 3.2. The sEMG circuit contains three subsystems: digital, power supply and analogue.

3.1.1 Digital System

With a device that involves an analogue-to-digital conversion, it is best to define the ADC first. The bipolar signal has an amplitude of $\leq 10\,\text{mV}$ pk-pk, containing its usable energy

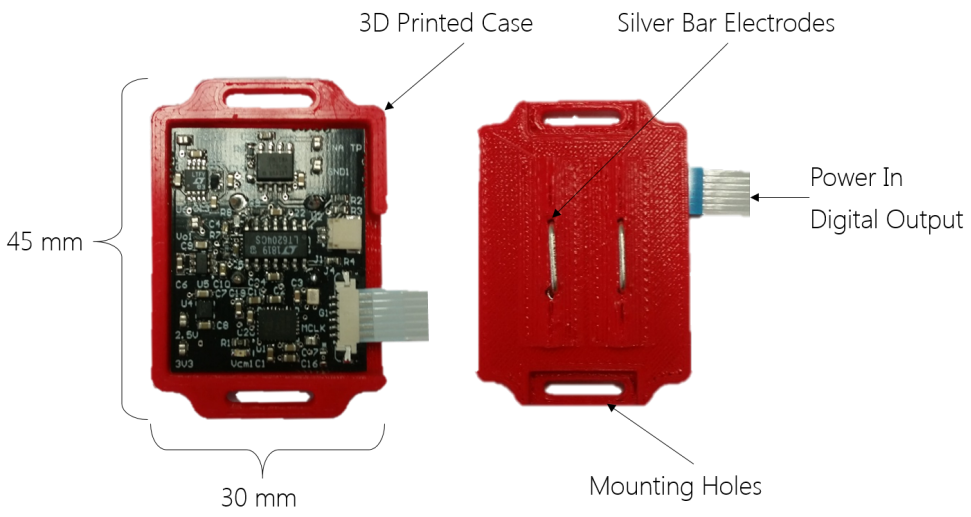

Figure 3.1: Custom open source sEMG device.

within 0–500 Hz, but predominantly in the range of 50–150 Hz (De Luca, 2002); therefore, a minimum sampling rate of 1 kHz is required. The most suitable ADC architecture for a low frequency, high precision signal is Σ-Δ, as this type of architecture typically has a high number of bits and implements oversampling.

As the signal is bipolar, there are multiple options for the ADC input method: single-ended input ADC with a DC offset being applied to the signal; a differential input ADC, by applying the bipolar signal to the inverting input, and a positive voltage to the non-inverting pin to offset the differential voltage; or a true bipolar ADC. Applying a shift to the bipolar signal without increasing the component count minimises the options. The most feasible option is to apply a shift within the filtering stage; however, this requires the filtering op-amps to have an asymmetric split power supply. Having an asymmetric split power supply decreases the op-amps power supply rejection ratio and removes ADC input voltage protection. Using the differential option is also limited as some ADC require the individual analogue inputs to be within the supply voltage rails. This means that the ADC requires a negative rail that matches the rest of the device and a positive rail that is twice the analogue positive supply voltage. The method used to avoid increasing component count, while ensuring the signal was within the ADC input limit is to use a true bipolar

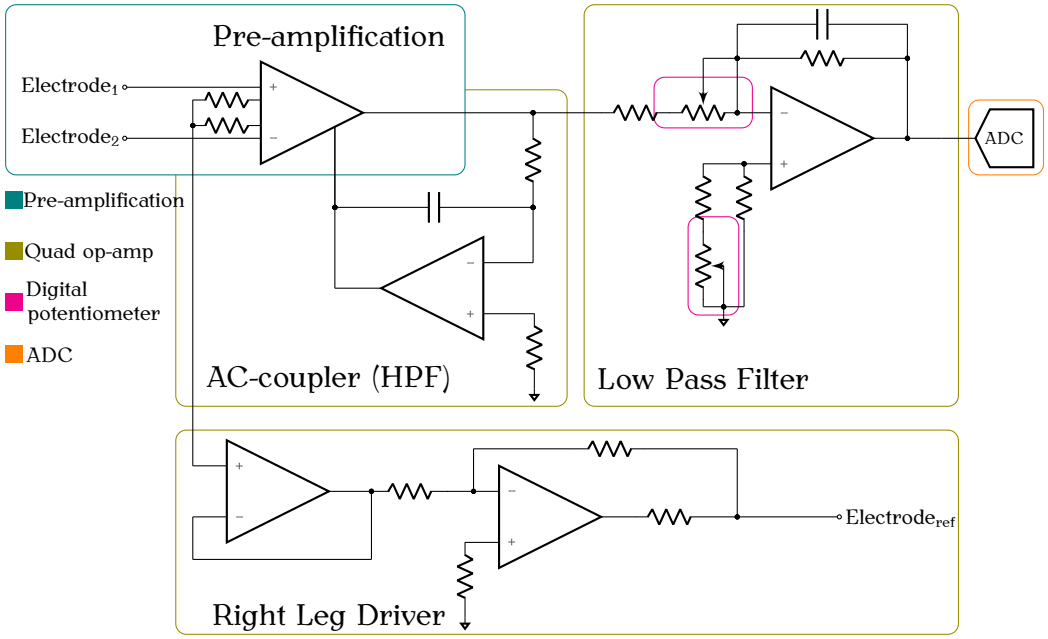

Figure 3.2: High level sEMG schematic.

ADC. The input signal is single-ended, but there are a greater number of options available for differential input ADC.

To make the sEMG device adaptable to many projects, an ADC that can operate from either 3.3 V or 5 V digital logic was beneficial. Ideally the serial interface would be I^2C (fewer wires), but SPI is the only option when applying the other ADC criteria. A Teensy 3.5 or 3.6 provides a suitable interfacing microcontroller, since it provides a fast and powerful solution with on-board data storage (SD card), therefore, the sEMG device was designed around the 3.3 V digital logic of the Teensy 3.6.

Analogue-to-digital converter (U1 : AD7768-1)

Analog Device's AD7768-1 was the chosen ADC, and is configured in SPI mode to increase device flexibility. The ADC pin connections are outlined in Appendix A, Table A.2. The ADC has a programmable 64^{th} order finite impulse response (FIR) filter, where both power consumption and bandwidth are tunable. A 2.048 MHz CMOS clock is used as recommend by the ADC manufacturer for lower power consumption (Analog Devices, 2018). The output data rate (ODR) is a function of the master clock frequency, MCLK; master clock

divider factor, $MCLK_{divider}$; and a decimation factor,

$$ODR = \frac{MCLK}{MCLK_{divider} \cdot Decimation} = \frac{2.048 \times 10^6}{2 \times 1024} = 1000\,Hz \tag{3.1}$$

The FIR filter pass-band and cut-off frequency are a function of the ODR, Equations 3.2 and 3.3 respectively (Analog Devices, 2018). The ODR was chosen to be 1 kHz, meeting the required minimum sampling frequency while producing a cut-off frequency of 433 Hz. The next available sampling frequency is 2 kHz, resulting in a FIR filter cut-off frequency of 860 Hz.

$$Passband = 0.4 \times ODR = 400\,Hz \tag{3.2}$$

$$Cutoff_{-3dB} = 0.433 \times ODR = 433\,Hz \tag{3.3}$$

3.1.2 Voltage Supplies

The sEMG device operates from a single 5 V supply. The voltage is split and regulated into ± 2.5 V and 3.3 V, producing the largest possible bipolar voltage range that permits both 3.3 V and 5 V digital logic options. An advantage of the ADC is its capability to operate from both 3.3 V and 5 V digital logic. Switching the digital logic level requires changing the CMOS clock, the IOVDD voltage (bypass the 3.3 V regulator), and the GPIO voltage divider (outlined in Section 3.1.3); however, the current CMOS clock cannot be replaced by an equivalent 5 V option as there is no 5 V device that shares the footprint. To make this design more versatile, the CMOS clock footprint should be replaced by one that is common to both 3.3 V and 5 V logic levels. Although changing the digital logic voltage has not been tested, the ADC should operate correctly (Analog Devices, 2018).

Three on-board voltage regulators are required: -2.5 V, 2.5 V and 3.3 V. The 3.3 V regulator

Table 3.1: Summary of voltage rail distribution. Coloured boxes correspond to integrated circuits outlined in Figure 3.2.

Device	**-2.5 V**	**2.5 V**	**3.3 V**
Pre-amplification	V-	V+	·
Quad op-amp	V-	V+	·
Digital potentiometer	V_{SS}	V_{DD}	·
CMOS clock	·	·	V_{CC}
ADC	AVSS, REF-	AVDD1, AVDD2, REF+	IOVDD, $\overline{PIN}$/SPI

from the ADP7104 family (ADP7104ARDZ-3.3-R7) was selected as recommended by the ADC manufacturer. The remaining regulators must also operate from a 5 V supply and have a small form factor. As the sEMG device has a low current draw, inductor-less charge pump regulators are the best option, and using separate regulators to provide the split supply provides a larger range of solutions. This resulted in the use of the LTC1550LCMS8-2.5 for the -2.5 V supply and the REG710NA-2.5/250 for the 2.5 V supply. Even though not all parts of the device have been introduced yet, a summary of the voltage supply distribution is outlined in Table 3.1.

3.1.3 Analogue System

The analogue system is comprised of three subsystems: pre-amplification, filtering and adjustable gain. The pre-amplification system amplifies the difference of the bioelectrical signal detected on the electrodes with respect to the reference electrode. The filtering stage is comprised of a quad operational amplifier (op-amp) for the analogue signal processing. A digital potentiometer is used to adjust the gain of the analogue signal.

Electrodes

The sEMG design has embedded silver bar recording electrodes, made from 1.0 mm diameter 99.99% pure silver wire. The bar electrodes are 10 mm long with an interelectrode distance of 10 mm. A single-use clip-on self-adhesive silver-silver chloride (Ag/AgCl) electrode placed on an electrically neutral part of the subject's body is used as the reference electrode, driven by the RLD.

Pre-amplification (U3:INA128U)

The pre-amplification of the differential signal with respect to the reference is performed using an instrumentation amplifier. The differential voltage associated with the half-cell potential produces approximately a 10 mV DC offset when adequate skin preparation is performed. To prevent pre-amplification saturation, while providing head room for less adequate skin preparation, the pre-amplifier gain is set to 50 V/V. The pre-amplifier is not required to be rail-to-rail, as an AC-coupler circuit is used to remove DC offsets within a ± 2.5 V range, and the bioelectrical signal after pre-amplification has a maximum amplitude of 0.5 V pk-pk (10 mV pk-pk × 50).

The INA128 was the selected instrumentation amplifier as it has the required performance: high common-mode rejection ratio (CMRR) (110 dB minimum over the pass band), low noise (10 nV/$\sqrt{Hz}$ in the pass band) and the common-mode input voltage range for a supply voltage of ±2.5 V was ±0.5 V minimum. The resistance required to achieve a gain of 50 is 1020 Ω with the INA128. To provide a centre tap, permitting access to the common-mode voltage needed for the RLD, two gain resistors of 510 Ω were used. A second generation of this chip has been released (INA828); however, it has not been tested in this design.

Filtering (U2:LT6204)

The signal conditioning process has three stages: RLD, AC coupler (HPF) and the low-pass filter. A quad op-amp package provided a compact solution to implement all three stages. The LT6204 quad op-amp package met the required performance: ±2.5 V power supply, rail-to-rail for both input and output, unity gain stability, and a gain bandwidth product of 100 kHz. However, the LT6204 requires input bias current compensation.

Input bias currents can cause erroneous DC offsets. The bias current flowing through an op-amp's input resistance produces a voltage at the input terminals, biasing the input voltage and producing a DC offset. To minimise erroneous voltage offsets, a compensation

resistor that is equal to the parallel combination of the source and feedback resistance is required. This will not remove all error associated with the input bias current as the currents are not truly equal (input offset current $\neq 0$) and vary with temperature.

The RLD operates as a feedback loop with the subject, minimising interference by driving the inverted common-mode voltage onto the subject. The RLD in this sEMG design follows the design outlined in (Winter & Webster, 1983a). The quad op-amp has two pairs of matched op-amps. A matched pair, op-amp A and op-amp D, are used for the RLD. As the feedback resistance to the RLD is much greater than the input resistance, the input bias current compensation resistor is equal to the input resistance.

The AC coupler is an integrating op-amp circuit providing feedback to the instrumentation amplifier's reference, removing DC offset while attenuating low frequency noise. The cut-off frequency of the AC coupler is defined in the same way as a first order RC filter. A 21.2 Hz cut-off frequency was obtained by using a 10 μF capacitor and a 750 Ω resistor. As the AC coupler is comprised of only one resistive component, the compensation resistor is equal to the filtering resistor (750 Ω).

A first order active low-pass filter with a cut-off frequency of 459 Hz was designed to meet the anti-aliasing requirements of the ADC. The anti-aliasing filter has an adjustable gain of 4.74–68 V/V, resulting in a sEMG device gain of 237–3400 V/V. This range in gain ensures the sEMG device can capture the maximum expected signal (10 mV pk-pk) while being sensitive enough to capture weak contractions (91.9 μV pk-pk with the equivalent resolution of a 20-bit device).

Adjustable gain (U4:AD5222)

The gain of the low-pass filter is tunable in real-time, producing a device that can record over a range of muscles, contraction strength, and different adipose layer thicknesses.

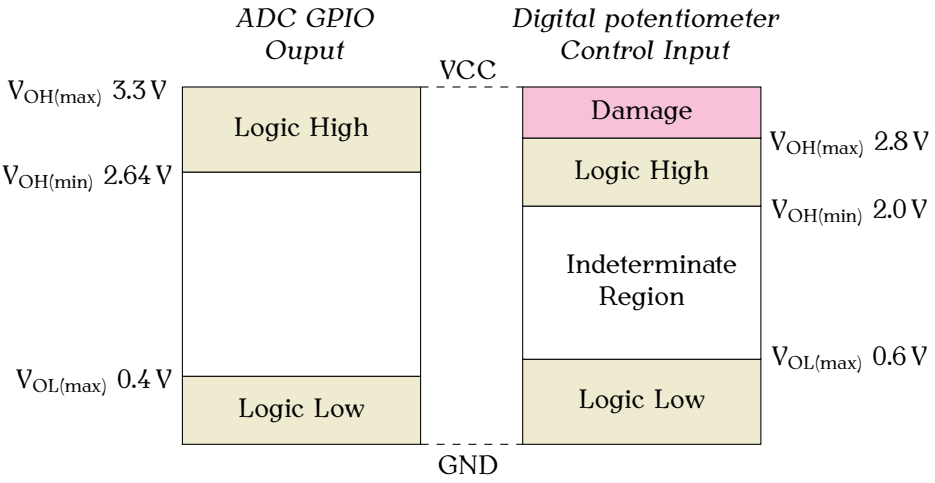

Figure 3.3: A voltage divider must be used to lower the logic levels from the ADC output to prevent exceeding the maximum input voltage of the digital potentiometer, preventing potential latch up.

The AD5222 was the only digital potentiometer that met the required performance: ± 2.5 V power supply, ensuring the analogue signals do not saturate; controllable through the ADC GPIO pins; and dual channel, permitting real-time tuning of both gain resistor and input bias compensation resistor. The AD5222 comes in a 10 kΩ option; however, the resistance tolerance is ± 30%. A digital logic voltage divider is also required as the maximum digital input is 2.8 V.

The voltage divider was designed to meet two requirements: current draw and noise margins. The ADC GPIO can source 500 µA, and the potentiometer's digital input draws ±1 µA. The logic high output from the ADC (2.64–3.3 V) is required to be within the logic high input range of the digital potentiometer (2.0–2.8 V), Figure 3.3. The divider network is formed from a 39 kΩ and a 220 kΩ resistor. The maximum current draw is 12.7 µA and the digital potentiometer input voltage range is 2.21–2.77 V, inclusive of the voltage associated with the digital potentiometer's input transistor bias current.

The digital potentiometer requires all four ADC GPIO pins, connections and functionality outlined in Table 3.2. The digital potentiometer is configured as a rheostat, pin A and pin W are tied together as a fail safe, prohibiting the filter from open loop gain.

Table 3.2: Summary table for the AD5222 digital potentiometer connections, values in the square brackets indicates the logic level required to implement that function.

Pin No.	GPIO	Mnemonic	Functions
1	·	B_1	Channel 1 input
2	·	A_1	Fail safe
3	·	W_1	Channel 1 output
4	·	V_{ss}	Negative power supply
5	·	W_2	Channel 2 output
6	·	A_2	Fail safe
7	·	B_2	Channel 2 input
8		GND	Analogue ground
9	**0**	MODE	Independent [**1**]/dependent [**0**] wiper control
10	**1**	DACSEL	Increment channel 1 [**0**] or channel 2 [**1**]
11	**2**	U/$\bar{D}$	Increase [**1**]/decrease [**0**] wiper position on CLK pulse
12	**3**	CLK	Increment channel(s) [**pulse**]
13	·	$\overline{CS}$	Chip select
14	·	V_{DD}	Positive power supply

3.2 Open Source Design Files

The sEMG device is publicly available from (Fortune, Pretty, Chatfield, McKenzie, & Hayes, 2019) under the open source license: CC BY–NC–ND 4.0. A summary of the available files are outlined in Appendix A, Table A.1. The sEMG circuit was developed using Altium Designer (18.1.9, Altium Limited). As Altium is proprietary software, PDF schematics have also been supplied, Appendix B. The Altium project .zip file contains the schematic library, PCB library, compiled library, schematic files (Analog.SchDoc, Digital.SchDoc, Power.SchDoc), the PCb project document and a rules file containing the design constraints for JLCPCB (the chosen PCB manufacturer). Although not tested with this design, the open source *Altium2kicad* package may convert the Altium files to open source cross platform KiCad EDA (5.1.2, KiCAD) files. The STL file for the 3D printable sEMG housing is provided. An example Arduino script that configures the on-board ADC registers, permits adjustable gain and captures the ADC data is also provided. This example script was used to capture the data for the results outlined in Section 3.4. Although proprietary software has been used in the development process of this sEMG device, all files required to manufacture and understand the operation of the product are supplied in an open source file format.

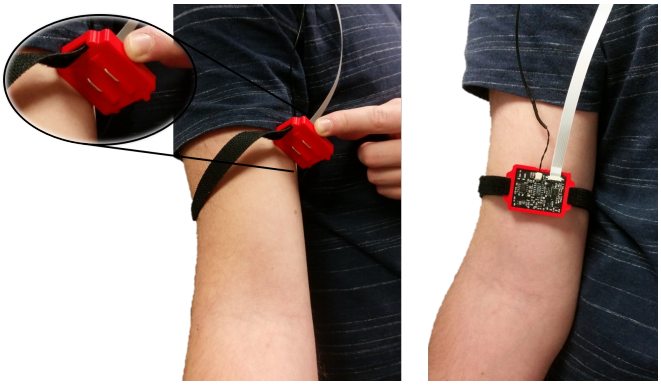

Figure 3.4: Electrode position for recording from the biceps brachii. The white flat flexible cable connects to the microcontroller. The black cable goes to the reference electrode on the elbow.

3.3 Device Validation Methods

This study was approved by the Human Ethics Committee, University of Canterbury (HEC 2019/68) and informed consent was obtained from each participant prior the experiment. To validate the efficacy of the sEMG device, sub-maximal isometric contractions were captured from the right biceps brachii for three able-body male subjects, aged 40, 26 and 24 years old respectively. The electrode position is shown in Figure 3.4.

Skin preparation was achieved by performing approximately 20 light uniform sweeps over the biceps brachii using 600 grit sand paper, followed by sterilisation with 75% ethyl alcohol wipes. A minimum period of two minutes was ensured before attaching the sEMG device above the subject's muscle belly. A 3M foam gel 2228 snap connector electrode, with a 15 mm diameter Ag/AgCl disc, and a 40x33 mm adhesive pad was used as the reference electrode. The reference electrode was placed on the subject's right elbow. The subjects were seated and had their right arm placed on a desk, resulting in an elbow angle of approximately 45 degrees from full extension. The subjects were instructed to perform an isometric contraction lasting between 1–2 seconds, then rest for 1–2 seconds. This process was repeated for 45 seconds, where subjects 1–3 performed 12, 16 and 21 contractions, receptively.

To be able to quantify the sEMG device's characteristics, input referred signals are required. This involves converting the digitised voltage back to voltage representation data, and removal of the applied amplification from the sEMG device.

The ADC on the sEMG device digitises the analogue voltage based on multiple built-in constants and three user defined parameters (Analog Devices, 2018),

$$\text{Data} = \left[\frac{3 \times V_{IN}}{V_{REF}} \times 2^{21} - \text{Offset}\right] \times \frac{\text{Gain}}{4} \times \frac{4,194,300}{2^{42}}, \tag{3.4}$$

where V_{REF} is the full-scale voltage, and Offset and Gain are 24-bit calibration variables. Equation (3.4) was rearranged to convert the digitised data back into voltage representation data,

$$V_{IN} = \left[\frac{\text{Data} \times 4 \times 2^{42}}{\text{Gain} \times 4,194,300} + \text{Offset}\right] \frac{V_{REF}}{2^{21} \times 3}. \tag{3.5}$$

With the digital offset set to zero and the digital gain set to 1 (by setting Gain variable to 0xAAAAB4, 11,184,820 decimal), the digitised to voltage conversion is simply,

$$V_{IN} = \frac{\text{Data} \times V_{REF}}{2^{24}} = \frac{\text{Data} \times 5}{2^{24}}. \tag{3.6}$$

To achieve an input referred signal, a known amplitude sinusoidal waveform was applied to the sEMG device and used to determine the applied gain. A 10 mV, 30 Hz sinusoidal waveform was produced using a Rigol DG1022U function waveform generator. The sEMG device was interfaced with a Teensy 3.6 microcontroller. The Arduino (1.8.10) IDE was

used to captured the data and transfer it to a computer over the serial interface.

Frequency spectral analysis was performed on the input referred signals using a single sided fast Fourier transform (FFT) and a power spectral density (PSD) estimate using the Welch's averaged, modified periodogram method. The spectral analysis was performed using MATLAB (R2017a, MathWorks), where a symmetric Hamming window and zero padding with a factor of 8 was applied for the FFT and a symmetric Hamming window was applied for the PSD. The PSD estimate was calculated by shorting the recording electrodes together and connecting the RLD driver cable to one of the electrodes. As the sampling rate of the sEMG was 1 kHz, the spectral range is DC–500 Hz. The FFT algorithm was applied to the entire raw sEMG data per subject.

3.4 Device Validation Results

The raw data for the three subjects, Figure 3.5, is publicly available from (Fortune, Pretty, Chatfield, McKenzie, & Hayes, 2020), under the open source license: CC BY–NC–ND 4.0. The FFT for the three subjects are shown in Figure 3.6, and the PSD for the sEMG device is shown in Figure 3.7. Device characteristics are based on these results, Table 3.3. This inexpensive open source sEMG device has a large full-scale input range, low baseline noise and good interference suppression, resulting in a device that bridges the gap between high quality sEMG and affordability.

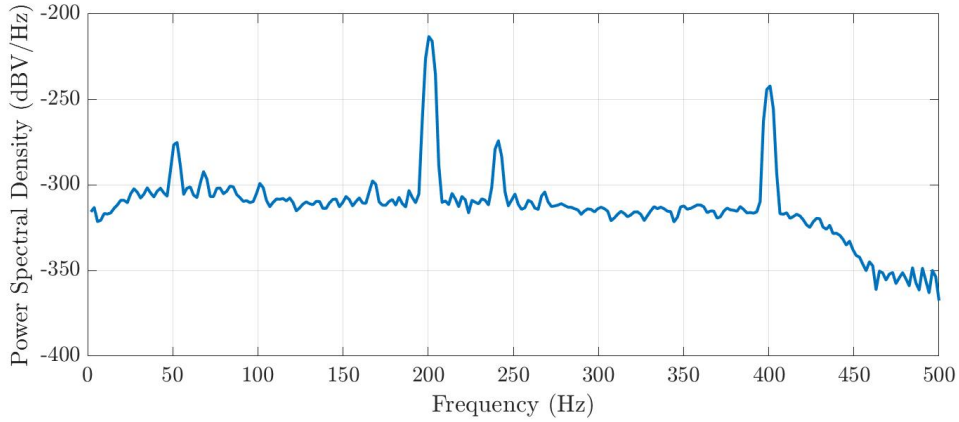

Figure 3.7: Power spectral density estimate of the input referred noise using Welch's method.

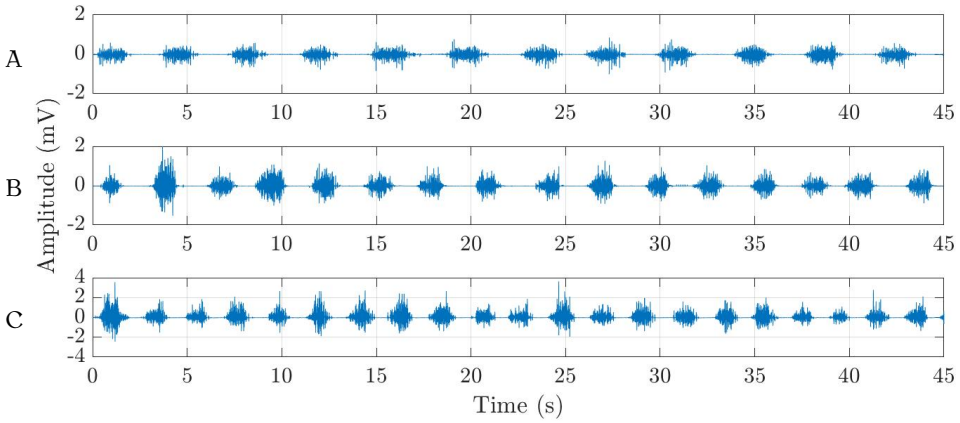

Figure 3.5: Raw sEMG captured from the biceps brachii contraction of three able-body subjects: A, B and C are Subject 1, Subject 2 and Subject 3 respectively. Note the difference in the vertical axis scales.

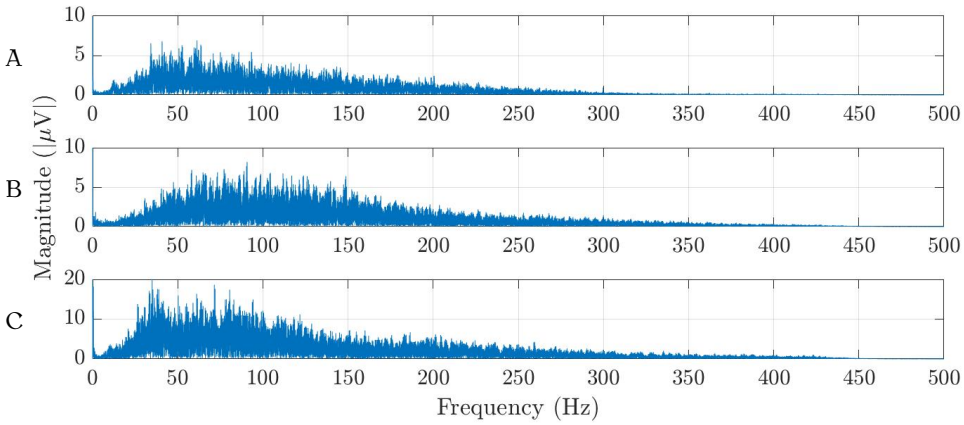

Figure 3.6: Fast Fourier transform (FFT) of the raw sEMG signal captured from the biceps brachii contraction of three able-body subjects: A, B and C are Subject 1, Subject 2 and Subject 3 respectively. Note the difference in the vertical axis scales.

Table 3.3: sEMG device performance parameters.

Parameter	Value	Unit
Resolution	298	nV
Bandwidth	21.2–433	Hz
Dimensions	44.5 x 31	mm
Gain Range	237–3400	V/V
Baseline Noise	$\leq$ 5.2, 3.4 typical	μV_{rms}
Full-scale Input	1.47–21.2	pk-pk mV
ADC Resolution	24	bit
Skin preparation	Abrasive	Required
Sampling Frequency	1,000	Hz

3.5 Design Limitations

The sEMG device has been used in multiple studies, which has lead to understanding the limitations of this design. As this sEMG design is open source, researchers can modify the device to reduce its limitations.

The sEMG board has a 6 pin flat flexible cable (FFC) connector that provides power and SPI transmission. The FFC style connector keeps the connection slim, but it means another surface mount FFC connector must be used. If the sEMG design is to be used without making a PCB that the microcontroller and FFC connector mounts to, a cable-adapter board can be used (files supplied through Fortune et al. (2019)). The cable adapter board converts the FFC style connector to a standard through hole male pin header with 2.54 mm spacing (breadboard/vero board spacing). For the FFC to FFC connection, the longest tested cable was 457 mm (18 inch). However, when an STM32F407VGT6 microcontroller was used instead of the Teensy microcontroller, a cable length over 203 mm (8 inch) resulted in signal degradation. If a longer cable is desired, terminating each SPI data line with a series resistor will slow down the signal edges, improving signal integrity (Johnson, Johnson, & Graham, 2003). When using the cable-adapter board, the jumper wires that connect to the chosen microcontroller are required to be short, otherwise the transmission lines become noisy, resulting in loss of data. The transmission line using the FFC to male pin header was successfully tested using a 228 mm FFC and 50 mm jumper wires. Although the maximum

length was not tested, it may be possible to have longer jumper wires without sacrificing signal transition integrity.

The FFC connector has limited mating cycles, and does not provide strong strain relief, therefore, if the transmission cable is expected to be removed regularly, or there is a possibility that the transmission cable will be under tension, a different style connector would be better suited.

The sEMG device would benefit from higher voltage power supply rails, permitting larger half-cell potentials without reducing the pre-amplifier gain and degrading the CMRR. This may permit recording bioelectrical signals without skin preparation. Another benefit of higher voltage power supply rails is the greater range in digital potentiometers, with the possibility of lower variable resistor tolerances, making the process of calculating the input referred signals simpler and more accurate. However, higher voltage power supply rails would require another dual rail voltage regulator, increasing the sEMG device's cost and possibly size.

The microcontroller is configured to retrieve the ADC data when it receives the $\overline{\text{RDY}}$ signal. This signal is obtained on the DOUT (MISO) line, and combined with the digitised bioelectrical signal. Although this was a suggested method by the ADC manufacturer for a more compact design, breaking out an extra pin for simplicity is beneficial in this case. The $\overline{\text{DRDY}}$ pin produces an independent signal that could trigger an interrupt when the ADC is ready, increasing bioelectrical signal recording simplicity.

3.6 Summary

Surface electromyography design considerations are often outlined in literature; however, as most sEMG designs are proprietary, design files are not available. This chapter has outlined a low-cost, open source, active sEMG device, outlined its performance, and high-

lighted its limitations. The sEMG device uses an active bipolar electrode configuration with silver bar electrodes, implements a band-pass filter and a RLD, and the analogue signal is digitised with a 24-bit sigma-delta ADC. These design choices results in a sEMG device that has a form factor of 45 mm x 30 mm, costs USD $112, has a resolution of 298 nV, a baseline noise of less than 5.2 μV_{rms}, a signal bandwidth of 21.2–433 Hz and a sampling rate of 1 kHz.

The aim of this study was to design an sEMG device that has high quality bioelectrical signal acquisition with a known signal processing architecture. This study was not designed to quantify the amount of electrical interference due to capacitive coupling of the human body and electrodes leads to the mains supply, or the amount of crosstalk contamination from endogenous sources in close proximity. Although the bioelectrical signals measured during this trial resulted in low noise on the limited number of test subjects, abrasive skin preparation was applied, limiting the impedance imbalance between electrode-skin interfaces.

This sEMG device results in high quality bioelectrical signal acquisition with a known signal processing architecture. Therefore, this sEMG device can assist in quantify the impact of balancing multiple electrode-skin interfaces. To continue research on balancing the electrode-skin interface, characterising the electrode-skin interface using time-domain analysis will be performed, Chapter 4.

CHAPTER 4

Modelling the Step Response of Electrode-Skin Interfaces in the Time Domain

Electrodes are used in multiple medical sensing applications: electromyography (EMG), electroencephalography (EEG) and electrocardiography (ECG). However, the data obtained from these methods is affected by coupled electrical interference from environmental sources, and crosstalk from endogenous sources. The severity of the electrical interference is a function of the impedance imbalance between electrode-skin interfaces. Balancing the impedance between electrode-skin interfaces using compensatory impedance may reduce the effect of interference on these bioelectrical signals. Quantitative insight into optimising the compensatory system could be acquired by characterising the electrode-skin interface. As the impedance of the electrode-skin interface is time dependent, this characterisation and compensation would be applied regularly in real-time during the recording process, minimising the variability associated with each individual subject and recording session.

4.1 Methods

To characterise the electrode-skin interface, a step input was applied to a bipolar electrode pair. The voltage and current step response was used to estimate component values for a single exponential model per electrode-skin interface.

4.1.1 Measuring Electrode-skin Interface Step Response

The step input was applied to the recording electrodes, and the step response was measured across one recording electrode (electrode B) with respect to the reference electrode (electrode C), Figure 4.1: where $V_S(t)$ is a constant voltage source, switched at $t = 0$, to produce the voltage step input; A, B and C are the physical electrodes in contact with the skin surface, producing three electrode-skin interfaces; R_{AX}, R_{BX} and R_{CX} are the resistances associated with the dermis and subcutaneous layers of the skin between the respective electrodes; X is a common node connection for the resistances associated with the dermis and subcutaneous layers of the skin; $V_{BC}(t)$ is the voltage step response measured across electrode B with respect to the reference electrode as a function of time, produced using an instrumentation amplifier; and R_S is a current sense resistor, used in combination with an instrumentation amplifier to produce the series current step response as a function of time, $I(t)$.

The voltage step response associated with electrode A is given by,

$$V_{AC}(t) = V_S(t) - \left[V_{BC}(t) + V_{R_S}\right], \tag{4.1}$$

where V_{R_S} is the voltage across R_S. Since the reference electrode is connected to a high impedance input, no current flows through R_{CX} and the reference electrode contact impedance, Z_{C_C}. Therefore, the step response of each recording electrode is measured

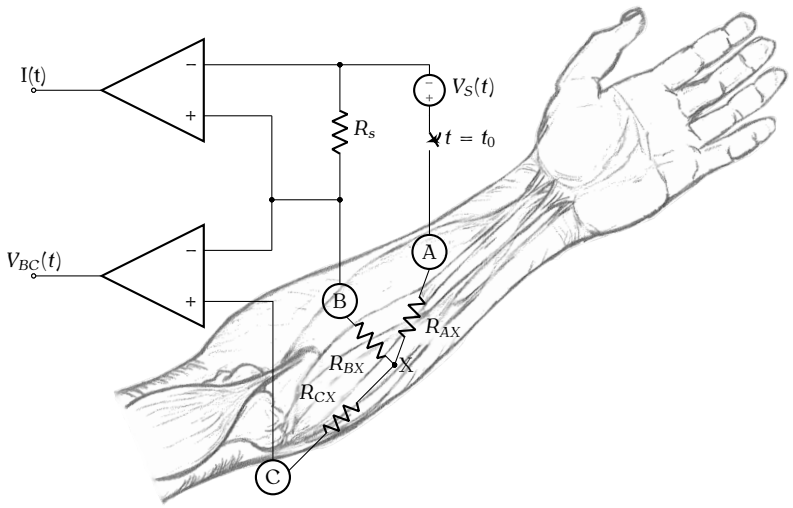

Figure 4.1: Electrode-skin interface voltage measurement across recording electrode B with respect to the reference electrode (electrode C).

across the electrode contact impedance (Z_{Ac}, Z_{Bc}) and its associated dermis and subcutaneous layer resistance.

4.1.2 Electrode-skin Step Response Equation Derivation

The electrode-skin interface component values can be estimated from the measured step response and the series current. A single exponential model is initially used for proof of concept. The resulting circuit diagram is shown in Figure 4.2: where R_1, R_2 and C_1 characterise electrode A, and R_3, R_4 and C_2 characterise electrode B.

The Thévenin equivalent circuit of the single exponential model was derived, where C_2 is the load and R_S is combined with R_4 for simplicity. The Thévenin voltage is,

$$V_T(t) = V_S(t)\,\frac{R_3}{R_1 + R_3 + R_4 + Z_{C_1 \| R_2}}\,, \tag{4.2}$$

and the Thévenin impedance is,

$$Z_T = \frac{R_3\,(R_1 + R_4 + Z_{C_1R_2})}{R_1 + R_3 + R_4 + Z_{C_1||R_2}}\,, \tag{4.3}$$

where

$$Z_{C_1||R_2} = \frac{R_2\,\frac{1}{C_1\,s}}{\left(R_2 + \frac{1}{C_1\,s}\right)} = \frac{\frac{1}{C_1}}{s + \frac{1}{R_2\,C_1}}\,. \tag{4.4}$$

The Thévenin equivalent circuit was used to derive a differential equation as a function of the capacitive load voltage,

$$\begin{aligned} V_T(t) &= V_{Z_T}(t) + V_{C_2}(t)\,, \\ &= C_2\,Z_T\,\frac{d\,V_{C_2}(t)}{dt} + V_{C_2}(t)\,, \end{aligned} \tag{4.5}$$

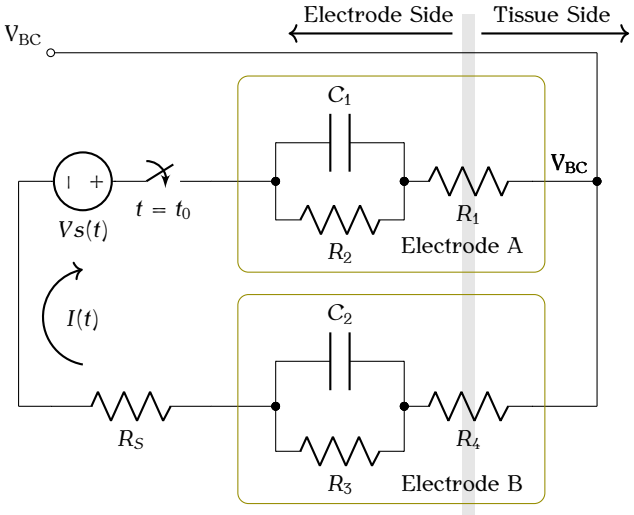

Figure 4.2: High level schematic of the circuit used to measure the step response of a bipolar electrode-skin interface after skin preparation. Olive rectangles outline the electrode-skin interfaces.

which was used in conjunction with the Thévenin equivalent current to derive a differential equation characterising the series current for the electrode-skin impedance model,

$$\begin{aligned} I(t) &= I_T(t) + I_{R_3}(t)\,, \\ &= C_2 \frac{d\,\mathrm{V}_{\mathrm{C}_2}(t)}{dt} + \frac{\mathrm{V}_{\mathrm{C}_2}(t)}{R_3}\,. \end{aligned} \tag{4.6}$$

Simultaneously solving Equations 4.5 and 4.6, and adding the effect of the electrode series resistance to the voltage, leads to general expressions that characterise the step response of the electrode-skin interfaces. The voltage step response,

$$V_{BC}(t) = V_1 \cdot \mathrm{e}^{\left(\frac{-t}{\tau_1}\right)} + V_2 \cdot \mathrm{e}^{\left(\frac{-t}{\tau_2}\right)} + V_3\,, \tag{4.7}$$

and the series current step response is,

$$I(t) = I_1 \cdot \mathrm{e}^{\left(\frac{-t}{\tau_1}\right)} + I_2 \cdot \mathrm{e}^{\left(\frac{-t}{\tau_2}\right)} + I_3\,. \tag{4.8}$$

The summed exponential form is expected due to the circuit being a series combination of two single exponential electrode-skin interface models. The general parameters, $P_1 \in \{V_{1\text{-}3}, I_{1\text{-}3}, \tau_1, \tau_2\}$, are characterised by non-linear expressions that consist of the model component variables, $P_2 \in \{R_1\text{-}R_4, C_1, C_2\}$ (the non-linear expressions which form the general parameters are shown in Appendix C). Therefore, the non-linear behaviour of the electrode-skin interfaces with respect to time is characterised in terms of the general parameters, $f_1(P_1)$, and non-linear expressions formed using the model parameters, $f_2(P_2)$.

4.1.3 Parameter Estimation Overview

Characterising a pair of electrode-skin interfaces using single exponential models results in six components. Using the parameters from fitting experimental data to either the voltage or current characterised by Equations 4.7 and 4.8, results in a underdetermined system. Therefore, using both the voltage and current equations is required. However, this produces eight independent parameters, P_1, resulting in an overdetermined system. Determining the eight parameter values and equating them to their respective model expressions,

$$V_{BC}(t) = f_1(P_1) = f_2(P_2) \ , \tag{4.9}$$

permits a non-linear system of solvable equations. Therefore, by applying a voltage step to the system and measuring the response, P_1 and P_2 were determined using non-linear least squares (NLLS) regression, utilising the trust-region reflective algorithm implemented in MATLAB (R2017a, MathWorks). To reduce computation time and limitations associated with local minima, a method for determining initial estimates for the NLLS regression was developed.

4.1.4 Experimental Data Parameter Initial Estimation, P_1

The series current waveform followed a general trend of an initial step response to an amplitude of I', followed by exponential decay. The general trend of the voltage waveform was an initial step response to an amplitude of V', followed by the four different decay variations associated with the sum of two exponentials, Figure 4.3. Therefore, knowing the specific shape of the voltage waveform assisted in producing initial parameter estimates.

A projected horizontal line at the offset of V' was used to determine if the data contained

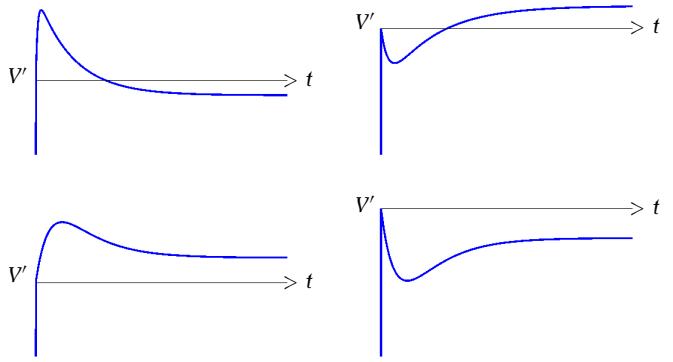

Figure 4.3: The four possible decay variations associated with the sum of two exponentials, where V' indicates the amplitude of the initial step response.

a peak or trough. If the projected line intersected the waveform, the mean of the data inclusive in the intersecting section was calculated, whereas if there was no intersection, the mean of the data subsequent V' was utilised. The waveform was classified as containing a peak if the mean was greater than V', whereas a trough was present if the mean was less than V'. As V' can be followed by an exponential increase, it is difficult to determine the moment it occurs using only the voltage. However, it coincides with I', therefore, $t(I') = t(I_{\max}) = t(V')$.

A good approximation of a single exponential system reaching steady state is the time associated with five times the decay constant: this is related to the exponential function reaching less than 1% of its initial value. This approximation is still adequate for a sum of two exponentials. The initial estimates for the decay constants, $\tau_{1,2}$, were a function of the time associated with the peak/trough, and the inverse settling time, respectively. The steady state mean was used for the initial estimate of the constant V_3. The scaling factors for the exponential bases, $V_{1,2}$, were required to be less than the difference between the supply voltage (or maximum recorded current) and steady state, therefore, half the difference was used for $V_{1,2}$ initial estimates. $V_{1,2}$ have to be opposite signs to achieve exponential decay and growth, therefore, the peak/trough identification during the waveform shape detection method was used to determine the sign of $V_{1,2}$.

4.1.5 Model Parameter Initial Estimation, P_2

Estimating the four resistances was achieved by analysing the system where the capacitive components had zero effect: during the initial step response to V', and steady state. A left-hand limit as time approaches zero was applied to Equations 4.7 and 4.8, forming expressions that describe the initial voltage and current behaviour,

$$\begin{aligned} V_{BC_{0^+}} &= \lim_{t\to 0^+} V_{BC}(t) = \lim_{t\to 0^+} \left(V_1 \cdot \mathrm{e}^{\left(\frac{-t}{\tau_1}\right)} + V_2 \cdot \mathrm{e}^{\left(\frac{-t}{\tau_2}\right)} + V_3 \right) , \\ &= \sum_{n=1}^{3} V_n , \end{aligned} \tag{4.10}$$

$$\begin{aligned} I_{0^+} &= \lim_{t\to 0^+} I(t) = \lim_{t\to 0^+} \left(I_1 \cdot \mathrm{e}^{\left(\frac{-t}{\tau_1}\right)} + I_2 \cdot \mathrm{e}^{\left(\frac{-t}{\tau_2}\right)} + I_3 \right) , \\ &= \sum_{n=1}^{3} I_n . \end{aligned} \tag{4.11}$$

Applying $f_1(P_1)$ and $f_2(P_2)$ to Equations 4.10 and 4.11, produces a set of solvable equations for the initial estimates of R_1 and R_4,

$$\sum_{n=1}^{3} V_n = V_S \frac{R_1}{R_1 + R_4} , \tag{4.12}$$

$$\sum_{n=1}^{3} I_n = V_S \frac{1}{R_1 + R_4} . \tag{4.13}$$

Simultaneously solving Equations 4.12 and 4.13 produces independent equations for the initial estimates of R_1 and R_4 as a function of P_1,

$$R_1 = \frac{\sum_{n=1}^{3} V_n}{\sum_{n=1}^{3} I_n}, \tag{4.14}$$

$$R_4 = \frac{V_s - \sum_{n=1}^{3} V_n}{\sum_{n=1}^{3} I_n}. \tag{4.15}$$

An expression that describes the system's steady state behaviour was derived by applying a limit as time approaches infinity to Equations 4.7 and 4.8,

$$\begin{aligned} V_{BC_\infty} &= \lim_{t\to\infty} V_{BC}(t) = \lim_{t\to\infty} \left(V_1 \cdot \mathrm{e}^{\left(\frac{-t}{\tau_1}\right)} + V_2 \cdot \mathrm{e}^{\left(\frac{-t}{\tau_2}\right)} + V_3 \right), \\ &= V_3, \end{aligned} \tag{4.16}$$

$$\begin{aligned} I_\infty &= \lim_{t\to\infty} I(t) = \lim_{t\to\infty} \left(I_1 \cdot \mathrm{e}^{\left(\frac{-t}{\tau_1}\right)} + I_2 \cdot \mathrm{e}^{\left(\frac{-t}{\tau_2}\right)} + I_3 \right), \\ &= I_3. \end{aligned} \tag{4.17}$$

Applying $f_1(P_1)$ and $f_2(P_2)$ to Equations 4.16 and 4.17, produces a set of solvable equations for the initial estimate of R_2,

$$V_3 = V_S \frac{(R_1 + R_2)}{\sum_{n=1}^{4} R_n}, \tag{4.18}$$

$$I_3 = V_S \frac{1}{\sum_{n=1}^{4} R_n}. \tag{4.19}$$

Simultaneously solving Equations 4.18 and 4.19 produces an independent equation for the initial estimate of R_2 as a function of P_1 and the estimated parameter R_1,

$$R_2 = \frac{V_3}{I_3} - R_1. \tag{4.20}$$

The total resistance can be obtained using the known voltage source, V_S, and the calculated steady state current, I_3, permitting the derivation of R_3. The estimates for R_1–R_4 contain errors related to the parameterised values. However, these are good initial estimates for solving for the model component values, P_2, using NLLS regression.

A grid search method was implemented to estimate the capacitor values, as fitting the data was sensitive to the initial estimate of the capacitor values. A linearly spaced grid search was implemented; however, there was a larger number of local minima related to the smaller capacitor values. Therefore, a logarithmically spaced grid search was used. This reduced erroneous estimates and the limitations associated with local minima. The minimum capacitance, C_{min}, was set to 1 nF, and the maximum capacitance, C_{max}, was set to 900 μF. A large capacitive range increased the possibility of finding a global minimum, where literature of modelling the electrode-skin interface estimates the capacitance to range from 10 nF (Rosell et al., 1988) to 6 μF (Assambo et al., 2007).

4.1.6 Model Parameter Value Estimation, P_2

Using the estimated resistance values and the logarithmic capacitance grid search, NLLS was used to solve for the six model variables, P_2. For each element of the grid search, the efficacy of the solution was quantified by substituting the estimated model values into $f_1(P_1)$. A normalised root mean square error (NRMSE) was calculated between the data using $f_1(P_1)$ and the raw data. The NRMSE was used as the NLLS exit criterion, where both voltage and current had to be below a tolerance of 8×10^{-3}. This value was chosen after examining the mean of the minimum NRMSE values for half the data sets and doubling it. This approach was verified on the remaining data sets.

4.1.7 Experimental Methods

Data was obtained using three methods: simulation; physical, passive circuitry and human subject. For the simulation and passive circuitry, a 10 V step was applied; however, the current applied to the subject was limited to 300 μA for safety.

Quite Universal Circuit Simulator (QUCS 0.0.19) was used to simulate the circuit and develop the electrode-skin parameter estimation method. Ideal components with initially discharged capacitors were used. Once the parameter estimation method was developed, it was tested on passive circuitry, Figure 4.4. A bench-top Rigol DM3058 LXI digital multimeter was used to measure each component, resulting in a 0.6% and 14% maximum tolerance for the resistive and capacitive components, respectively. The measured component values were used to define the test data sets for the simulation data, permitting comparisons between data types. The voltage across R_S was measured using a Texas Instruments INA128 instrumentation amplifier and used to measure $I(t)$. The step input was applied with an Agilent 33522A wave generator and the response measured with a Tektronix DPO3014 Digital Phosphor oscilloscope.

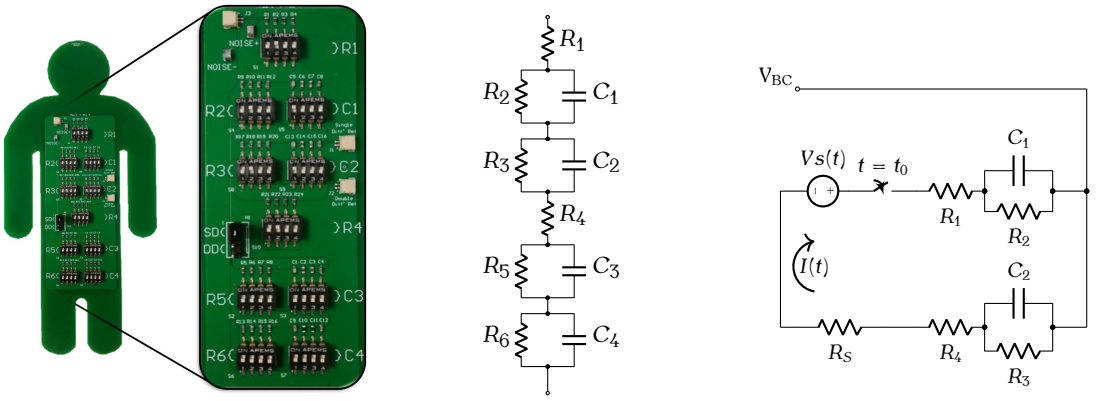

Figure 4.4: (a) Passive circuitry used to emulate the human electrode-skin interface using a single or summed exponential model, where the dip switches allowed the component values to be changed. (b) Equivalent circuit of the passive circuitry. (c) High level circuit schematic used to measure the step response of two single exponential models formed from the passive circuitry.

Ten data sets were obtained for both simulation and passive circuitry. The resistor values ranged from 1 kΩ to 334 kΩ and the capacitors ranged from 20 nF to 8 μF. Data set 8 was arranged to mimic a balanced electrode-skin interface, with resistors of (41.5 ± 0.2) kΩ, and capacitors of $(6.75 \pm 0.05)\,\mu$F .

This study was approved by the Human Ethics Committee, University of Canterbury (HEC 2015/53/LR-PS). Data from one healthy subject (male, age 25) was collected for this study. An electrical stimulator (McKenzie, Fortune, Chatfield, Stewart, & Pretty, 2018), was utilised to apply a current to the electrode-skin interface above the biceps brachii muscle belly. The area was stimulated eight separate times on the subject using Verity Medical Ltd reusable 25 mm diameter disk surface electrodes, constructed with a conductive carbon film and a water based hydrogel. Skin preparation was achieved using 600 grit sand paper. The skin surface was sterilised using USL medical alcohol pads, 70% isopropyl alcohol, and left for a minimum of two minutes to dry. The Tektronix oscilloscope was used to record the data at 5 kS/s.

4.2 Results

Nine of the ten simulation and passive circuitry data sets resulted in accurate estimates, Table 4.1, with a maximum error of 0.763% and 10.2% for simulation and passive circuitry, respectively. The mean error per component was 0.076% and 3.49% for simulation and passive circuitry, respectively. Data set 8 resulted in errors greater than 100%. This is due to fitting curve constants to the square wave response of the balanced electrode-skin interface, which means that the system is not uniquely identifiable. The efficacy of the parameter estimation with respect to the raw data for data set 1 is shown in Figure 4.5.

Performing electrode-skin component estimation on a human subject was unsuccessful, Figure 4.6. The data was recorded for 8.3 minutes, and the system did not reach steady state, a requirement for the electrode-skin component estimation method to be successful.

Table 4.1: Tabulated results for the ten data sets showing the accuracy of the simulated and physical component electrode-skin parameter estimates.

Data Set 1

		Estimated		**Error %**	
Parameter	Known	Sim'	Physical	Sim'	Physical
C1	1.00 μF	1.00 μF	1.05 μF	0.040	5.30
C2	6.80 μF	6.80 μF	6.74 μF	0.044	0.926
R1	28.0 kΩ	28.0 $k\Omega$	26.4 $k\Omega$	0.072	5.58
R2	46.7 $k\Omega$	46.7 $k\Omega$	48.4 $k\Omega$	0.043	3.58
R3	69.9 $k\Omega$	67.9 $k\Omega$	66.3 $k\Omega$	0.044	2.36
R4	55.5 $k\Omega$	55.5 $k\Omega$	55.6 $k\Omega$	0.036	0.252

Data Set 2

		Estimated		**Error %**	
Parameter	Known	Sim'	Physical	Sim'	Physical
C1	672 nF	672 nF	653 nF	0.030	2.81
C2	6.70 μF	6.70 μF	7.04 μF	0.044	5.12
R1	27.0 $k\Omega$	27.1 $k\Omega$	27.2 $k\Omega$	0.078	0.484
R2	46.8 $k\Omega$	46.9 $k\Omega$	48.4 $k\Omega$	0.026	3.36
R3	68.4 $k\Omega$	68.4 $k\Omega$	67.1 $k\Omega$	0.034	1.84
R4	56.1 $k\Omega$	56.1 $k\Omega$	56.1 $k\Omega$	0.034	0.052

Data Set 3

		Estimated		**Error %**	
Parameter	Known	Sim'	Physical	Sim'	Physical
C1	672 nF	673 nF	656 nF	0.089	2.35
C2	6.70 μF	6.70 μF	7.39 μF	0.030	10.2
R1	47.3 $k\Omega$	47.5 $k\Omega$	47.8 $k\Omega$	0.347	1.13
R2	47.0 $k\Omega$	46.8 $k\Omega$	48.2 $k\Omega$	0.243	2.68
R3	47.2 $k\Omega$	47.2 $k\Omega$	45.3 $k\Omega$	0.032	4.16
R4	47.2 $k\Omega$	47.2 $k\Omega$	48.4 $k\Omega$	0.066	2.57

Data Set 4

		Estimated		**Error %**	
Parameter	Known	Sim'	Physical	Sim'	Physical
C1	672 nF	672 nF	671 nF	0.0298	0.164
C2	6.80 μF	6.80 μF	7.36 μF	0.0411	8.115
R1	27.05 $k\Omega$	27.1 $k\Omega$	26.9 $k\Omega$	0.0776	0.477
R2	46.8 $k\Omega$	46.9 $k\Omega$	46.9 $k\Omega$	0.0256	0.026
R3	68.4 $k\Omega$	68.4 $k\Omega$	65.2 $k\Omega$	0.0336	4.661
R4	56.7 $k\Omega$	56.1 $k\Omega$	54.6 $k\Omega$	0.0339	2.552

Data Set 5

		Estimated		**Error %**	
Parameter	Known	Sim'	Physical	Sim'	Physical
C1	7.47 μF	7.49 μF	7.87 μF	0.241	5.33
C2	6.80 μF	6.80 μF	7.25 μF	0.071	6.59
R1	17.2 $k\Omega$	17.2 $k\Omega$	17.8 $k\Omega$	0.195	3.33
R2	23.4 $k\Omega$	23.4 $k\Omega$	22.1 $k\Omega$	0.258	5.68
R3	27.9 $k\Omega$	27.9 $k\Omega$	25.9 $k\Omega$	0.038	7.23
R4	25.6 $k\Omega$	25.6 $k\Omega$	25.7 $k\Omega$	0.188	0.40

Table 4.1: Tabulated results for the ten data sets showing the accuracy of the simulated and physical component electrode-skin parameter estimates (cont.).

Data Set 6

		Estimated		Error %	
Parameter	Known	Sim'	Physical	Sim'	Physical
C1	672 nF	672 nF	686 nF	0.000	2.05
C2	105 nF	104 nF	103 nF	0.763	1.34
R1	27.0 $k\Omega$	27.1 $k\Omega$	27.9 $k\Omega$	0.004	2.96
R2	46.8 $k\Omega$	46.8 $k\Omega$	45.7 $k\Omega$	0.004	2.41
R3	68.4 $k\Omega$	68.4 $k\Omega$	65.5 $k\Omega$	0.004	4.22
R4	56.1 $k\Omega$	56.1 $k\Omega$	55.1 $k\Omega$	0.002	1.77

Data Set 7

		Estimated		Error %	
Parameter	Known	Sim'	Physical	Sim'	Physical
C1	69.2 nF	69.2 μF	69.6 nF	0.000	0.64
C2	20.8 nF	20.8 μF	19.7 nF	0.000	5.14
R1	999 Ω	999 Ω	953 Ω	0.001	4.56
R2	3.29 $k\Omega$	3.29 $k\Omega$	3.37 $k\Omega$	0.021	2.58
R3	2.19 $k\Omega$	2.19 $k\Omega$	2.153, $k\Omega$	0.027	1.85
R4	999 Ω	999 Ω	957 Ω	0.003	4.17

Data Set 8

		Estimated		Error %	
Parameter	Known	Sim'	Physical	Sim'	Physical
C1	6.80 μF	139 MF	133 nF	195	98.0
C2	6.70 μF	19.4 μF	132 nF	189	98.0
R1	47.3 $k\Omega$	2.40 $k\Omega$	-0.246 $k\Omega$	94.9	100
R2	46.9 $k\Omega$	227 Ω	43.7 $k\Omega$	99.5	99.9
R3	47.2 $k\Omega$	17.0 $k\Omega$	40.5 $k\Omega$	64.1	99.9
R4	47.2 $k\Omega$	84.6 Ω	57.8 $k\Omega$	99.8	99.9

Data Set 9

		Estimated		Error %	
Parameter	Known	Sim'	Physical	Sim'	Physical
C1	6.80 μF	6.80 μF	7.17 μF	0.015	5.47
C2	105 nF	105 nF	105 nF	0.000	0.19
R1	101 $k\Omega$	101 $k\Omega$	103 $k\Omega$	0.006	1.98
R2	334 $k\Omega$	336 $k\Omega$	332 $k\Omega$	0.003	0.42
R3	220 $k\Omega$	220 $k\Omega$	209 $k\Omega$	0.000	5.01
R4	82.7 $k\Omega$	82.7 $k\Omega$	81.9 $k\Omega$	0.002	1.00

Data Set 10

		Estimated		Error %	
Parameter	Known	Sim'	Physical	Sim'	Physical
C1	7.47 μF	7.46μF	7.05 μF	0.120	5.59
C2	6.81 μF	6.80μF	6.40 μF	0.115	6.04
R1	999 Ω	1.00 $k\Omega$	1.03 $k\Omega$	0.120	3.33
R2	46.9 $k\Omega$	47.0 $k\Omega$	51.1 $k\Omega$	0.113	8.94
R3	47.2 $k\Omega$	47.3 $k\Omega$	51.1 $k\Omega$	0.116	8.14
R4	999 Ω	1.00 $k\Omega$	1.09 $k\Omega$	0.117	9.23

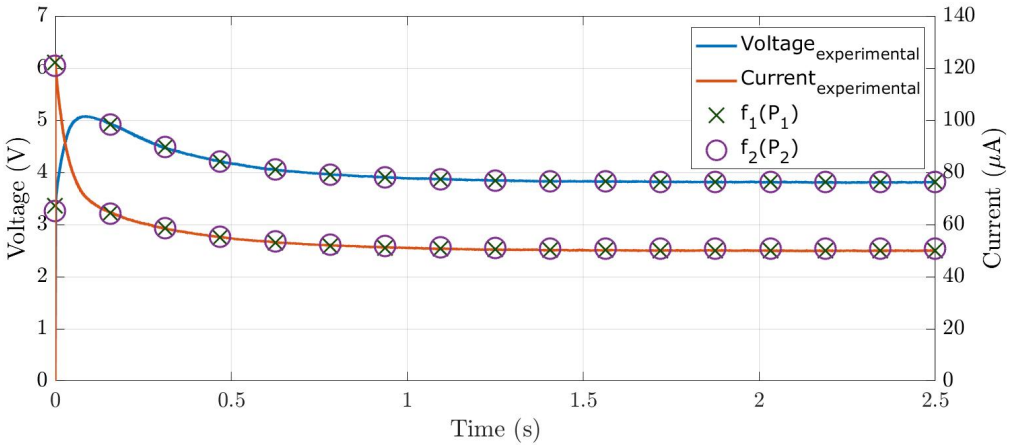

Figure 4.5: Efficacy of component estimation for the test circuit, data set 1.

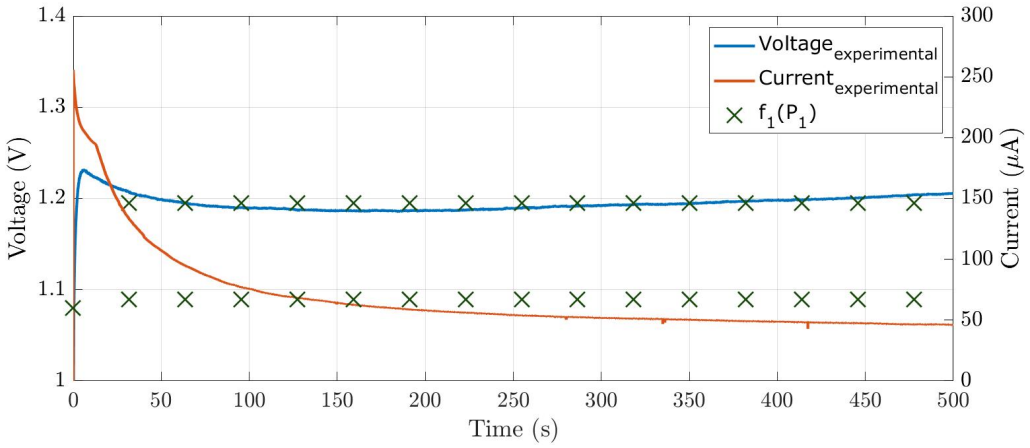

Figure 4.6: Efficacy of component estimation for subject data, the fit of $f_1(P_1)$ was poor. Note the scale of the x-axis.

4.3 Discussion

The simulation and passive circuitry data sets validated the electrode-skin component estimation method. However, estimating the electrode-skin component values for the human subject was unsuccessful.

The step response of the electrode-skin interface did not reach steady state during the 8.3 minutes of stimulation. The voltage step response appeared as if it was near reaching steady state at approximately 100 seconds. However, as the current was consistently decreasing and the voltage started to increase again after approximately 200 seconds, it was

verified that steady state had not occurred. As the electrode-skin component estimation method required the step response to reach steady state, experimental data parameter estimates (P_1) could not be achieved, prohibiting the estimation for the electrode-skin interface component values (P_2).

Even if the settling time associated with the voltage and current step response was 200 seconds, the recording is too long for real-time electrode-skin impedance balancing. As the characteristics of the electrode-skin interface have a temporal relationship, large measurement times may lead to the electrode-skin characteristics changing during measuring the step response. Therefore, a method with large recording times is not suitable for characterising the electrode-skin interface.

A small electrode-skin impedance imbalance results in a small differential voltage across the electrodes during the step response, therefore, the step response tends to a square wave as the impedance imbalance between the electrode-skin interfaces decreases. This leads to a system that is not uniquely identifiable, as seen with passive circuitry data set 8. Since the purpose of developing this method was to assist in balancing the impedance between electrode-skin interfaces, not being able to characterise electrode-skin interfaces when there is little impedance imbalance limits the efficacy of the system. This limitation also increases the difficulty of verifying balanced electrode-skin interfaces. Although a known impedance could be applied to unbalance the electrode-skin interfaces, the application of this impedance has the potential to add complexity and increase the time associated to balance electrode-skin interfaces.

Although the method could possibly be modified to cope when steady state has not be achieved, the step response appears to be the sum of four exponential decays: two obvious gradient changes can be seen in the first 20 seconds of the step response, then another two over the remaining 480 seconds. Therefore, a summed exponential model is

required to characterise each electrode-skin interface. Although skin preparation is meant to shunt the parallel RC components related to the epidermis, resulting in an interface that can be characterised by a single exponential model, it is likely that skin preparation does not remove the contribution of the epidermis, but increases the time constant of the electrode-skin interface. Therefore, a summed exponential model, where one exponential characterises the early step response and the second exponential characterises the long term behaviour of the electrode-skin interface would better characterise the electrode-skin interface. Using the current method, increasing from a single exponential model to a summed exponential model has the potential to result in large, complex equations that characterise the step response. The step voltage may also be changing the chemistry of the electrodes, causing ions to be removed from one electrode and attached to the other, slowly altering the impedance of each electrode-skin interface. Therefore, due to the limitations of characterising the electrode-skin interface in the time domain, the impedance of the electrode-skin interface will be modelled using frequency spectral analysis.

Stimulating the electrode-skin interface using discrete frequencies compared to a continuous time signal decreases the time associated with capturing the data, permit capturing the chosen frequencies required to model the system and simplify the model equation derivation and parameter estimation.

4.4 Summary

The electrode-skin component estimation method worked for nine of the ten simulation and passive circuitry data sets, resulting in mean component estimation errors of 0.076% and 3.49%, respectively. However, the method could not provide viable results for the human subject data due to not reaching steady state. This study outlined limitations of using the time domain to estimate the component values of the electrode-skin interface: the equations are complex and the recording process is long, therefore, to continue research on balancing the electrode-skin interface, the component values were measured (Chapter 5) and estimated (Chapter 6) using frequency dependent stimulation and spectral analysis.

CHAPTER 5

Electrode-Skin Impedance Imbalance Measured in the Frequency Domain

Bioelectrical instrumentation is used to measure weak bioelectrical signals. However, these signals can be contaminated by several forms of interference: mains supply (common-mode) interference, mains supply (differential-mode) interference due to common-mode conversion, and crosstalk from endogenous sources in close proximity. The severity of the electrical interference is a function of the impedance imbalance between electrode-skin interfaces. If the impedance of the electrode-skin interface can be measured, compensatory impedance may be used to reduce the effect of interference on these bioelectrical signals. As the impedance of the electrode-skin interface is time dependent, this characterisation and compensation would need to be applied regularly in real-time during the recording process, minimising the variability associated with each individual subject and recording session. Although electrode-skin impedance imbalance impacts many bioelectrical recording techniques, this chapter focuses on the application to surface electromyography (sEMG).

5.1 Methods

To measure the impedance imbalance between multiple electrode-skin interfaces, the voltage-current relationship of the electrode-skin interface must be measured. By definition, impedance is time-invariant; however, the impedance of the electrode-skin interface has a temporal relationship. Therefore, the system needs to be measured over a window, where the resulting data is considered time-invariant. The voltage across each electrode-skin interface and the series current was measured during a frequency sweep, where each excitation frequency (f_k) excited the interface for a period T. Applying a discrete-time Fourier transform (DTFT) to the voltage and current signals for each frequency, k, results in a complex voltage across each electrode-skin interface and the series current. These complex values form the frequency dependent impedance of each electrode-skin interface.

5.1.1 Data Collection and Impedance Extraction

Measuring the individual electrode-skin impedance was achieved using a custom impedance analyser (CIA), with a stimulation path through recording electrodes A and B, measuring both electrodes separately with respect to the reference electrode, Figure 5.1: where $V_S(f,t)$ is the excitation voltage of the CIA as a function of excitation frequency and time; $I(f,t)$ is the series current of the CIA as a function of excitation frequency and time; $V_{AC}(f,t)$ is the voltage measured across one electrode-skin interface (electrode A) with respect to the reference electrode (electrode C) as a function of excitation frequency and time; $V_{BC}(f,t)$ is the voltage measured across the second electrode-skin interface (electrode B) with respect to the reference electrode as a function of excitation frequency and time; R_{AX}, R_{BX} and R_{CX} are the resistances associated with the dermis and subcutaneous layers of the skin between the respective electrodes; X is a common node connection for the resistances associated with the dermis and subcutaneous layers of the skin. As the reference electrode is connected to a high input impedance, no current flows through R_{CX} and the reference electrode contact impedance, Z_{C_C}, therefore, $V_{AC}(f,t)$ and $V_{BC}(f,t)$ are referenced to the

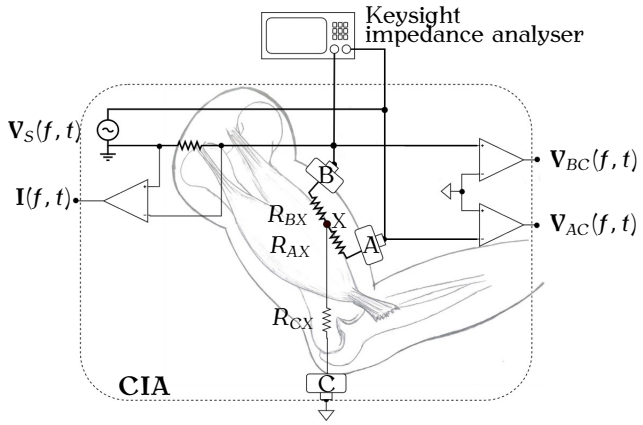

Figure 5.1: High level schematic of how the custom impedance analyser (CIA) measures the individual impedance of the electrode-skin interface.

subcutaneous node X. The individual electrode-skin impedances (Z_A, Z_B) are the sum of the electrode contact impedances (Z_{A_C}, Z_{B_C}) and the resistance associated with the dermis and subcutaneous layers,

$$Z_A(f) = Z_{A_C}(f) + R_{AX} = \frac{V_{AC}(f)}{I(f)}\,, \tag{5.1}$$

$$Z_B(f) = Z_{B_C}(f) + R_{BX} = \frac{V_{BC}(f)}{I(f)}\,. \tag{5.2}$$

The CIA was developed using Analog Device's AD9838 Direct Digital Synthesis device that produces the sinusoidal excitation voltage $V_S(f,t)$, with controllable amplitude and frequency. The amplitude of $V_S(f,t)$ was varied in the range of 50–800 mV peak-to-peak. The CIA produced 40 logarithmically spaced discrete frequencies, where $V_S(f,t)$, $I(f,t)$, $V_{AC}(f,t)$ and $V_{BC}(f,t)$ were sampled at 125 kS/s to 3.125 MS/s, with an excitation period of 10 s for frequencies below 10 Hz and 1 s for the remaining frequencies using a Saleae Logic Analyser, Logic Pro 16. For each known excitation frequency, a DTFT was applied to $I(f,t)$, $V_{AC}(f,t)$ and $V_{BC}(f,t)$,

$$\widehat{V}_{AC}(f) = \sum_{n=0}^{N-1} V_{AC}(f_k, t) \times \mathrm{e}^{-j2\pi f_k n \Delta t}, \tag{5.3}$$

where N is the length of $V_{AC}(f_k, t)$ and Δt is the sampling period. This process was performed in MATLAB (R2019b, MathWorks) for each of the 40 frequencies, resulting in a complex array for the two electrode voltages and the series current. The impedance associated with the electrode-skin interfaces can then be determined,

$$\mathbf{Z}_A(f) = \frac{\widehat{V}_{AC}(f)}{\widehat{I}(f)}, \tag{5.4}$$

$$\mathbf{Z}_B(f) = \frac{\widehat{V}_{BC}(f)}{\widehat{I}(f)}. \tag{5.5}$$

5.1.2 Data Validation

Passive circuitry

To validate the efficacy of the impedance measurement method, passive circuitry was used as a proxy device under test (DUT), Figure 5.2. The proxy DUT was designed to model a pair of single or summed exponential electrode-skin interfaces. However, the single exponential interfaces were used in this study. The proxy DUT was formed from known component values (measured using a Tonghui TH2822E handheld LCR meter). This permitted comparison of the theoretical impedance to the data captured using the CIA. The theoretical impedance is given by $Z_{T_A}(f) = R_1 + R_2 \| Z_{C_1}$ and $Z_{T_B}(f) = R_4 + R_3 \| Z_{C_2}$, where $Z_{T_A}(f)$ and $Z_{T_B}(f)$ are the theoretical impedances of the first and second electrodes respectively.

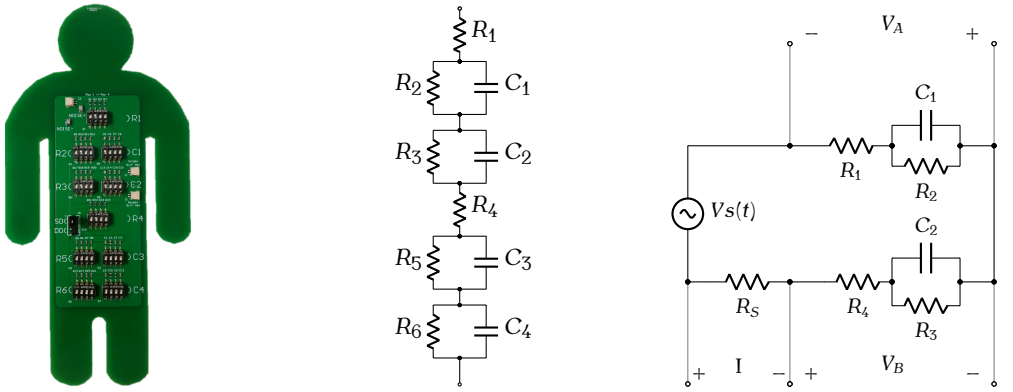

Figure 5.2: (a) Passive circuitry used to emulate the human electrode-skin interface using a single or summed exponential model, where the dip switches allowed the component values to be changed. (b) Equivalent circuit of the passive circuitry. (c) High level circuit schematic used to measure the frequency sweep of two single exponential models formed from the passive circuitry.

Three data sets were obtained using the CIA and the proxy DUT, with component values outlined in Table 5.1. This process highlighted that the CIA was affected by parasitic inductance, as the CIA could not accurately measure the phase at frequencies above 10 kHz and the magnitude above 100 kHz. To quantify the accuracy of the system, a normalised root mean square error (NRMSE) was applied to the data captured using the CIA, $Z_{\mathrm{CIA}}(f)$, and the theoretical impedance, $Z_T(f)$,

$$Z_{\mathrm{NRMSE_{DUT}}} = 100 \times \frac{\sqrt{\frac{1}{K}\sum_{k=0}^{K-1}\left\{|Z_{\mathrm{CIA}}(f_k)| - |Z_{\mathrm{T}}(f_k)|\right\}^2}}{|\overline{Z}_{\mathrm{T}}|}, \tag{5.6}$$

$$\phi_{\mathrm{NRMSE_{DUT}}} = 100 \times \frac{\sqrt{\frac{1}{K}\sum_{k=0}^{K-1}\left\{\phi_{\mathrm{CIA}}(f_k) - \phi_{\mathrm{T}}(f_k)\right\}^2}}{\overline{\phi}_{\mathrm{T}}}, \tag{5.7}$$

where K = 40 (the number of discrete excitation frequencies), $|\overline{Z}_T|$ is the mean magnitude of Z_T and $\overline{\phi}_T$ is the mean phase of Z_T.

Table 5.1: Component values used for the three control DUT data sets.

	$\mathbf{Z_A}$			$\mathbf{Z_B}$		
Data set	$R_1(\Omega)$	$R_2(k\Omega)$	$C_1(nF)$	$R_1(\Omega)$	$R_2(k\Omega)$	$C_1(nF)$
1	998.2	333.5	3.4	998.8	219.5	0.96
2	998.2	46.9	1,029.0	998.8	47.2	1,000
3	998.2	333.5	1.2	998.8	219.5	1.1

Human subjects

To further validate human values for $Z_{A_{\text{CIA}}}(f)$ and $Z_{B_{\text{CIA}}}(f)$ obtained using the CIA, a Keysight Technologies E4990A impedance analyser (KIA) was used. The KIA has an excitation frequency range of 20 Hz–20 MHz, however, a 20 Hz–1 MHz range with 201 samples was implemented for this study. To compare the CIA and KIA data sets, interpolation and truncation of the data had to be performed. The KIA data was truncated to the first data point below or equal to 100 kHz (97.7 kHz) for the magnitude data and 10 kHz (9.5 kHz) for the phase data. The CIA data were up-sampled using cubic spline interpolation, then truncated. This process produced data sets that had a frequency span of 20 Hz–97.7 kHz for the magnitude data and 20 Hz–9.5 kHz for the phase data. Both the magnitude and phase data sets were sampled at the same fixed frequencies for comparison.

Measuring the electrode-skin impedance at 50 Hz was avoided since coupled mains interference can effect the measurement. The interpolated data was used for $Z_{A_{\text{CIA}}}(f)$ and $Z_{B_{\text{CIA}}}(f)$ at 50 Hz. Besides the impedance at mains frequency, the interpolated data was only used in the validation process. The 100 kHz–1 MHz data from the KIA was not used in the validation process, but it gave valuable insight to the high frequency characteristics of the electrode-skin interface.

As the impedance measurements from the CIA are independent of the reference electrode impedance, a single excitation method using two electrodes was used to produce the KIA data. This ensures that a change in reference electrode impedance does not effect the impedance data, however, a two electrode configuration with a single excitation can

only measure the combined impedance across the two electrode-skin interfaces, $Z_{AB_{KIA}}$. Therefore, the sum of the CIA data was used in the validation process. This was calculated using,

$$|Z_{AB_{CIA}}(f)| = \sqrt{\left[\mathbb{R}\{Z_{A_{CIA}}(f)\} + \mathbb{R}\{Z_{B_{CIA}}(f)\}\right]^2 + \left[\mathbb{I}\{Z_{A_{CIA}}(f)\} + \mathbb{I}\{Z_{B_{CIA}}(f)\}\right]^2}, \tag{5.8}$$

$$\phi_{AB_{CIA}}(f) = \arctan\left[\frac{\mathbb{I}\{Z_{A_{CIA}}(f)\} + \mathbb{I}\{Z_{B_{CIA}}(f)\}}{\mathbb{R}\{Z_{A_{CIA}}(f)\} + \mathbb{R}\{Z_{B_{CIA}}(f)\}}\right], \tag{5.9}$$

where $\mathbb{R}(Z)$ symbolises the real component and $\mathbb{I}(Z)$ symbolises the imaginary component. A NRMSE was used to quantify the accuracy of the magnitude and phase of the CIA,

$$Z_{NRMSE} = 100 \times \frac{\sqrt{\frac{1}{K}\sum_{k=0}^{K-1}\left\{|Z_{AB_{CIA}}(f_k)| - |Z_{AB_{KIA}}(f_k)|\right\}^2}}{|\overline{Z}_{AB_{KIA}}|}, \tag{5.10}$$

$$\phi_{NRMSE} = 100 \times \frac{\sqrt{\frac{1}{K}\sum_{k=0}^{K-1}\left\{\phi_{AB_{CIA}}(f_k) - \phi_{AB_{KIA}}(f_k)\right\}^2}}{\overline{\phi}_{AB_{KIA}}}, \tag{5.11}$$

where $|\overline{Z}_{AB_{KIA}}|$ is the mean magnitude of $Z_{AB_{KIA}}$ and $\overline{\phi}_{AB_{KIA}}$ is the mean phase of $Z_{AB_{KIA}}$.

5.1.3 Electrode-skin Impedance Imbalance Metric

A root mean square error (RMSE) between $\mathbf{Z}_{A_{CIA}}(f)$ and $\mathbf{Z}_{B_{CIA}}(f)$ was used to quantify the imbalance of the electrode-skin impedance. The metric was not normalised as bioelectrical signal interference is a function of the absolute impedance imbalance. The RMSE was

calculated for the bioelectrical signal range (1 Hz–500 Hz), the entire data range and mains frequency. Using the truncated data, this resulted in a bioelectrical signal range of 1 Hz–492.4 Hz, and an entire data range of 1 Hz–100 kHz for the magnitude and 1 Hz–9.4 kHz for the phase. The electrode-skin impedance imbalance at mains frequency (50 Hz) was calculated using the interpolated data.

5.1.4 Electrode Configurations

The electrode-skin impedance was measured for three different electrode configurations:

1. silver/silver chloride disc electrodes without skin preparation ($Ag/AgCl_{NSP}$)

2. silver/silver chloride disc electrodes with skin preparation ($Ag/AgCl_{SP}$)

3. silver bar electrodes with skin preparation ($Ag_{\text{-}SP}$).

The electrode-skin impedance for Ag electrodes without skin preparation was not measured, as the large electrode-skin impedance produced by dry electrodes without skin preparation was outside the measurement range of the CIA and KIA.

The Ag bar electrodes are imbedded within the CIA. When the excitation current from the KIA was applied to the Ag electrodes, the excitation current would also backfeed through the CIA. The multiple current paths resulted in erroneous impedance measurements, therefore, there is no validation data using the KIA for the $Ag_{\text{-}SP}$ electrode configuration. Backfeeding current using the Ag/AgCl electrodes was avoided as the electrode leads could be disconnected from the CIA without disrupting the electrode-skin interface.

5.1.5 Subject Data

This study was approved by the Human Ethics Committee, University of Canterbury (HEC 2019/68). Data from ten healthy subjects (five male and five female with a mean age of 25 ± 4) were collected for this study. The first data set collected was for the $Ag/AgCl_{NSP}$ electrodes, where the electrodes were placed above the right biceps brachii muscle belly. The second recorded data set was for the Ag_{-SP} electrodes, placed above the left biceps brachii muscle belly and the last data set was for the $Ag/AgCl_{SP}$ electrodes, also placed above the left biceps brachii muscle belly. This order of recording ensured the adhesive and electrode gel from the Ag/AgCl electrodes did not affect the impedance of the succeeding recordings. Another Ag/AgCl electrode was placed on the elbow to use as the reference electrode. This electrode configuration mimics the set up typically used during sEMG for recording the electrical activity of the biceps brachii.

The Ag/AgCl electrodes were VERMED VersaTrode, polyethylene foam, single use, wet gel teardrop electrodes. The adhesive foam had a diameter of 38.1 mm, and the electrode eyelet was 10.6 mm in diameter, resulting in an interelectrode distance of approximately 40 mm. The CIA had imbedded Ag electrodes, constructed from 1 mm round, 99.99% pure, silver wire, producing a 1x10 mm electrode, with a 10 mm interelectrode distance. The skin preparation was achieved using 600 grit sand paper. The skin surface was abraded using approximately 20 light uniform sweeps over a large area above the biceps brachii to reduce the possibility of producing a local area of impedance difference related to variations in skin preparation. The skin surface was sterilised using alcohol pads, 75% Ethyl Alcohol, and left for a minimum of two minutes to dry. The subjects were required to relax their arm on a table, while maintaining an elbow angle of approximately 90 degrees. The KIA is sensitive to electrostatic discharge (ESD), therefore, to protect the device and maintain consistency, an ESD band was worn for all recordings. The impedance measurements were not effected by the ESD band.

Table 5.2: Error between the custom impedance analyser (CIA) and the theoretical impedance of the control DUT over the range of 1 Hz–100 kHz (magnitude) and 1 Hz–10 kHz (phase), quantified by the root-mean-square error normalised using the mean of the theoretical impedance of the control DUT.

	$\mathbf{Z_A}$		$\mathbf{Z_B}$	
Subject	$\lvert Z\rvert$ (%)	ϕ (%)	$\lvert Z\rvert$ (%)	ϕ (%)
1	4.7	2.7	5.7	5.3
2	5.3	1.6	5.6	1.5
3	3.8	3.4	4.6	4.2
Mean (SD)	4.6 (0.7)	2.6 (0.9)	5.3 (0.6)	3.6 (2.0)

5.2 Results

5.2.1 Proxy Device Under Test (DUT)

The accuracy of the CIA using the proxy DUT is outlined in Table 5.2, resulting in a mean error and standard deviation of (4.6 ± 0.7) % for the magnitude and (2.6 ± 0.9) % for the phase of electrode A; and (5.3 ± 0.6) % for the magnitude and (3.6 ± 2.0) % for the phase of electrode B. These results indicate that impedance measurement methods using the CIA can accurately measure the magnitude up to 100 kHz, and the phase up to 10 kHz.

5.2.2 Subject Trial

The accuracy of the CIA for the ten subjects is outlined in Table 5.3, resulting in a mean error and standard deviation of (12.5 ± 19.2) % for the magnitude and (2.7 ± 3.7) % for the phase using the $Ag/AgCl_{NSP}$ electrode configuration, and (5.7 ± 5.3) % for the magnitude and (10.6 ± 6.8) % for the phase using the $Ag/AgCl_{SP}$ electrode configuration.

The imbalance of the electrode-skin interface for the ten subjects and three electrode configurations as measured by the CIA is outlined in Table 5.4, resulting in an electrode-skin impedance imbalance that ranges from 0.1–143.2 kΩ and 0.0–22.2 degrees, and a mean imbalance and standard deviation at mains frequency (50 Hz) of (37.6 ± 47.1) kΩ for the magnitude and (15.0 ± 18.3) degrees for the phase using the $Ag/AgCl_{NSP}$ electrode configuration, (4.52 ± 7.65) kΩ for the magnitude and (4.6 ± 6.9) degrees for the phase using the $Ag/AgCl_{SP}$

Table 5.3: Error between the custom impedance analyser (CIA) and the Keysight impedance analyser (KIA) over the range of 1 Hz–100 kHz (magnitude) and 1 Hz–9.4 kHz (phase), quantified by the root-mean-square error normalised using the mean of the Keysight impedance analyser.

	Ag/AgCl$_{NSP}$		**Ag/AgCl$_{SP}$**	
Subject	$\|Z\|$ (%)	ϕ (%)	$\|Z\|$ (%)	ϕ (%)
1	3.3	0.9	1.7	14.9
2	7.6	3.7	6.4	11.3
3	14.4	2.7	3.4	4.4
4	1.8	0.8	1.2	24.0
5	16.9	1.7	1.6	19.0
6	9.4	0.6	3.2	4.2
7	4.4	1.3	17.4	5.5
8	64.8	12.8	11.3	9.8
9	1.5	0.9	8.6	4.2
10	0.8	1.1	2.6	8.9
Mean (SD)	12.5 (19.2)	2.7 (3.7)	5.7 (5.3)	10.6 (6.8)

electrode configuration, and $(36.2 \pm 45.1)\,k\Omega$ for the magnitude and (3.4 ± 3.6) degrees for the phase using the Ag$_{SP}$ electrode configuration. As the standard deviation is larger than the mean, and the data is non negative, the data has a right skewed distribution.

Data from subjects 4, 7 and 10 for the three electrode configurations are presented in Figures 5.3, 5.4 and 5.5. These subjects were chosen because they show a range of interesting results. Subject 4 had the least balanced magnitude data over the bioelectrical signal range (Ag/AgCl$_{NSP}$ electrode configuration), and the most balanced data set (Ag/AgCl$_{SP}$ electrode configuration); Subject 7 had the largest recording error (Ag/AgCl$_{NSP}$ electrode configuration, but as the recording error is below 20 Hz, the validation error is still low), and the least balanced data set at 50 Hz (Ag$_{SP}$ electrode configuration); Subject 10 had the least balanced phase data set (Ag/AgCl$_{NSP}$ electrode configuration). Figures for all ten data sets are shown in Appendix D.

Table 5.4: Electrode-skin impedance imbalance quantified using a root mean square error between Z_A and Z_B for ten healthy subjects over three different frequency ranges: 50 Hz, 1 Hz–492.4 Hz and the entire range, 1 Hz–100 kHz (magnitude) and 1 Hz–9.4 kHz (phase).

$Ag/AgCl_{NSP}$

	50 Hz		**Bio-signal range**		**Whole range**	
Subject	$\|Z\|\,(k\,\Omega)$	$\phi\,(deg)$	$\|Z\|\,(k\,\Omega)$	$\phi\,(deg)$	$\|Z\|\,(k\,\Omega)$	$\phi\,(deg)$
1	20.6	16.2	473.0	30.1	350.8	25.1
2	9.2	4.7	9.8	3.8	7.3	3.4
3	12.5	6.7	13.8	4.7	10.3	4.0
4	2.8	12.4	1,447.0	14.8	1,073.1	12.3
5	120.5	14.8	142.8	16.2	106.0	13.6
6	116.9	10.1	264.3	12.4	196.1	10.4
7	21.6	10.0	298.9	7.8	221.7	6.6
8	2.1	6.4	32.6	6.6	24.2	5.6
9	0.9	2.7	82.4	4.1	61.1	3.4
10	69.2	65.5	607.1	56.3	450.3	47.7
Mean (SD)	37.6 (47.1)	15.0 (18.3)	337.2 (439.3)	15.7 (16.4)	250.1 (325.8)	13.2 (13.8)

$Ag/AgCl_{SP}$

	50 Hz		**Bio-signal range**		**Whole range**	
Subject	$\|Z\|\,(k\,\Omega)$	$\phi\,(deg)$	$\|Z\|\,(k\,\Omega)$	$\phi\,(deg)$	$\|Z\|\,(k\,\Omega)$	$\phi\,(deg)$
1	0.26	0.0	0.26	1.1	0.21	3.2
2	1.39	1.1	1.40	3.8	1.12	10.9
3	8.28	6.6	8.28	11.5	6.28	23.2
4	0.05	0.7	0.05	0.6	0.04	1.5
5	0.2	0.0	0.21	0.7	0.18	1.6
6	1.83	2.0	1.89	3.3	1.44	6.5
7	24.63	22.2	29.41	21.6	21.82	21.9
8	1.31	4.0	1.32	6.7	1.01	14.1
9	6.97	9.2	6.91	15.1	5.12	22.2
10	0.32	0.5	0.33	1.2	0.27	4.8
Mean (SD)	4.52 (7.65)	4.6 (6.9)	5.00 (9.01)	6.6 (7.2)	3.75 (6.72)	11.0 (8.8)

$Ag_{\text{-SP}}$

	50 Hz		**Bio-signal range**		**Whole range**	
Subject	$\|Z\|\,(k\,\Omega)$	$\phi\,(deg)$	$\|Z\|\,(k\,\Omega)$	$\phi\,(deg)$	$\|Z\|\,(k\,\Omega)$	$\phi\,(deg)$
1	7.8	1.5	12.5	2.0	9.3	4.5
2	37.4	1.5	39.4	6.5	29.4	7.4
3	63.8	1.3	113.1	7.2	83.9	7.6
4	7.4	2.8	16.1	2.8	12.0	2.6
5	0.8	0.4	0.8	0.8	0.6	1.8
6	14.9	1.0	39.0	2.6	28.9	3.8
7	143.2	10.4	245.2	10.4	181.9	9.3
8	0.8	3.0	13.6	4.9	10.1	4.1
9	69.3	9.8	529.6	6.2	39.3	5.2
10	16.6	2.2	26.4	3.2	19.6	4.4
Mean (SD)	36.2 (45.1)	3.4 (3.6)	103.6 (166.8)	4.7 (2.9)	76.9 (123.7)	5.1 (2.3)

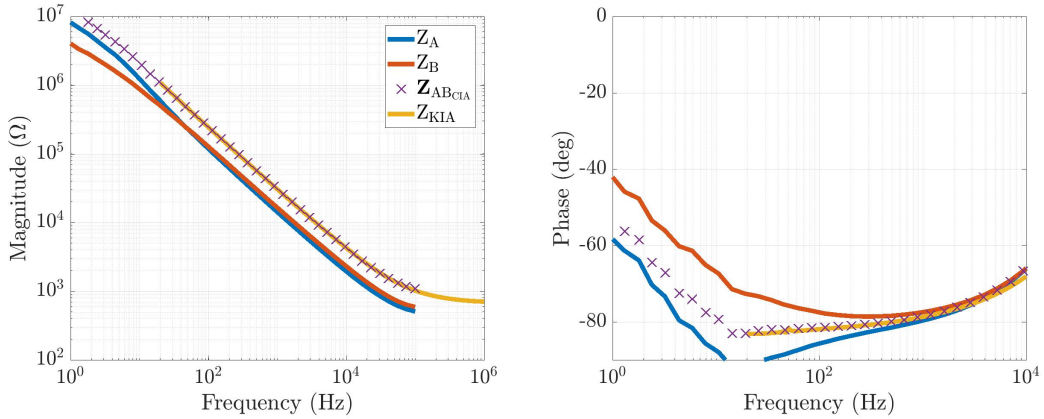

(a) Subject 4: least balanced (magnitude) data set (1 Hz–500 Hz).

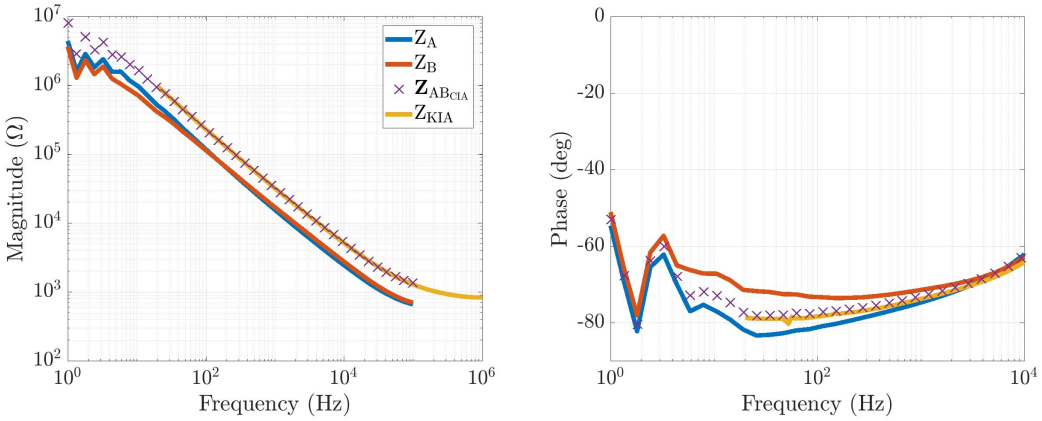

(b) Subject 7: largest recording error data set.

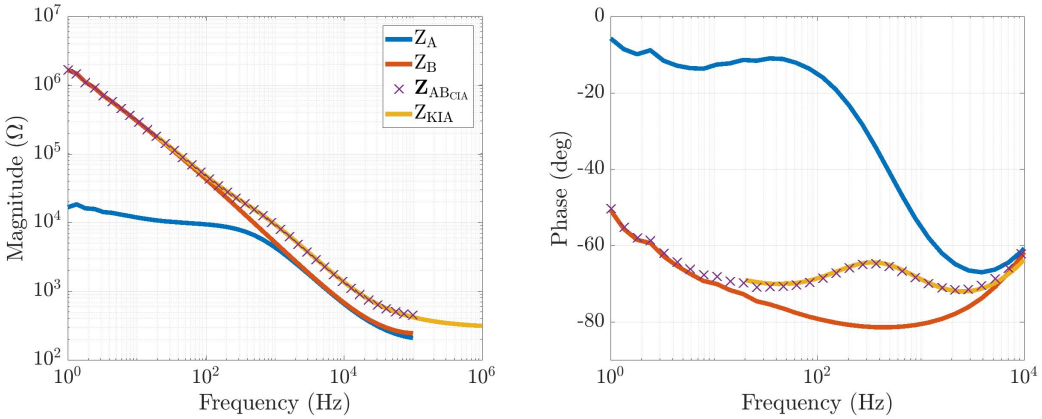

(c) Subject 10: least balanced (phase) data set.

Figure 5.3: Electrode-skin impedance imbalance for 3 healthy subjects using $Ag/AgCl_{NSP}$ electrodes.

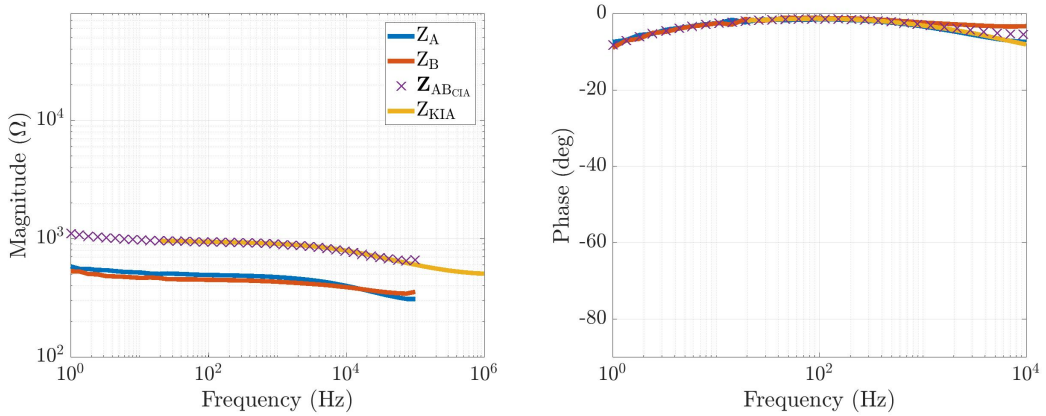

(a) Subject 4: most balanced data set.

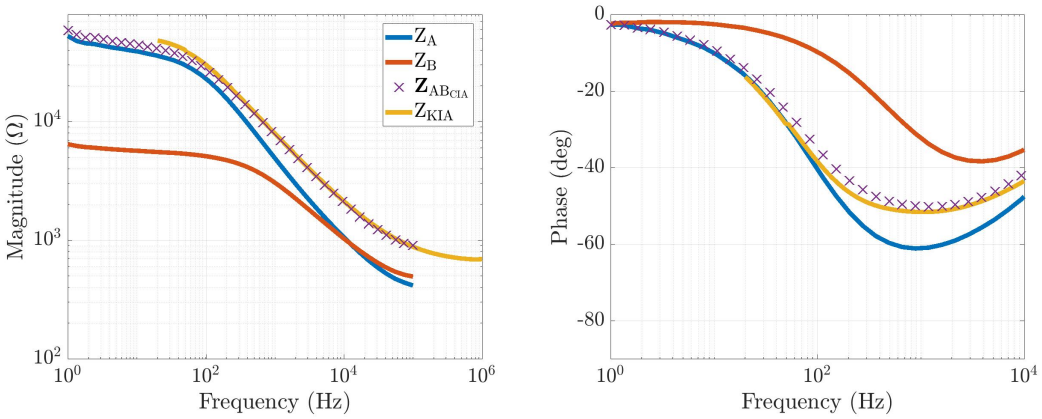

(b) Subject 7.

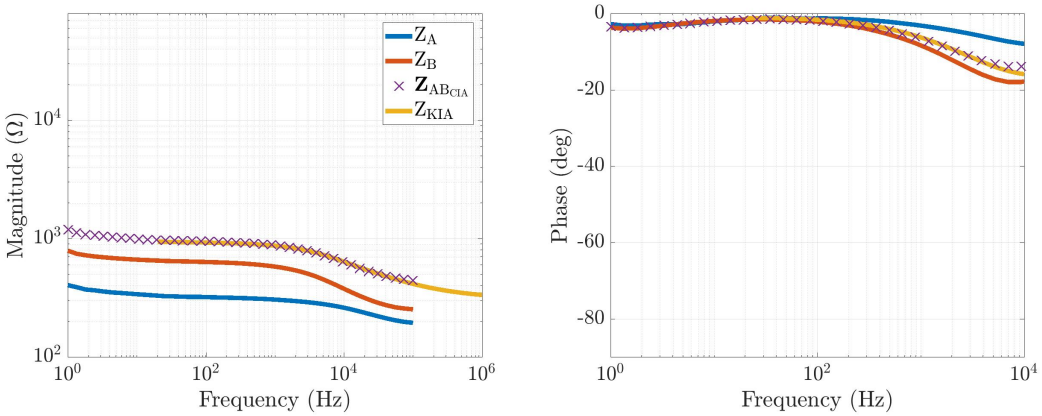

(c) Subject 10.

Figure 5.4: Electrode-skin impedance imbalance for 3 healthy subjects using $Ag/AgCl_{SP}$ electrodes. Note the impedance is substantially lower due to the skin preparation.

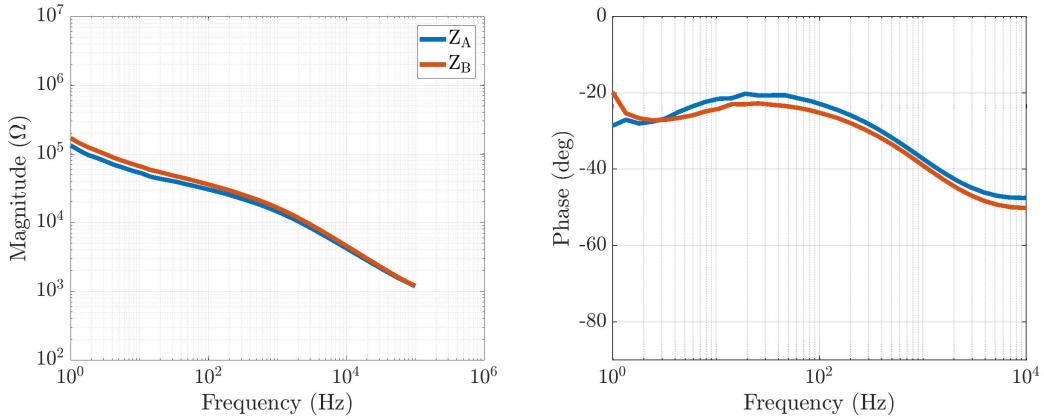

(a) Subject 4.

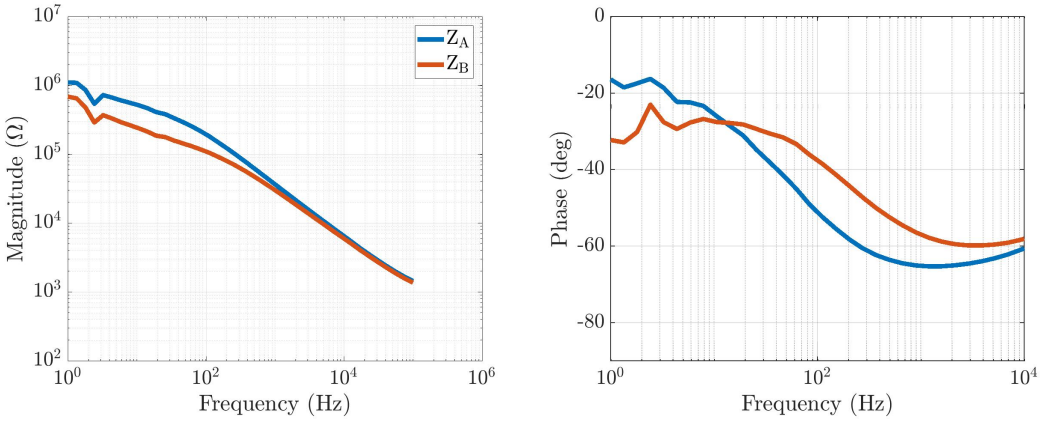

(b) Subject 7: least balanced at 50 Hz (143.2 kΩ).

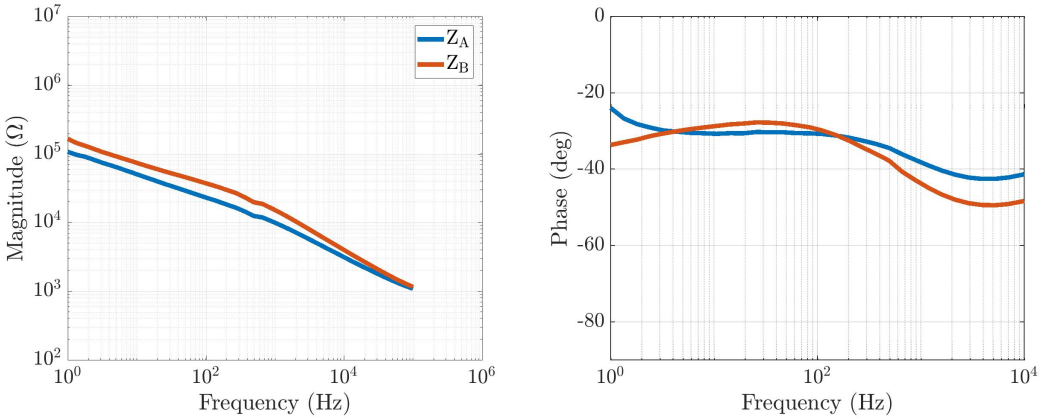

(c) Subject 10.

Figure 5.5: Electrode-skin impedance imbalance for 3 healthy subjects using Ag_{-SP} electrodes.

5.3 Discussion

The validation error between the CIA and the KIA is typically low. However, 25% of the validated recordings have a NRMSE above 10%, where most of these data sets had a small absolute phase leading to a large relative error. It is believed that the temporal relationship of the electrode-skin impedance is the main cause for the observed NRMSE. The impedance measuring process had a set-up time after electrode placement of 2–5 minutes, with recording times of 9.7 ± 2.3 minutes. Due to the large validation error of Subject 8, a 15 minute wait period was performed between applying the $Ag/AgCl_{NSP}$ electrodes and recording the impedance for Subjects 9 and 10. The wait period was aimed at providing a more stable electrode-skin interface during the recording process. This likely contributed to the low NRMSE observed for these subjects. As the electrode-skin impedance and frequency have an inverse relationship, and the interface is more susceptible to time variance at low frequencies, the time dependence of the interface has a large impact on the validation error. Due to this phenomenon, it is believed that the CIA can accurately measure the impedance of the electrode-skin interface.

Skin preparation is a good method to reduce electrode-skin impedance imbalance: Subject 4 went from the largest recorded magnitude imbalance (1.4 MΩ for the bioelectrical signal range using the $Ag/AgCl_{NSP}$ electrode configuration) to the lowest recorded magnitude imbalance (50 Ω for the bioelectrical signal range using the $Ag/AgCl_{SP}$ electrode configuration). However, this level of abrasion is not suitable for infants or subjects with sensitive skin, existing skin irritations and those requiring frequent recordings. Although skin preparation lowers the electrode-skin impedance, it does not guarantee balanced electrode-skin interfaces. This is highlighted by the data collected from Subjects 3, 7 and 9 using the $Ag/AgCl_{SP}$ electrode configuration, resulting in phase imbalances of 11.5-21.6 degrees and magnitude imbalances of 6.9–29.4 kΩ over the bioelectrical signal range.

Several methods were applied to reduce limitations of this study. During skin preparation, approximately 20 light uniform sweeps over a large area above the biceps brachii were performed. This reduced the possibility of skin preparation producing an impedance imbalance. To ensure the electrode adhesive and gel did not effect the impedance measurements between the different electrode configurations, the $Ag/AgCl_{NSP}$ electrode-skin impedance was measured on the right arm, and the $Ag/AgCl_{SP}$ electrode-skin impedance was measured on the left arm. This does introduce another potential limitation that the impedance imbalance will vary from limb-to-limb. However, the issue that an impedance imbalance can be present after skin preparation is proven in this study. The impedance imbalance of the $Ag_{\text{-SP}}$ and $Ag/AgCl_{SP}$ electrode-skin interfaces were measured on the same arm, but due to electrode size, the interelectrode distance was different. However, the large area of uniformly prepared skin should have resulted in an interface with similar characteristics.

The impedance imbalance between electrode-skin interfaces converts the coupled conduction currents flowing through the electrode leads into a differential-mode interference. An unshielded 3 m electrode lead with a diameter of 0.81 mm results in a conduction current, I_{lead}, of 6 nA peak-to-peak when mains supplied equipment is nearby. The mean electrode-skin impedance imbalance of the $Ag/AgCl_{NSP}$ and $Ag_{\text{-SP}}$ electrode configurations was $(36.9 \pm 44.9)\,\text{k}\Omega$, resulting in $221\,\mu\text{V}_{\text{pk-pk}}$ differential-mode interference, $V_{AB_{\text{LEAD}}}$. Equation 2.8 is reiterated here for clarity, substituted with the mean electrode-skin impedance imbalance of the $Ag/AgCl_{NSP}$ and $Ag_{\text{-SP}}$ electrode configurations,

$$\begin{aligned} V_{AB_{\text{LEAD}}} &= (Z_A - Z_B)\, I_{lead} \\ &= (36.9 \times 10^{3}) \times (6 \times 10^{-9}) = 221\,\mu\text{V}_{\text{pk-pk}}\,, \end{aligned} \tag{2.8}$$

The potential divider effect distorts common-mode interference into differential-mode interface due to imbalanced source or input impedance. Bioelectrical instrumentation have a typical common-mode input impedance of 100 GΩ || 9 pF (Texas Instruments, 2018), resulting in 353.7 MΩ common-mode input impedance at mains frequency (50 Hz), Equation 2.18. Therefore, the mean impedance imbalance between electrode-skin interfaces for the $Ag/AgCl_{NSP}$ and Ag_{SP} electrode configurations at mains frequency results in $3.3\,\mu V_{pk-pk}$ differential-mode interference due to the potential divider effect. Equation 2.15 is reiterated here for clarity, substituted with the mean electrode-skin impedance imbalance of the $Ag/AgCl_{NSP}$ and Ag_{SP} electrode configurations at mains frequency,

$$V_{AB_{COM}} = V_{CM}\left[\frac{Z_A - Z_B}{Z_I}\right] \qquad (Z_{A,B} \ll Z_I)$$
$$= 32 \times 10^{-3}\left[\frac{36.9 \times 10^3}{353.7 \times 10^6}\right] = 3.3\,\mu V_{pk-pk}\,, \tag{2.15}$$

where V_{CM} is the sum of the common-mode interferences produced from capacitive coupling of the electrode leads and the human body to the mains supply, Equation 2.9.

The total differential-mode interference due to capacitive coupling and the potential divider effect using the mean impedance imbalance between electrode-skin interfaces for the $Ag/AgCl_{NSP}$ and Ag_{SP} electrode configurations at mains frequency is approximately $232\,\mu V_{pk-pk}$. As the bioelectrical signal of sEMG ranges from microvolts to millivolts, this level of interference can greatly degrade the signal-to-noise ratio (SNR) of sEMG signal acquisition. The total differential-mode interference, Equation 2.19, is reiterated with substituted values for clarity,

$$\begin{aligned} V_{AB} &= V_{AB_{BODY}} + V_{AB_{LEAD}} + V_{AB_{\mathrm{COM}}}\,, \\ &= 7.5 \times 10^{-6} + 221 \times 10^{-6} + 3.3 \times 10^{-6}\,, \\ &= 232\,\mu V_{pk-pk}\,. \end{aligned} \tag{2.19}$$

The experimental data from this study resulted in a maximum impedance imbalance between electrode-skin interfaces of 143.2 kΩ at mains frequency. This could lead to a total differential-mode interference of 880 μV_{pk-pk} for passive electrodes, or a differential-mode interference of 20.5 μV_{pk-pk} for a system using active electrodes (limited interference due to capacitive coupling of the electrodes leads to the mains supply). Active electrodes remove a large portion of the differential-mode interference. However, active electrodes are typically dry electrodes used without skin preparation, resulting in large electrode-skin impedances. These large electrode-skin impedances can increase impedance imbalances between electrode-skin interfaces, leading to large differential-mode interferences.

As the electrode-skin impedance imbalance causes interference within bioelectrical recordings, the impedance imbalance between electrode-skin interfaces cannot be ignored. Modelling the electrode-skin impedance may provide an understanding of the behaviour at the electrode-skin interface and assist in optimising a system to reduce the impedance imbalance between electrode-skin interfaces.

5.4 Summary

Although abrasive skin preparation reduces the impedance imbalance between multiple electrode-skin interfaces, it does not guarantee balanced electrode-skin interfaces. As there is no commercial product to determine the impedance imbalance between electrode-skin interfaces, it is difficult to verify that electrode-skin interfaces are balanced, particularly if

the imbalance at mains frequency is low compared to the imbalance over the bioelectrical signal range.

Typically, only the magnitude is considered when the electrode-skin impedance is measured. However, the phase can also be imbalanced. The results from this study indicate that the electrode-skin impedance imbalance ranges from 0.1–143.2 kΩ and 0.0–22.2 degrees, where the largest magnitude imbalance is not associated with the largest phase imbalance.

The impedance imbalance between electrode-skin interfaces is time variant, and is inconsistent between subjects, electrode type and skin preparation. The mean impedance imbalance between electrode-skin interfaces for the $Ag/AgCl_{NSP}$ and Ag_{SP} electrode configurations was (36.9 ± 44.9) kΩ, which could lead to a differential mode interference of approximately $232\,\mu V_{pk-pk}$ due to capacitive coupling and the potential divider effect. As the bioelectrical signal of sEMG ranges from microvolts to millivolts, this level of interference degrades the performance of sEMG signal acquisition. Therefore, to improve the noise immunity of bioelectrical signal recordings, repeated monitoring and automatic compensation is required to balance the electrode-skin interface. Therefore, to continue research on reducing the impedance imbalance between electrode-skin interfaces, the electrode-skin impedance will be modelled (Chapter 6) using the experimental data from this chapter.

CHAPTER 6

Modelling the Impedance of Electrode-Skin Interfaces in a Bipolar Electrode Configuration

Electrodes are used in multiple medical sensing applications: electromyography (EMG), electroencephalography (EEG) and electrocardiography (ECG). However, the data obtained from these methods are affected by coupled electrical interference from environmental sources, and crosstalk from endogenous sources. The severity of the electrical interference is a function of the impedance imbalance between electrode-skin interfaces, which can be as large as 140 kΩ when using dry electrodes with skin preparation. Modelling the electrode-skin interface will assist in understanding the impedance behaviour at the interface. Therefore, modelling the electrode-skin interface may assist in the development

of a system to reduce the impedance imbalance between electrode-skin interfaces, reducing the effect of electrical interference, and improving the quality of bioelectrical signal acquisition.

6.1 Methods

The electrode-skin impedance from ten healthy subjects (five female and five male with a mean age of 25 ± 4) was collected using a bipolar electrode configuration, described in Section 5.1. A brief summary of the experimental data is outlined in Section 6.1.1. This experimental data was used in developing a model to characterise the electrode-skin impedance, outlined in this Chapter. The model was developed from the first five data sets (development data set) and tested using all ten data sets (validation data set). In some instances, sample means formed from the development data sets were used to assist in parameter estimation. As the electrode-skin interface is non-linear with respect to frequency, non-linear least squares (NLLS) regression was used to solve for the model parameter values. A method was developed to calculate suitable initial estimates for the NLLS regression.

6.1.1 Experimental Data

The impedance magnitude data ranged from 1 Hz to 100 kHz using 40 logarithmically-spaced discrete frequencies. Parasitic inductance affected the high frequency phase data, therefore, it was originally truncated to 9.5 kHz for use in quantifying the impedance imbalance between electrode-skin interfaces, Chapter 5. However, an extra data point assisted in developing the electrode-skin impedance model, therefore, the phase data used to develop the electrode-skin impedance model ranged from 1 Hz to 12.7 kHz. To validate the electrode-skin impedance data, a Keysight E4990A impedance analyser was employed. However, it could only measure the combined impedance of the bipolar electrode pair and had a minimum excitation frequency of 20 Hz. The Keysight impedance analyser was used to measure the impedance from 20 Hz–1 MHz, providing insight to high frequency

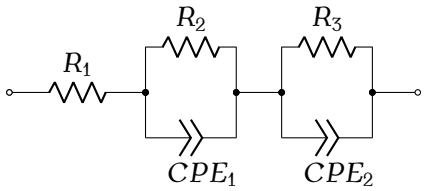

Figure 6.1: Electrode-skin interface model: R_1 represents the combined resistance of the electrode gel, sweat and subcutaneous tissue; R_2 and CPE_1 represent the impedance of the electrode-electrolyte interface; and R_3 and CPE_2 represent the impedance of the epidermal layers of the skin.

electrode-skin characteristics.

The electrode-skin impedance data was measured for three bipolar electrode configurations:

1. silver/silver chloride disc electrodes without skin preparation ($Ag/AgCl_{NSP}$)

2. silver/silver chloride disc electrodes with skin preparation ($Ag/AgCl_{SP}$)

3. silver bar electrodes with skin preparation (Ag_{-SP}).

6.1.2 Model Assumptions

A modified summed exponential model was used to characterise the behaviour of the electrode-skin interface, Figure 6.1. In this model, R_1 represents the series combination of the electrolyte resistance and the dermis and subcutaneous resistance; R_2 and CPE_1 characterise the impedance associated with the electrode-electrolyte interface; and R_3 and CPE_2 represent the impedance of the epidermis. The DC potentials were not modelled as the minimum frequency of the experimental data was 1 Hz. As capacitors cannot represent the frequency dependence of the electrode-skin interface, the capacitors were replaced with constant phase elements (CPEs). CPEs have an impedance defined as,

$$Z_{\mathrm{CPE}}(\omega) = \frac{1}{Q \times (j\omega)^{\beta}}\,, \tag{6.1}$$

where β is a dimensionless parameter, ranging from 0–1, that dictates the phase of the CPE, $\phi_{\mathrm{CPE}} = (-90 \cdot \beta)^{\circ}$. When $\beta = 1$, the CPE characterises a purely capacitive element, when $\beta = 0$, the CPE characterises a purely resistive element. Q is referred to as the magnitude of the CPE, and is numerically equivalent to the admittance of the CPE at $\omega = 1\,\mathrm{rad/s}$, otherwise it has a unit of $\mathrm{S} \cdot \mathrm{s}^{\beta}$.

The impedance of the electrode-skin interface, Z_{ESI}, from Figure 6.1 is,

$$\begin{aligned} Z_{\mathrm{ESI}} &= R_1 + R_2 || Z_{\mathrm{CPE}_1} + R_3 || Z_{\mathrm{CPE}_2}\,, \\ &= R_1 + \frac{R_2}{1 + R_2 \times Q_1 \times (j\omega)^{\beta_1}} + \frac{R_3}{1 + R_3 \times Q_2 \times (j\omega)^{\beta_2}}\,. \end{aligned} \tag{6.2}$$

The magnitude of the electrode-skin impedance settles to a finite resistance at both low and high frequencies, and has an inverse frequency relationship. The low frequency resistance is characterised by the sum of the three resistive elements, $R_{1,2,3}$, and the high frequency resistance is characterised by R_1. The impedance between these sections is a function of the parallel segment component values. The phase of the electrode-skin impedance has two local minima, and one local maximum, tending to zero at both high and low frequencies. A simulated electrode-skin impedance is used to exaggerate these features, Figure 6.2, where Z_{α} represents the region where the phase is near zero degrees and the magnitude is a maximum; Z_{β} is the region where the phase is reaching a local minimum and the magnitude has a constant negative gradient, where both are a function of CPE_2; Z_{γ} represents the region of the local phase maximum and a zero gradient magnitude; Z_{δ}

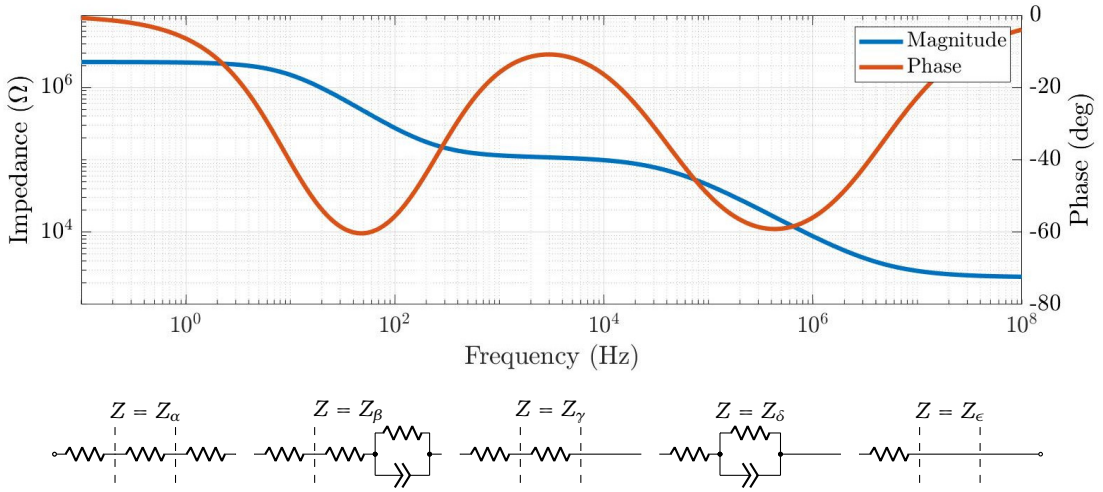

Figure 6.2: Simulated electrode-skin impedance and contributing model segments. Component values were chosen to exaggerate the five different frequency response regions, $\alpha - \epsilon$.

is the region of the second local phase minima and constant gradient magnitude associated with CPE_1; and Z_ϵ represents the region where the phase is returning to zero degrees and the magnitude is settling to a minimum. These five regions are represented by,

$$Z_\alpha = R1 + R2 + R3\,, \qquad (f \to 0) \tag{6.3}$$

$$Z_\beta = R1 + R2 + R3||Z_{\text{CPE}_2}\,, \tag{6.4}$$

$$Z_\gamma = R1 + R2\,, \tag{6.5}$$

$$Z_\delta = R1 + R2||Z_{\text{CPE}_1}\,, \tag{6.6}$$

$$Z_\epsilon = R1\,. \qquad (f \to \infty) \tag{6.7}$$

6.1.3 Non-linear Least Squares Regression

As expected, the five regions were not as well-defined in the experimental data as in Figure 6.2. Each region could influence the adjacent one, therefore, NLLS regression using the interior-point algorithm was implemented in MATLAB (R2019b, MathWorks) to determine the model parameter values.

The experimental data were used to calculate initial estimates. However, the experimental data contained recording noise that impacted the ability of the algorithm to identify model parameter values. Therefore, the data were processed to assist in initial parameter estimation. The impedance data were interpolated from 40 logarithmically spaced data points to 250 logarithmically spaced data points using the MATLAB-specific makima interpolation, a modified Akima piecewise cubic Hermite interpolation. This algorithm was chosen as it reduces the overshoot that occurs when two consecutive data points have a consistent amplitude when using Akima interpolation, and the makima algorithm has reduced overshoot compared to spline interpolation and a smoother derivative than cubic interpolation. A moving mean value algorithm with a window size of 21 was applied to the experimental data to smooth it. The window size was reduced at the end points when there was fewer than 21 data points, ensuring the mean was not biased due to only having data on one side of the window centre point. The interpolated and smoothed data was only used to provide initial estimates for the NLLS regression.

6.1.4 Resistor Initial Value Estimation

The data obtained using the Keysight impedance analyser indicated the high frequency data settled above 100 kHz, therefore, the magnitude data from the Keysight impedance analyser were used to estimate the average high frequency break point of the magnitude data. This was estimated to be 500 kHz for all electrode configurations. The estimated break frequency was used to logarithmically extrapolate the experimental magnitude data, and used to calculate the initial estimate of R_1,

$$R_{1_0} = |\mathbf{Z}'(\omega_N)| \times \left[\frac{\omega_{ex}}{\omega_N}\right]^k, \tag{6.8}$$

where $\mathbf{Z}'$ is the processed experimental data, ω is the interpolated frequency array, N is the index of the last data point, ω_{ex} is the desired extrapolation frequency and k is the

extrapolation gradient. The one-dimensional numerical gradient was calculated using the processed magnitude data. The one-dimensional numerical gradient was also filtered using the same method applied to smooth the experimental data. The mean gradient of the last five data points, between 79 kHz to 100 kHz, was used as the extrapolation gradient.

The local phase maximum was used to validate the assumption that frequency response region γ was purely resistive. However, this assumption was only valid for the $Ag/AgCl_{SP}$ data sets. The phase of the remaining data sets were affected by the capacitance associated with the CPEs. This was evident as the phase maximum was more negative. To quantify the contribution of the CPEs, Equation 6.5 was modified. The CPEs were treated as capacitors ($\beta_{1,2}$ fixed at 1), and it was assumed that a phase of -90 degrees was a purely capacitive segment, which linearly decreased to 0 degrees, resulting in a purely resistive segment. Treating the CPEs as capacitors was only applied during the initial value estimation process of R_2. The initial estimate of R_2 was calculated using,

$$R_{2_0} = |\mathbf{Z}'(\phi_{\max})| \times \left(1 - \frac{\boldsymbol{\phi}_{\max}}{-90 \cdot \alpha}\right) - R_1 \,, \tag{6.9}$$

where $\phi_{\max}$ is the phase at the local maximum and α is a correction factor that accounts for the over simplification of the linear equation for a non-linear system and fixing $\beta_{1,2}$ to 1. The sample mean was used to determine α, which was equal to 4 or 5. Typically, the $Ag/AgCl_{NSP}$ data sets did not have a local maximum due to the two parallel segments simultaneously contributing to the phase. Therefore, the phase minimum was used as a close approximation.

The initial estimate for R_3 was performed using the same logarithmic extrapolation method used for R_1. However, the magnitude data were extrapolated back to 0.5 Hz and used to solve Equation 6.3. Typically the first five data points had a larger level of recording noise,

therefore, the second five data points (1.5–1.9 Hz) were used to calculate the mean gradient used in the extrapolation process.

6.1.5 CPE Initial Value Estimation

As each CPE has two independent unknown parameters, $Q_{1,2}$ and $\beta_{1,2}$, a second NLLS regression method was used to estimate values for $Q_{1_0,2_0}$ and $\beta_{1_0,2_0}$. The interior-point algorithm was utilised to simultaneously minimise the error at multiple points of interest. When the data featured a local phase maximum, it was assumed that two phase minima existed and were independent, such that the impedance of each parallel segment would not affect the other. The error associated with impedance at the phase minima were minimised for Equations 6.4 and 6.6, while enforcing a zero gradient at the frequency of the phase minima. When the two parallel segments were simultaneously contributing to the impedance, $Ag/AgCl_{NSP}$ data sets, the impedance was solved at two distinct points of interest. These points were chosen depending on the features the data sets contained, where the order of priority was: differentiated phase minima, phase minima, and 1 Hz.

The contribution of the low frequency parallel segment was occasionally below the minimum frequency of the experimental data, 1 Hz. Therefore, the initial parameter estimates for the CPE corresponding to that region were set to the sample mean. The initial estimates for these data sets were originally chosen using values that visually best modelled the low frequency data. This resulted in 2.4 $mS.s^{\beta_2}$ and 0.6 for Q_2 and β_2, respectively.

6.1.6 Model Fitting

The upper and lower bounds of the NLLS regression were determined using a one-off iterative method, where the bounds were extended until all test data parameters were within the bounded limits, Table 6.1. The magnitude data were truncated to the same length as the phase data (12.7 kHz), permitting simultaneous minimisation of the root mean square error (RMSE) for both the magnitude and phase data,

Table 6.1: Model parameter upper and lower bounds as a function of the initial estimates used in the non-linear least square solver.

Parameter	**Lower bound**	**Upper bound**
R_1	$0.7\,R_{1_0}$	$1.4\,R_{1_0}$
R_2	$0.2\,R_{2_0}$	$5\,R_{2_0}$
R_3	$0.2\,R_{3_0}$	$5\,R_{3_0}$
Q_1	$0.05\,Q_{1_0}$	$20\,Q_{1_0}$
Q_2	$0.05\,Q_{2_0}$	$20\,Q_{2_0}$
β_1	$0.7\,\beta_{1_0}$	1
β_2	$0.6\,\beta_{2_0}$	1

$$\varepsilon_{\text{RMSE}} = \sqrt{\frac{\sum_{n=0}^{N-1}\left\{\boldsymbol{\varepsilon}_{|\hat{\mathbf{Z}}|}(\omega_n)\right\}^2}{N}} + \sqrt{\frac{\sum_{n=0}^{N-1}\left\{\boldsymbol{\varepsilon}_{\hat{\boldsymbol{\phi}}}(\omega_n)\right\}^2}{N}}, \tag{6.10}$$

where N = 33 (the number of data points in the truncated data), and $\varepsilon_{|\hat{\mathbf{Z}}|}(\omega_n)$ and $\boldsymbol{\varepsilon}_{\hat{\boldsymbol{\phi}}}(\omega_n)$ are the normalised residual errors of the magnitude and phase respectively. The magnitude and phase residuals were normalised to the experimental data to ensure the regression did not bias the magnitude data, as the phase data had a smaller amplitude span,

$$\boldsymbol{\varepsilon}_{|\hat{\mathbf{Z}}|} = \frac{|\mathbf{Z}_{\text{meas}}| - |\mathbf{Z}_{\text{model}}|}{|\mathbf{Z}_{\text{meas}}|}, \tag{6.11}$$

$$\boldsymbol{\varepsilon}_{\hat{\boldsymbol{\phi}}} = \frac{\boldsymbol{\phi}_{\text{meas}} - \boldsymbol{\phi}_{\text{model}}}{\boldsymbol{\phi}_{\text{meas}}}, \tag{6.12}$$

where $|\boldsymbol{Z}_{\text{meas}}|$ and $\boldsymbol{\phi}_{\text{meas}}$ are the raw experimental magnitude and phase data respectively, and $|\boldsymbol{Z}_{\text{model}}|$ and $\boldsymbol{\phi}_{\text{model}}$ are the modelled magnitude and phase data respectively.

The estimated parameters were used with Equation 6.2 to produce modelled data at the same frequencies as the raw experimental data. The modelled data and the raw experimen-

tal data were used to quantify the model accuracy using a normalised root mean square error (NRMSE), where the mean of the experimental data were used as the normalisation metric. However, unlike the residuals used to minimise the error while solving for the parameter values, the model fit residuals were not normalised when calculating the RMSE. The NRMSE was calculated for two frequency ranges: 1–492 Hz, and the phase data range (1 Hz to 12.7 kHz). The two ranges highlight the efficacy of the model over the bioelectrical bandwidth, and the measured data range. As the model is fitted to the raw experimental data, recording noise of the raw data will increase the model fit error. The magnitude and phase for both electrode-skin interfaces on the three electrode configurations over the ten subjects took 15.8 s to model using a PC with an Intel Core i7-6700 processor running on Arch Linux.

6.2 Results

The accuracy of the model fit for the ten subjects over the three electrode configurations are outlined in Tables 6.2, 6.3 and 6.4, where Z_A and Z_B are the two electrode-skin impedances. The mean error and standard deviation for the two electrodes over the bioelectrical bandwidth are (12.5 ± 14.7) % for the magnitude and (4.5 ± 4.9) % for the phase using the $Ag/AgCl_{NSP}$ electrode configuration, (3.2 ± 1.7) % for the magnitude and (6.2 ± 8.9) % for the phase using the $Ag/AgCl_{SP}$ electrode configuration, and (15.5 ± 17.9) % for the magnitude and (4.4 ± 1.8) % for the phase using the $Ag_{\text{-SP}}$ electrode configuration.

The parameter values for the ten subjects and the three electrode configurations are outlined in Tables 6.5 to 6.7, and the mean parameter values for the three different electrode configurations are shown in Table 6.8.

The raw experimental data and fitted model data for Subjects 3, 4 and 7 for the three electrode configurations are presented in Figures 6.3, 6.4 and 6.5. These subjects were chosen because they show a range of interesting results. Subject 3 had the largest NRMSE

Table 6.2: Normalised root mean square error between the raw experimental data and the modelled electrode-skin impedance using the $Ag/AgCl_{NSP}$ electrode configuration for ten healthy subjects over the two frequency ranges: bio-signal (1 Hz–492 Hz) and whole (1 Hz–12.7 kHz).

$Ag/AgCl_{NSP}$ (Magnitude)

	Bio-signal range		**Whole range**	
Subject	Z_A (%)	Z_B (%)	Z_A (%)	Z_B (%)
1	3.1	2.7	3.7	3.2
2	1.9	2.9	2.4	3.5
3	2.9	2.6	3.5	3.1
4	5.5	5.0	6.8	6.2
5	41.1	28.3	50.2	34.5
6	19.1	8.7	23.3	10.6
7	44.0	43.0	53.6	52.4
8	17.6	7.4	21.4	9.0
9	2.6	2.4	3.2	2.9
10	4.5	5.0	5.0	6.2
MEAN (SD)	14.2 (16.2)	10.8 (13.7)	17.3 (19.8)	13.2 (16.7)

$Ag/AgCl_{NSP}$ (Phase)

	Bio-signal range		**Whole range**	
Subject	Z_A (%)	Z_B (%)	Z_A (%)	Z_B (%)
1	1.2	1.8	2.2	2.0
2	1.0	1.6	1.6	1.8
3	1.1	1.4	1.0	1.1
4	5.6	2.6	4.7	2.2
5	3.9	3.6	3.4	3.0
6	2.5	3.2	2.2	2.6
7	12.3	8.5	10.4	7.2
8	18.4	13.5	13.8	10.8
9	2.1	1.8	2.2	1.8
10	3.4	1.4	1.5	1.2
MEAN (SD)	5.1 (5.7)	3.9 (4.0)	4.3 (4.3)	3.4 (3.1)

for the magnitude data (Ag_{-SP} electrode configuration) and the largest NRMSE for the phase data ($Ag/AgCl_{SP}$ electrode configuration). Subject 4 had the smallest NRMSE for the magnitude data ($Ag/AgCl_{SP}$ electrode configuration), and highlights the possible recording error that can occur, as the phase was below -90 degrees for the $Ag/AgCl_{NSP}$ electrode configuration. Subject 7 had the smallest NRMSE for the phase data ($Ag/AgCl_{SP}$ electrode configuration), and also the noisiest raw data ($Ag/AgCl_{NSP}$ electrode configuration). Figures for all ten data sets are shown in Appendix E.

Table 6.3: Normalised root mean square error between the raw experimental data and the modelled electrode-skin impedance using the $Ag/AgCl_{SP}$ electrode configuration for ten healthy subjects over the two frequency ranges: bio-signal (1 Hz–492 Hz) and whole (1 Hz–12.7 kHz).

$Ag/AgCl_{SP}$ (Magnitude)

	Bio-signal range		**Whole range**	
Subject	$\mathbf{Z_A}$ (%)	$\mathbf{Z_B}$ (%)	$\mathbf{Z_A}$ (%)	$\mathbf{Z_B}$ (%)
1	4.8	3.8	4.5	3.6
2	2.4	1.5	2.3	1.4
3	1.5	2.0	1.7	1.8
4	1.3	1.5	1.3	1.5
5	2.8	3.0	2.7	2.9
6	4.9	5.2	4.7	5.2
7	8.3	3.7	9.8	3.9
8	2.9	3.3	2.7	3.4
9	2.7	2.0	2.6	2.3
10	4.1	3.1	3.7	2.9
MEAN (SD)	3.6 (2.1)	2.9 (1.2)	3.6 (2.4)	2.9 (1.2)

$Ag/AgCl_{SP}$ (Phase)

	Bio-signal range		**Whole range**	
Subject	$\mathbf{Z_A}$ (%)	$\mathbf{Z_B}$ (%)	$\mathbf{Z_A}$ (%)	$\mathbf{Z_B}$ (%)
1	4.6	5.4	3.2	2.7
2	5.7	1.9	3.5	0.7
3	2.8	42.5	3.4	22.5
4	6.8	9.7	4.5	8.3
5	1.7	2.5	0.9	1.7
6	6.1	2.1	3.4	1.3
7	1.4	1.0	1.1	2.2
8	10.5	4.3	4.0	2.1
9	5.0	3.0	2.4	1.3
10	5.2	2.5	3.1	2.3
MEAN (SD)	5.0 (2.7)	7.5 (12.5)	2.9 (1.2)	4.5 (6.7)

Table 6.4: Normalised root mean square error between the raw experimental data and the modelled electrode-skin impedance using the $Ag_{\text{-SP}}$ electrode configuration for ten healthy subjects over the two frequency ranges: bio-signal (1 Hz–492 Hz) and whole (1 Hz–12.7 kHz).

$Ag_{\text{-SP}}$ (Magnitude)

	Bio-signal range		**Whole range**	
Subject	$\mathbf{Z_A}$ (%)	$\mathbf{Z_B}$ (%)	$\mathbf{Z_A}$ (%)	$\mathbf{Z_B}$ (%)
1	3.7	3.1	4.2	3.5
2	8.1	11.5	9.2	12.7
3	52.3	68.3	61.7	80.0
4	15.7	11.9	17.7	13.5
5	2.8	4.5	3.1	5.0
6	14.7	34.1	17.0	39.7
7	23.3	27.3	27.9	32.2
8	9.0	5.5	10.5	6.4
9	6.8	4.7	8.3	5.7
10	1.4	2.2	1.7	2.5
MEAN (SD)	13.8 (15.1)	17.3 (20.9)	16.1 (17.9)	20.1 (24.5)

$Ag_{\text{-SP}}$ (Phase)

	Bio-signal range		**Whole range**	
Subject	$\mathbf{Z_A}$ (%)	$\mathbf{Z_B}$ (%)	$\mathbf{Z_A}$ (%)	$\mathbf{Z_B}$ (%)
1	2.3	3.8	2.0	3.0
2	3.9	4.2	4.9	5.5
3	6.8	4.3	4.4	3.4
4	3.6	5.4	2.8	4.2
5	4.0	1.9	3.2	1.7
6	9.5	5.5	6.7	3.8
7	3.8	6.4	2.7	4.3
8	4.4	5.2	2.9	3.7
9	3.6	3.9	3.0	2.9
10	1.6	3.3	1.3	2.6
MEAN (SD)	4.4 (2.3)	4.4 (1.3)	3.4 (1.6)	3.5 (1.0)

Table 6.5: Electrode-skin interface component values using the $Ag/AgCl_{NSP}$ electrode configuration for ten healthy subjects.

$Ag/AgCl_{NSP}$ (Z_A)

Subject	$R_1(\Omega)$	$R_2(k\Omega)$	$R_3(k\Omega)$	$Q_1(nS.s^{\beta_1})$	β_1	$Q_2(\mu S.s^{\beta_2})$	β_2
1	281.5	215.1	4,355.4	211.3	1.0	0.1	0.9
2	386.0	181.9	8,142.5	164.4	1.0	0.1	0.9
3	356.7	101.0	257.4	163.9	0.8	0.1	1.0
4	244.4	10,217.1	253,977.7	14.0	1.0	2.3	0.6
5	187.0	12,723.8	109,448.9	28.0	1.0	4.0	0.5
6	174.6	9,690.4	8,128.0	26.2	1.0	1.0	0.6
7	554.9	5,486.8	5,492.3	228.1	1.0	0.0	0.8
8	208.5	22.6	971.0	181.2	1.0	0.1	0.9
9	194.6	131.3	1,573.2	3,873.4	1.0	0.1	0.9
10	213.6	9.4	7.7	60.7	0.9	8.1	0.8
MEAN (SD)	280.2 (120.4)	3,877.9 (5,164.2)	39,235.4 (82,512.3)	495.1 (1,189.8)	1.0 (0.1)	1.6 (2.6)	0.8 (0.2)

$Ag/AgCl_{NSP}$ (Z_B)

Subject	$R_1(\Omega)$	$R_2(k\Omega)$	$R_3(k\Omega)$	$Q_1(nS.s^{\beta_1})$	β_1	$Q_2(\mu S.s^{\beta_2})$	β_2
1	293.2	144.3	77.3	382.1	0.8	0.2	0.9
2	412.0	60.1	7,352.2	242.4	1.0	0.1	0.8
3	383.0	186.5	168.3	70.3	0.9	0.2	0.8
4	467.8	820.9	4,929.6	461.5	1.0	0.0	0.9
5	424.0	1,321.2	10,524.0	849.7	1.0	0.0	0.8
6	339.1	578.5	8,840.9	100.8	0.8	0.0	0.9
7	293.1	1,255.2	7,825.6	1,267.4	1.0	0.1	0.8
8	168.5	90.9	1,195.3	3,897.1	0.9	0.1	0.9
9	219.0	62.8	1,199.1	276.9	0.9	0.1	0.9
10	247.2	116.2	3,044.3	181.3	0.9	0.1	0.9
MEAN (SD)	324.7 (97.2)	463.7 (501.6)	4,515.7 (3,898.3)	773.0 (1,158.7)	0.9 (0.1)	0.1 (0.1)	0.9 (0.1)

Table 6.6: Electrode-skin interface component values using the $Ag/AgCl_{SP}$ electrode configuration for ten healthy subjects.

$Ag/AgCl_{SP}$ (Z_A)

Subject	$R_1(\Omega)$	$R_2(k\Omega)$	$R_3(k\Omega)$	$Q_1(nS.s^{\beta_1})$	β_1	$Q_2(\mu S.s^{\beta_2})$	β_2
1	280.2	0.2	1.4	2,943.8	0.7	3,705.7	0.5
2	231.5	0.3	0.6	2,129.4	0.7	2,109.2	0.6
3	342.6	9.2	1.1	189.4	0.8	318.8	0.8
4	310.0	0.2	2.1	3,811.7	0.7	3,470.8	0.6
5	291.1	0.4	0.3	1,711.4	0.7	1,834.0	0.6
6	284.3	1.8	0.5	401.5	0.7	1,205.8	0.8
7	323.7	35.4	8.8	128.0	0.9	12.0	0.5
8	204.2	0.3	0.1	926.7	0.8	2,452.1	0.8
9	220.2	0.7	0.1	526.3	0.8	2,673.0	0.7
10	182.3	0.1	0.1	5,202.1	0.6	2,858.2	0.8
MEAN (SD)	267.0 (54.2)	4.9 (11.1)	1.5 (2.7)	1,797.0 (1,724.9)	0.7 (0.1)	2,064.0 (1,241.6)	0.7 (0.1)

$Ag/AgCl_{SP}$ (Z_B)

Subject	$R_1(\Omega)$	$R_2(k\Omega)$	$R_3(k\Omega)$	$Q_1(nS.s^{\beta_1})$	β_1	$Q_2(\mu S.s^{\beta_2})$	β_2
1	269.3	0.4	0.4	2,034.9	0.6	2,123.5	0.7
2	285.0	1.6	0.9	409.3	0.8	1,714.7	0.5
3	335.4	0.3	0.2	2,723.3	0.7	1,013.3	1.0
4	371.1	0.1	0.5	9,679.5	0.7	2,675.2	0.7
5	232.1	0.2	0.2	4,209.6	0.6	2,174.4	0.7
6	275.4	3.7	0.4	393.1	0.7	601.4	0.9
7	516.4	5.1	2.1	349.4	0.7	1,105.4	0.6
8	211.2	1.7	0.4	453.0	0.8	2,864.1	0.4
9	245.9	8.1	0.7	161.4	0.9	471.6	0.4
10	242.4	0.4	0.1	1,216.4	0.7	1,788.7	0.8
MEAN (SD)	298.4 (90.4)	2.2 (2.7)	0.6 (0.6)	2,163.0 (2,950.4)	0.7 (0.1)	1,653.2 (832.5)	0.7 (0.2)

Table 6.7: Electrode-skin interface component values using the $Ag_{\text{-SP}}$ electrode configuration for ten healthy subjects.

$Ag_{\text{-SP}}$ (Z_A)							
Subject	$R_1(\Omega)$	$R_2(k\Omega)$	$R_3(k\Omega)$	$Q_1(nS.s^{\beta_1})$	β_1	$Q_2(\mu S.s^{\beta_2})$	β_2
1	277.0	9.1	58.7	1,726.4	0.5	10.0	0.6
2	649.2	68.0	68.9	65.0	0.8	3.2	0.6
3	350.6	138.5	226.6	63.5	0.7	0.8	0.7
4	379.6	33.0	252.1	225.1	0.6	3.6	0.6
5	285.2	40.0	9.8	11,087.6	0.7	2.3	0.5
6	330.3	62.9	221.6	220.9	0.6	1.5	0.7
7	884.1	473.1	719.1	28.9	0.8	0.5	0.7
8	320.6	78.4	336.4	50.5	0.8	0.5	0.6
9	1,176.1	1,528.2	2,581.2	11.6	0.9	0.1	0.7
10	631.2	10.8	227.1	352.0	0.7	2.6	0.5
MEAN (SD)	528.4 (303.7)	244.2 (471.4)	470.1 (767.9)	1,383.1 (3,448.4)	0.7 (0.1)	2.5 (2.9)	0.6 (0.1)

$Ag_{\text{-SP}}$ (Z_B)							
Subject	$R_1(\Omega)$	$R_2(k\Omega)$	$R_3(k\Omega)$	$Q_1(nS.s^{\beta_1})$	β_1	$Q_2(\mu S.s^{\beta_2})$	β_2
1	248.1	13.8	119.6	578.9	0.6	6.5	0.5
2	522.5	106.2	24.0	7,056.5	0.5	0.1	0.7
3	276.5	44.5	367.1	187.0	0.7	2.1	0.6
4	380.8	42.9	157.7	198.5	0.6	1.5	0.7
5	243.9	8.6	65.6	1,480.4	0.6	13.8	0.6
6	287.7	73.9	323.2	102.5	0.7	1.4	0.6
7	421.7	136.7	1,190.0	53.7	0.8	0.7	0.6
8	324.3	675.4	115.2	927.7	0.6	0.1	0.8
9	1,071.8	1,161.2	1,867.6	13.5	0.8	0.1	0.8
10	401.3	39.2	468.0	248.0	0.6	2.0	0.6
MEAN (SD)	417.9 (246.1)	230.2 (382.3)	469.8 (597.5)	1,084.7 (2,149.1)	0.7 (0.1)	2.8 (4.3)	0.6 (0.1)

Table 6.8: Electrode-skin interface mean component values for the ten healthy subjects using the three electrode configurations.

Z_A

Electrode configuration	$R_1(\Omega)$	$R_2(k\Omega)$	$R_3(k\Omega)$	$Q_1(nS.s^{\beta_1})$	β_1	$Q_2(\mu S.s^{\beta_2})$	β_2
Ag/AgCl$_{NSP}$	280.2 (120.4)	3,877.9 (5,164.2)	39,235.4 (82,512.3)	495.1 (1,189.8)	1.0 (0.1)	1.6 (2.6)	0.8 (0.2)
Ag/AgCl$_{SP}$	267.0 (54.2)	4.9 (11.1)	1.5 (2.7)	1,797.0 (1,724.9)	0.7 (0.1)	2,064.0 (1,241.6)	0.7 (0.1)
Ag$_{-SP}$	528.4 (303.7)	244.2 (471.4)	470.1 (767.9)	1,383.1 (3,448.4)	0.7 (0.1)	2.5 (2.9)	0.6 (0.1)

Z_B

Electrode configuration	$R_1(\Omega)$	$R_2(k\Omega)$	$R_3(k\Omega)$	$Q_1(nS.s^{\beta_1})$	β_1	$Q_2(\mu S.s^{\beta_2})$	β_2
Ag/AgCl$_{NSP}$	324.7 (97.2)	463.7 (501.6)	4,515.7 (3,898.3)	773.0 (1,158.7)	0.9 (0.1)	0.1 (0.1)	0.9 (0.1)
Ag/AgCl$_{SP}$	298.4 (90.4)	2.2 (2.7)	0.6 (0.6)	2,163.0 (2,950.4)	0.7 (0.1)	1,653.2 (832.5)	0.7 (0.2)
Ag$_{-SP}$	417.9 (246.1)	230.2 (382.3)	469.8 (597.5)	1,084.7 (2,149.1)	0.7 (0.1)	2.8 (4.3)	0.6 (0.1)

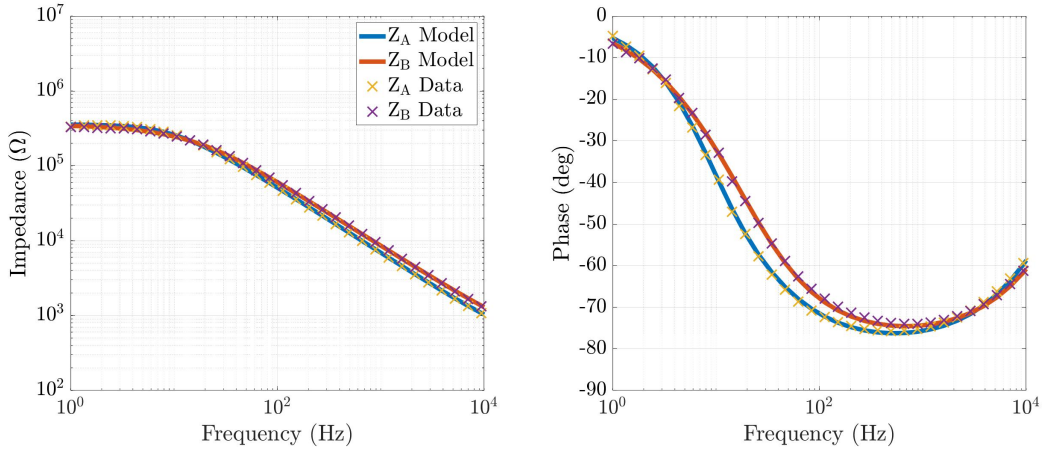

(a) Subject 3.

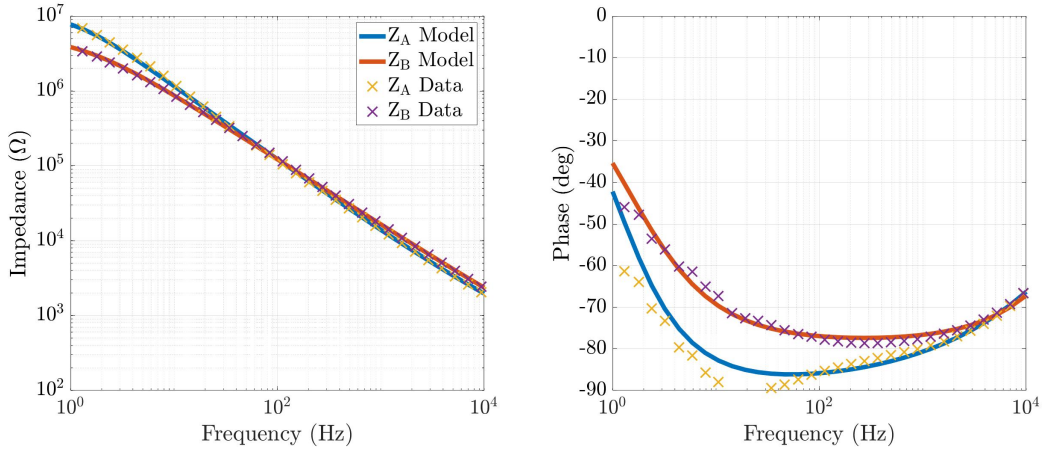

(b) Subject 4.

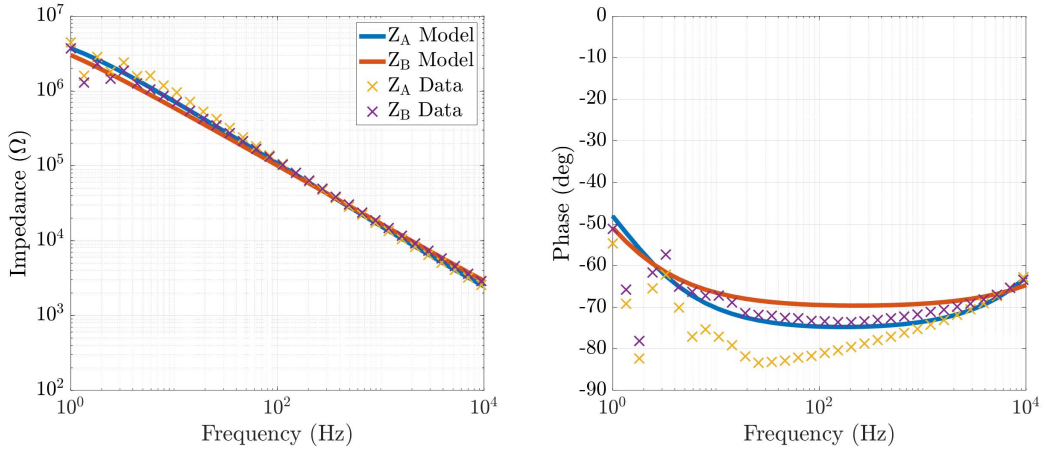

(c) Subject 7.

Figure 6.3: Electrode-skin impedance model fit for Subjects 3, 4 and 7 using $Ag/AgCl_{NSP}$ electrodes.

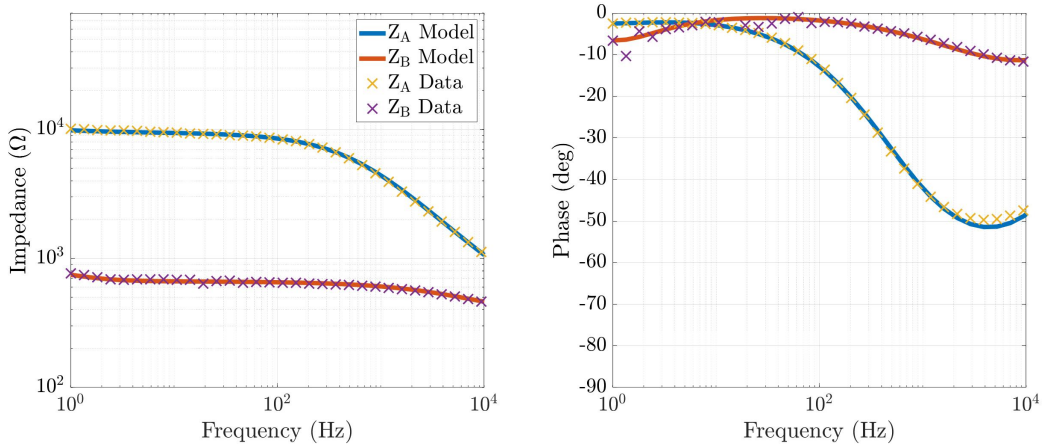

(a) Subject 3.

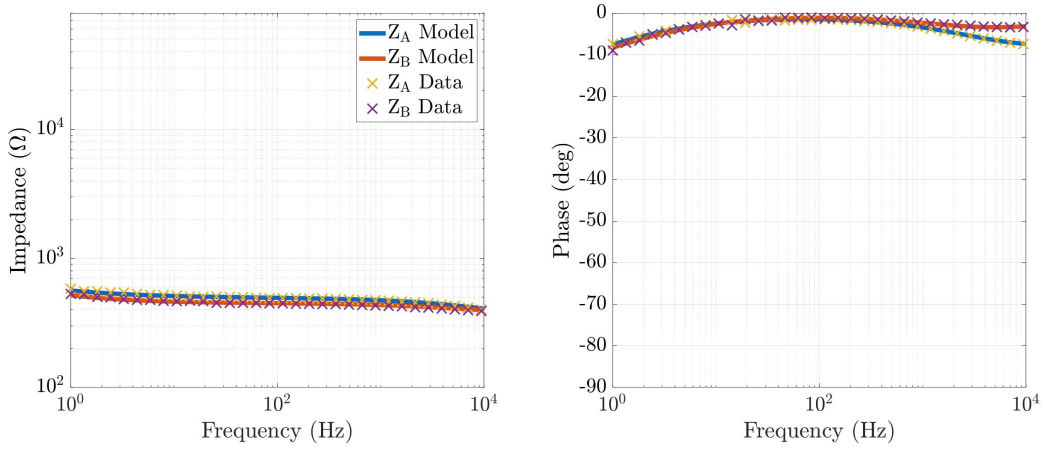

(b) Subject 4.

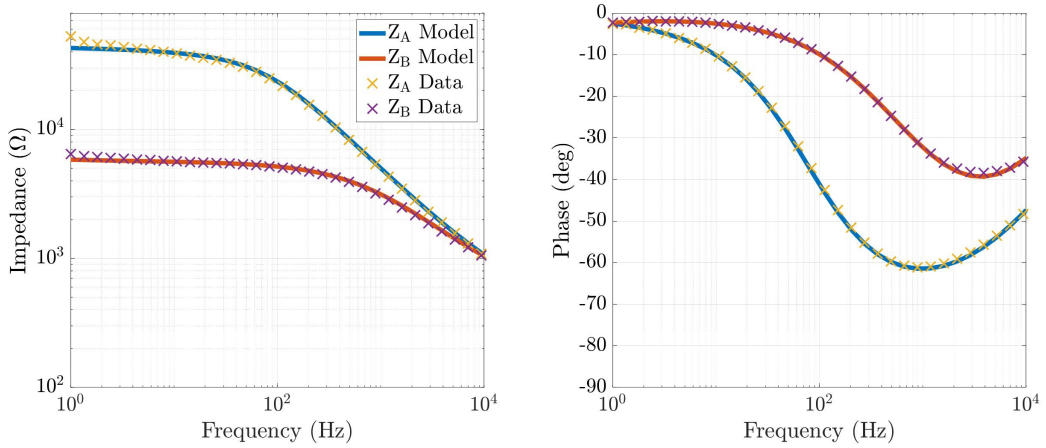

(c) Subject 7.

Figure 6.4: Electrode-skin impedance model fit for Subjects 3, 4 and 7 using $Ag/AgCl_{SP}$ electrodes.

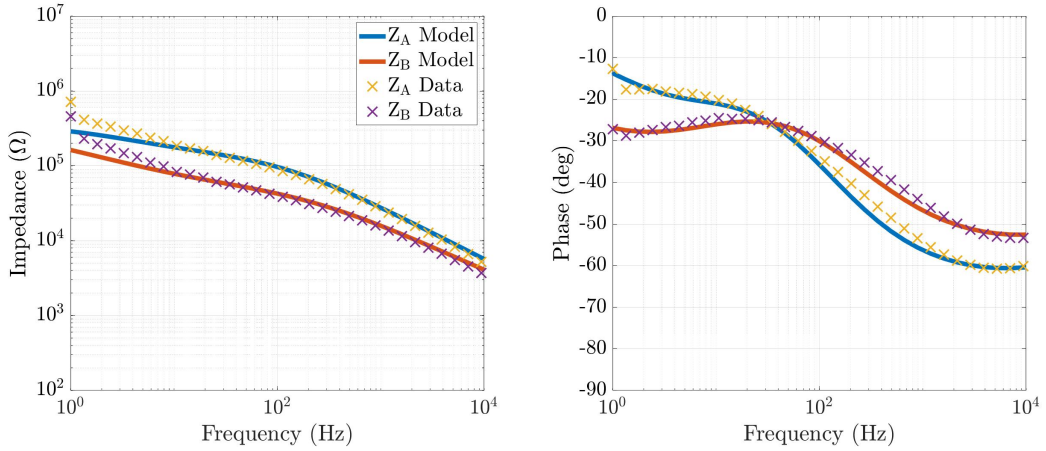

(a) Subject 3.

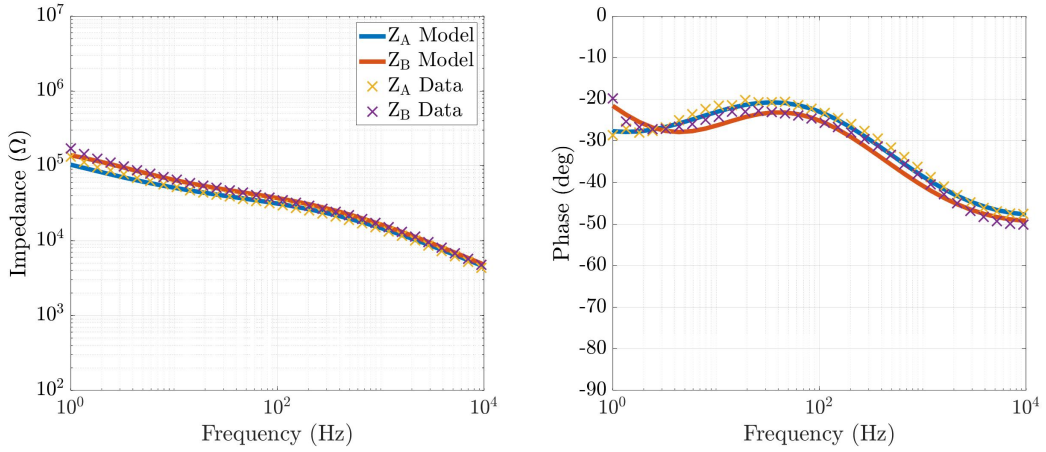

(b) Subject 4.

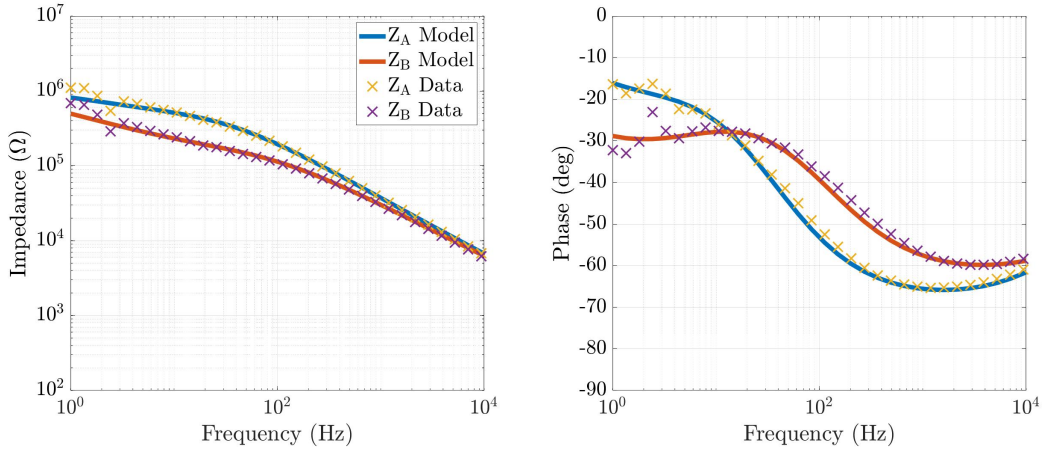

(c) Subject 7.

Figure 6.5: Electrode-skin impedance model fit for Subjects 3, 4 and 7 using Ag_{-SP} electrodes.

6.3 Discussion

There are two key features which highlight the need for a summed exponential model: a local phase maximum and phase asymmetry. A local phase maximum indicates that there are two dominantly capacitive elements with different parameter values. When these capacitive elements are contributing to the impedance at a similar frequency, there is no local phase maximum. However, due to the different parameter values of each capacitive element, the phase is asymmetric about the phase minimum. A summed exponential model can be used to fit a local phase maximum and phase asymmetry. However, purely capacitive elements result in a fixed gradient.

Researchers have attempted to use purely resistive and capacitive elements when modelling the electrode-skin interface. However, this results in fixed gradients of the impedance magnitude. As the magnitude gradients vary between subjects, electrode configuration and within each data set, being able to fit to a wide range of magnitude gradients was required. Replacing the purely capacitive elements with CPEs permitted fitting the magnitude gradient over multiple subjects, electrode configurations and data sets. The model parameter values for $\beta_{1,2}$ ranged from 0.5–1.0, indicating that CPEs are necessary to properly characterise the non-linear frequency behaviour of the electrode-skin interface.

Some data sets resulted in a large NRMSE for the model parameters. This is believed to be due to noise in the raw data and recording error due to the temporal impedance relationship of the electrode-skin interface. Low frequency noise is apparent in the raw $Ag/AgCl_{NSP}$ and Ag_{SP} electrode configuration data sets for Subject 7. Noisy raw data decreases the ability to accurately fit the model parameters to the data, and inherently increases the NRMSE. All three Ag_{SP} electrode configurations shown in Figure 6.5 over-estimate the low frequency impedance. This is believed to be due to the temporal impedance relationship of the electrode-skin interface. A separate measurement was performed for one

subject using the $Ag/AgCl_{NSP}$ electrode configuration. The electrode-skin impedance was measured twice, 30 minutes apart. Due to the temporal relationship, there was a 30% reduction in electrode-skin impedance at 50 Hz. The raw data for this trial had a set-up time, after electrode placement, of 2–5 minutes, with recording times of 9.7 ± 2.3 minutes. The effect of the temporal relationship was noticed late in the trial. As the temporal relationship is characterised as a negative exponential function, the impedance reductions are greatest immediately after electrode placement. Therefore, a 15 minute wait period was performed between applying the $Ag/AgCl_{NSP}$ electrodes and recording the impedance for Subjects 9 and 10. The wait period was aimed at providing a more stable electrode-skin interface during the recording process. This likely contributed to the low NRMSE observed for these subjects. It is likely that most of the recorded data were affected by the temporal relationship of the electrode-skin interface, and may not truly represent the instantaneous electrode-skin impedance, as we have a NLLS regression minimising the error of time-invariant parameters for what is actually a time-variant system. These two factors are believed to be the main contribution to the size of the observed error. To reduce this error, the performance of the electrode-skin impedance measuring device should be increased. This may be achieved by decreasing recording time and optimising the gain of the device, decreasing the impact of the temporal relationship and increasing the signal-to-noise ratio (SNR), respectively.

Comparing data from $Ag/AgCl_{NSP}$ and $Ag/AgCl_{SP}$ electrode configurations can assist in understanding the effect skin preparation has on the electrode-skin interface. Skin preparation is thought to reduce the effect of the epidermis by shunting the impedance of the stratum corneum. Comparing Figures 6.3 and 6.4 shows that skin preparation lowers the break frequency of one parallel segment of the $Ag/AgCl_{NSP}$ data sets. The biological phenomenon causing this behaviour is believed to be caused by puncturing and thinning of the stratum corneum. Puncturing and thinning the stratum corneum produces channels for ions to flow, while decreasing the distance between charge accumulating layers, resulting

in an increased capacitive element. It is difficult to confirm this theory by directly comparing the parameter values, since the $Ag/AgCl_{NSP}$ and $Ag/AgCl_{SP}$ data were obtained on different arms and the parameters of the $Ag/AgCl_{NSP}$ parallel segments were not fully independent due to them contributing to the impedance simultaneously. However, comparing Q_2 between the two electrode configurations highlights the increased capacitive element, resulting in the impedance contribution of that segment being at a lower frequency. This theory highlights why skin preparation reduces the electrode-skin impedance, and how different electrode-skin impedance can occur between recording electrode pairs, producing an electrode-skin impedance imbalance despite the application of skin preparation.

As the electrode-skin interface is non-linear with respect to frequency, non-linear compensation will likely provide a better solution for balancing the impedance of multiple electrode-skin interfaces when compared to linear compensation. Modelling the electrode-skin impedance may provide quantitative insight to assist in developing a compensatory network. This will be achieved by assisting in selecting the required component values and configuration.

6.4 Summary

This study presents a method to model the electrode-skin interface from 1 Hz to 100 kHz. NLLS regression was used to fit a seven-parameter model to the experimental data. Due to the varying magnitude gradient between subjects and electrode configurations, a summed exponential model with CPEs is required. The model was applied to impedance data collected from ten subjects using three bipolar electrode configurations measured above the biceps brachii. Initial estimates for the NLLS regression were formed using features of both the magnitude and phase of the impedance data. Some features used to provide an accurate fit required data in the range of 0.5 Hz to 1 MHz. However, extrapolation below 1 Hz and above 100 kHz was successfully used in this study.

The electrode-skin impedance has a temporal relationship, therefore, the ability to model the electrode-skin interface is affected by the time taken to record the electrode-skin impedance. The raw data for this trial had a set-up time after electrode placement of 2–5 minutes, with recording times of 9.7 ± 2.3 minutes, and the data were affected by the temporal relationship. A faster set-up and recording method would result in superior data that better characterises the instantaneous electrode-skin impedance, and therefore, permit a better fit.

The accuracy of the model fit for the ten subjects using the three electrode configurations resulted in a mean error and standard deviation for the two electrodes over the bioelectrical bandwidth of $(12.5 \pm 14.7)\,\%$ for the magnitude and $(4.5 \pm 4.9)\,\%$ for the phase using the $Ag/AgCl_{NSP}$ electrode configuration, $(3.2 \pm 1.7)\,\%$ for the magnitude and $(6.2 \pm 8.9)\,\%$ for the phase using the $Ag/AgCl_{SP}$ electrode configuration, and $(15.5 \pm 17.9)\,\%$ for the magnitude and $(4.4 \pm 1.8)\,\%$ for the phase using the $Ag_{\text{-}SP}$ electrode configuration. The error is thought to be largely due to the temporal relationship of the electrode-skin interface and not the method used to model the electrode-skin interface.

Modelling the magnitude and phase for all three electrode configurations on the ten subjects took 15.8 s, therefore, with a faster method of recording the electrode-skin impedance, the method outlined in this study could be used in real-time during a bioelectrical recording session to model the electrode-skin impedance and the imbalance between electrodes. As a large portion of electrical interference detected in bioelectrical signals is a function of the electrode-skin impedance imbalance, modelling the electrode-skin impedance may permit the development of a method that quantitatively balances multiple electrode-skin interfaces, and therefore, reduces electrical interference. To continue this research, Chapter 7 investigates the development of a faster electrode-skin impedance measurement system, alongside developing a method for actively balancing the electrode-skin impedance in real-time.

CHAPTER 7

Development of an Electrode-skin Impedance Compensatory System

Bioelectrical signals can be contaminated by interference from extrinsic sources, such as the mains power supply, and crosstalk from intrinsic sources in close proximity, such as other muscles. The severity of electrical interference from extrinsic sources is a function of the impedance imbalance between electrode-skin interfaces. By measuring and modelling the impedance of each electrode-skin interface, a system to compensate the impedance imbalance between electrode-skin interfaces can be developed. As the impedance of the electrode-skin interface is time variant, the characterisation and compensation would be applied regularly, in real-time, during the recording process, minimising variabilities associated with each subject and recording session. Although impedance imbalances between electrode-skin interfaces affect many bioelectrical recording techniques, this chapter focuses on the application to surface electromyography (sEMG). This chapter presents a

novel device which compensates electrode-skin impedance imbalances in real-time for sEMG.

7.1 Methods

Compensating impedance imbalances between electrode-skin interfaces can be achieved by controlling the source impedance (electrode-skin interface), or the common-mode input impedance of the bioelectrical instrumentation device. Controlling the source impedance is performed by adding compensatory impedance in series between the electrode-skin interface and the bioelectrical instrumentation device, Figure 7.1a, where R_A and C_A symbolise a simplified electrode-skin interface, Z_A, and R'_A and C'_A form the compensatory impedance Z'_A. Series compensation aims at directly minimising the impedance imbalance between electrode-skin interfaces. Controlling the common-mode input impedance of the bioelectrical instrumentation device is achieved by adding compensatory impedance in parallel with the bioelectrical instrumentation device, Figure 7.1b. Parallel compensation aims at balancing the resulting transfer functions formed between each electrode-skin interface in series with the compensated bioelectrical instrumentation device. Both compensation methods aim to reduce electrical interference caused by impedance imbalances between electrode-skin interfaces.

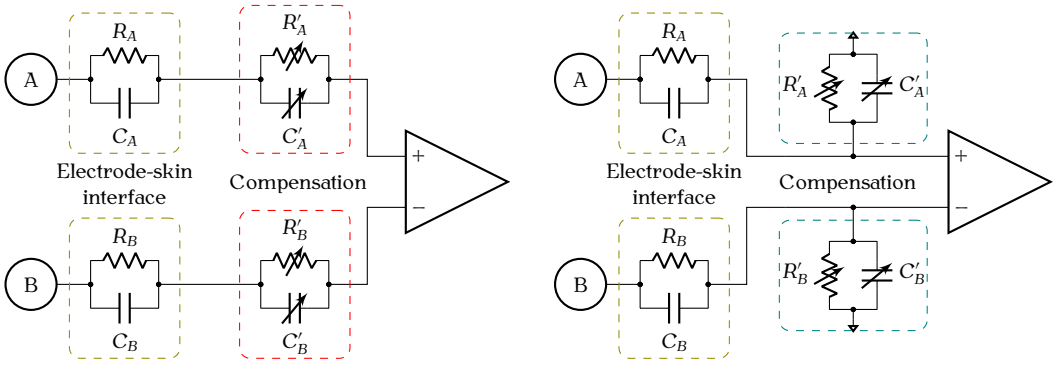

(a) Series compensation (b) Parallel compensation

Figure 7.1: Two methods of compensating for impedance imbalances between electrode-skin interfaces.

To compensate impedance imbalances between electrode-skin interfaces in real-time, digitally controllable compensatory impedance is required. The variable compensatory impedance should have a low tolerance, a large variable span and be able to implement large impedances. Series compensation requires a floating compensatory impedance. Since floating variable impedances are harder to implement with the desired performance than ground referenced variable impedances, parallel compensation was implemented to reduce the affect of impedance imbalances between electrode-skin interfaces.

7.1.1 Compensation Overview

The process implemented to compensate for the impedance imbalance between electrode-skin interfaces has six steps. This chapter outlines compensatory steps 2-5, and Chapter 8 validates the system by performing all steps on human subjects. The six steps implemented to perform impedance compensation are:

1. Measure a set of muscle contractions and relaxation periods using sEMG. This forms a pre-compensated electrical interference baseline detected in the bioelectrical signals

2. Measure the impedance of each electrode-skin interface

3. Simultaneously characterising the impedance of each electrode-skin interface using a resistive-capacitive model, where the residual error is a function of the transfer functions formed by each electrode-skin interface and compensatory impedance. The resulting parameters form direct estimates for the compensatory impedance.

4. Apply the unique resistive-capacitive compensatory impedance to each electrode-skin interface.

5. Measure and verify the applied compensatory impedance. This process permits the

calculation of the frequency dependent gain applied to each electrode-skin interface due to the transfer function formed by the impedance of the electrode-skin interface and compensatory impedance

6. Reperform the set of muscle contractions and relaxation periods. This permits quantifying the reductions in electrical interference due to applying the compensatory impedance.

Performing these steps on a tripolar electrode configuration permits quantifying the reduction in electrical interference due to implementing the compensatory system, and has the added benefit of crosstalk reduction. Therefore, the compensatory system is developed for a tripolar electrode configuration. Electrical circuit schematics for the compensatory system are outlined in Appendix F.

7.1.2 Measuring the Electrode-skin Impedance

Measuring the electrode-skin impedance is based off the technique outlined in Chapter 5. However, the process needs to be preformed twice to measure the impedance of the three electrode-skin interfaces, and twice to confirm the applied compensatory impedance. Therefore, a multiplexer was used to switch the excitation voltage between electrodes, and analogue switches were used to disconnect the compensatory impedance from the electrode-skin interfaces. A simplified schematic of the measurement process is outlined in Figure 7.2, where $V_S(t)$ is the excitation voltage as a function of time; $I^{LS}(f,t)$ is the low-side current flowing through the excited electrode-skin interfaces as a function of excitation frequency and time; $I^{HS}(f,t)$ is the high-side current flowing through the excited electrode-skin interfaces as a function of excitation frequency and time; $V^{AC}(f,t)$ is the voltage measured across electrode A with respect to electrode C as a function of excitation frequency and time; $V^{BC}(f,t)$ is the voltage measured across electrode B with respect to electrode C as a function of excitation frequency and time; R_{AX}, R_{BX} and R_{CX} are the

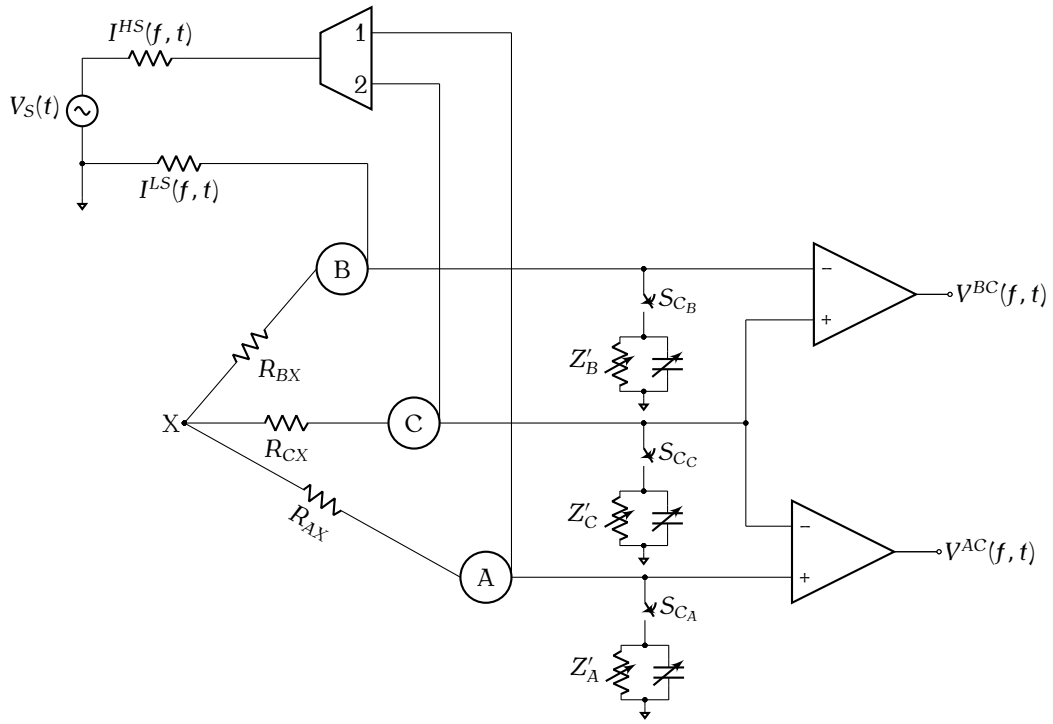

Figure 7.2: High level schematic of the electrode-skin impedance measurement technique.

resistances associated with the dermis and subcutaneous layers of the skin between the respective electrodes; X is a common node connection for the resistances associated with the dermis and subcutaneous layers of the skin.

To measure the impedance of the three electrode-skin interfaces, Z_A, Z_B and Z_C, and the applied compensatory impedance, Z'_A, Z'_B and Z'_C, the measurement system had four configurations, Table 7.1. *Excitation 1* produced an excitation path through electrode A and electrode B, and *excitation 2* produced an excitation path through electrode C and electrode B. *Excitation* 1α and 2α use the same excitation paths as *excitation* 1 and 2, respectively, but have the compensatory impedance switched on. *Excitation* 1α is used to measure the compensatory impedance for electrode A, and *excitation* 2α is used to measure the compensatory impedance for electrode C. The compensatory impedance for electrode B cannot be measured using this configuration, another excitation path would be required. If the error between the expected and measured compensatory impedance for electrode A and electrode C is small, it is assumed that the compensatory impedance of electrode B is also correctly implemented.

Table 7.1: Positions of the multiplexer and analogue switches to achieve four excitation configurations.

Excitation number	**Multiplexer**	S_{C_A}	S_{C_B}	S_{C_C}
1	Position 1	0	0	0
2	Position 2	0	0	0
1α	Position 1	1	0	0
2α	Position 2	0	0	1

0: Open circuit, 1: Closed circuit

The voltage across each electrode-skin interface and the series current was measured using a frequency sweep from 20–500 Hz. The data were sampled at 4 kS/s, where each of the 14 logarithmically spaced discrete excitation frequencies (f_k) excited the interface for 20-periods ($T = 20 \times f_k^{-1}$), or a minimum of 1024 samples. Applying a discrete-time Fourier transform (DTFT) to the voltage and current signals for each frequency, k, results in a complex voltage across each electrode-skin interface and the series current.

The theory of measuring the impedance of each electrode-skin interface is based on the principal that the impedance measurement reference electrode (the tripolar recording electrode that is not in the primary excitation path) has a high impedance to ground. This high impedance ensures that no current flows through the impedance measurement reference electrode, and therefore, is at the same potential as the common node X. However, the analogue multiplexer and switches introduce parasitic capacitance, lowering the effective impedance of the impedance measurement reference electrode to ground and violating the assumption that no current flows through the impedance measurement reference electrode. Therefore, the impedance measurement reference electrode is not at the same potential as the common node X. To account for this, the parasitic capacitance introduced by the multiplexer and analogue switches was accounted for in the impedance calculations.

A high level schematic diagram for *excitation* 1 and 1α, and 2 and 2α is outlined in Figure 7.3 and Figure 7.4, respectively, where C_{pp} is the parasitic capacitance prior the electrode-skin interface; $I^{prior}(f)$ characterises the current due to C_{pp}; $I^{A}_{1,1\alpha}(f)$ is the current through

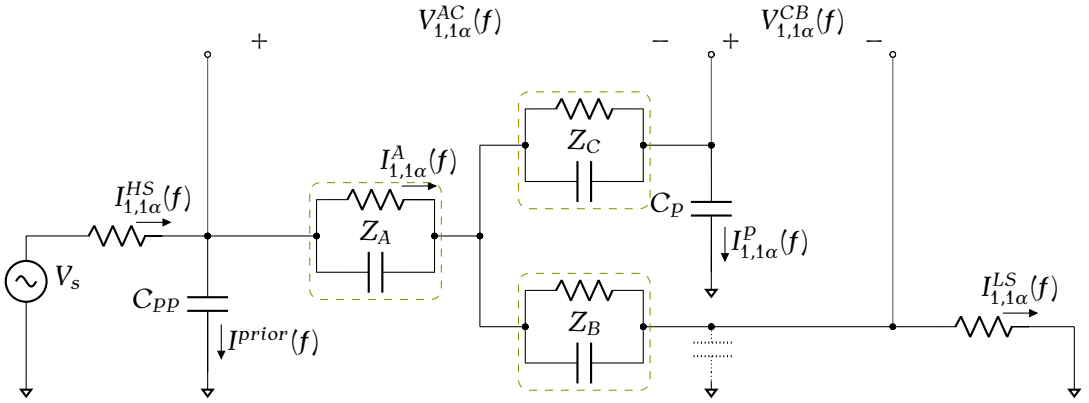

Figure 7.3: A high level circuit diagram for *excitation* 1 and 1α. The dashed parasitic capacitance is in parallel with the low-side sense current. Therefore, the dashed parasitic capacitance has negligible effect on the circuit.

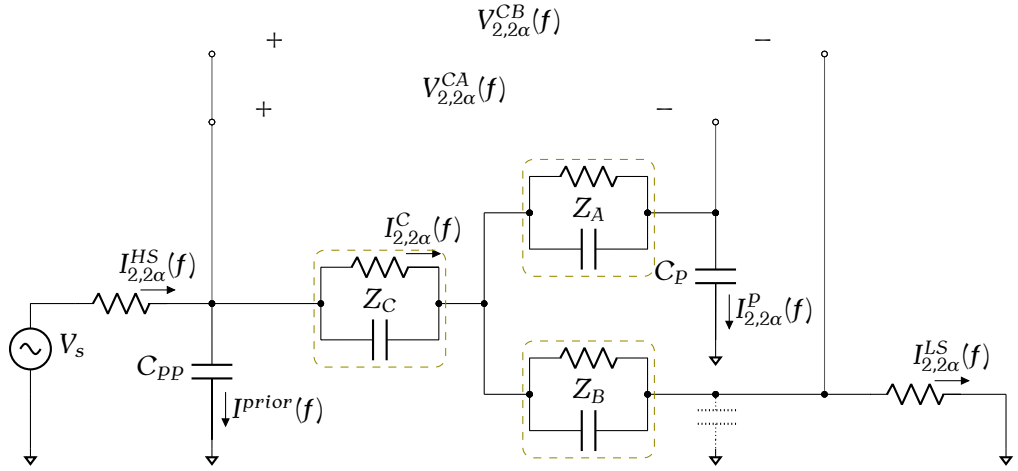

Figure 7.4: High level circuit diagram for *excitation* 2 and 2α. The dashed parasitic capacitance is in parallel with the low-side sense current. Therefore, the dashed parasitic capacitance has negligible effect on the circuit. Note the difference in position of electrode A (Z_A), electrode C (Z_C) and $V^{CB}(f)$ between the different excitations.

electrode A during *excitation* 1 and 1α; $I^{P}_{1,1\alpha}(f)$ characterises the current that is passing through the impedance measurement reference electrode during *excitation* 1 and 1α due to the parasitic capacitance, C_P ; $I^{C}_{2,2\alpha}(f)$ is the current through electrode C during *excitation* 2 and 2α; and $I^{P}_{2,2\alpha}(f)$ characterises the current that is passing through the impedance measurement reference electrode during *excitation* 2 and 2α due to C_P.

Excitation 1 and 2 produce a set of eight measurements, S_m, and eight unknown parameters, S_u. Equation 7.28 and 7.29 list S_m and S_u, respectively,

$$S_m = \left\{ V_1^{AC}(f)\,,\ V_1^{CB}(f)\,,\ I_1^{HS}(f)\,,\ I_1^{LS}(f)\,,\ V_2^{CA}(f)\,,\ V_2^{CB}(f)\,,\ I_2^{HS}(f)\,,\ I_2^{LS}(f) \right\}, \tag{7.1}$$

$$S_u = \left\{ I_1^{A}(f)\,,\ I_1^{P}(f)\,,\ I_2^{C}(f)\,,\ I_2^{P}(f)\,,\ I^{prior}(f)\,,\ Z_A(f)\,,\ Z_B(f)\,,\ Z_C(f) \right\}. \tag{7.2}$$

The sets, S_m and S_u form a solvable set of equations. The voltage of electrode A with respect to electrode C is characterised by,

$$V_1^{AC}(f) = Z_A(f) \times I_1^{A}(f) + Z_C(f) \times I_1^{P}(f)\,. \tag{7.3}$$

The differential recording which was implemented to measure the voltage of electrode B with respect to the impedance measurement reference electrode, now measures the voltage across the parasitic impedance of the impedance measurement reference electrode, $Z_1^P(f)$, with respect to the voltage across the low-side current sense impedance, $V_1^{LS}(f)$. This measurement is characterised by,

$$V_1^{CB}(f) = I_1^{P}(f) \times Z_1^{P}(f) - V_1^{LS}(f)\,. \tag{7.4}$$

The low-side current measurement is the difference between the current through electrode A and the current through the impedance measurement reference electrode due to the parasitic impedance,

$$I_1^{LS}(f) = I_1^{A}(f) - I_1^{P}(f)\,. \tag{7.5}$$

The high-side current measurement gives,

$$I_1^{HS}(f) = I_1^A(f) + I^{prior}(f)\,. \tag{7.6}$$

The voltage across electrode C with respect to electrode A is characterised by,

$$V_2^{CA}(f) = Z_C(f) \times I_2^C(f) + Z_A(f) \times I_2^P(f)\,. \tag{7.7}$$

The differential measurement of $V_2^{CB}(f)$ has a different configuration than *excitation* 1, and is characterised by,

$$V_2^{CB}(f) = Z_C(f) \times I_2^C(f) + Z_B(f) \times I_2^{LS}(f)\,. \tag{7.8}$$

The low-side and high-side current measurements for *excitation* 2 have the same layout as *excitation* 1, and are given by,

$$I_2^{LS}(f) = I_2^C(f) - I_2^P(f)\,, \tag{7.9}$$

$$I_2^{HS}(f) = I_2^C(f) + I^{prior}(f)\,. \tag{7.10}$$

Although, $I^{prior}(f)$ is a function of the parasitic capacitance of the multiplexer and analogue switch, where these parasitic capacitances are documented in the associated device data sheets, treating $I^{prior}(f)$ as an unknown reduces recording errors influencing I_1^A and I_2^C, as Equations 7.6 and 7.10 result in being the sum of two unknowns, with one shared parameter.

Equations 7.3, 7.7 and 7.8 contain the product of two unknown parameters. Therefore, Equations 7.4 – 7.6, 7.9 and 7.10 were used to form a 5 × 5 matrix of solvable equations to determine the parameter values for the unknown currents, $I_1^A(f), I_1^P(f), I^{prior}(f), I_2^C(f), I_2^P(f)$. Linear least squares was implemented in MATLAB (R2019b, MathWorks) to solve the matrix equation, which is defined as,

$$\begin{bmatrix} \widehat{V}_1^{CB} + \widehat{V}_1^{LS} \\ \widehat{I}_1^{LS} \\ \widehat{I}_1^{HS} \\ \widehat{I}_2^{HS} \\ \widehat{I}_2^{LS} \end{bmatrix} = \begin{bmatrix} \widehat{Z}_p & \widehat{0} & \widehat{0} & \widehat{0} & \widehat{0} \\ -\widehat{1} & \widehat{1} & \widehat{0} & \widehat{0} & \widehat{0} \\ \widehat{0} & \widehat{1} & \widehat{1} & \widehat{0} & \widehat{0} \\ \widehat{0} & \widehat{0} & \widehat{1} & \widehat{1} & \widehat{0} \\ \widehat{0} & \widehat{0} & \widehat{0} & \widehat{1} & -\widehat{1} \end{bmatrix} \begin{bmatrix} I_1^p(f) \\ I_1^A(f) \\ I^{prior}(f) \\ I_2^p(f) \\ I_2^C(f) \end{bmatrix}, \tag{7.11}$$

where $\widehat{X}$ denotes a 14 × 14 diagonal matrix formed from the elements of $X(f)$, which results from measurements at the 14 frequencies. Since each parameter is a vector with k elements, a diagonal matrix of each parameter must be used.

Using the remaining three equations, Equations 7.3, 7.7 and 7.8, the electrode-skin impedances can be determined. The matrix equation is define as,

$$\begin{bmatrix} \widehat{V}_1^{AC} \\ \widehat{V}_2^{CA} \\ \widehat{V}_2^{CB} \end{bmatrix} = \begin{bmatrix} \widehat{I}_1^A & \widehat{0} & \widehat{I}_1^p \\ \widehat{I}_2^p & \widehat{0} & \widehat{I}_2^C \\ \widehat{0} & \widehat{I}_2^{LS} & \widehat{I}_2^C \end{bmatrix} \begin{bmatrix} Z_A(f) \\ Z_B(f) \\ Z_C(f) \end{bmatrix}. \tag{7.12}$$

Obtaining the impedance of each electrode-skin interface permits modelling the inter-

faces, and calculating compensatory impedances to reduce the impact of the electrode-skin impedance imbalance.

7.1.3 Modelling the Impedance of Electrode-skin Interfaces

Parallel compensation applies compensatory impedance in parallel with the bioelectrical instrumentation device, to balance the resulting transfer functions formed between each electrode-skin interface in series with the compensated bioelectrical instrumentation device. The transfer function of one electrode-skin interface in series with one compensatory impedance is characterised as,

$$H_A(f) = \frac{Z'_A}{Z'_A + Z_A} \,. \tag{7.13}$$

To compensate for impedance imbalances between electrode-skin interfaces, the transfer functions formed for each electrode-skin interface and compensatory impedance must be balanced,

$$H_A(f) = H_B(f) = H_C(f) \,, \tag{7.14}$$

where $H_{A,B,C}$ are the three transfer functions of the three electrodes in the tripolar electrode configuration.

The potential divider effect converts common-mode interference into differential-mode interference due to imbalances between electrode-skin interfaces, even when the electrode-skin interface is coupled with a high common-mode input impedance amplifier. Therefore, the compensatory impedance is not required to produce a high common-mode input impedance. However, low compensatory impedances will result in bioelectrical signals

being largely attenuated, which may lead to signal degradation.

The individual transfer functions, $H_i(f)$, should have a flat response and zero phase shift over the bioelectrical signal frequency range, ensuring the bioelectrical signals are not distorted by a frequency dependent attenuation. According to Equation 7.13, balancing the compensatory impedance with the electrode-skin impedance will produce transfer functions with a flat magnitude response of -6 dB (0.5 $\frac{V}{V}$) attenuation and a 0 degrees phase shift. Therefore, simultaneously modelling the impedance of each electrode-skin interface can produce direct estimates for the compensatory impedance.

Constant phase elements (CPEs) can characterise the frequency dependence of the electrode-skin interface, Chapter 6. However, CPEs are not physical components, and therefore, cannot be realised in a physical circuit. Purely resistive and capacitive components cannot truly represent the frequency dependence of the electrode-skin interface. Therefore, the implementation of purely resistive and capacitive compensation cannot produce an ideal transfer function. However, purely resistive and capacitive compensation can still be implemented to balance multiple transfer functions. Therefore, purely resistive and capacitive components are implemented to produce the compensatory impedance.

The bioelectrical signal recorded using sEMG has a frequency spectrum of 20–500 Hz. Therefore, measuring and fitting a model to the impedance of each electrode-skin interface using a parallel resistive-capacitive model over the bioelectrical signal spectrum produces the parameter values required for each compensatory impedance. The resulting model equation is,

$$\begin{aligned} Z' &= R' \,||\, Z_{C'}\,, \\ Z' &= \frac{\frac{1}{C'}}{j\,2\pi f + \frac{1}{R'\,C'}}\,. \end{aligned} \tag{7.15}$$

The three electrode-skin interfaces of the tripolar electrode configuration were simultaneously modelled using non-linear least squares (NLLS) regression. The interior-point algorithm was implemented in MATLAB (R2019b, MathWorks). The foundation of the modelling method was based off the techniques outlined in Chapter 6. However, a simple resistive-capacitive model was used.

Initial measurements of the electrode-skin interface during testing assisted in defining the bounds and initial estimates for the parameters used in modelling the electrode-skin interface. The low frequency impedance of the electrode-skin interface was within the range of 1–100 MΩ, which formed the upper and lower bounds for the resistive component, while minimising the required resistive span of the compensatory system. The minimum capacitance which could be implemented was limited by the parasitic capacitance of the compensatory device, which was formed by the multiplexer and analogue switch configured for compensating the impedance imbalances. This parasitic capacitance limited the lower bound for the capacitive element to 220 pF. The upper bound was formed during initial testing, and set to 4.7 nF. The initial estimates for the resistive and capacitive elements were set to 10 MΩ and 1 nF, respectively. These bounds were implemented for each of the recording electrodes.

Ten objective functions were implemented to minimise the imbalance between each transfer function while simultaneously producing a flat transfer function with -6 dB amplification and zero phase shift. Three of the objective functions focused on producing transfer functions with a flat magnitude of -6 dB. These three objective functions are defined as,

$$S_{1,2,3} = \sqrt{\frac{1}{K}\sum_{k=0}^{K-1}\Big\{|H_i(f_k)| - \mathbf{0.5}\Big\}^2}, \tag{7.16}$$

where $|H_i|$ symbolises the magnitude of the three transfer functions, H_A, H_B and H_C. Three

objective functions focused on producing transfer functions with zero phase shift. These three objective functions are given as,

$$S_{4,5,6} = \sqrt{\frac{1}{K}\sum_{k=0}^{K-1}\left\{\phi_i^H(f_k) - \mathbf{0}\right\}^2}, \tag{7.17}$$

where ϕ_i^H symbolises the phase of the three transfer functions, H_A, H_B and H_C. Two objective functions focused on balancing the magnitudes of the transfer functions between the three electrodes. This objective function is defined as,

$$S_{7,8} = \sqrt{\frac{1}{K}\sum_{k=0}^{K-1}\left\{|H_{A,C}(f_k)| - |H_B(f_k)|\right\}^2}, \tag{7.18}$$

where S_7 minimises the magnitude imbalance between electrode A and electrode B, and S_8 minimises the magnitude imbalance between electrode B and electrode C. Two objective functions focused on balancing the phase of the transfer functions between the three electrodes. This objective function is given by,

$$S_{9,10} = \sqrt{\frac{1}{K}\sum_{k=0}^{K-1}\left\{\phi_{A,C}^H(f_k) - \phi_B^H(f_k)\right\}^2}, \tag{7.19}$$

where S_9 minimises the phase imbalance between electrode A and electrode B, and S_{10} minimises the phase imbalance between electrode B and electrode C.

The objective functions that prioritise producing a flat transfer function have a different range to the objection functions that focus on balancing the transfer functions. Therefore, a

normalisation process needs to be implemented to scale all values in the range of 0–1, such that the values are all equally weighted. The equation used to calculate the normalisation factors is,

$$f_i^{norm} = \frac{f_i(x) - f_i^o}{f_i^{max} - f_i^o}, \tag{7.20}$$

where f_i^{norm} is the i^{th} normalisation factor, which typically ranges from 0–1; $f_i(x)$ is the objective function; f_i^o is the utopia point; and f_i^{max} is the maximum objective function value for the i^{th} objection function when calculating the utopia points. f_i^o is calculated by weighting the other objective function values to zero. This allows to determine the minimum possible residual error for that one objective function. The ten normalised objective functions form the minimisation parameter, which is defined as,

$$S = \sum_{n=0}^{N-1} \left\{ f_n^{norm} \times S_n \right\}. \tag{7.21}$$

7.1.4 Compensatory Impedance Design

Impedance bootstrapping utilising positive feedback can be used to control the input impedance of an operational amplifier. To produce digitally controllable compensatory impedance, two positive feedback paths with independent digitally controllable gains are required: one for resistive compensation and one for capacitive compensation, Figure 7.5.

The input impedance of the operational amplifier is given by,

$$Z_i = \frac{V_i}{I_i}, \tag{7.22}$$

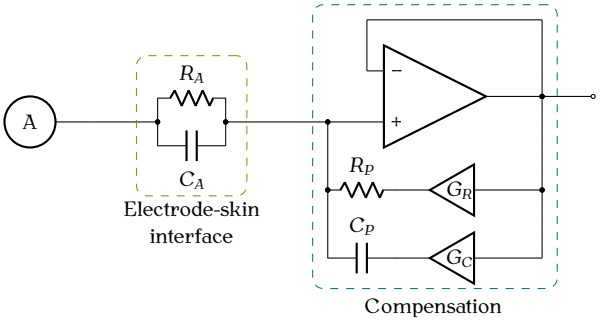

Figure 7.5: Bootstrapped operational amplifier for digitally controllable input impedance.

where V_i is input voltage and I_i is the input current. I_i is the sum of the currents in the positive feedback loops,

$$Z_i = \frac{V_i}{\frac{1}{R_p}(V_i - V_o G_R) + (V_i - V_o G_C)\, j\, 2\pi f\, C_p}, \tag{7.23}$$

where G_R and G_C are the variable gains in the resistive and capacitive positive feedback loops, respectively; R_p and C_p are the physical resistive and capacitive components implemented in the positive feedback loop, respectively; and V_o is the output voltage of the operational amplifier. As the bootstrapped operational amplifier has unity gain, $V_o = V_i$, Equation 7.23 can be simplified,

$$Z_i = \frac{1}{\frac{1}{R_p}(1 - G_R) + (1 - G_C)\, j\, 2\pi f\, C_p}. \tag{7.24}$$

Rearranging Equation 7.24 provides the equation that characterises the variable compensatory impedance,

$$Z_i = \frac{\frac{1}{C_p\,(1 - G_C)}}{j\, 2\pi f + \frac{1 - G_R}{R_p\, C_p (1 - G_C)}}. \tag{7.25}$$

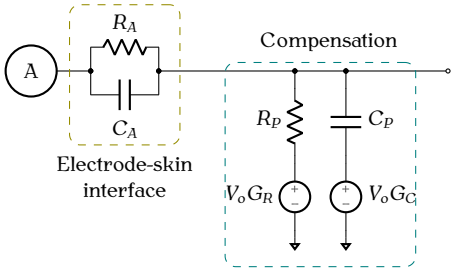

Figure 7.6: Simplified schematic of the effective variable common-mode input impedance.

This results in a compensatory impedance which is equivalent to a parallel variable resistive-capacitive network in series with the electrode-skin interface and ground, Figure 7.6 and Equation 7.15. The effective resistance, R_E, of the compensatory impedance is given by,

$$R_E = \frac{R_p}{1 - G_R}\,, \tag{7.26}$$

and the effective capacitance, C_E, is given by,

$$C_E = C_p\,(1 - G_C)\,. \tag{7.27}$$

Therefore, to control the compensatory impedance, the variable gains (G_R, G_C) need to be controlled. The values of the variable gains result in three scenarios:

- $G_{R,C} > 1$ results in a negative effective impedance, and the variable gain device requires larger supply rails than the operational amplifier to ensure the dynamic range of the operational amplifier is not reduced.

- $0 \leq G_{R,C} < 1$ produces an effective impedance that is greater than or equal to the physical impedance. As the gain increases, so does the effective impedance.

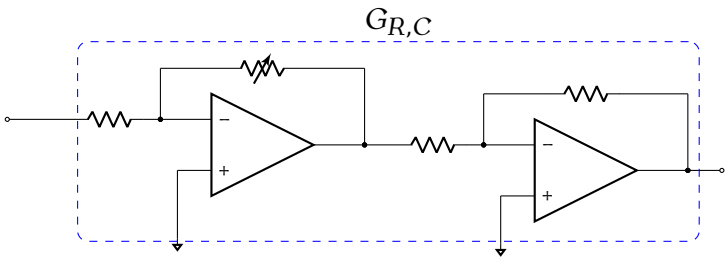

Figure 7.7: The variable gain configuration used to control the gain within the positive feedback loop of the bootstrapped operational amplifier. The first stage inverting opamp has a digitally controllable gain implemented using a rheostat, and the second inverting opamp re-inverts the signal, leading to a total gain range of 0-1.

- $G_{R,C} \leq 0$ results in an effective impedance that is less than or equal to the physical impedance. Therefore, compensating electrode-skin interfaces with large impedances requires large passive impedances.

The gain range of $0 \leq G_{R,C} < 1$ was chosen to be the most suitable method of producing variable compensation, as it does not require a larger supply voltage, and components with lower absolute impedance tolerances can be used. There are multiple methods to implement this gain range, including variable gain amplifiers (VGA) and programmable gain amplifiers (PGA). However, VGA and PGA typically have non-linear gain responses, which further increases the effective impedance tolerance as a function of gain. Increased impedance tolerance can decrease the accuracy of the desired effective compensatory impedance, reducing the affect of attempting to balance the transfer functions. VGA and PGA typically do not have a large number of gain options between 0 and 1, making them unsuitable for this application.

Therefore, a digitally controlled variable resistor was implemented as the feedback resistance in a inverting amplifier configuration. To ensure a non-inverted signal, two inverting amplifiers were required, Figure 7.7. The variable resistor was not configured to operate ratiometrically (the segment of the variable resistor prior the wiper arm for the source impedance, and the segment of the variable resistor after the wiper arm for the feedback impedance) as this would produce non-linear variable gain.

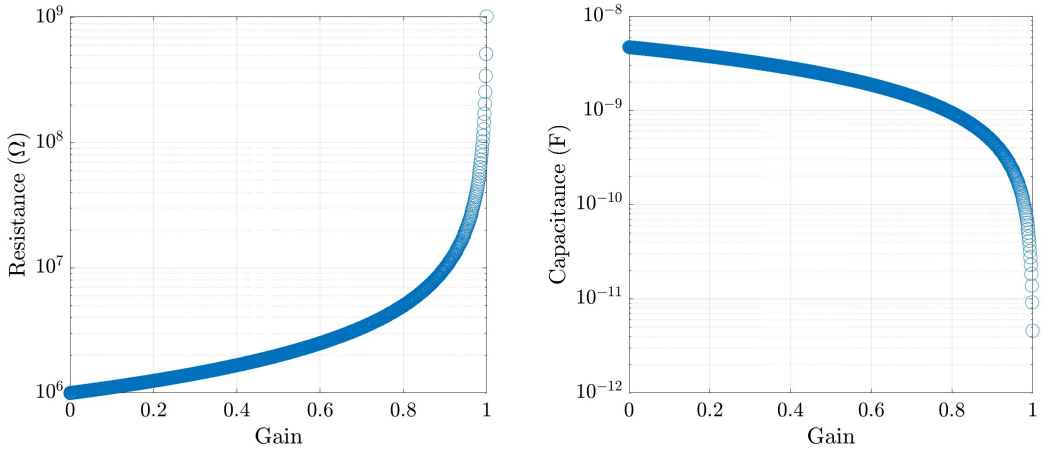

(a) Possible effective resistances

(b) Possible effective capacitances

Figure 7.8: The 1024 realisable effective resistance and capacitance values.

Analog Device's AD5272 10-bit, 1% end-to-end tolerance rheostat was implemented as the variable feedback resistance. The rheostat in conjunction with R_p and C_p of 1 MΩ and 4.7 nF, respectively, resulted in the 1024 effective resistance and capacitance values, shown in Figure 7.8. These physical component values were chosen since measured electrode-skin impedances during testing were never below this range, and it gave a large span which captured high impedance occurrences.

7.1.5 Measuring Compensatory Impedance

Measuring the compensatory impedance was performed using a similar method to measuring the electrode-skin impedance. However, $Z_A(f)$, $Z_B(f)$ and $Z_C(f)$ were known, and I^{prior} was a function of the compensatory impedance. Therefore, $I_{1\alpha}^{prior}$ and $I_{2\alpha}^{prior}$ characterise the current to ground after $I^{HS}(f)$ but prior to entering the electrode-skin interface for *excitation* 1α and 2α, respectively. Resulting in eight measurements, $S_{m\alpha}$, and six unknown parameters, $S_{u\alpha}$. The set, $S_{m\alpha}$ is defined as,

$$S_{m\alpha} = \left\{ V_{1\alpha}^{AC}(f)\,,\ V_{1\alpha}^{CB}(f)\,,\ I_{1\alpha}^{HS}(f)\,,\ I_{1\alpha}^{LS}(f)\,,\ V_{2\alpha}^{CA}(f)\,,\ V_{2\alpha}^{CB}(f)\,,\ I_{2\alpha}^{HS}(f)\,,\ I_{2\alpha}^{LS}(f) \right\}, \tag{7.28}$$

and the set, $S_{u\alpha}$ is defined as,

$$S_{u\alpha} = \left\{ I_{1\alpha}^{A}(f)\,,\, I_{1\alpha}^{P}(f)\,,\, I_{1\alpha}^{prior}(f)\,,\, I_{2\alpha}^{C}(f)\,,\, I_{2\alpha}^{P}(f)\,,\, I_{2\alpha}^{prior}(f) \right\}. \tag{7.29}$$

Therefore, the high-side current measurement when the compensatory impedance is applied for *excitation* 1α, is given by,

$$I_{1\alpha}^{HS}(f) = I_{1\alpha}^{A}(f) + I_{1\alpha}^{prior}(f)\,, \tag{7.30}$$

and the high-side current measurement when the compensatory impedance is applied for *excitation* 2α, is given by,

$$I_{2\alpha}^{HS}(f) = I_{2\alpha}^{C}(f) + I_{2\alpha}^{prior}(f)\,. \tag{7.31}$$

The eight measurements and the six unknown parameters for the compensated system formed an overdetermined set of equations, which were used to form a matrix of solvable equations. Linear least squares was implemented in MATLAB (R2019b, MathWorks) to solve the matrix equation. The matrix is defined as,

$$\begin{bmatrix} \widehat{V}_{1\alpha}^{AC} \\ \widehat{V}_{1\alpha}^{CB} + \widehat{V}_{1\alpha}^{LS} \\ \widehat{I}_{1\alpha}^{LS} \\ \widehat{I}_{1\alpha}^{HS} \\ \widehat{V}_{2\alpha}^{CA} \\ \widehat{V}_{2\alpha}^{CB} - Z_B \times \widehat{I}_{2\alpha}^{LS} \\ \widehat{I}_{2\alpha}^{LS} \\ \widehat{I}_{2\alpha}^{HS} \end{bmatrix} = \begin{bmatrix} \widehat{Z}_C & \widehat{Z}_A & \widehat{0} & \widehat{0} & \widehat{0} & \widehat{0} \\ \widehat{Z}_P & \widehat{0} & \widehat{0} & \widehat{0} & \widehat{0} & \widehat{0} \\ -\widehat{1} & \widehat{1} & \widehat{0} & \widehat{0} & \widehat{0} & \widehat{0} \\ \widehat{0} & \widehat{1} & \widehat{1} & \widehat{0} & \widehat{0} & \widehat{0} \\ \widehat{0} & \widehat{0} & \widehat{0} & \widehat{Z}_A & \widehat{Z}_C & \widehat{0} \\ \widehat{0} & \widehat{0} & \widehat{0} & \widehat{0} & \widehat{Z}_C & \widehat{0} \\ \widehat{0} & \widehat{0} & \widehat{0} & -\widehat{1} & \widehat{1} & \widehat{0} \\ \widehat{0} & \widehat{0} & \widehat{0} & \widehat{0} & \widehat{1} & \widehat{1} \end{bmatrix} \begin{bmatrix} \widehat{I}_{1\alpha}^{P}(f) \\ \widehat{I}_{1\alpha}^{A}(f) \\ \widehat{I}_{1\alpha}^{prior}(f) \\ \widehat{I}_{2\alpha}^{P}(f) \\ \widehat{I}_{2\alpha}^{C}(f) \\ \widehat{I}_{2\alpha}^{prior}(f) \end{bmatrix}. \tag{7.32}$$

The parasitic capacitance of the multiplexer and analogue switches are known, and the supply voltage is given by,

$$V_S = V_{2\alpha}^{CB}(f) + V_{2\alpha}^{LS}(f). \tag{7.33}$$

Therefore, the current passing through the parasitic capacitance prior the electrode-skin interface after the application of the compensatory impedance is given by,

$$I^{pp}(f) = \frac{V_S}{Z^{pp}(f)}, \tag{7.34}$$

where $Z^{pp}(f)$ is the impedance of C_{pp}. The difference between $I_{1,2\alpha}^{prior}(f)$ and $I^{pp}(f)$ is the current associated with the compensatory impedance. Therefore, the compensatory impedance for electrode A is given by,

$$Z'_A(f) = \frac{V_S}{I_{1\alpha}^{prior}(f) - I^{PP}(f)}, \tag{7.35}$$

and the compensatory impedance for electrode C is given by,

$$Z'_C(f) = \frac{V_S}{I_{2\alpha}^{prior}(f) - I^{PP}(f)}. \tag{7.36}$$

7.2 Discussion

To simultaneously reduce electrical interference and crosstalk contamination, the compensatory system was developed for a tripolar electrode configuration. Implementing the compensatory system for a tripolar electrode configuration increases the complexity of the measurement, modelling, and verification processes. Since the excitation voltage needed to be switched between electrodes, analogue switches and a multiplexer were implemented. However, these devices introduced parasitic capacitance. The parasitic capacitance lowered the impedance of the impedance measurement reference electrode, causing current to flow through this electrode, violating the high impedance and negligible current flow assumption of this measurement technique. Accounting for these parasitic capacitances was achieved. However, it increased the complexity the compensatory system. Implementing analogue switches and a multiplexer with lower parasitic capacitance would be beneficial, but the electrical characteristic trade-off by achieving lower parasitic capacitance would have to be investigated.

Since CPEs cannot be realised in a physical circuit, the impedance of the electrode-skin interface was characterised using a resistive-capacitive model. A resistive-capacitive model cannot truly represent the frequency dependence of the electrode-skin interface, and therefore cannot produce a flat transfer function with zero phase. However, a resistive-capacitive

compensatory impedance can still be implemented to balance multiple transfer functions, while reducing the implementation complexity of the physical compensatory impedance.

7.3 Summary

This study presents the development of a compensatory system which reduces the affects of impedance imbalances between electrode-skin interfaces. The transfer functions formed between each electrode-skin interface in series with the input impedance of the bioelectrical instrumentation device is controlled, and the imbalance between each transfer function is minimised. The system is developed for a tripolar electrode configuration. Therefore, the successful implementation of the compensatory system will reduce electrical interference and crosstalk contamination.

Implementing the compensatory system, and quantifying the reduction in electrical interference and crosstalk contamination for a tripolar electrode configuration requires six steps. The six steps are: measure the bioelectrical signal of a set of muscle contractions and relaxation periods using sEMG; measure the impedance of the three electrode-skin interfaces; simultaneously characterise the impedance of the electrode-skin interfaces using a resistive-capacitive model, which forms the direct estimates of the required compensatory impedance; apply the unique compensatory impedance to each electrode-skin interface; measure and verify the compensatory impedance, allowing the frequency dependent attenuation of the bioelectrical signal to be estimated; reperform the set of muscle contractions and relaxation periods. The compensatory system is validated on ten subjects, where the results are presented in Chapter 8.

CHAPTER 8

Experimental Validation of the Electrode-skin Impedance Compensatory System

Bioelectrical instrumentation is used to measure weak bioelectrical signals. However, these signals can be contaminated by several forms of interference: extrinsic sources, such as the mains power supply, and crosstalk from endogenous sources in close proximity, such as other muscles. The severity of electrical interference from extrinsic sources is a function of the impedance imbalance between electrode-skin interfaces. A compensatory system was developed to reduce the affects of impedance imbalances between electrode-skin interfaces while simultaneously implementing a common crosstalk reduction technique. This chapter presents the results from implementing the novel compensatory device on ten subjects, in real-time, for recording bioelectrical signals using surface electromyography (sEMG).

8.1 Methods

To implement and quantify the efficacy of the compensatory system, six steps are required. The six steps are: measure the bioelectrical signal of a set of muscle contractions and relaxation periods using sEMG; measure the impedance of the three electrode-skin interfaces; simultaneously characterise the impedance of the electrode-skin interfaces using a resistive-capacitive model, which forms the direct estimates of the required compensatory impedances; apply the unique compensatory impedance to each electrode-skin interface; measure and verify the compensatory impedance, allowing the frequency dependent attenuation of the bioelectrical signal to be estimated; reperform the set of muscle contractions and relaxation periods. To measure crosstalk contamination and the reduction in crosstalk due to implementing a tripolar electrode configuration, the bioelectrical signals from the biceps brachii and triceps brachii were simultaneously measured. To validate the efficacy of the compensatory system, the device needs to be implemented on human subjects.

8.1.1 Subjects

Data from ten healthy subjects (five male and five female with a mean age of 25 ± 2) were collected for this study. This study was approved by the Human Ethics Committee, University of Canterbury (HEC 2019/68).

8.1.2 Experimental Procedure

To detect the presence and quantify the reduction in crosstalk contamination, three sEMG devices were implemented:

1. *bipolar* electrode configuration on the *biceps* brachii

2. *tripolar* electrode configuration on the *biceps* brachii

3. *bipolar* electrode configuration on the *triceps* brachii

This configuration permitted the detection, and possible reduction, of crosstalk contamination on the biceps brachii during contraction of the triceps brachii. The impedance compensatory system was implemented on the tripolar electrode configuration, permitting quantifying the reduction in electrical interference and crosstalk contamination.

The sEMG devices were attached to the subject using elastic fabric, where the elastic fabric was tightened so the electrodes were securely fastened, but would not restrict muscle contractions. After sEMG device placement, the subject was informed with a detailed structure of the trial, and performed a practice run of the trial.

The subjects performed five biceps/triceps contractions, had a two-second rest period, performed five triceps/biceps contractions followed by another two-second rest period. This process was performed twice, then a 20 second rest period was performed. After this period, the impedance of the tripolar electrode-skin interfaces were measured, characterised using a resistive-capacitive model (which directly formed the values for each of the three compensatory impedances) followed by applying and verifying the compensatory impedance. The subjects remained at rest until they were informed to perform the second contraction set.

8.1.3 Measurement

The time associated with placing the electrodes on the subject, describing the structure of the trial, and the subject performing a practice run of the trial, was (14.2 ± 7.4) minutes. The bioelectrical signals were simultaneously measured from the right biceps brachii muscle belly and the lateral head of the right triceps brachii muscle belly, where electrode A of the tripolar electrode configuration was arranged to be the most distal electrode, ensuring consistent sEMG device orientation. The pre- and post-compensated bioelectrical signals were

each recorded over a 100-second period, using a sampling rate of 1 kS/s. Measuring, modelling, and verifying the applied compensatory impedance took approximately 2 minutes. Therefore, the trial took approximately 5 minutes per subject.

Silver (Ag) bar was used for the recording electrodes, and a Ag/AgCl electrode was placed on the right elbow to use as the reference electrode. The Ag bar electrodes were constructed from 1 mm round, 99.99% pure, silver wire, producing a 1x10 mm electrode, with a 10 mm interelectrode distance for each electrode configuration. The Ag/AgCl electrode was a VERMED VersaTrode, polyethylene foam, single use, wet gel teardrop electrode. The adhesive foam had a diameter of 38.1 mm, and the electrode eyelet was 10.6 mm in diameter.

The bioelectrical signal detected on the triceps brachii from Subject 2 was affected by baseline drift, leading to saturation of the bioelectrical instrumentation device. Therefore, skin preparation was performed to produce a stable recording. Since the skin preparation was only applied to skin above the triceps brachii, the skin preparation did not effect the electrode-skin impedance compensation. Skin preparation was achieved using 600 grit sand paper, applying approximately 20 light uniform sweeps over a large area above the lateral head of the triceps brachii muscle belly. The skin surface was sterilised using an alcohol pad, 75% Ethyl Alcohol, and left for two minutes to dry.

The biceps contractions were performed using a 5 kg dumbbell, and the triceps contractions were performed using a resistive fitness (elastic) band. The elastic band was 750 mm length, with a mean load of 60 N at full triceps extension. The elastic band was attached overhead, with the bottom of the band suspended 1.44 m from the ground. A knot in the end of the elastic band ensured repeatable hand placement. The subjects were aligned with their right arm directly in front of the elastic band, and the dumbbell placed on a raised surface below the elastic band. Both contractions were performed with the palm facing inwards.

The biceps contraction was performed by contracting the arm from full extension to an elbow angle of approximately 100 degrees, with approximately a 1 second contraction cycle and a 0.5 second rest after each contraction. The triceps extension had the same contraction period. The triceps contraction was performed by reaching up to the elastic band, bringing the shoulder back if required, followed by fully extending the triceps brachii. Subjects 1,5,7,9 and 10 performed biceps contractions first, and Subjects 2, 3, 4, 6 and 8 performed triceps contractions first. During the rest period, the subject was informed to rest their arm by their side. The data from this period was used to quantify the level of electrical interference.

8.1.4 Analyses

The compensatory system produces a transfer function with the electrode-skin interface and the compensatory impedance. This transfer function does not have a flat response, therefore, the bioelectrical signal recorded from the tripolar electrode configuration has a frequency dependent attenuation factor applied to it. Since the bipolar electrode configurations do not have the compensatory system applied to it, and therefore, are not affected by a frequency dependent attenuation factor, the bioelectrical signals from the three sEMG devices are not directly comparable.

Since the transfer functions applied to electrode A and electrode C, of the tripolar electrode configuration are calculated, the effective frequency dependent attenuation factor applied to the bioelectrical signal measured using the tripolar electrode configuration can be estimated. This was achieved by interpolating the magnitude and phase of the transfer functions for electrode A and electrode C. The transfer functions were interpolated to contain the same frequencies as the resulting frequency domain results. The interpolation is performed using the MATLAB-specific makima interpolation, a modified Akima piecewise cubic Hermite interpolation. This algorithm was chosen as it reduces the overshoot that occurs when two consecutive data points have a consistent amplitude when using Akima

interpolation, and the makima algorithm has reduced overshoot compared to spline interpolation and a smoother derivative than cubic interpolation. The magnitude and phase were then converted to cartesian form. The mean of the two transfer functions were used to produce the frequency dependent attenuation factor for the compensated bioelectrical signal. As the electrode-skin impedance was measured using an excitation range of 20–500 Hz, the resulting scaling factor, and therefore the frequency based results, have a frequency spectrum of 20–500 Hz.

Electrical interference analyses

The process of quantifying the reduction in electrical interference involved five metrics. The first four metrics were quantified by calculating the root mean square error (RMSE) for both the magnitude and phase at mains frequency (50 Hz) and over the bioelectrical bandwidth. The five metrics are:

1. impedance imbalances between electrode-skin interfaces

2. the accuracy of the resistive-capacitive model fit

3. the accuracy of the applied compensatory impedance

4. the imbalance between the simulated transfer functions, formed from the parameters produced by modelling the electrode-skin interface

5. the reduction in electrical interference due to the application of the compensatory impedance

The impedance imbalance between electrode-skin interfaces was calculated between electrode A and electrode B, electrode A and electrode C, and electrode B and electrode C.

The parameters produced by characterising the impedance of the electrode-skin interfaces were used to form simulated resistive-capacitive compensatory impedance data sets, with the same frequencies as the measured electrode-skin impedance data. The simulated compensatory impedance data theoretically produce the optimal resistive-capacitive compensation for the three measured electrode-skin impedances. The error between the measured compensatory impedance and the simulated compensatory impedance was used to quantify the accuracy of the applied compensatory impedance. This metric was calculated for electrode A and electrode C, as the compensatory impedance of electrode B could not be measured using this impedance compensatory system. The imbalance between each of the simulated transfer functions was calculated for electrode A and electrode B, electrode A and electrode C, and electrode B and electrode C.

To quantify the level of electrical interference, a 15-second period was extracted from the rest period after the muscle contraction sets had been preformed. Frequency spectral analysis was performed using a single sided fast Fourier transform (FFT), where a symmetric Hamming window and zero padding with a factor of 8 was applied. The maximum value within a ± 0.5 Hz range at five frequencies of interest were used to quantify the level of electrical interference. The bioelectrical signals were contaminated with a large portion of mains interference and interference from mains even-multiple harmonics. The even-multiple harmonics are thought to be due to the fluorescent lights that were in the room where the trial took place. Therefore, the five frequencies of interest were 50 Hz, 100 Hz, 200 Hz, 300 Hz and 400 Hz. The calculations were performed for pre- and post-compensated bioelectrical signals, allowing the reduction in electrical interference across the five frequencies of interest to be quantified.

Crosstalk contamination analyses

Each contraction set (the five biceps/triceps contractions) of the bioelectrical signals were manually extracted. The data obtained during the triceps contractions were used to form

crosstalk contamination and reduction results. This resulted in six contraction sets for the pre- and post-compensated data: two contraction sets from the *bipolar* electrode configuration on the *biceps*, two contraction sets from the *tripolar* electrode configuration on the *biceps* and two contraction sets from the *bipolar* electrode configuration on the *triceps*.

Since the compensatory system results in a frequency dependent attenuation, the compensated bioelectrical signals needed scaling before quantifying crosstalk. As the transfer function was estimated in the frequency-domain, and there is controversy as to whether a correlation-based index can reliably quantify crosstalk (De Luca & Merletti, 1988; Farina et al., 2002), an amplitude-based metric calculated in the frequency-domain was used for quantifying crosstalk. To quantify the presence and reduction of crosstalk, an FFT was applied to each contraction set, and the mean of each contraction set pair was calculated.

The FFT of each contraction set pair was integrated with respect to the FFT frequency, by approximating the cumulative integral via the trapezoidal method. The maximum of the integral was used as the crosstalk detection metric, and the ratio between biceps-bipolar and biceps-tripolar integral maximum was used to quantify crosstalk reduction. The FFT data at the mains harmonics used to quantify crosstalk contamination was blanked, this ensured that electrical interference would not skew the crosstalk metrics.

8.2 Results

8.2.1 Impedance Compensation

The impedance imbalance between the three electrode-skin interfaces for the ten subjects is outlined in Table 8.1. The impedance imbalance between electrode-skin interfaces ranges from (58.8–2,714) kΩ and (0.9–12.0) degrees over the bioelectrical signal range, with a mean imbalance and standard deviation at mains frequency (50 Hz) of (725.8 ± 645.5) kΩ for the magnitude and (3.8 ± 2.9) degrees for the phase.

Table 8.1: Electrode-skin impedance imbalance between the three electrodes.

Mains frequency (50 Hz)

Electrodes	**A–B**		**A–C**		**B–C**	
Subject	$\|Z\|\,(k\,\Omega)$	$\phi\,(deg)$	$\|Z\|\,(k\,\Omega)$	$\phi\,(deg)$	$\|Z\|\,(k\,\Omega)$	$\phi\,(deg)$
1	1,263.4	3.6	5.7	3.9	1,269.1	0.4
2	818.4	10.5	464.4	4.4	354.0	6.1
3	1,544.6	5.8	66.7	0.2	1,477.9	5.6
4	1,114.2	4.1	290.9	3.9	823.3	0.2
5	140.6	3.0	62.9	1.4	203.6	1.6
6	271.1	3.0	180.8	10.5	451.9	7.5
7	798.5	0.6	1,973.2	7.2	2,771.7	7.7
8	106.9	3.3	1,232.8	0.5	1,125.9	3.8
9	620.4	1.1	216.8	2.6	403.6	1.5
10	430.9	4.3	860.5	5.3	429.6	1.1
MEAN (SD)	710.9 (489.0)	3.9 (2.8)	535.5 (639.0)	4.0 (3.2)	931.1 (779.8)	3.5 (3.0)

Whole range (20–500 Hz)

Electrodes	**A–B**		**A–C**		**B–C**	
Subject	$\|Z\|\,(k\,\Omega)$	$\phi\,(deg)$	$\|Z\|\,(k\,\Omega)$	$\phi\,(deg)$	$\|Z\|\,(k\,\Omega)$	$\phi\,(deg)$
1	1,212.2	3.2	171.2	3.3	1,356.2	1.7
2	777.9	8.3	491.2	4.4	291.8	4.9
3	1,268.6	3.3	141.2	1.7	1,298.9	2.8
4	1,044.6	4.9	187.4	2.8	871.8	2.4
5	121.4	2.3	58.8	1.5	178.4	0.9
6	254.7	2.0	223.5	9.1	472.8	7.4
7	736.4	1.4	1,978.5	10.8	2,714.2	12.0
8	206.5	1.8	1,124.7	4.5	924.4	6.0
9	638.0	1.2	111.2	2.1	544.3	1.3
10	475.0	3.7	651.5	5.4	194.0	1.8
MEAN (SD)	673.5 (413.1)	3.2 (2.1)	513.9 (610.5)	4.6 (3.1)	884.7 (771.4)	4.1 (3.5)

The accuracy of the resistive-capacitive model fit for the ten subjects over the three electrode-skin interfaces is outlined in Appendix G, Table G.1. The normalised mean error and standard deviation for the three electrode-skin interfaces over the bioelectrical bandwidth are $(13.2 \pm 7.2)\%$ for the magnitude and $(17.8 \pm 4.1)\%$ for the phase.

The error between the measured compensatory impedance and the simulated compensatory impedance for the ten subjects using electrode A and electrode C is outlined in Appendix G, Table G.2. The normalised mean error and standard deviation for the two electrode-skin interfaces over the bioelectrical bandwidth are $(7.3 \pm 4.5)\%$ for the magnitude and $(3.3 \pm 4.3)\%$ for the phase. As the standard deviation of the phase is larger than the mean, and the data is non negative, the data has a right skewed distribution.

The imbalance between the three simulated transfer functions for the ten subjects is outlined in Appendix G, Table G.3. The mean error and standard deviation for the three transfer functions over the bioelectrical bandwidth are $(9.2 \pm 4.7)\%$ for the magnitude and (1.6 ± 1.4) degrees for the phase.

The error between the simulated and measured transfer functions for the ten subjects using electrode A and electrode C is outlined in Appendix G, Table G.4. The mean error and standard deviation for the three transfer functions over the bioelectrical bandwidth are $(12.1, \pm 8.0)\%$ for the magnitude and (1.0 ± 1.3) degrees for the phase.

The magnitude of electrical interference at the five frequencies of interest, 50 Hz, 100 Hz, 200 Hz, 300 Hz and 400 Hz, for the ten subjects are $(107.0 \pm 80.0)\ \mu V$ for the pre-compensated bioelectrical signals and $(64.6 \pm 36.7)\ \mu V$ for the post-compensated bioelectrical signals. The pre- and post-compensated results are outlined in Appendix G.5 and G.6, respectively.

Table 8.2: Reduction in electrical interference due to the application of the compensatory system, measured at the 5 frequencies of interest

Frequency (Hz)	50	100	200	300	400
Subject	$\|H\|$ (%)	$\|H\|$ (%)	$\|H\|$ (%)	$\|H\|$ (%)	$\|H\|$ (%)
1	91.5	89.0	87.6	87.4	87.8
2	61.2	94.4	86.4	80.0	82.2
3	92.9	95.3	91.6	86.2	83.5
4	60.4	86.8	96.8	95.6	92.3
5	47.4	48.9	52.0	55.0	54.9
6	58.8	72.4	70.2	69.2	71.0
7	39.9	87.2	78.5	87.1	93.0
8	-81.9	-24.8	-15.8	-16.2	-1.4
9	45.8	81.8	87.0	88.6	89.5
10	22.8	62.9	61.2	58.9	57.4
MEAN (SD)	43.9 (49.2)	69.4 (36.2)	69.6 (33.2)	69.2 (32.9)	71.0 (28.9)

The reduction of electrical interference at the five frequencies of interest, 50 Hz, 100 Hz, 200 Hz, 300 Hz and 400 Hz, for the ten subject is outlined in Table 8.2. The mean and standard deviation of reduction in electrical interference at the five frequencies of interest is $(64.6 \pm 36.7)\%$.

The measured electrode-skin impedance, simulated compensatory impedance and the measured compensatory impedance for Subjects 3, 7 and 8 are presented in Figure 8.1. Figures for all ten subjects are shown in Appendix I. These subjects were chosen because they show a range of interesting results. Subject 3 had the largest reduction in electrical interference at mains frequency due to applying the compensatory system; Subject 7 had the largest impedance imbalance between uncompensated electrode-skin interfaces; Subject 8 was the only subject to have an increase in electrical interference due to applying the compensatory system.

The simulated and measured transfer functions for Subjects 3, 7 and 8 are presented in Figure 8.2. Figures for all ten subjects are shown in Appendix J.

The data obtained from applying an FFT to the pre- and post-compensated bioelectrical signals extracted during the resting period for Subjects 3, 7 and 8 are presented in Figure 8.3. Figures for all ten subjects are shown in Appendix K.

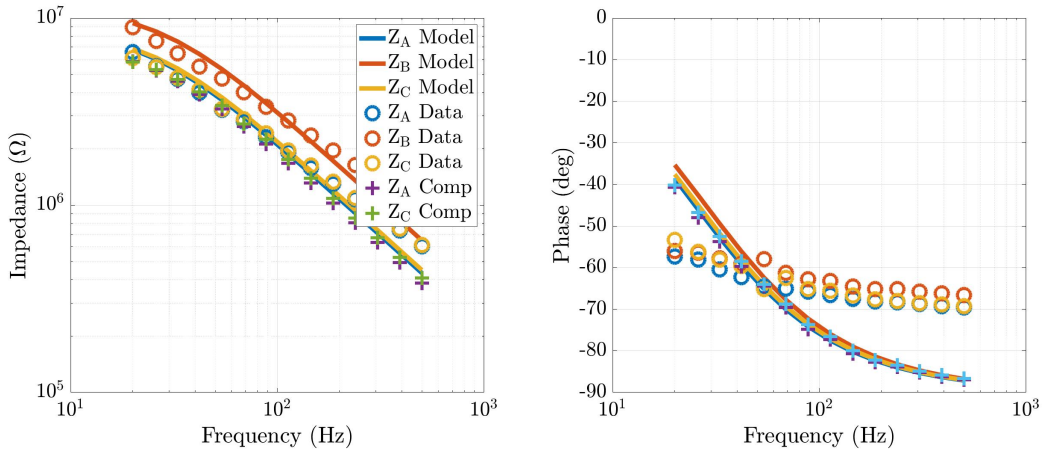

(a) Subject 3.

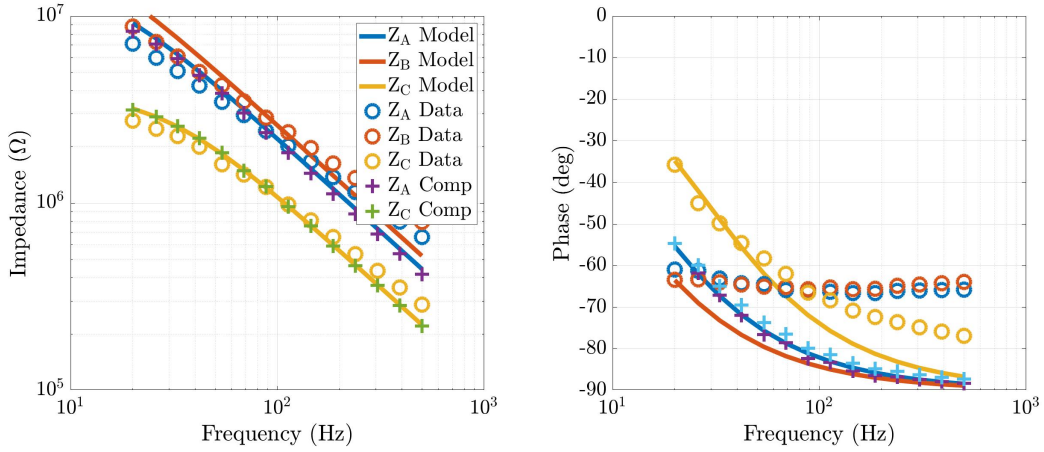

(b) Subject 7.

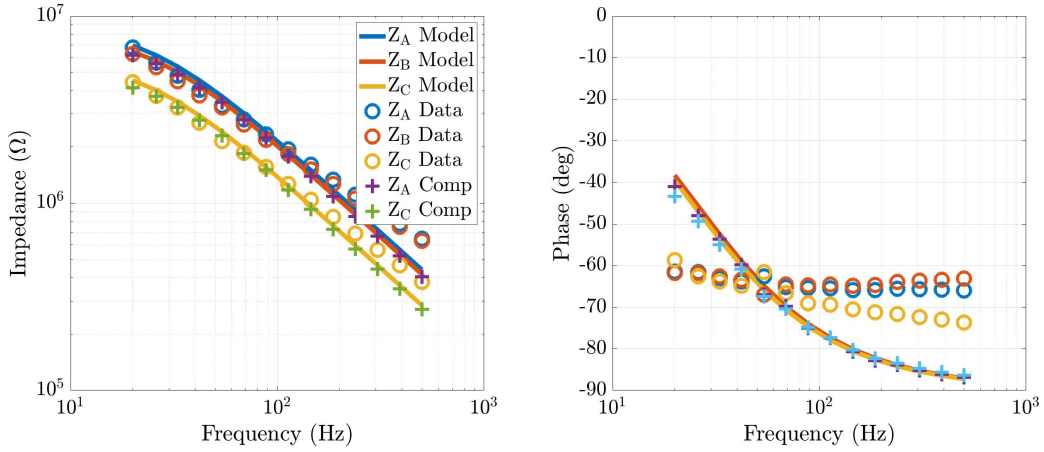

(c) Subject 8.

Figure 8.1: Electrode-skin impedance, simulated compensatory impedance and measured compensatory impedance for Subjects 3, 7 and 8.

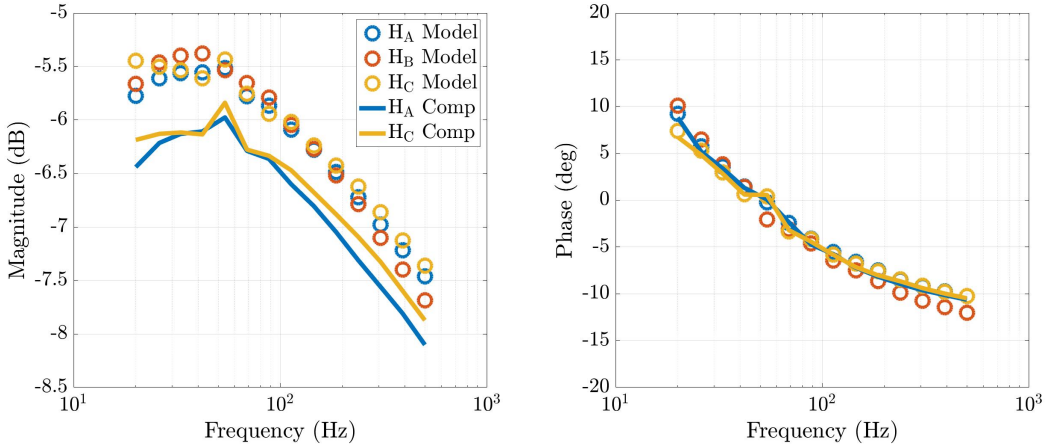

(a) Subject 3.

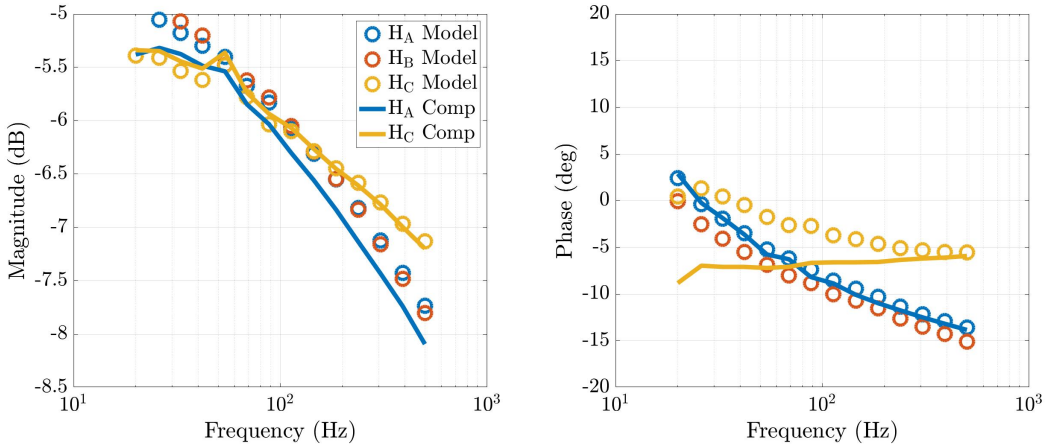

(b) Subject 7.

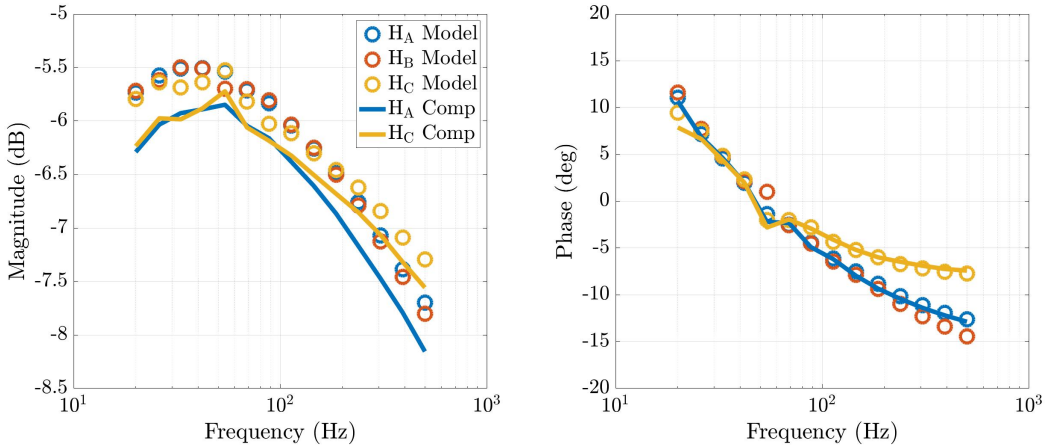

(c) Subject 8.

Figure 8.2: Simulated and measured transfer functions for Subjects 3, 7 and 8.

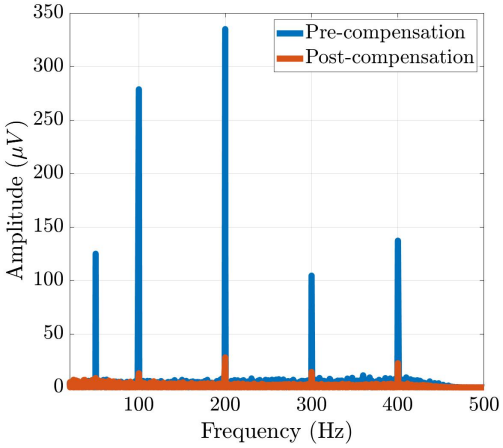

(a) Subject 3.

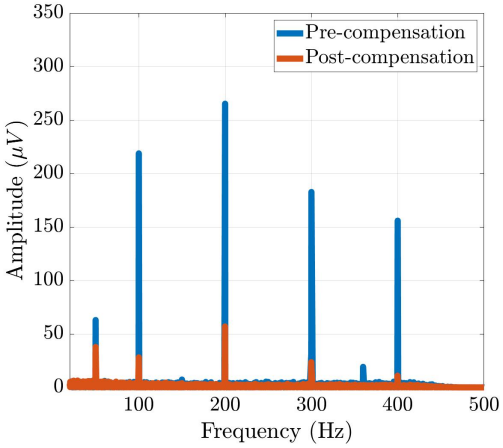

(b) Subject 7.

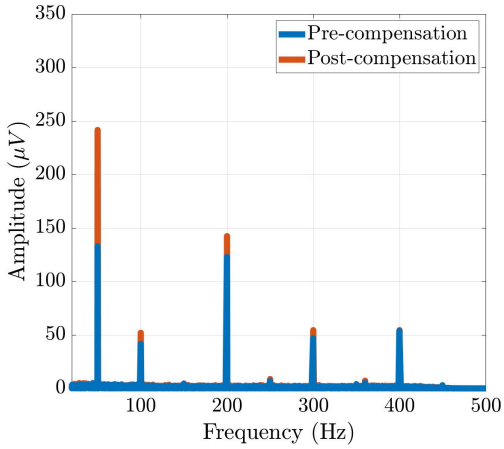

(c) Subject 8.

Figure 8.3: FFT for pre- and post-compensated bioelectrical signals for Subjects 3, 7 and 8.

Table 8.3: Integration ratio between the pre- and post-compensated bioelectrical signals.

	Pre–compensation	Post–compensation
Subject	$\text{Bicep}_{\text{DD-SD}}$ (%)	$\text{Bicep}_{\text{DD-SD}}$ (%)
1	316	203
2	412	853
3	466	255
4	219	165
5	210	276
6	244	672
7	414	343
8	371	343
9	321	230
10	201	250
MEAN (SD)	317 (96)	359 (224)

8.2.2 Crosstalk

The integration results for the bioelectrical signals recorded from the three sEMG devices during triceps brachii contractions from the ten subjects, pre- and post-compensation are outlined in Appendix G, Table H.1 and H.2, respectively. The comparison between the integral of the bioelectrical signals recorded from the biceps brachii using the tripolar and bipolar electrode configurations during triceps brachii contractions are outlined in Table 8.3.

The pre- and post-compensated bioelectrical signals recording during muscle contractions, for Subjects 3, 7 and 8 are presented in Figure 8.4. The red and blue highlighted sections indicate the regions where the five contractions were extracted from. Since the transfer function due to applying the compensatory impedance has an approximate amplification factor of 0.5, the compensated bioelectrical signal recorded using the tripolar electrode configuration had an amplification factor of 2 applied using post processing. This was performed only for visual comparison between the three electrode configurations. Figures for all ten subjects are shown in Appendix L.

The data obtained from applying an FFT to the pre- and post-compensated bioelectrical signals extracted from the triceps brachii contraction regions for Subjects 3, 7 and 8

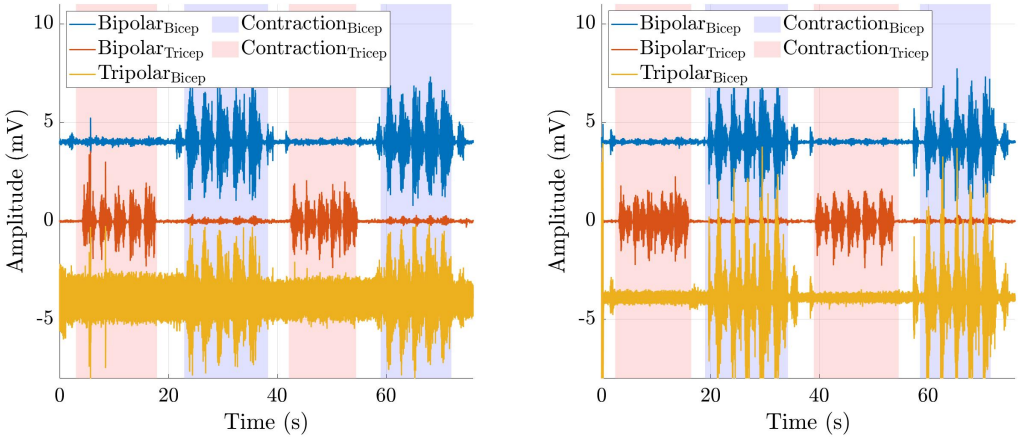

(a) Subject 3.

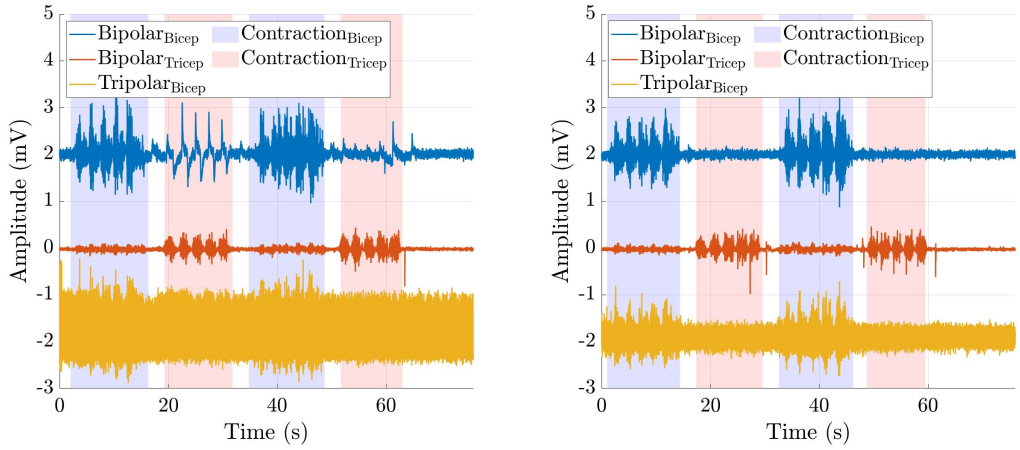

(b) Subject 7.

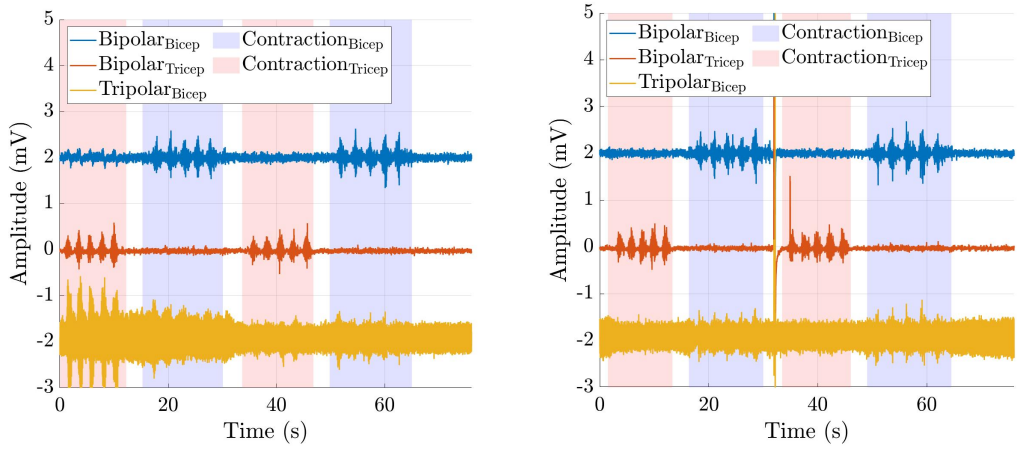

(c) Subject 8.

Figure 8.4: Bioelectrical signals from the three sEMG devices, pre- and post-compensation for Subjects 3, 7 and 8.

are presented in Figure 8.5. Figures for all ten subjects are shown in Appendix M. The integrated FFT data for the three sEMG devices during triceps brachii contractions for the ten Subjects pre- and post-compensation are presented in Appendix N.

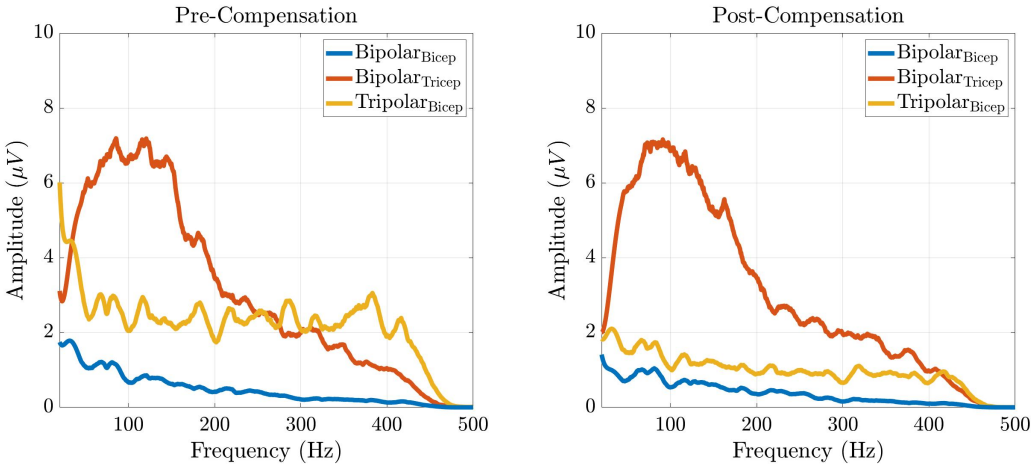

(a) Subject 3.

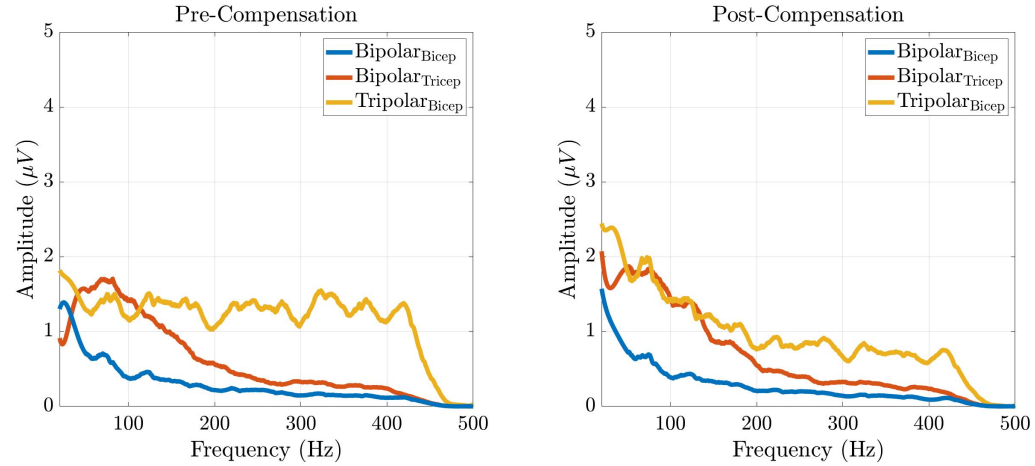

(b) Subject 7.

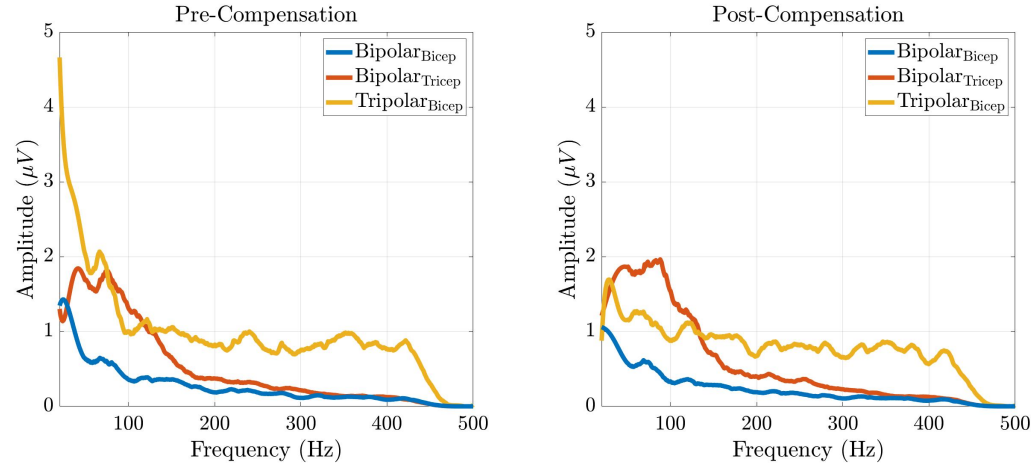

(c) Subject 8.

Figure 8.5: FFT applied to the bioelectrical signals during contraction of the triceps, for Subjects 3, 7 and 8. A Savitzky-Golay finite impulse response filter was applied to increase visual ability.

8.3 Discussion

The impedance imbalance between the three electrode-skin interfaces of the tripolar electrode configuration does not indicate an obvious trend. In some instances two interface pairs had an impedance imbalance far larger than the mean impedance imbalance, with the third interface pair having a smaller impedance imbalance. The interface pair with the small impedance balance was not consistent, and changed between the electrode A-B and A-C interface pairs. In four occurrences all three interface pairs were below the mean impedance imbalance. This indicates that the sEMG device did not cause a consistent impedance imbalance between two electrode-skin interfaces, and that impedance imbalances between electrode-skin interfaces can be large and are unpredictable.

As the Ag electrodes were the same dimensions as used in Chapter 5, the reduction in electrode-skin impedance imbalance due to abrasive skin preparation can be determined. The mean and standard deviation of the impedance imbalance at mains frequency (50 Hz), using the Ag bar electrodes, with skin preparation applied, was $(36.2 \pm 45.1)\,\mathrm{k\Omega}$ for the magnitude and (3.4 ± 3.6) degrees for the phase. When skin preparation was not applied, the mean and standard deviation of the impedance imbalance at mains frequency (50 Hz) was $(725.8 \pm 645.5)\,\mathrm{k\Omega}$ for the magnitude and (3.8 ± 2.9) degrees for the phase. Therefore, on average, applying skin preparation to this electrode configuration should reduce electrical interference by a factor of 20, with minimal effect of the phase imbalance.

As expected, a resistive-capacitive model cannot capture the frequency dependence of the electrode-skin interface. Since the model cannot truly characterise the electrode-skin interface, the physical implementation of the compensatory impedance will not produce a flat transfer function with zero phase. The error associated with the fit of the phase data has a larger mean, and smaller standard deviation than the magnitude error, indicating that the phase is the primary problem for modelling of the electrode-skin interface.

The normalised error between the simulated and measured compensatory impedance is $(7.3 \pm 4.5)\%$ for the magnitude and $(3.3 \pm 4.3)\%$ for the phase. This indicates that the method of producing the digitally controllable variable impedance using the bootstrapped operational amplifier was successful. This successful implementation lead to reductions in electrical interference in nine of the ten subjects. The reduction in electrical interference ranged from (22.8–92.9)%. Subjects 7, 8 and 10 had the lowest reductions in electrical interference. Subject 7 had the largest impedance imbalance between electrode-skin interfaces. This is thought to be the reason why the impedance modelling error and imbalance between simulated transfer functions had the largest errors of all subjects. However, Subject 7 still resulted in a reduction of mains interference of 39.9%. Subject 10 had the lowest reduction in electrical interference, and Subject 8 had an increase in electrical interference. Except for the level of electrical interference reduction, the results from these subjects were not outlying. It is thought that the limited reduction in electrical interference may be due to the electrodes shifting after the final contraction and prior the resting period, causing the electrode-skin impedance to varying, and not be balanced with the compensatory impedance. Subjects 1, 2, 3 and 4 had reductions in electrical interference above 60%. These subjects also had the largest impedance imbalances between electrode A and B, and electrode B and C, with a small impedance imbalance between electrode A and C. This combination produces the largest form of electrical noise, leading to the largest possibility of reducing the electrical interference. This is due to the potential divider effect impacting a tripolar electrode configuration more than a bipolar electrode configuration. The potential divider effect results in an interference potential from electrode A and electrode B, and a second interference potential from electrode B and electrode C. The differential-mode signal from these two interference potentials are then amplified by the third differential amplifier in the tripolar electrode configuration.

Two methods were used to quantify the presence of crosstalk. One visual and one quantitative method. In the presence of crosstalk, the FFT results of the bioelectrical signal

detected from the biceps brachii would have a scaled down version of the FFT result of the bioelectrical signal from the triceps brachii, and the integration of the FFT results would have similar amplitudes. To quantify crosstalk reduction, the bioelectrical signal detected from the tripolar electrode configuration on the biceps brachii should be less than the bipolar electrode configuration on the biceps brachii. Comparing the pre- and post-compensated results for the bipolar sEMG devices shows that contraction strength was consistent throughout the trial. Therefore, pre- and post-compensated contraction data can be compared.

The integration results indicate that Subjects 1, 2, 4, 7 and 8 may have crosstalk present. However, visual inspection of the bioelectrical signals indicate that subjects 2, 7 and 8 were affected by motion artefact. The motion artefact is likely due to the large sEMG device lifting throughout the contraction as the biceps brachii changes shape. Therefore, only Subjects 1 and 4 potentially had crosstalk present in there contractions. Literature indicates that crosstalk can range from 4–60%, but the upper arm is expected to be in the lower of this range. As only two subjects were detected with crosstalk, co-contraction of the biceps brachii and triceps brachii may have occurred. In all subjects, the bioelectrical signal detected from the tripolar electrode configuration was larger than the bipolar electrode configuration on the biceps brachii, both pre- and post-compensation. This indicates that the tripolar electrode configuration did not reduce crosstalk contamination.

8.4 Summary

This study presents a method to measure the impedance of three electrode-skin interfaces, simultaneously characterise the impedance of the electrode-skin interfaces using a resistive-capacitive model, which are used to form the direct estimates for the impedance compensatory system. The compensatory impedances are then measured, verifying the correct implementation, and allowing the frequency dependent attenuation of the bioelectrical signal to be estimated. Bioelectrical signals were measured pre- and post-compensation,

permitting quantifying the reduction in electrical interference. The compensatory system was implemented using a tripolar electrode configuration, allowing crosstalk to be investigated.

Crosstalk was detected on two subjects, but is thought to be due to co-contraction. Therefore, the tripolar electrode configuration, implemented in this study, was not required for improving bioelectrical signal acquisition. The implementation of the compensatory system on the tripolar electrode configuration only increased the complexity of implementing the compensatory impedance, without any added advantage. However, crosstalk is expected on the forearm. Therefore, if bioelectrical signals were being measured on the forearm, implementing the compensatory system using a tripolar electrode configuration may be beneficial.

The compensatory system was successful in reducing electrical interference in nine of the ten subjects, where the reduction ranged from (23–93)%. There was even a 40% reduction in electrical interference when a 2.7 MΩ (at mains frequency, 50 Hz) electrode-skin impedance imbalance was present. Therefore, the novel compensatory system successfully improved real-time, bioelectrical signal acquisition.

CHAPTER 9

Conclusions

Stroke is the third leading cause of disability (Feigin et al., 2014) and the fifth most common cause of death worldwide (Benjamin et al., 2017). It is common for stroke to impair a subject's ability to perform activities of daily living, removing a subject's independence. Physical therapy can enable a subject to regain their lost functionalities (Dam et al., 1993; Smith et al., 1981). However, traditional rehabilitation is time consuming and labour intensive, potentially resulting in a costly rehabilitation. Assistive robotic devices can reduce the time and physical exertion required from a therapist, allowing more intensive repetitive training while reducing the cost of therapy (Díaz et al., 2011).

The incorporation of surface electromyography (sEMG) into assistive robotics can enable patient-driven intention-based control, leading to increased patient interaction and a more natural, unconscious interface. sEMG is the non-invasive technique of measuring the bioelectrical activity of the skeletal muscle at the skin surface (Basmajian & De Luca, 1979). However, electrical interference and bioelectrical crosstalk limit the practical ability to use bioelectrical signals for assistive robotic control.

Bioelectrical signals can be contaminated by interference from extrinsic sources, such as the mains power supply, and crosstalk from intrinsic sources in close proximity, such as other muscles. In built-up environments, the human body is capacitively coupled to the mains power supply and ground, causing conduction currents to flow through the human body (Huhta & Webster, 1973; Metting van Rijn et al., 1990; Webster, 2009). The conduction currents result in a common-mode potential at the recording electrodes. Each electrode in contact with the skin has a high impedance electrode-skin interface, which has the potential to convert the common-mode signal into a differential-mode signal due to the potential divider effect (Huhta & Webster, 1973; Metting van Rijn et al., 1990; Pacela, 1967). The severity of electrical interference from extrinsic sources is a function of the impedance imbalance between electrode-skin interface.

There are methods of reducing this interference, but the efficacy of these techniques are limited. Shielded electrode leads reduce the input impedance of the bioelectrical instrumentation device, increasing the differential-mode interference produced due to the potential divider effect (Huhta & Webster, 1973; Metting van Rijn et al., 1990); the performance of the right leg driver (RLD) is limited; skin preparation can be time consuming, leading to skin irritation and large interference potentials when performed incorrectly; and signal processing can attenuate a portion of the signal of interest.

Bioelectrical crosstalk, detected with sEMG, is the phenomenon of one muscle's signal influencing the recording of another. Crosstalk contamination makes it difficult to measure the bioelectrical signal from a single muscle, which can lead to misrepresentation of the target signal, making it difficult to provide accurate biofeedback. The tripolar electrode-configuration is commonly used to reduce crosstalk contamination. Therefore, balancing the impedance of three electrode-skin interfaces may reduce electrical interference and crosstalk contamination simultaneously, with the potential to improve bioelectrical signal acquisition.

Previous research has been conducted on balancing the impedance between two electrode-skin interfaces by adding some form of compensation, but there are limitations in these studies. These compensatory methods are limited due to being non-real-time, not being capable of being realised on humans subjects, require manual tuning or applying a frequency dependent attenuation to the bioelectrical signal, limiting the ability to use the bioelectrical signal for biofeedback and assistive robotic control.

The aim of this thesis was to develop a novel, real-time electrode-skin impedance compensatory system to improve bioelectrical signal acquisition, particularly for sEMG. This was achieved by developing an open source sEMG device; a system to measure the impedance, and impedance imbalance of electrode-skin interfaces formed using dry electrodes; a method to characterise the measured electrode-skin impedance; and the novel electrode-skin impedance compensatory system, which was implemented using a tripolar electrode configuration.

The impedance imbalance between electrode-skin interfaces ranged from (58.8–2,714) kΩ and (0.9–12.0) degrees over the bioelectrical signal range (20–500 Hz), with a mean imbalance and standard deviation at mains frequency (50 Hz) of (725.8 ± 645.5) kΩ for the magnitude and (3.8 ± 2.9) degrees for the phase. The compensatory system was implemented on a tripolar electrode configuration, resulting in a reduction of electrical interference in nine of the ten subjects, which ranged from (23–93)%. This reduction in electrical interference highlighted the successful development and implementation of the novel compensatory system. By performing electrode-skin impedance compensation, a higher quality bioelectrical signal can be realised, requiring less signal processing while resulting in more information from the raw bioelectrical signal. Therefore, the compensatory system improves bioelectrical signal acquisition, with the potential to lead to improved biofeedback used in controlling assistive robotic devices for stroke rehabilitation.

CHAPTER 10

Future Work

To continue this research, multiple areas could be investigated. Validating the need for the tripolar electrode configuration by performing a study on forearm crosstalk should be performed. Although literature suggests crosstalk contamination is a concern, there was limited evidence to support this claim while measuring the bioelectrical signal from the biceps/triceps. In the absence of crosstalk, implementing the compensatory system using a bipolar electrode configuration will reduce system complexity, with the potential to optimise the compensatory system.

By implementing a bipolar electrode configuration for the compensatory system, the measurement and characterisation of the electrode-skin impedance, and the implementation of the compensatory impedance is simplified. This simplification has the potential to reduce system size, cost and complexity, while increasing system performance. Without the need to measure and quantify the reduction of crosstalk contamination, the non-compensated bipolar electrode configuration on the compensatory board can be removed. The removal of the non-compensated bipolar electrode configuration permits increasing the physical

electrode area. Since the electrode-skin impedance is inversely proportional to the electrode area, an increased electrode area will reduce the electrode-skin impedance and the impedance imbalance between electrode-skin interfaces, leading to a reduction in electrical interference.

If a tripolar electrode configuration is not required, the multiplexer used to switch the excitation path during the impedance measurement process can be removed. Therefore, the amount of parasitic capacitance impacting the electrode-skin impedance measurement would be reduced. A further reduction in parasitic capacitance could be achieved by replacing the analogue switches with more optimised variants. This has the potential to reduce the complexity of measuring the impedance of the electrode-skin interface, leading to the use of the original impedance measurement method outlined in Chapter 5.

The electrode-skin interface has a temporal relationship. Therefore, the impedance of the electrode-skin interface is time-variant. To manage this phenomenon, the impedance of the electrode-skin interface may need to be measured regularly. However, if the temporal relationship is investigated and characterised, updating the implemented compensatory impedance may be required less regularly. This is due to having an understanding of how the required compensatory impedance will change with respect to time.

The bioelectrical signal is also affected by muscle fatigue. However, this relationship is not well defined. Investigation into the effect muscle fatigue has on the bioelectrical signal may provide further information for improving bioelectrical signal acquisition and biofeedback. With improved bioelectrical signal acquisition, more information can be obtained from the bioelectrical signal due to requiring less signal processing. With more information, a superior control algorithm can be developed, and incorporated with an assistive robotic device to provide better stroke rehabilitation, with increased voluntary control and a more natural interface.

Appendices

APPENDIX A

Open Source Bipolar Electromyography Design Files and ADC Pin Connections

The open source bipolar surface electromyography (sEMG) design has eight open source files supplied with it. The available files are outlined in Table A.1. A summary of the analogue-to-digital converter (ADC) pin connections are outlined in Table A.2.

Table A.1: Open source design files available for the sEMG design.

Design filename	**File type**
EMG_project_altium.zip	Altium project
EMG.pdf	pdf Schematic
EMG_BOM.xlsx	BOM spreadsheet
EMG_gerber_files.zip	Gerber and drill files
cable_adapter.zip	Gerber and drill files
EMG_case.STL	3D print file
electrode_spacing.STL	3D print file
EMG_example_code.ino	Ardiuino script

Table A.2: Summary of the ADC (AD7768-1) connections.

Pin No.	**Mnemonic**	**Note**
1	$\overline{\text{RESET}}$	NC, controlled through SPI register write
2	$\overline{\text{SYNC IN}}$	Connected to $\overline{\text{SYNC OUT}}$
3	$\overline{\text{SYNC OUT}}$	Synchronises the ADC with MCLK
4	REGCAPD	For decoupling an internal regulator
5	IOVDD	Internal digital voltage supply
6	$\overline{\text{PIN}}$/SPI	Pulled high, sets ADC to SPI mode
7	DGND	Digital ground
8	CLKSEL	Clock type selection controlled through SPI register write
9	DOUT	MISO, the mnemonic are with respect to the ADC
10	SCLK	SPI clock
11	SDI	MOSI
12	$\overline{\text{CS}}$	Active low chip select
13	XTAL1	Tied to ground for using CMOS clock
14	MCLK	Connect to external CMOS oscillator chip
15	GPIO_0	Digital potentiometer, Mode control selection
16	GPIO_1	Digital potentiometer, Channel selection
17	GPIO_2	Digital potentiometer, Increment/decrement mode selection
18	GPIO_3	Digital potentiometer, Increment/decrement wiper position
19	$\overline{\text{DRDY}}$	Can obtain through SPI, pin DOUT/$\overline{\text{RDY}}$
20	REGCAPA	For decoupling an internal regulator
21	AVSS	-2.5 V, provided to operate in true bipolar mode
22	AVDD2	+2.5 V, analogue supply voltage
23	AVDD1	+2.5 V, analogue supply voltage
24	REF+	+2.5 V, provides full positive voltage swing
25	REF-	-2.5 V, provides full negative voltage swing
26	AIN-	Re-inverts the signal after filtering stage
27	AIN+	Permits single-ended inverting true bipolar ADC configuration
28	VCM	LED is used for debugging

APPENDIX B

Open Source Bipolar Electromyography Schematics

The Altium Schematics for the open source bipolar sEMG device are provided. Figure B.1 outlines the digital circuitry schematic, Figure B.2 shows the schematic of the power distribution, and Figure B.3 outlines the analogue circuitry schematic.

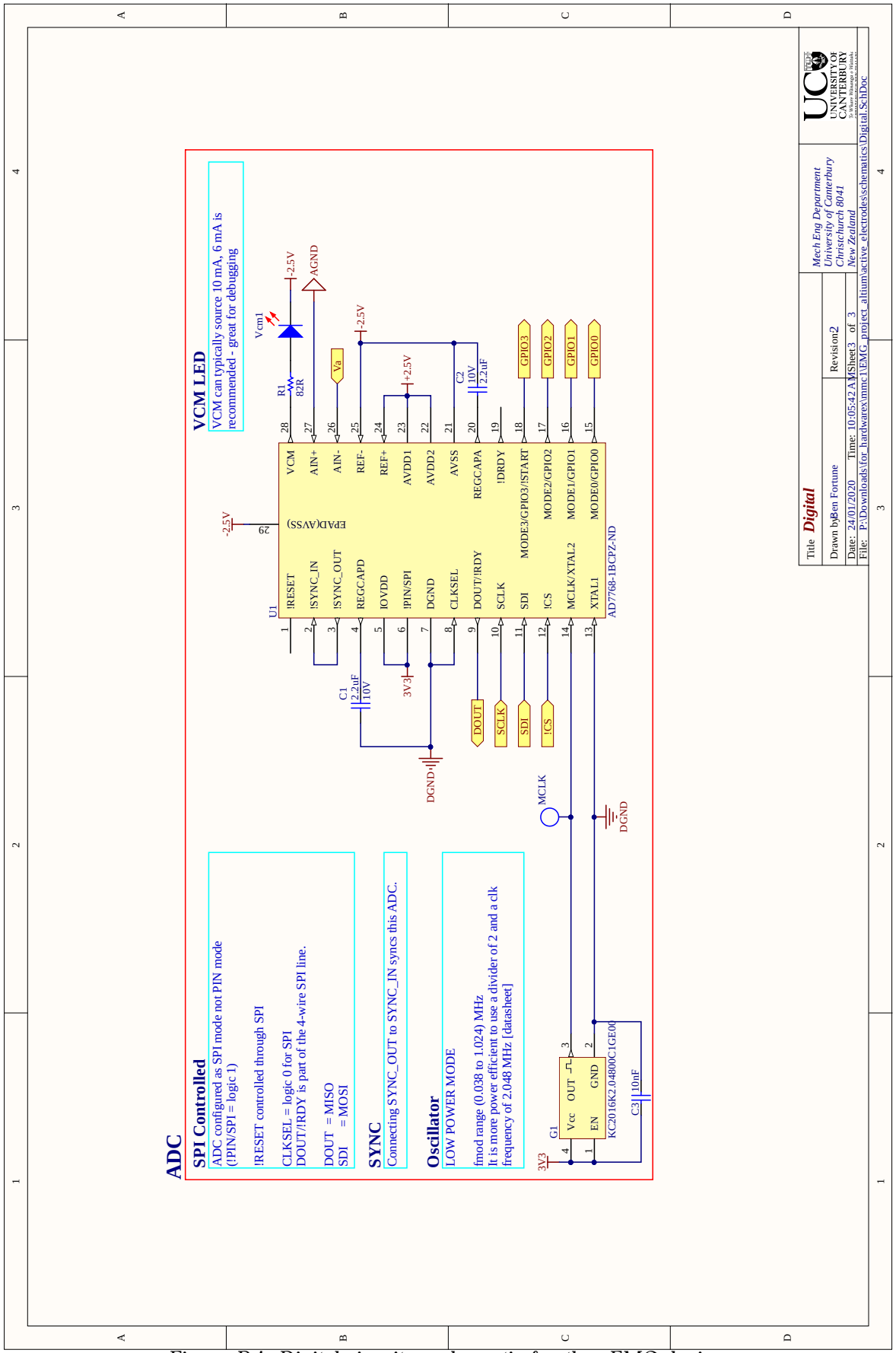

Figure B.1: Digital circuitry schematic for the sEMG device.

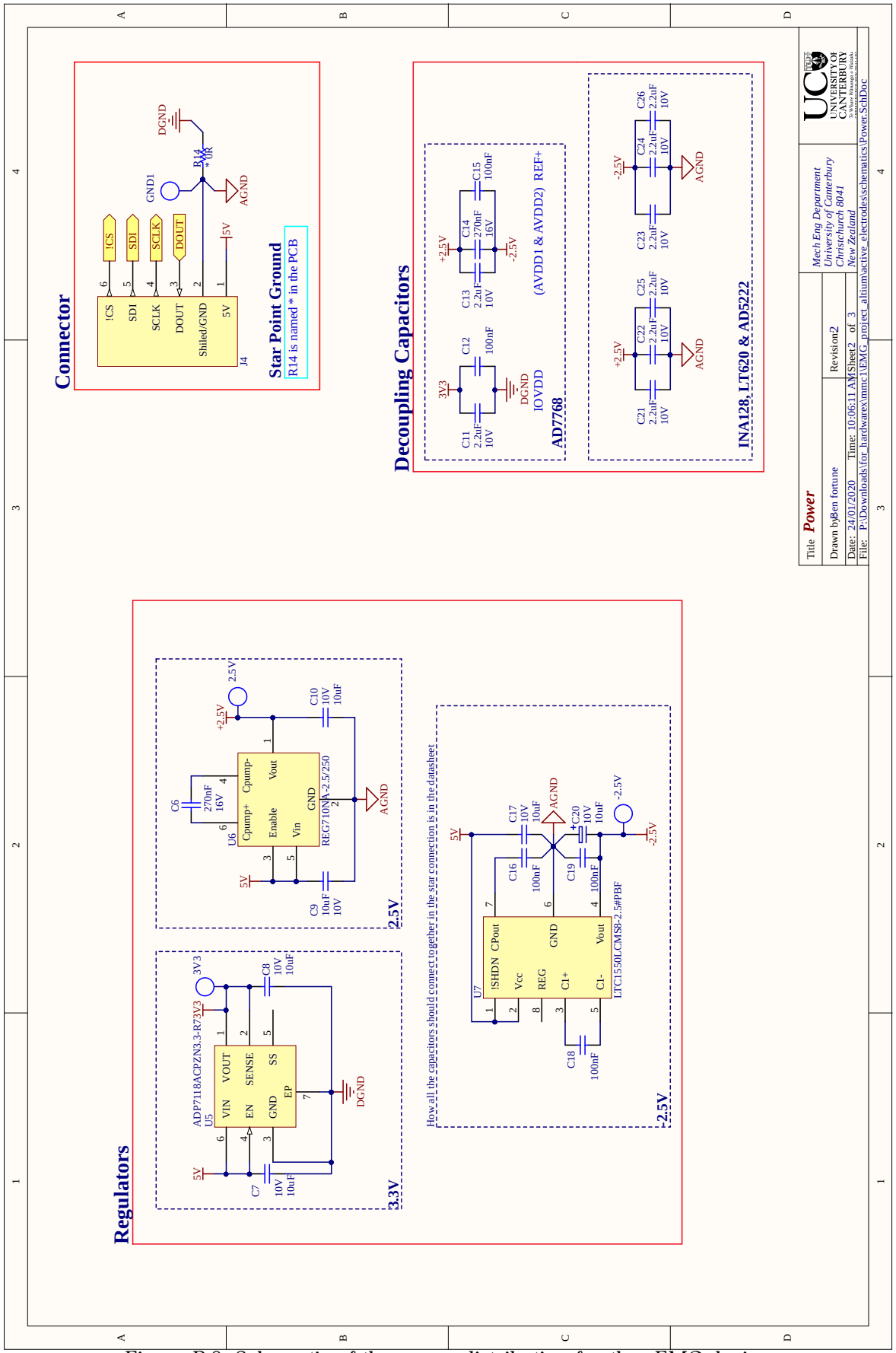

Figure B.2: Schematic of the power distribution for the sEMG device.

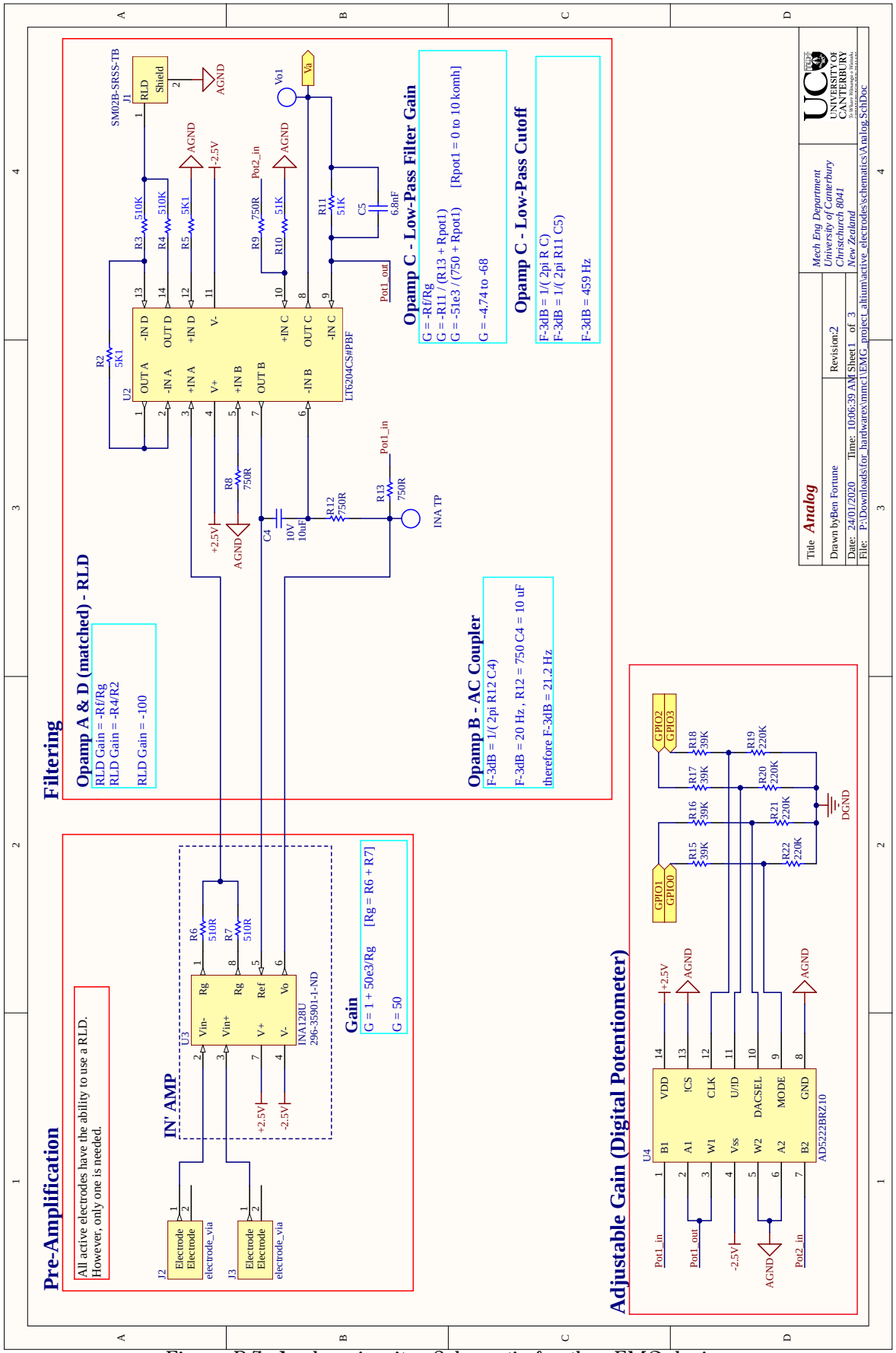

Figure B.3: Analog circuitry Schematic for the sEMG device.

APPENDIX C

Modelling the Step Response of Electrode-Skin Interfaces in the Time Domain

The general equations which characterise the step response of the electrode-skin interface in the time domain are characterised by non-linear expressions that consist of the model component variables.

The first exponential base scalar for the general voltage expression is,

$$
\begin{aligned}
V_1 = \frac{V_S(t)}{2\,\alpha\,(R_1 + R_4)\,(R_1 + R_2 + R_3 + R_4)} \Big[\\
&- 2\,(\,C_1\,R_1\,{R_2}^2\,R_4 + \,C_2\,R_1\,{R_3}^2\,R_4 \\
&+ C_1\,{R_1}^2\,{R_2}^2 + C_2\,{R_1}^2\,{R_3}^2) \\
&+ \alpha\,(R_1\,R_3 - R_2\,R_4) \\
&+ \beta\,(R_1\,R_2 + R_1\,R_3) \\
&- \gamma\,(R_1\,R_2 + R_2\,R_4)\Big]\,,
\end{aligned}
\tag{C.1}
$$

where α, β and γ are functions of the component values, R_1 - R_4, C_1, C_2,

$$
\begin{aligned}
\alpha = &\sqrt{{C_1}^2\,{R_1}^2\,{R_2}^2 + 2\,{C_1}^2\,R_1\,{R_2}^2\,R_3} \\
&+ \sqrt{2\,{C_1}^2\,R_1\,{R_2}^2\,R_4 + {C_1}^2\,{R_2}^2\,{R_3}^2} \\
&+ \sqrt{2\,{C_1}^2\,{R_2}^2\,R_3\,R_4 + {C_1}^2\,{R_2}^2\,{R_4}^2} \\
&- \sqrt{2\,C_1\,C_2\,{R_1}^2\,R_2\,R_3 + 2\,C_1\,C_2\,R_1\,{R_2}^2\,R_3} \\
&- \sqrt{2\,C_1\,C_2\,R_1\,R_2\,{R_3}^2 + 4\,C_1\,C_2\,R_1\,R_2\,R_3\,R_4} \\
&+ \sqrt{2\,C_1\,C_2\,{R_2}^2\,{R_3}^2 - 2\,C_1\,C_2\,{R_2}^2\,R_3\,R_4} \\
&- \sqrt{2\,C_1\,C_2\,R_2\,{R_3}^2\,R_4 + 2\,C_1\,C_2\,R_2\,R_3\,{R_4}^2} \\
&+ \sqrt{{C_2}^2\,{R_1}^2\,{R_3}^2 + 2\,{C_2}^2\,R_1\,R_2\,{R_3}^2} \\
&+ \sqrt{2\,{C_2}^2\,R_1\,{R_3}^2\,R_4 + {C_2}^2\,{R_2}^2\,{R_3}^2} \\
&+ \sqrt{2\,{C_2}^2\,R_2\,{R_3}^2\,R_4 + {C_2}^2\,{R_3}^2\,{R_4}^2}\,,
\end{aligned}
\tag{C.2}
$$

$$\begin{aligned}\beta = {} & C_1 R_1 R_2 + C_1 R_2 R_3 + C_2 R_1 R_3 + \\ & C_1 R_2 R_4 + C_2 R_2 R_3 + C_2 R_3 R_4 ,\end{aligned} \tag{C.3}$$

$$\begin{aligned}\gamma = {} & 2 C_2 {R_3}^2 - C_1 R_1 R_2 - C_1 R_2 R_3 + C_2 R_1 R_3 \\ & - C_1 R_2 R_4 + C_2 R_2 R_3 + C_2 R_3 R_4 .\end{aligned} \tag{C.4}$$

The second exponential base scalar for the general voltage expression is,

$$\begin{aligned}V_2 = {} & \frac{V_S(t)}{2\,\alpha\,(R_1 + R_4)\,(R_1 + R_2 + R_3 + R_4)} \Big[\\ & + 2\,(\,C_1 R_1 {R_2}^2 R_4 + \, C_2 R_1 {R_3}^2 R_4 \\ & + C_1 {R_1}^2 {R_2}^2 + C_2 {R_1}^2 {R_3}^2) \\ & + \alpha\,(R_1 R_3 - R_2 R_4) \\ & - \beta\,(R_1 R_2 + R_1 R_3) \\ & + \gamma\,(R_1 R_2 + R_2 R_4) \Big] ,\end{aligned} \tag{C.5}$$

the steady state voltage constant is,

$$V_3 = \frac{(R_1 + R_2)\,V_S(t)}{R_1 + R_2 + R_3 + R_4} , \tag{C.6}$$

the first exponential base scalar for the general current expression is,

$$\begin{aligned} I_1 = \frac{V_S(t)}{2\,\alpha\,(R_1 + R_4)\,(R_1 + R_2 + R_3 + R_4)}\Big[\\ + \alpha\,(R_2 + R_3) + \beta\,(R_2 + R_3) \\ - 2(C_1 R_1 {R_2}^2 + C_2 R_1 {R_3}^2 \\ + \quad C_1 {R_2}^2 R_4 + C_2 {R_3}^2 R_4)\Big]\,, \end{aligned} \tag{C.7}$$

the second exponential base scalar for the general current expression is,

$$\begin{aligned} I_2 = \frac{V_S(t)}{2\,\alpha\,(R_1 + R_4)\,(R_1 + R_2 + R_3 + R_4)}\Big[\\ + \alpha\,(R_2 + R_3) - \beta\,(R_2 + R_3) \\ + 2(C_1 R_1 {R_2}^2 + C_2 R_1 {R_3}^2 \\ + C_1 {R_2}^2 R_4 + C_2 {R_3}^2 R_4)\Big]\,, \end{aligned} \tag{C.8}$$

the steady state current constant is,

$$I_3 = \frac{V_S(t)}{R_1 + R_2 + R_3 + R_4}\,, \tag{C.9}$$

the time constant associated with the first exponential is,

$$\tau_1 = \frac{\alpha + \beta}{2\,C_1\,C_2\,R_2\,R_3\,(R_1 + R_4)}\,, \tag{C.10}$$

and the time constant associated with the second exponential is,

$$\tau_2 = \frac{-\alpha + \beta}{2\,C_1\,C_2\,R_2\,R_3\,(R_1 + R_4)}\,. \tag{C.11}$$

APPENDIX D

Electrode-Skin Impedance Imbalance Measured in the Frequency Domain

The electrode-skin impedance of ten subjects using the three electrode configurations, $Ag/AgCl_{NSP}$, $Ag/AgCl_{SP}$ and Ag_{-SP}, are outlined in Sections D.1, D.2 and D.3, respectively.

D.1 Ag/AgCl$_{NSP}$ electrodes

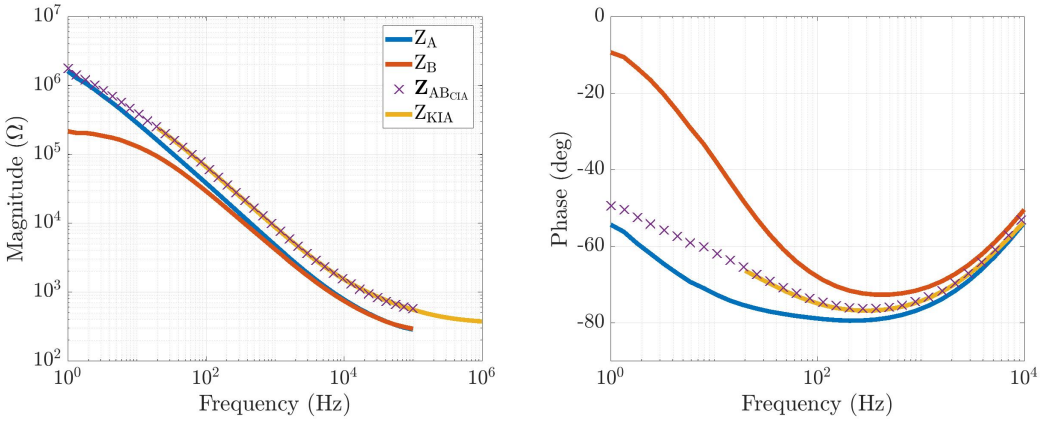

(a) Subject 1.

Figure D.1: Electrode-skin impedance imbalance for 10 healthy subjects using Ag/AgCl$_{NSP}$ electrodes

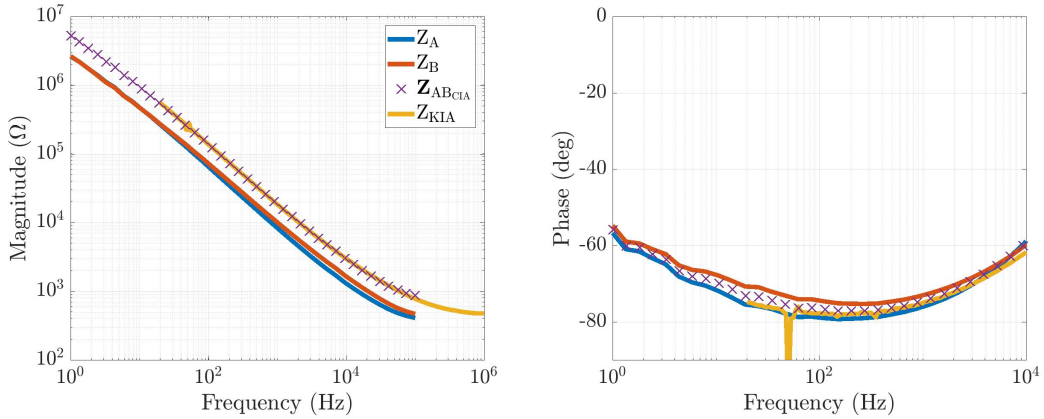

(b) Subject 2.

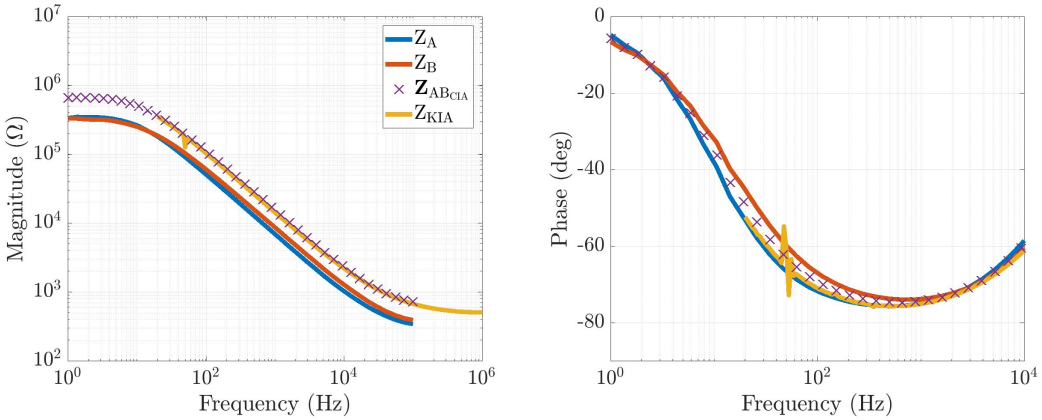

(c) Subject 3.

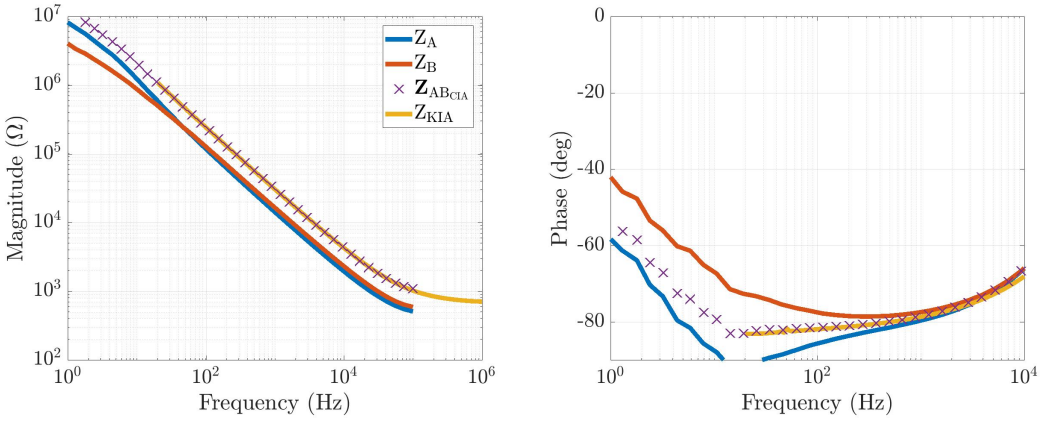

(d) Subject 4.

Figure D.1: Electrode-skin impedance imbalance for 10 healthy subjects using $Ag/AgCl_{NSP}$ electrodes (cont.).

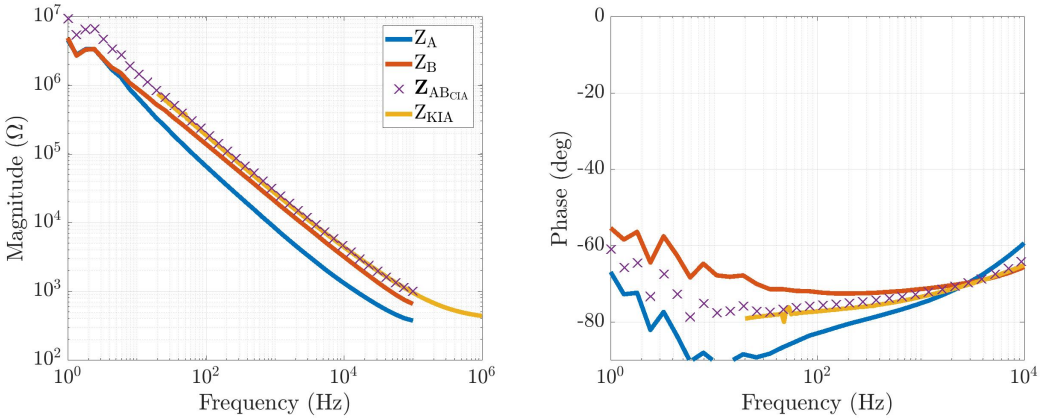

(e) Subject 5.

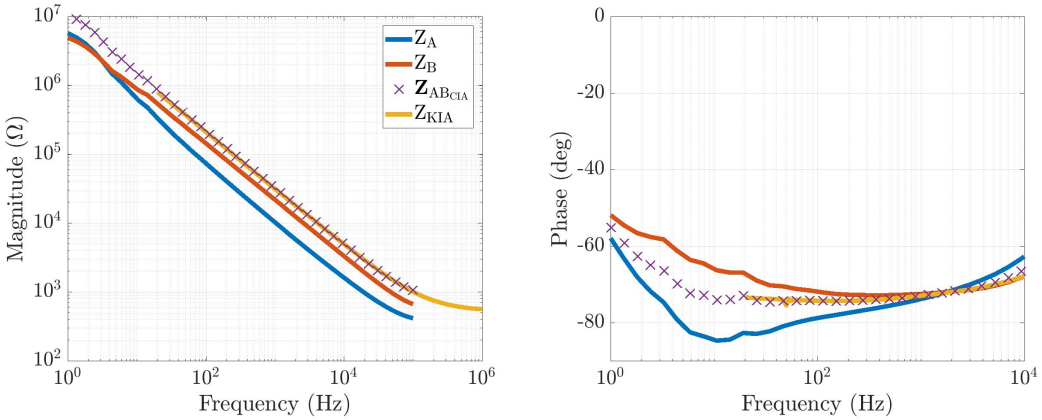

(f) Subject 6.

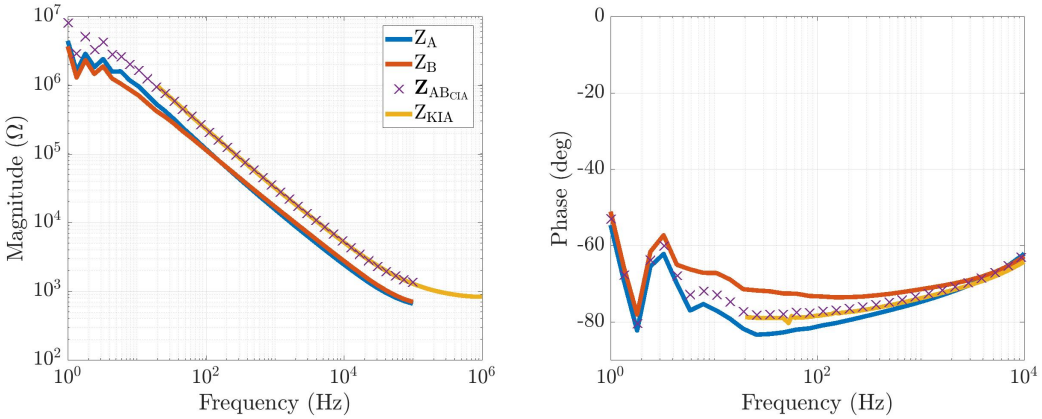

(g) Subject 7.

Figure D.1: Electrode-skin impedance imbalance for 10 healthy subjects using $Ag/AgCl_{NSP}$ electrodes (cont.).

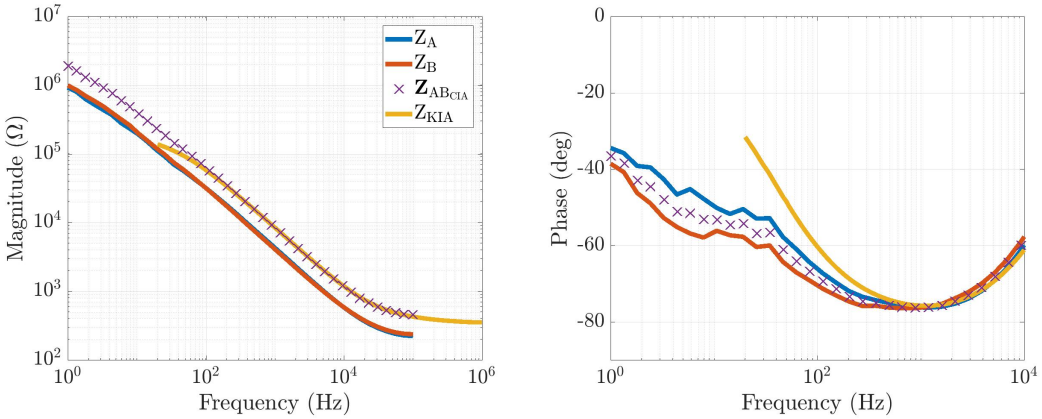

(h) Subject 8.

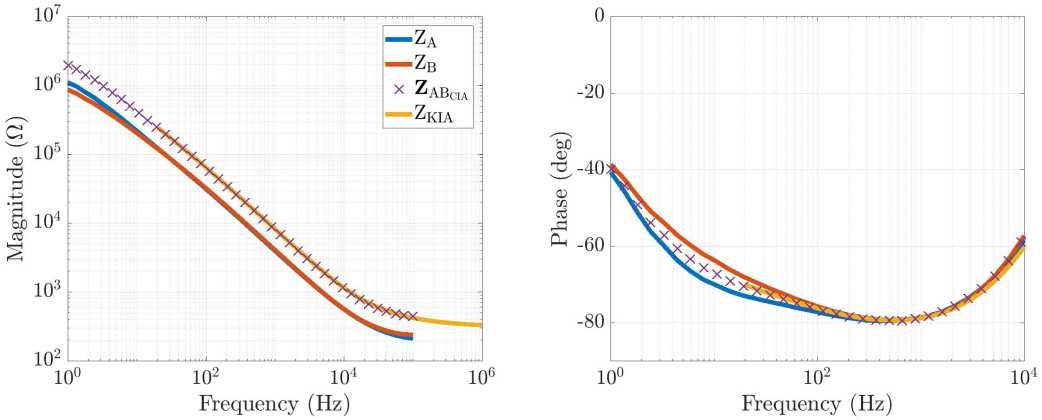

(i) Subject 9.

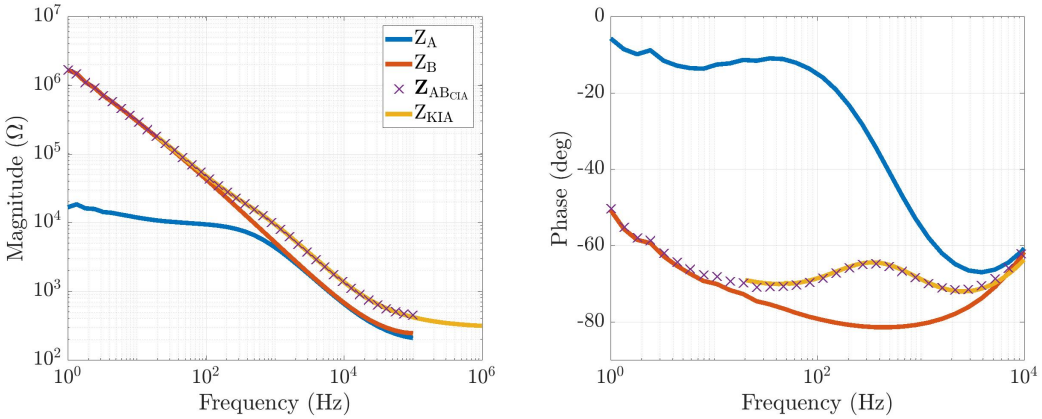

(j) Subject 10.

Figure D.1: Electrode-skin impedance imbalance for 10 healthy subjects using $Ag/AgCl_{NSP}$ electrodes (cont.).

D.2 Ag/AgCl$_{SP}$ electrodes

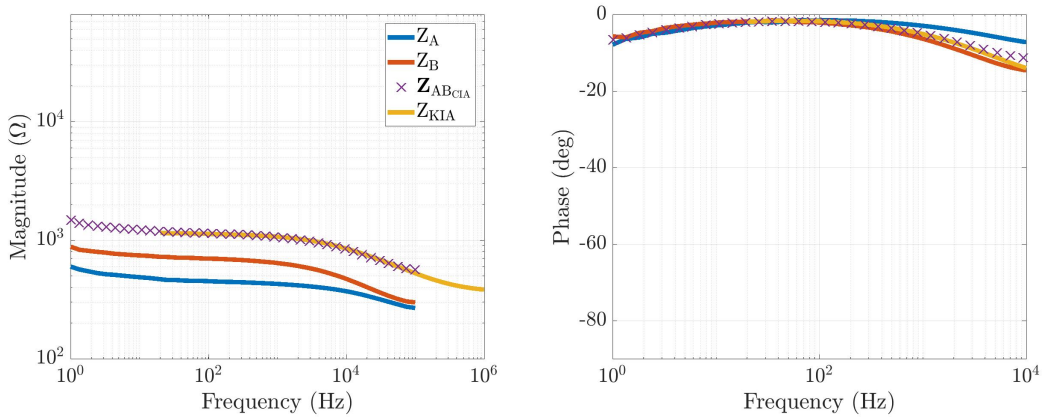

(a) Subject 1.

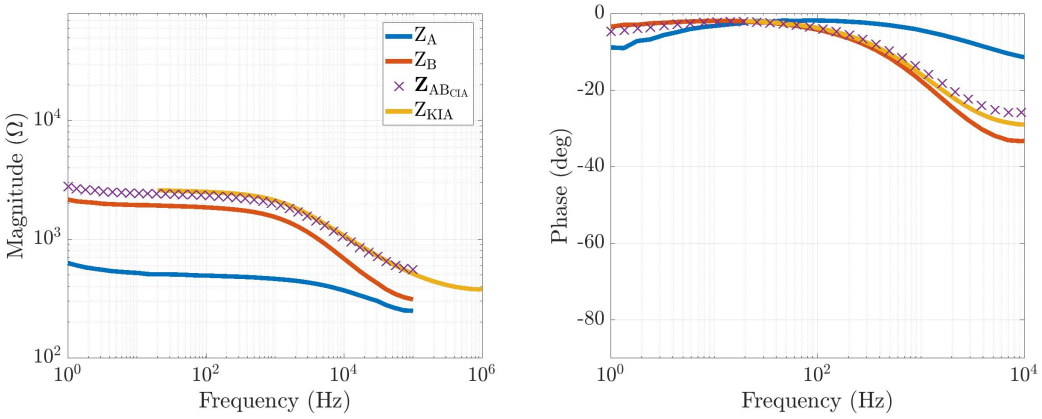

(b) Subject 2.

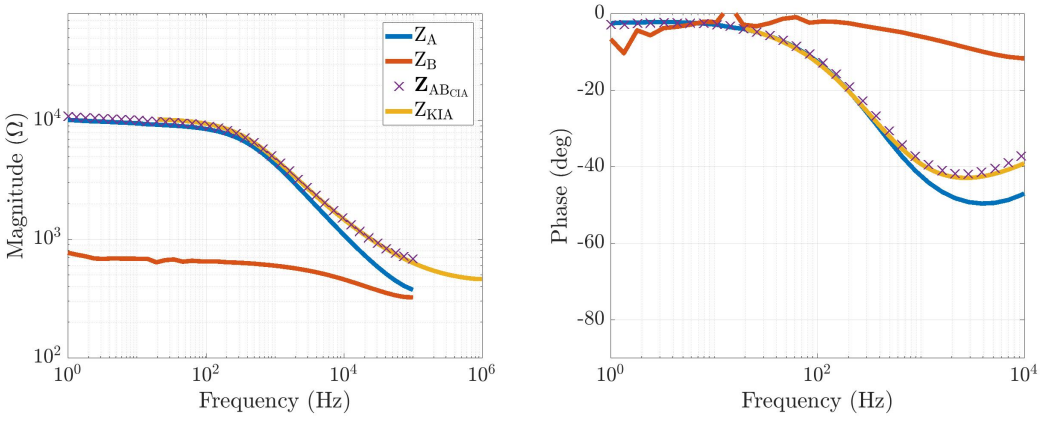

(c) Subject 3.

Figure D.2: Electrode-skin impedance imbalance for 10 healthy subjects using Ag/AgCl$_{SP}$ electrodes.

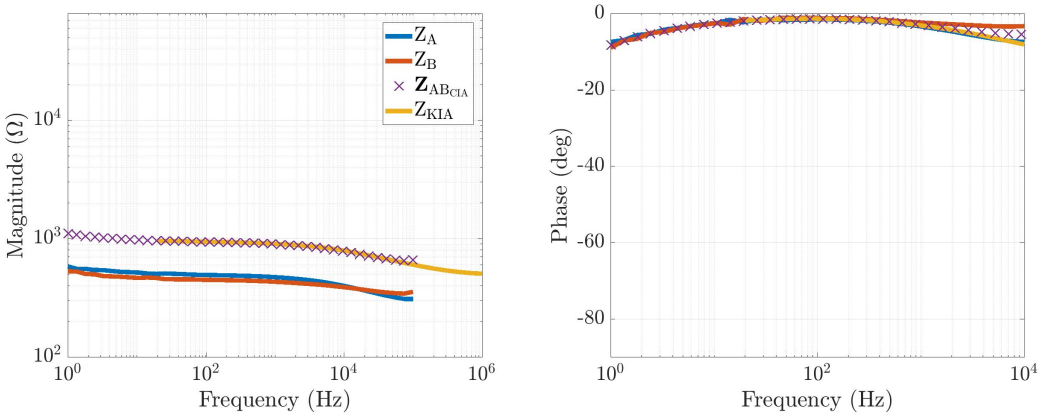

(d) Subject 4.

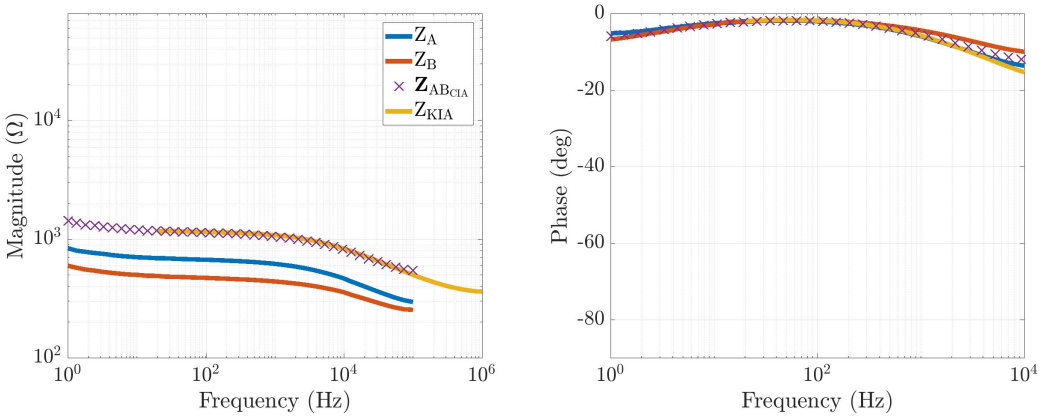

(e) Subject 5.

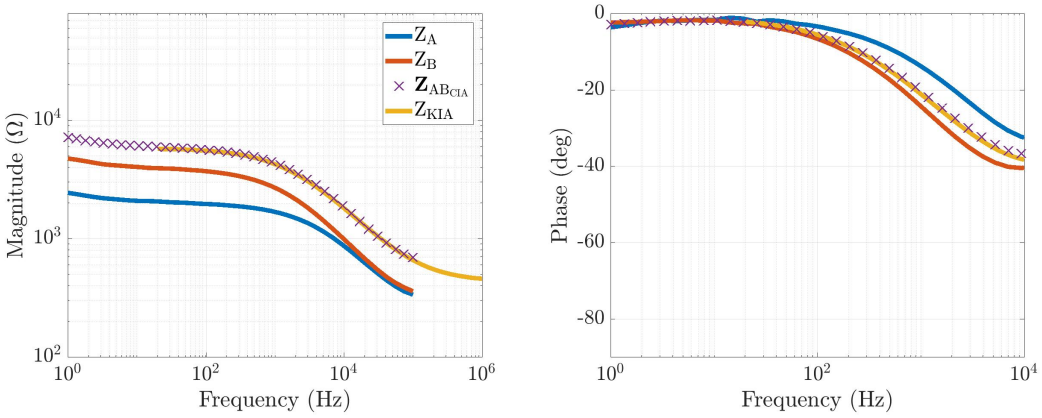

(f) Subject 6.

Figure D.2: Electrode-skin impedance imbalance for 10 healthy subjects using $Ag/AgCl_{SP}$ electrodes (cont.).

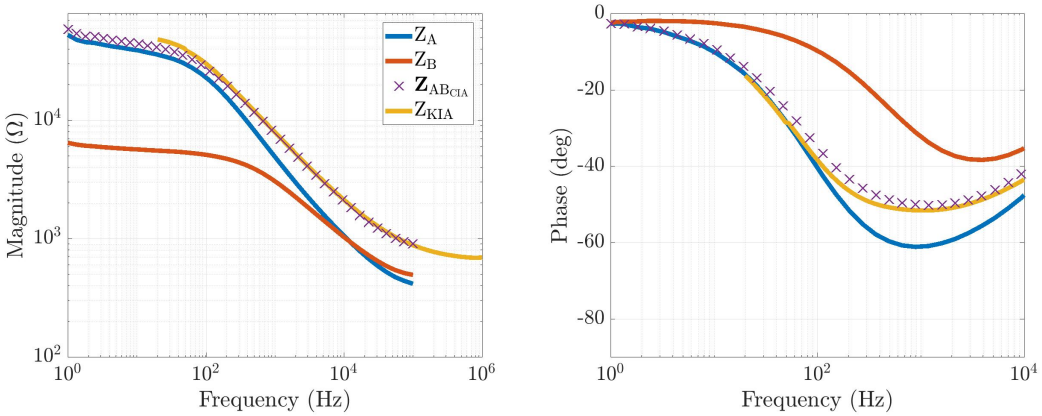

(g) Subject 7.

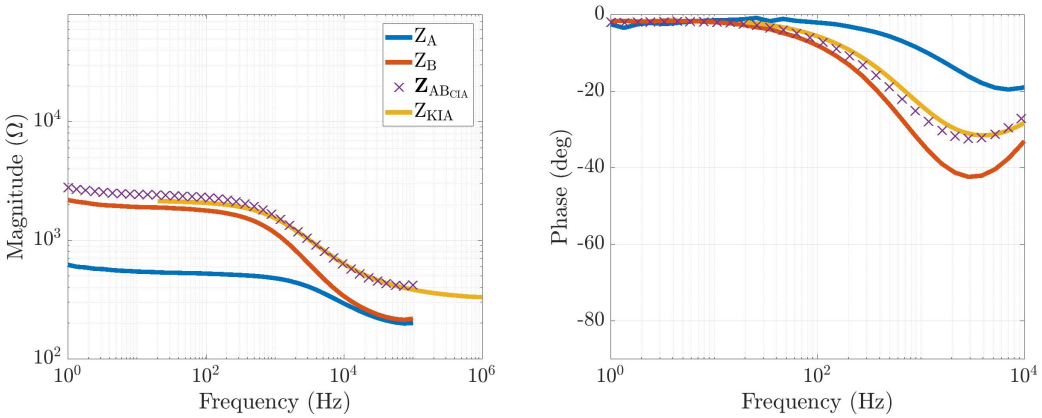

(h) Subject 8.

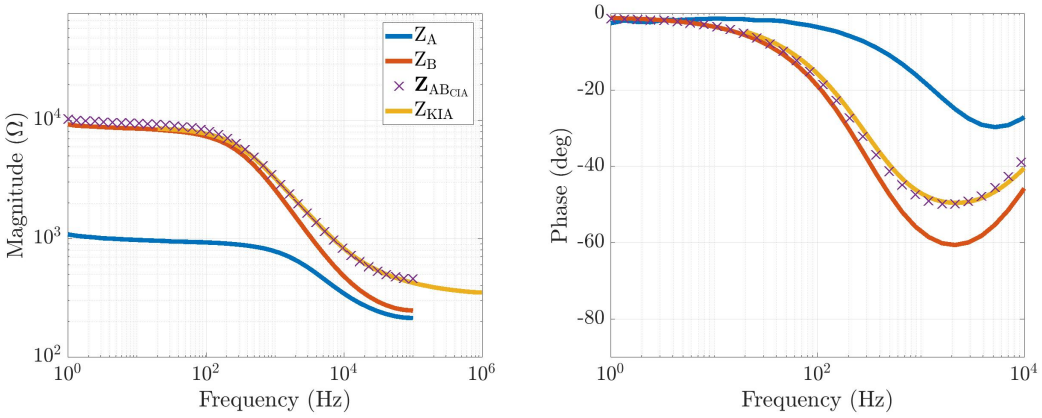

(i) Subject 9.

Figure D.2: Electrode-skin impedance imbalance for 10 healthy subjects using $Ag/AgCl_{SP}$ electrodes (cont.).

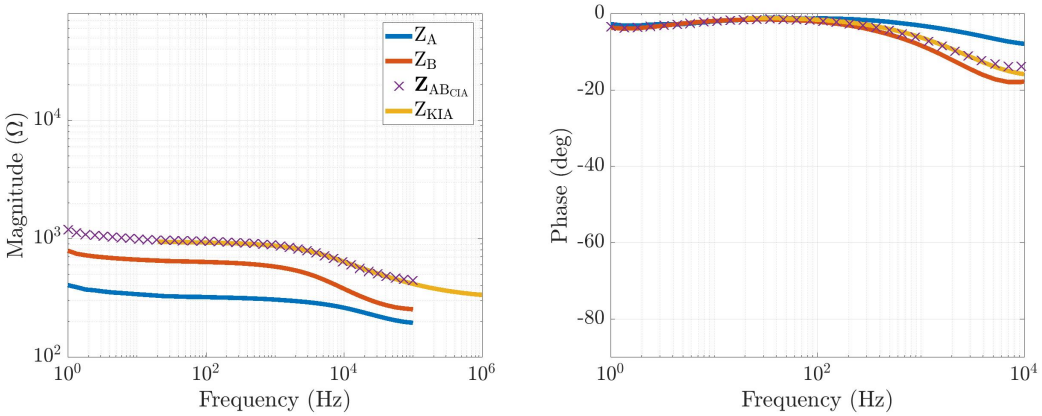

(j) Subject 10.

Figure D.2: Electrode-skin impedance imbalance for 10 healthy subjects using $Ag/AgCl_{SP}$ electrodes (cont.).

D.3 Ag_{-SP} electrodes

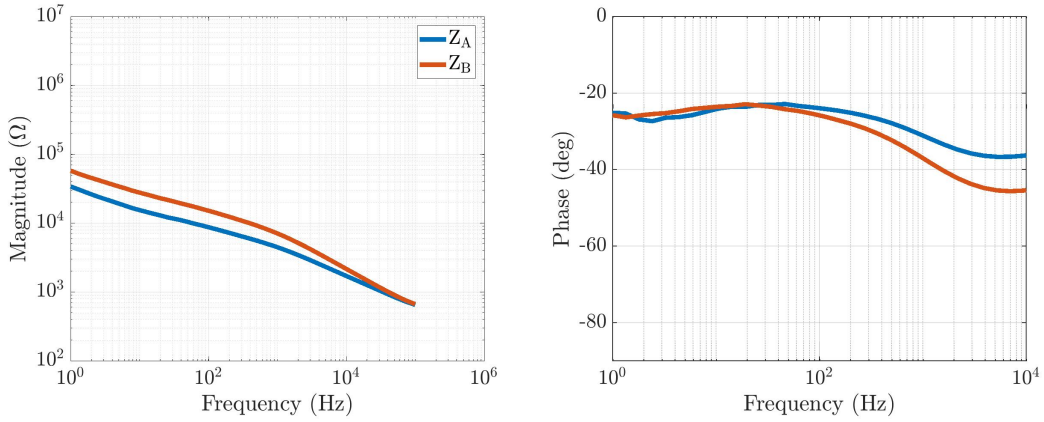

(a) Subject 1.

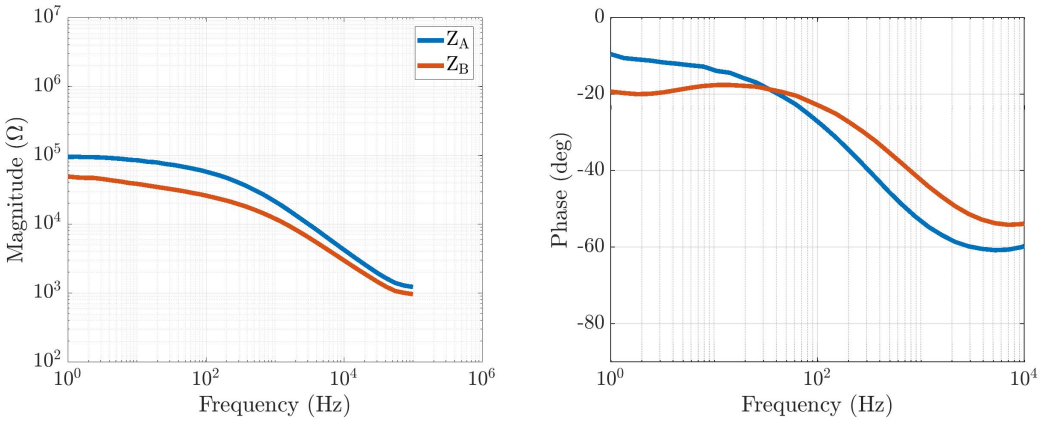

(b) Subject 2.

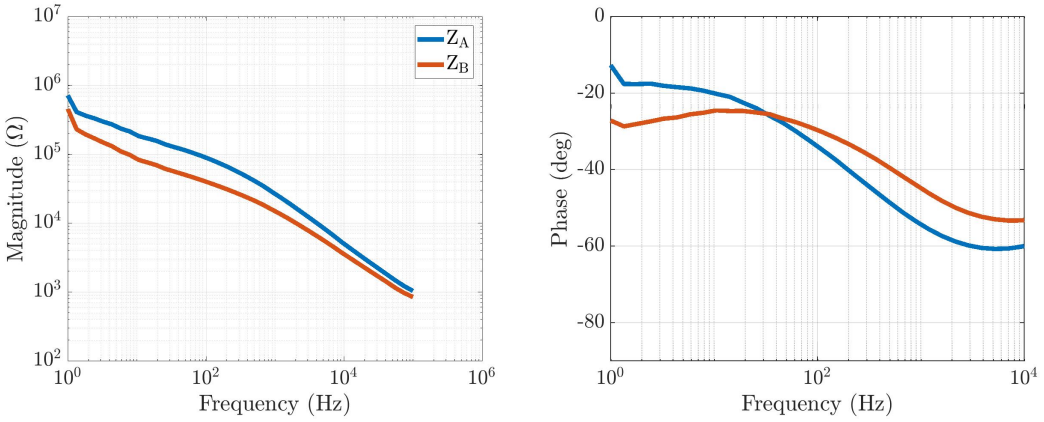

(c) Subject 3.

Figure D.3: Electrode-skin impedance imbalance for 10 healthy subjects using Ag_{-SP} electrodes.

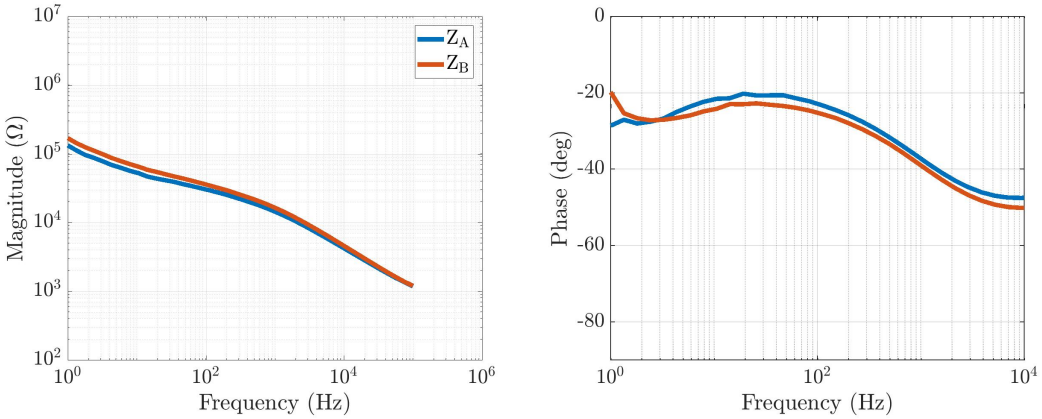

(d) Subject 4.

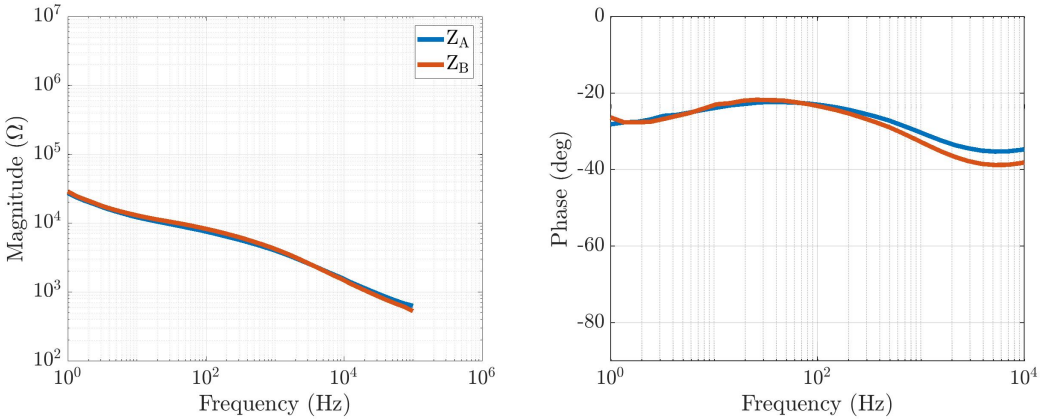

(e) Subject 5.

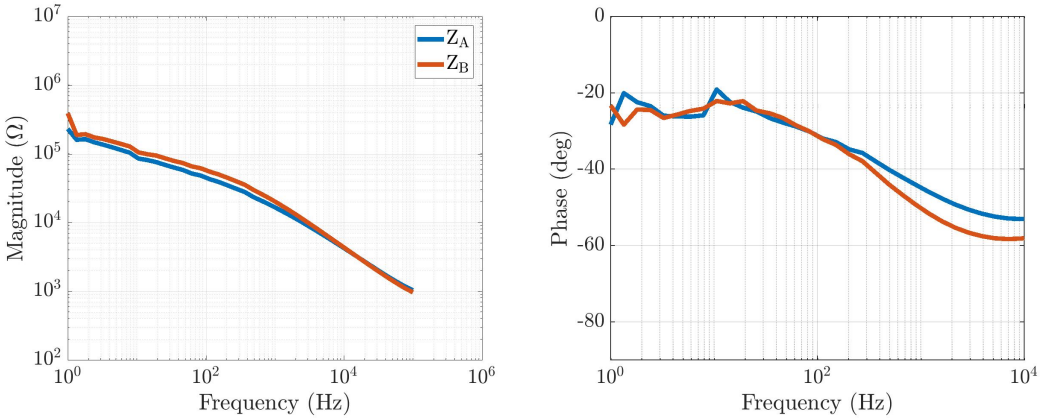

(f) Subject 6.

Figure D.3: Electrode-skin impedance imbalance for 10 healthy subjects using Ag_{SP} electrodes (cont.).

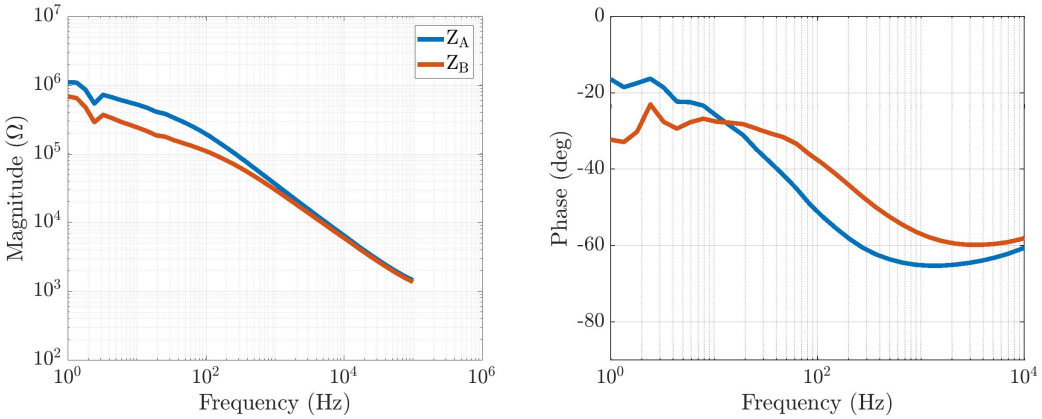

(g) Subject 7.

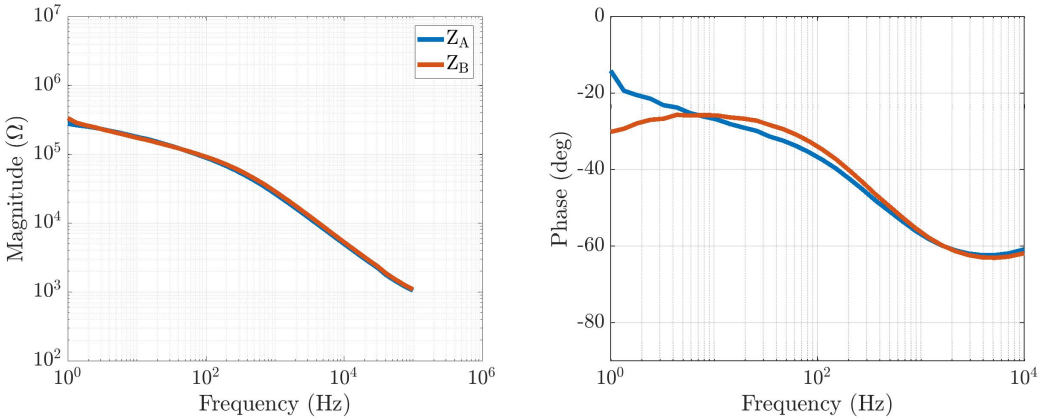

(h) Subject 8.

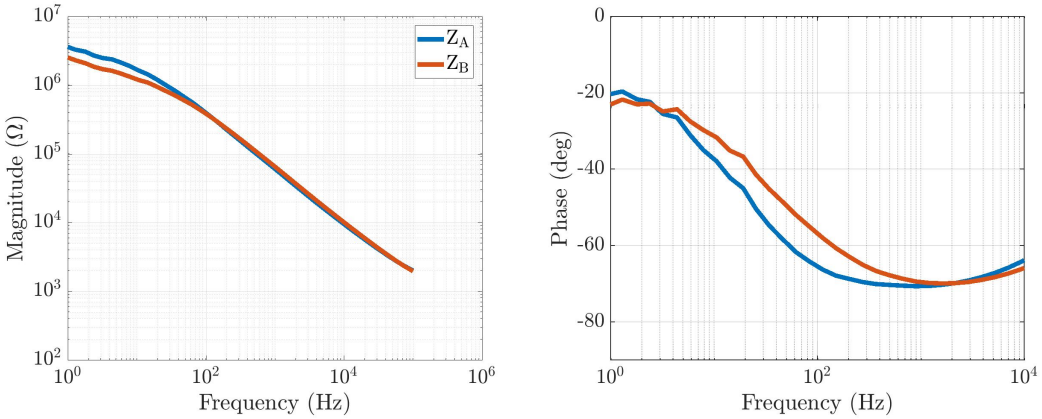

(i) Subject 9.

Figure D.3: Electrode-skin impedance imbalance for 10 healthy subjects using Ag_{-SP} electrodes (cont.).

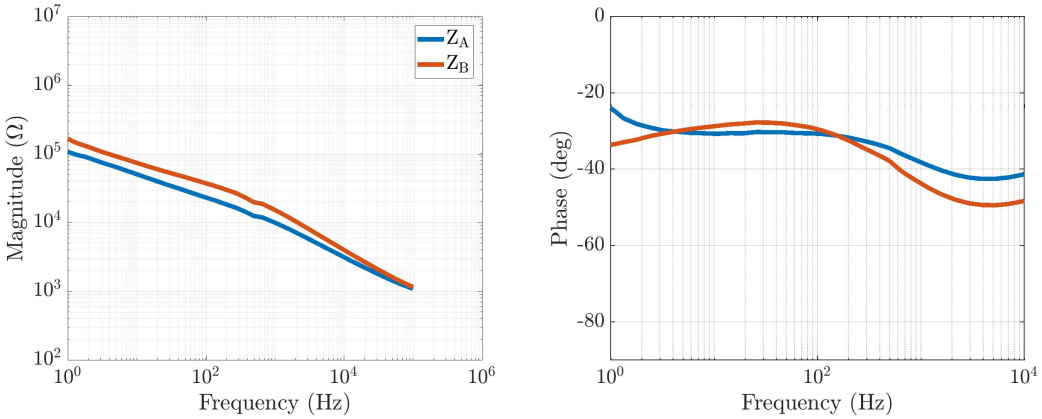

(j) Subject 10.

Figure D.3: Electrode-skin impedance imbalance for 10 healthy subjects using Ag_{SP} electrodes (cont.).

APPENDIX E

Electrode-Skin Impedance Imbalance Modelled in the Frequency Domain

The electrode-skin impedance model fit for ten subjects using the three electrode configurations, $Ag/AgCl_{NSP}$, $Ag/AgCl_{SP}$ and Ag_{-SP}, are outlined in Sections E.1, E.2 and E.3, respectively.

E.1 Ag/AgCl$_{NSP}$ electrodes

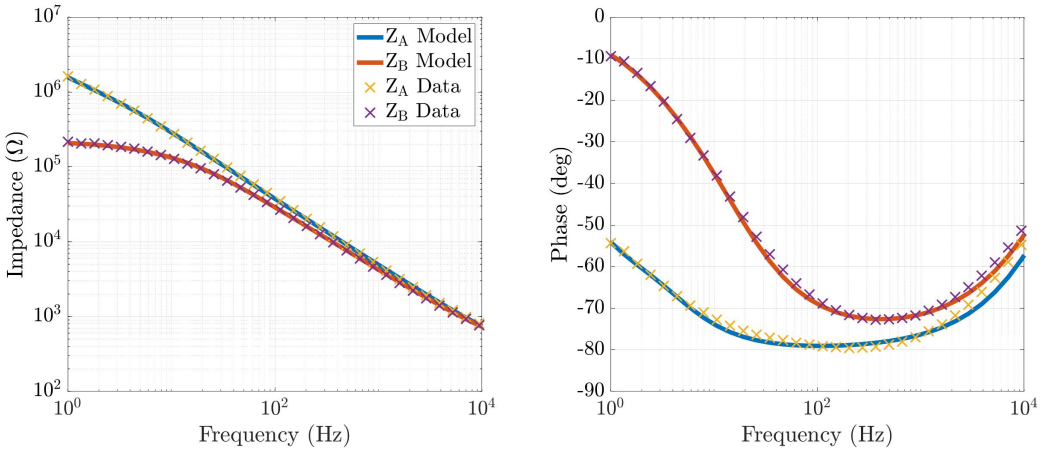

(a) Subject 1.

Figure E.1: Electrode-skin impedance model fit for 10 healthy subjects using Ag/AgCl$_{NSP}$ electrodes.

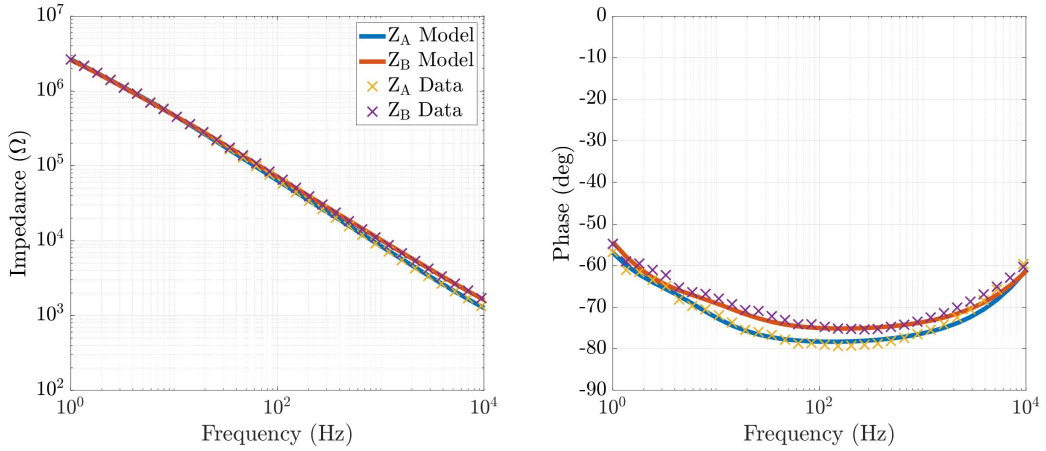

(b) Subject 2.

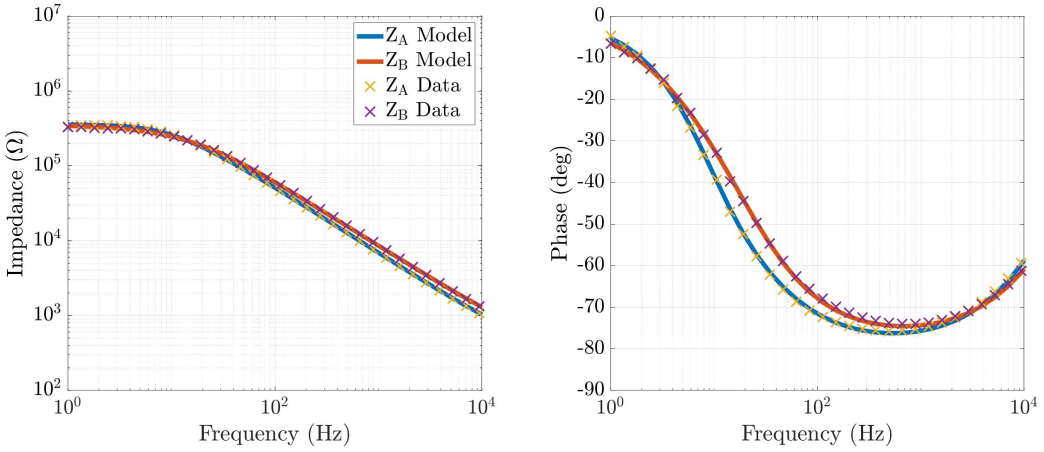

(c) Subject 3.

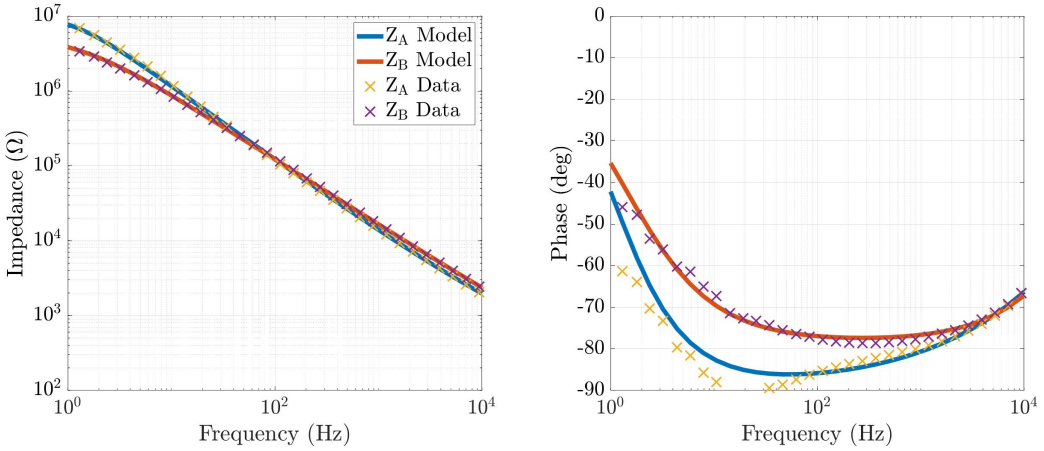

(d) Subject 4.

Figure E.1: Electrode-skin impedance model fit for 10 healthy subjects using $Ag/AgCl_{NSP}$ electrodes (cont.).

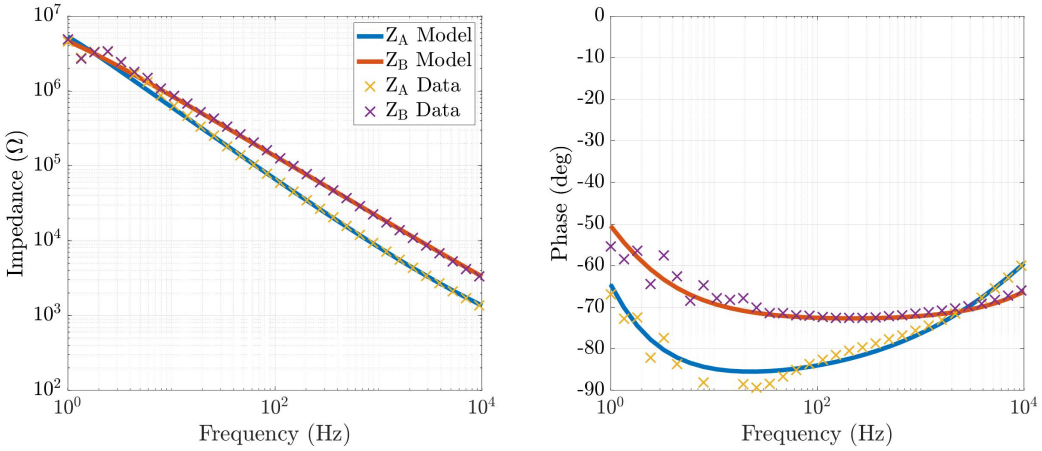

(e) Subject 5.

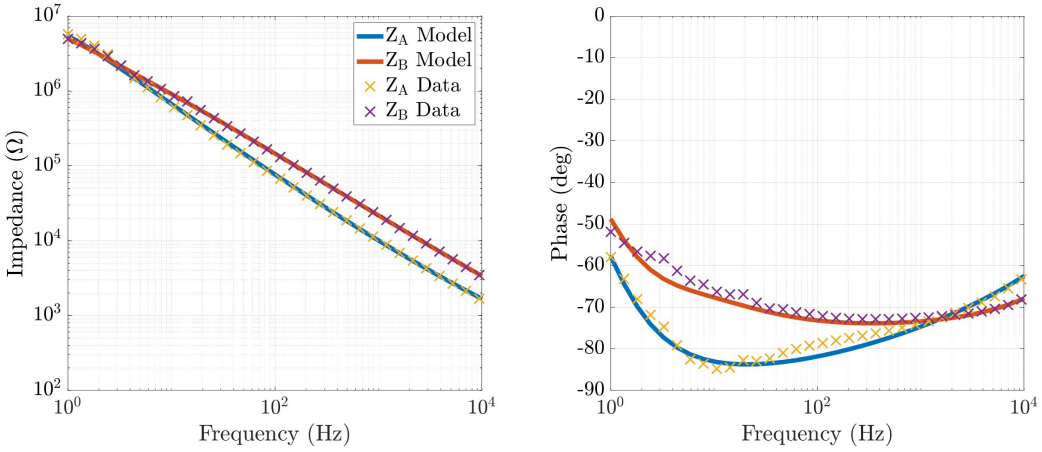

(f) Subject 6.

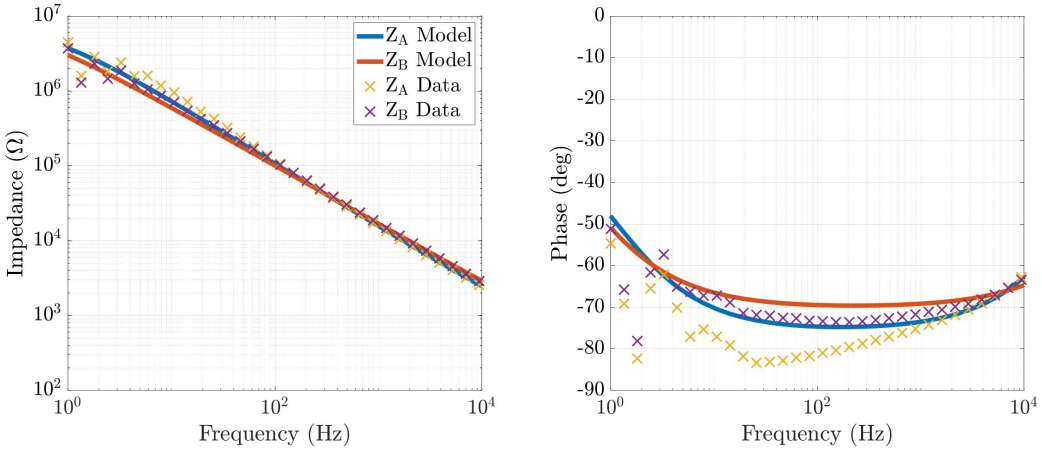

(g) Subject 7.

Figure E.1: Electrode-skin impedance model fit for 10 healthy subjects using $Ag/AgCl_{NSP}$ electrodes (cont.).

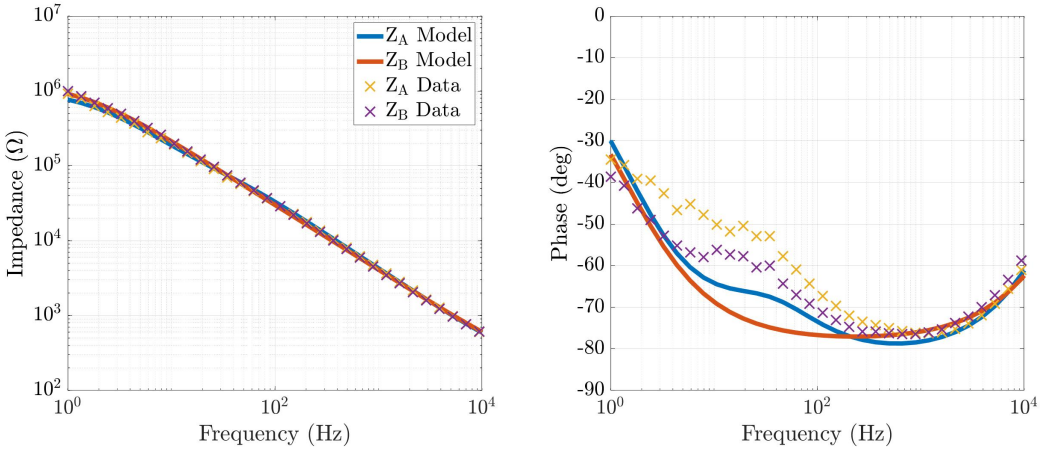

(h) Subject 8.

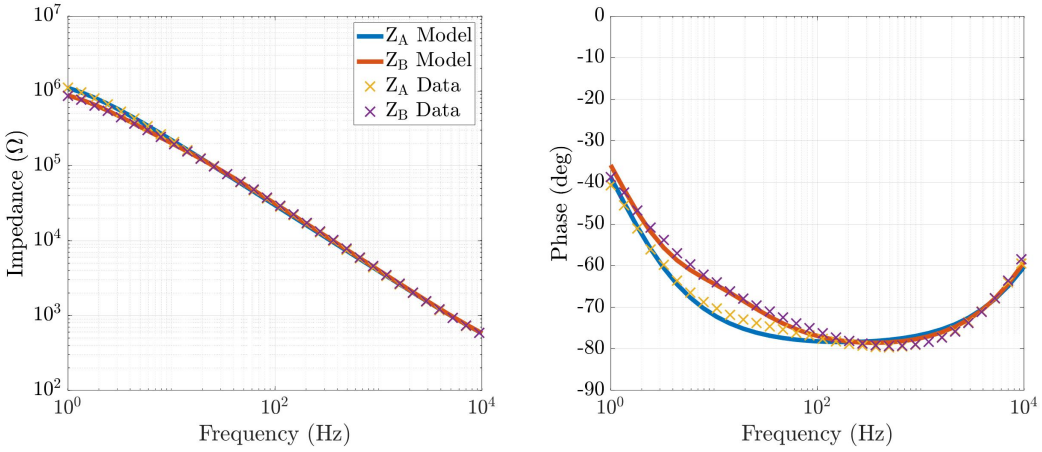

(i) Subject 9.

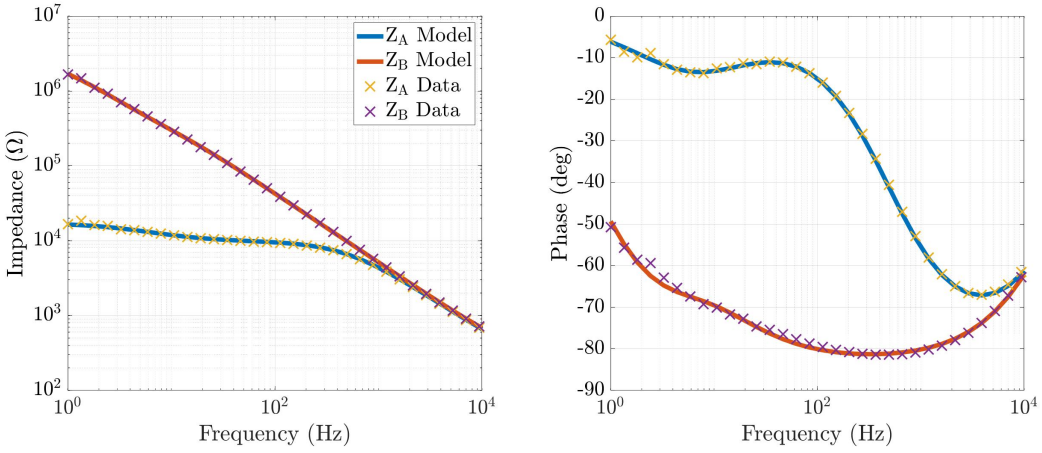

(j) Subject 10.

Figure E.1: Electrode-skin impedance model fit for 10 healthy subjects using $Ag/AgCl_{NSP}$ electrodes (cont.).

E.2 Ag/AgCl$_{SP}$ electrodes

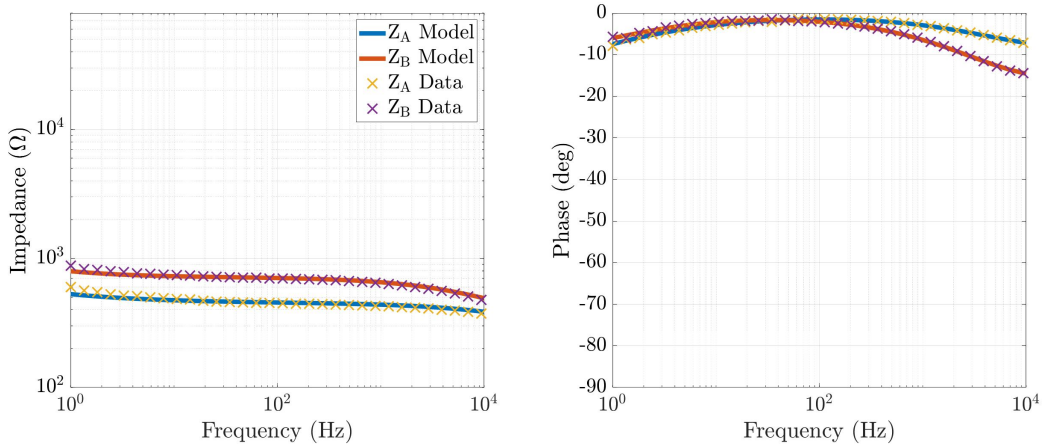

(a) Subject 1.

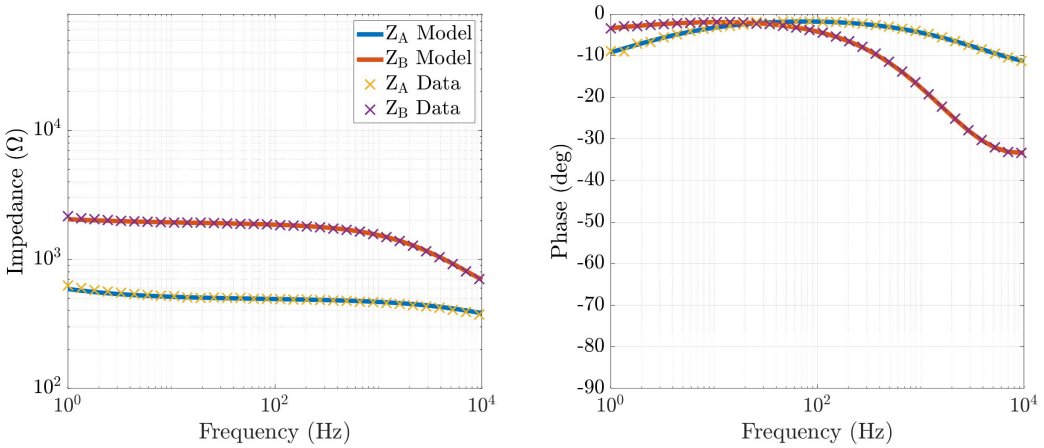

(b) Subject 2.

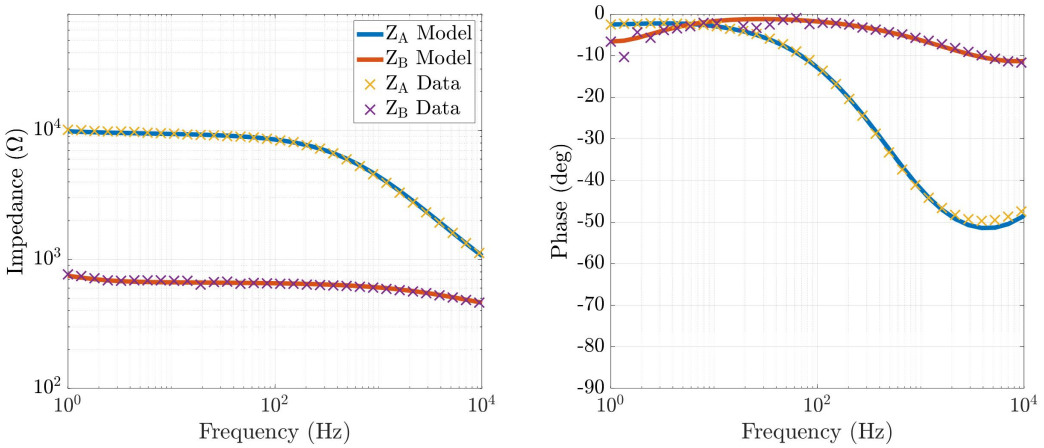

(c) Subject 3.

Figure E.2: Electrode-skin impedance model fit for 10 healthy subjects using Ag/AgCl$_{SP}$ electrodes.

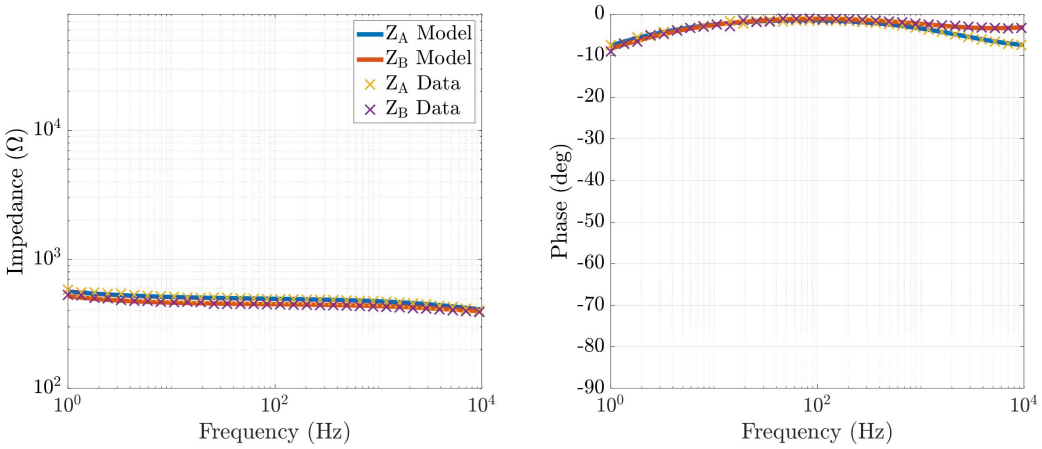

(d) Subject 4.

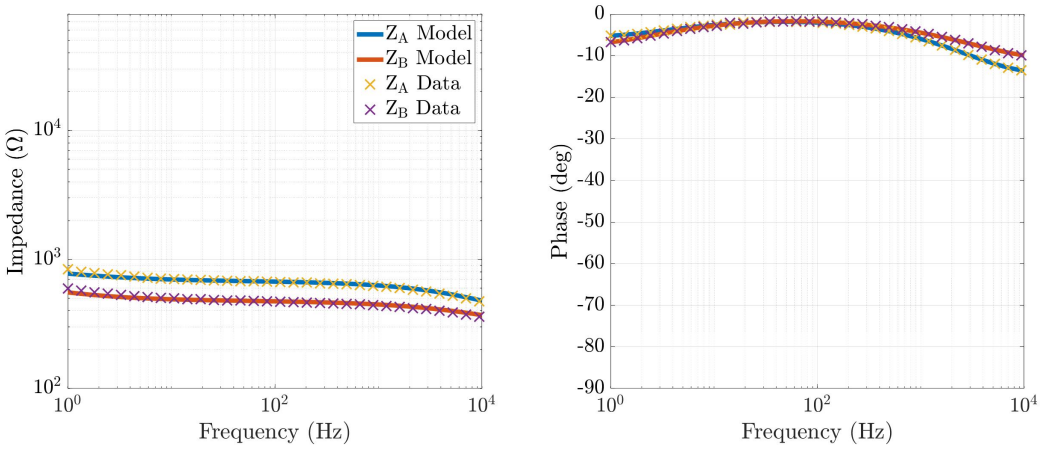

(e) Subject 5.

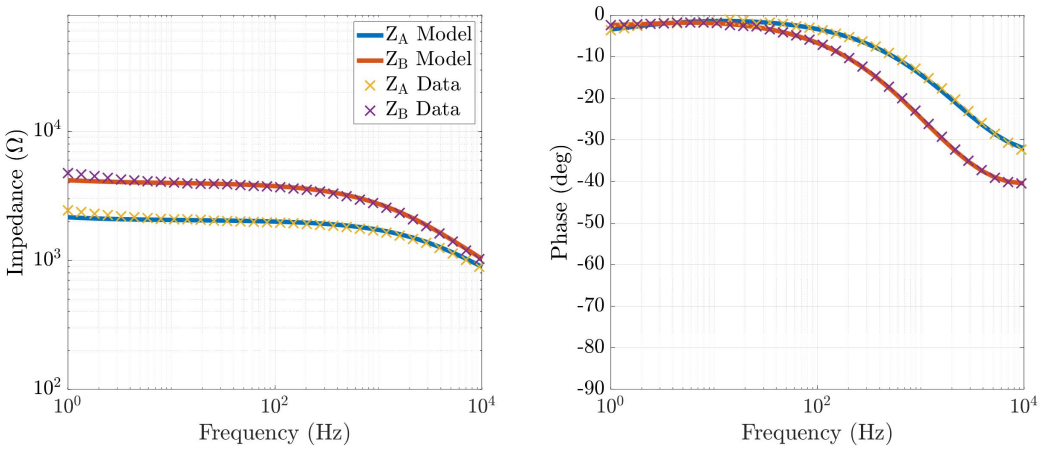

(f) Subject 6.

Figure E.2: Electrode-skin impedance model fit for 10 healthy subjects using $Ag/AgCl_{SP}$ electrodes (cont.).

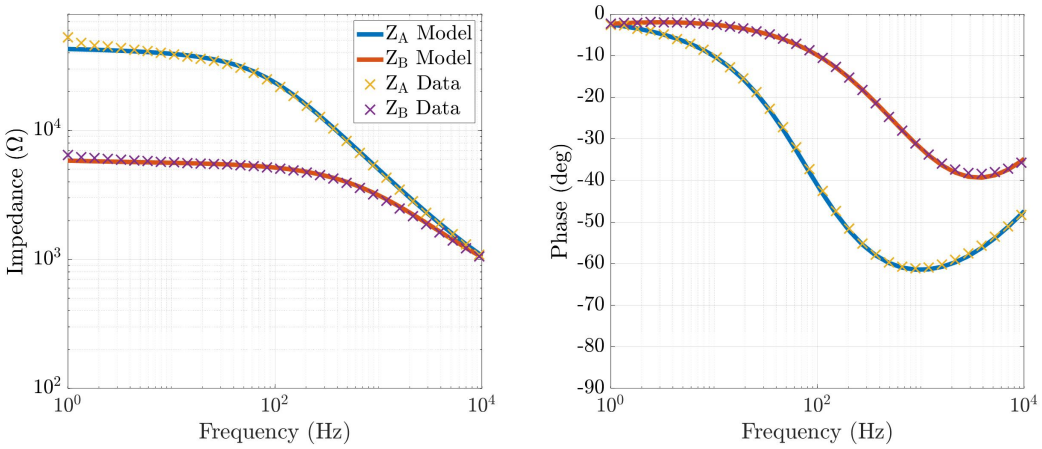

(g) Subject 7.

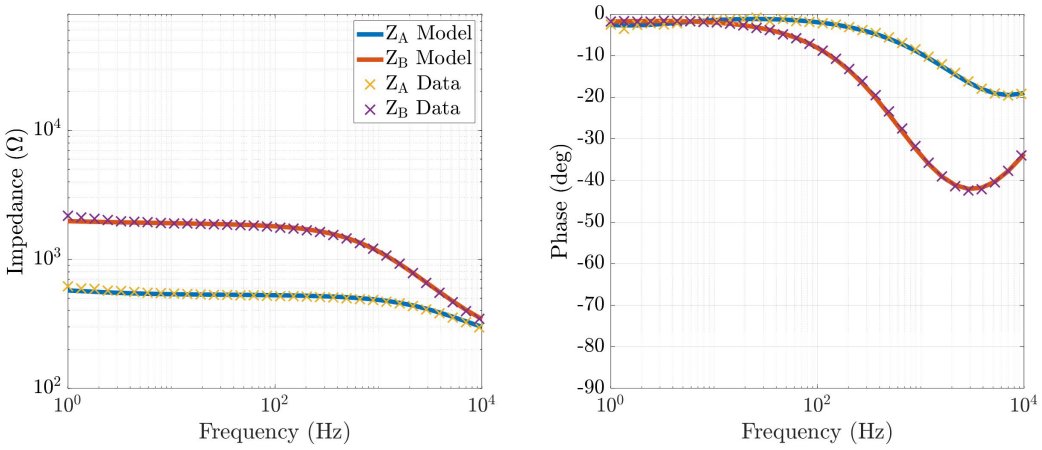

(h) Subject 8.

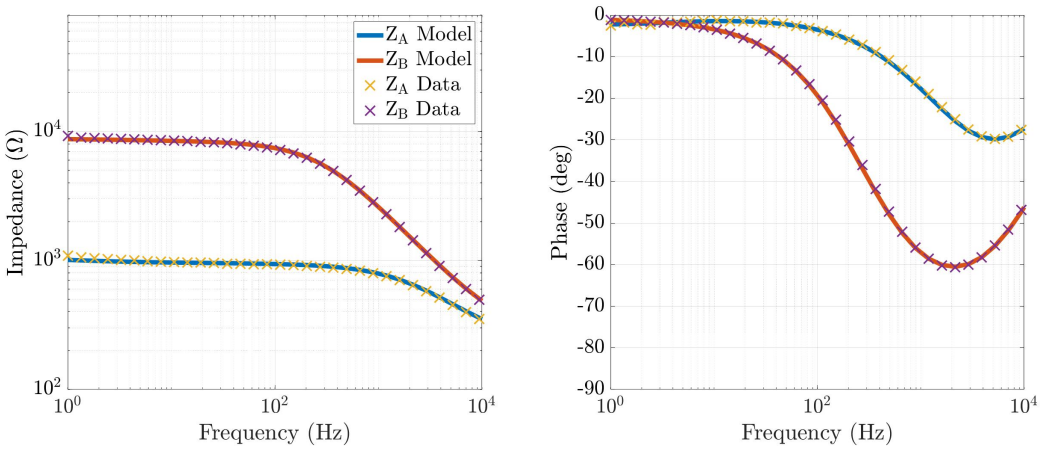

(i) Subject 9.

Figure E.2: Electrode-skin impedance model fit for 10 healthy subjects using $Ag/AgCl_{SP}$ electrodes (cont.).

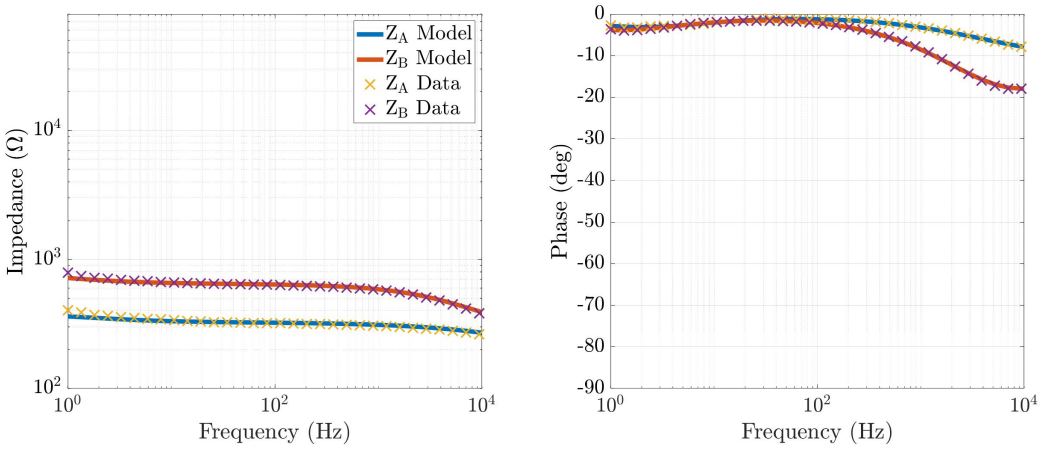

(j) Subject 10.

Figure E.2: Electrode-skin impedance model fit for 10 healthy subjects using $Ag/AgCl_{SP}$ electrodes (cont.).

E.3 Ag_{-SP} electrodes

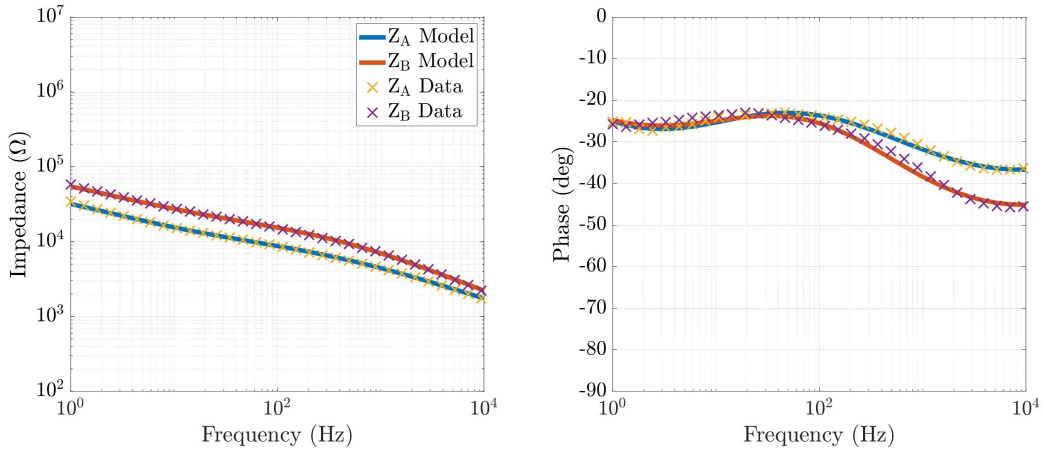

(a) Subject 1.

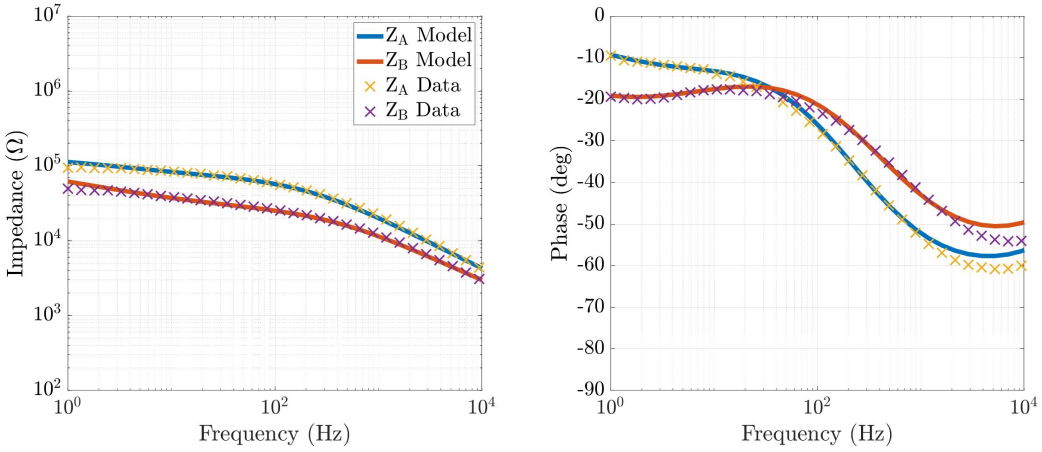

(b) Subject 2.

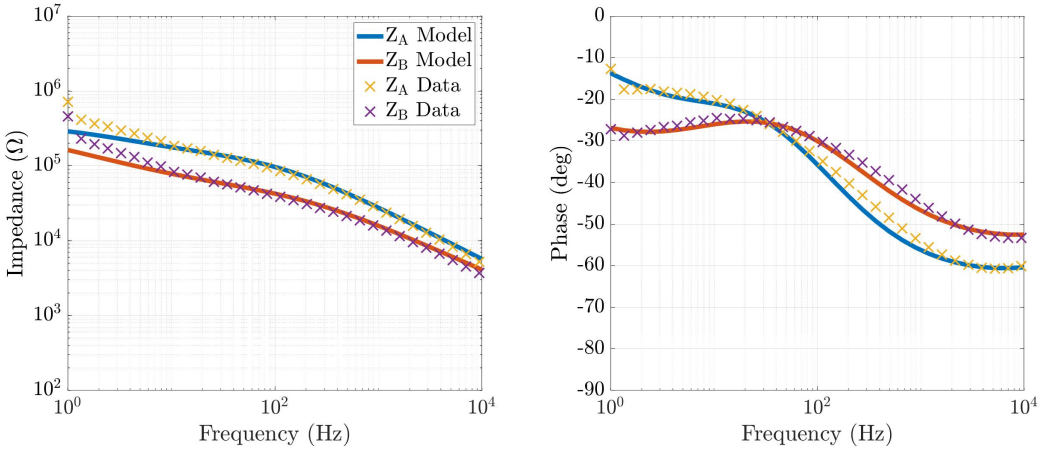

(c) Subject 3.

Figure E.3: Electrode-skin impedance model fit for 10 healthy subjects using Ag_{-SP} electrodes.

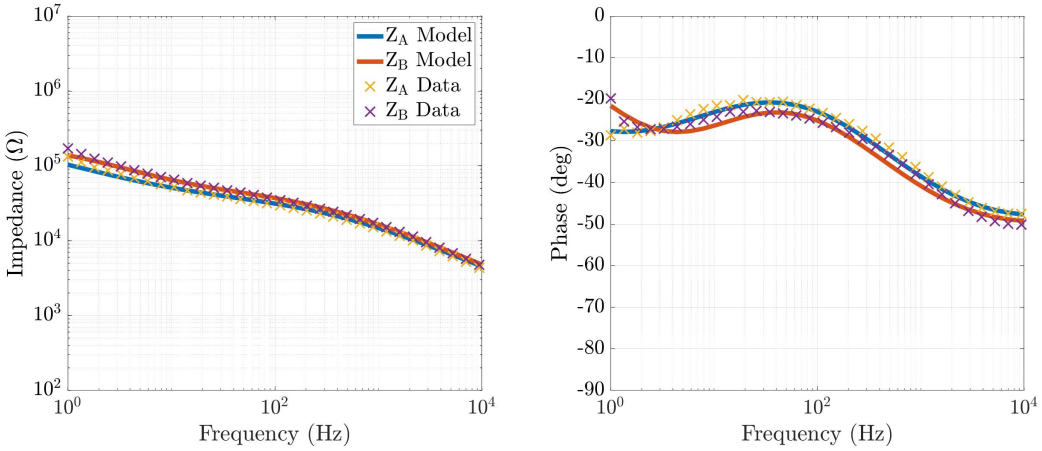

(d) Subject 4.

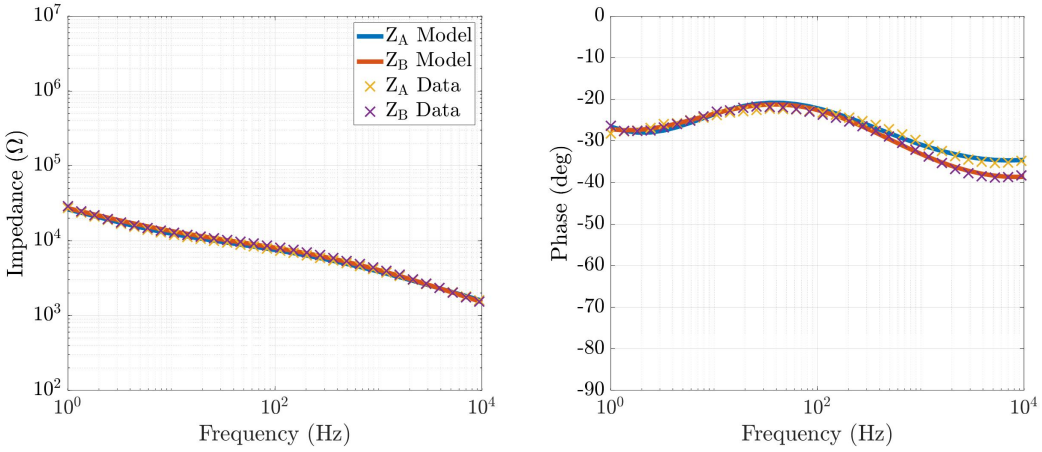

(e) Subject 5.

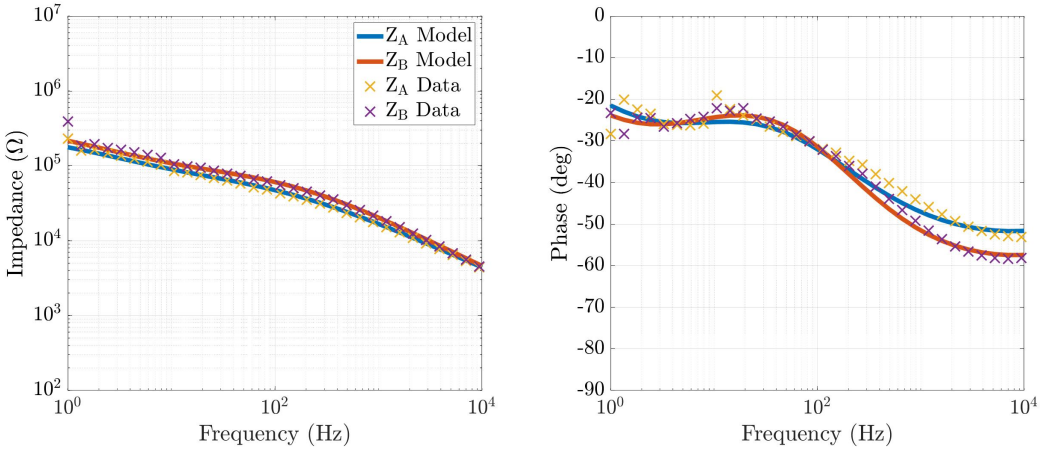

(f) Subject 6.

Figure E.3: Electrode-skin impedance model fit for 10 healthy subjects using Ag_{-SP} electrodes (cont.).

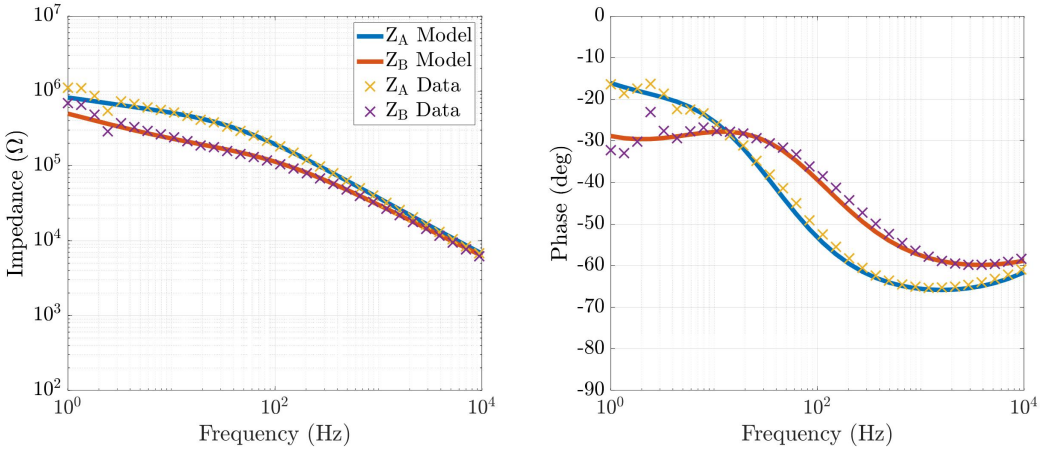

(g) Subject 7.

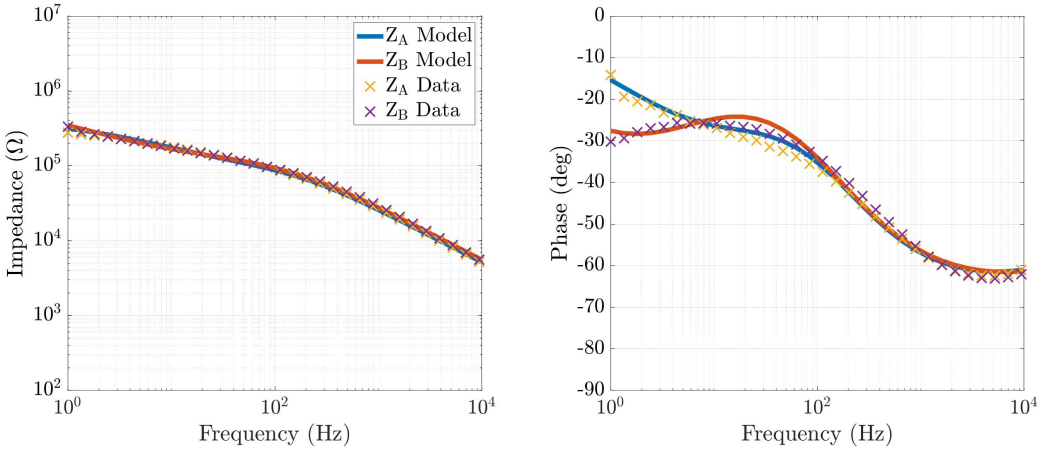

(h) Subject 8.

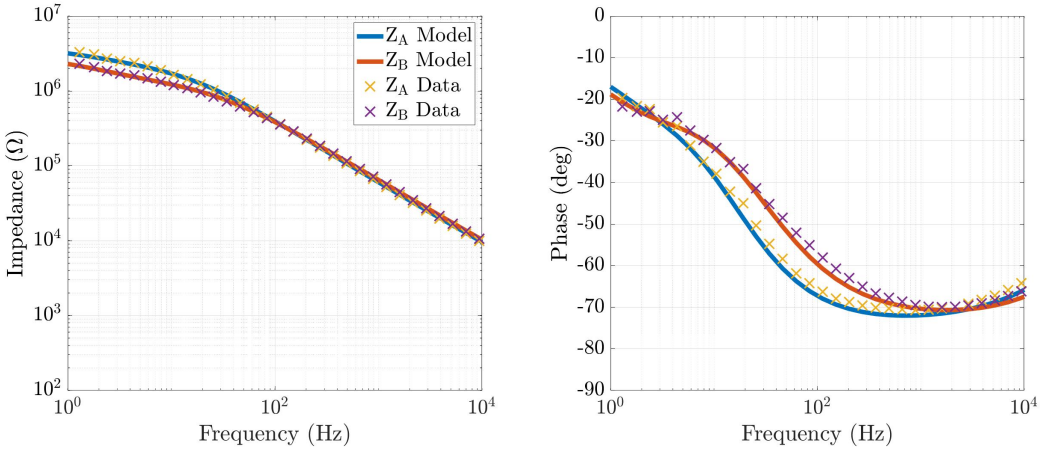

(i) Subject 9.

Figure E.3: Electrode-skin impedance model fit for 10 healthy subjects using Ag_{-SP} electrodes (cont.).

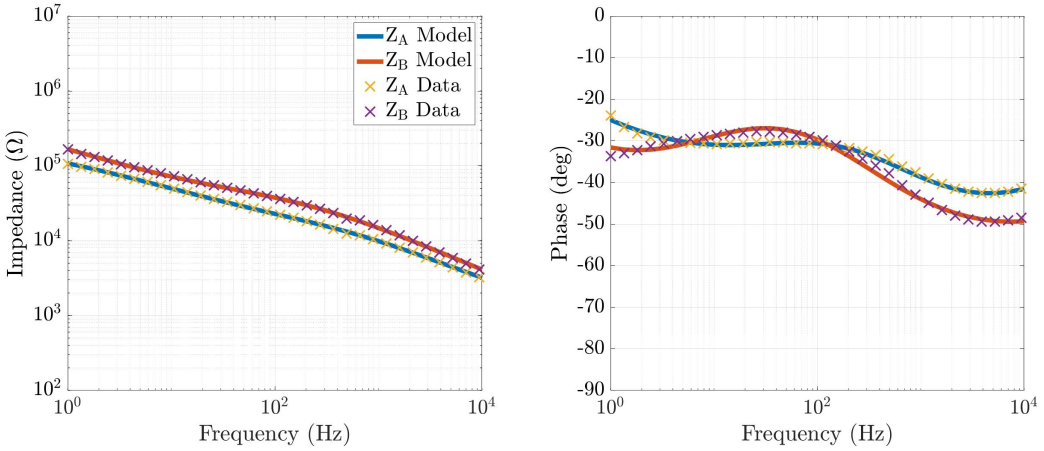

(j) Subject 10.

Figure E.3: Electrode-skin impedance model fit for 10 healthy subjects using Ag_{SP} electrodes (cont.).

APPENDIX F

Impedance Compensatory System Schematics

The circuit schematics for the impedance compensatory system are provided. Figure F.1 outlines the ADC circuitry schematic, Figure F.2 shows the schematic of the power distribution, Figure F.3 presents the schematic of the circuitry which generates the sinusoidal excitation voltage, Figure F.4 outlines the impedance measurement circuitry schematic, Figure F.5 presents the schematic for the microcontroller, Figure F.6 outlines the analogue circuitry of the bipolar sEMG device, Figure F.7 shows the analogue circuitry of the tripolar sEMG device, Figure F.8 outlines the compensatory circuitry schematic for electrode A, and Figure F.9 presents the compensatory circuitry schematic for electrode B and electrode C.

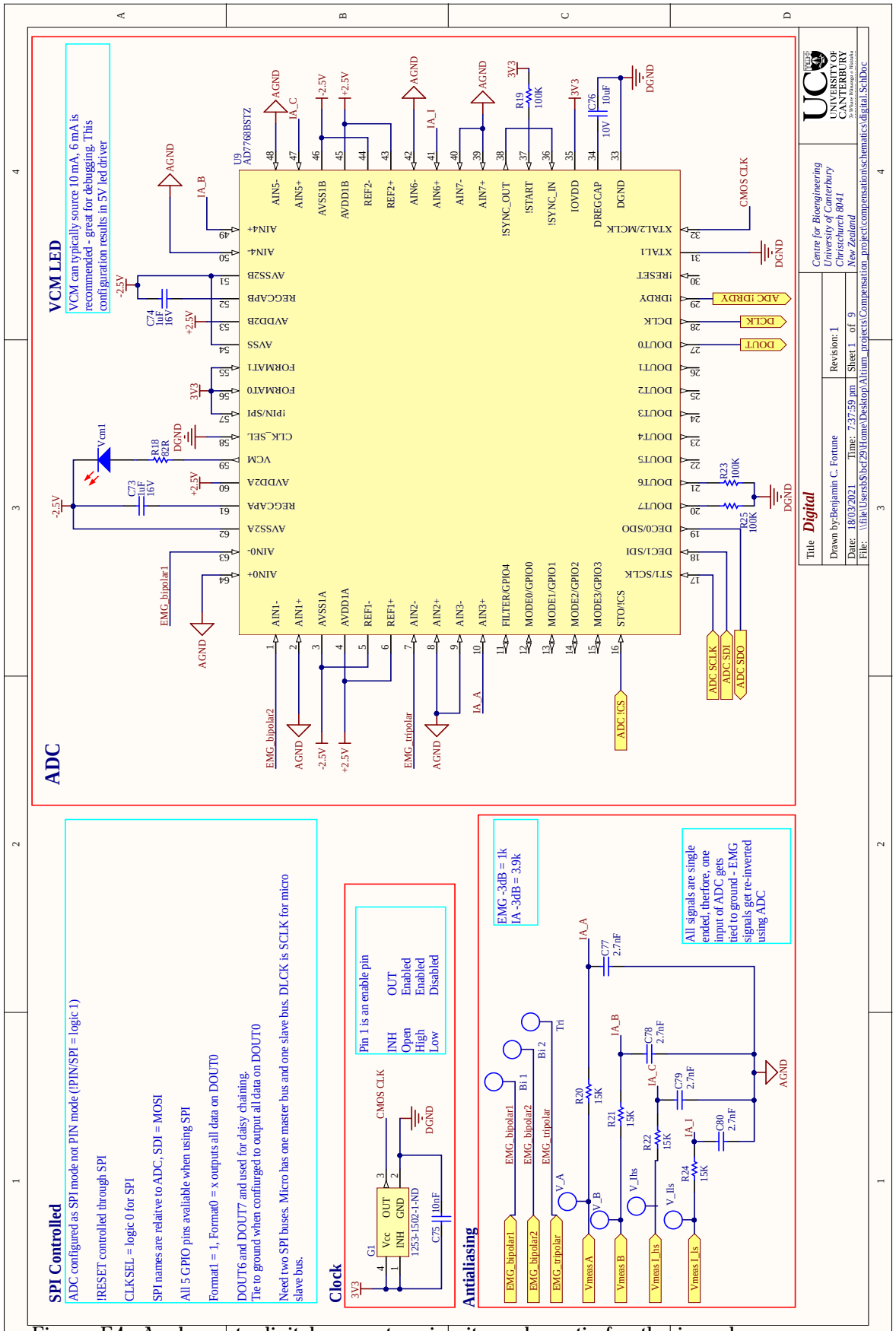

Figure F.1: Analogue-to-digital converter circuitry schematic for the impedance compensatory system.

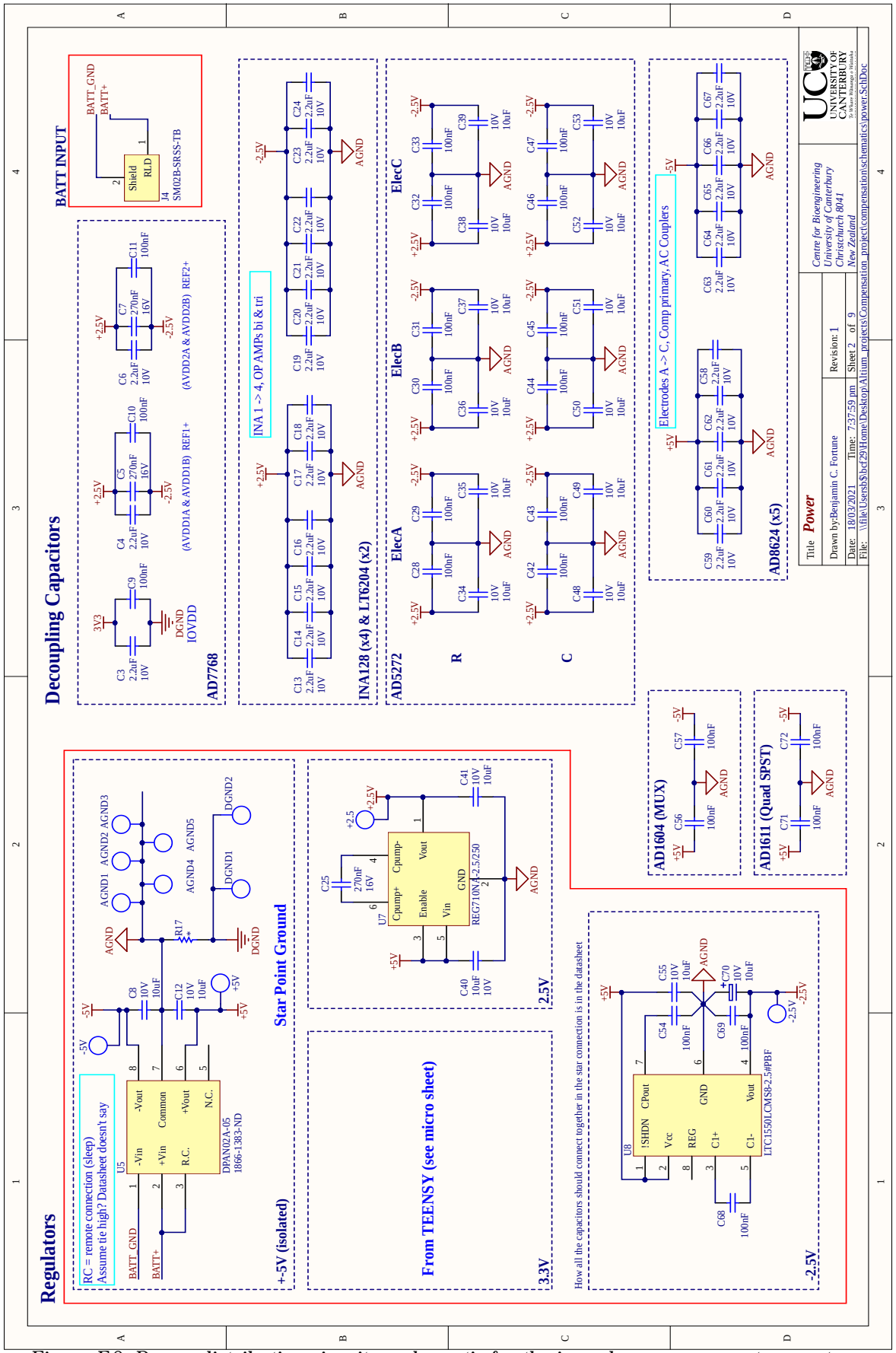

Figure F.2: Power distribution circuitry schematic for the impedance compensatory system.

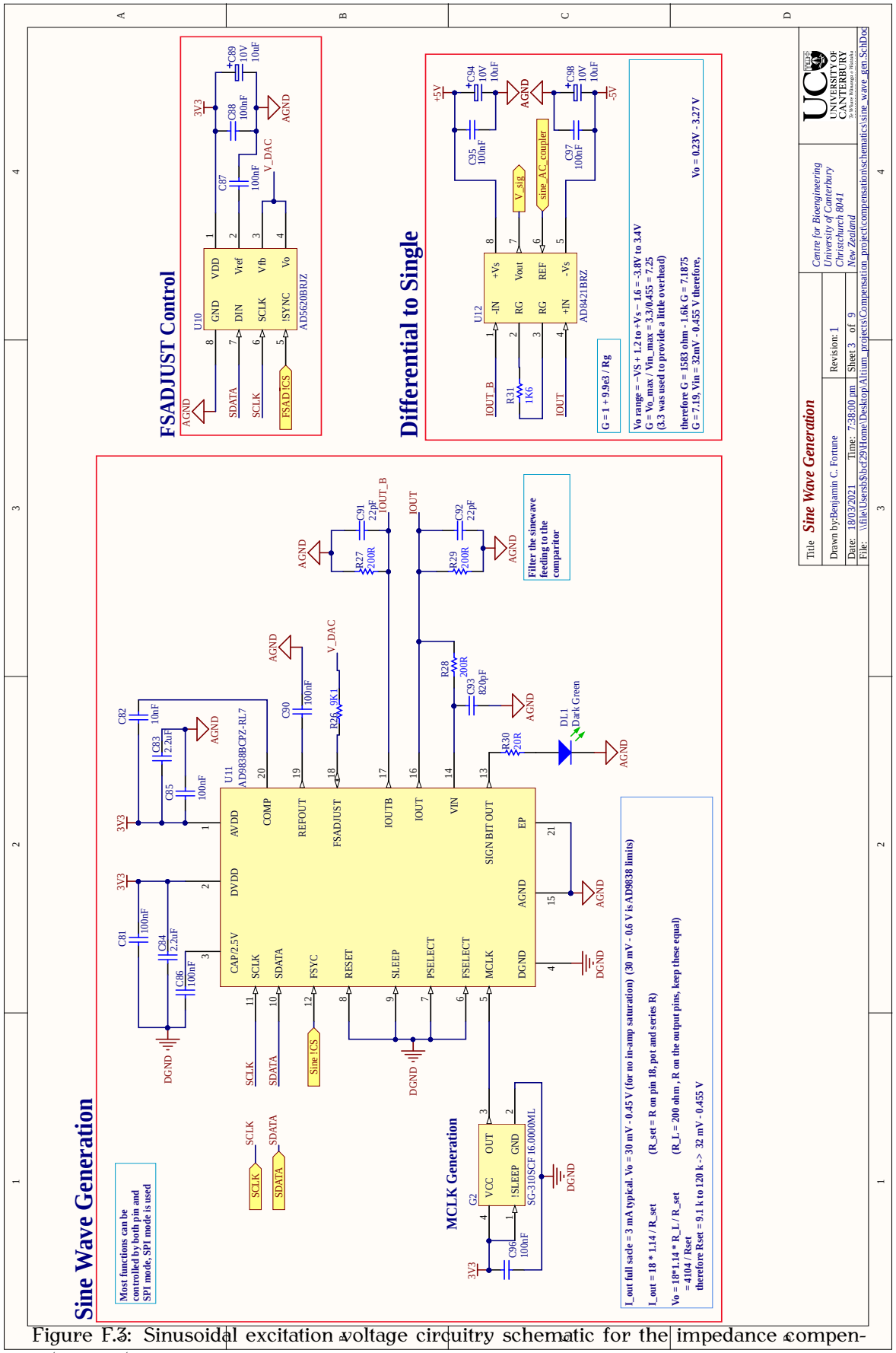

Figure F.3: Sinusoidal excitation voltage circuitry schematic for the impedance compensatory system.

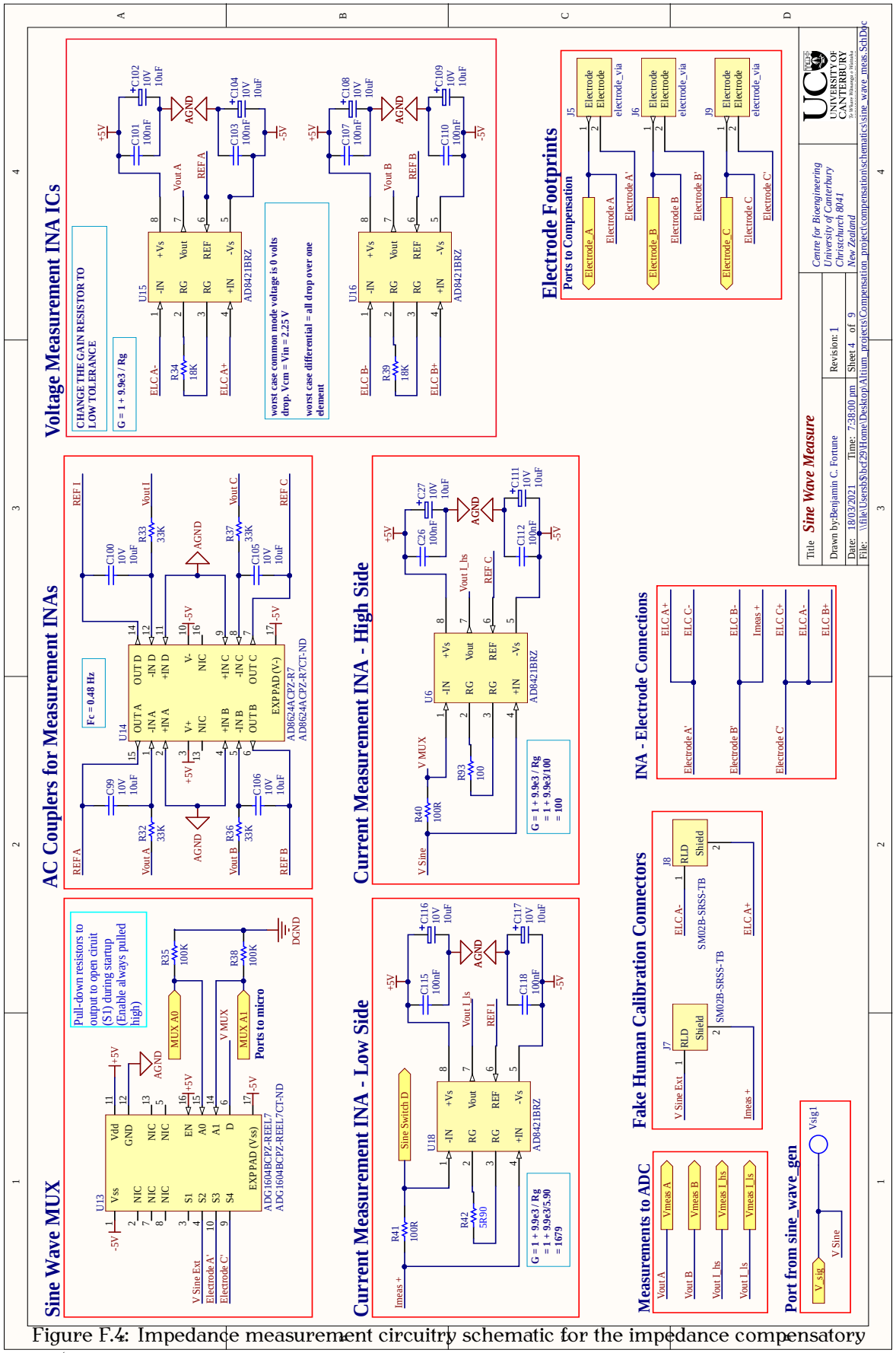

Figure F.4: Impedance measurement circuitry schematic for the impedance compensatory system.

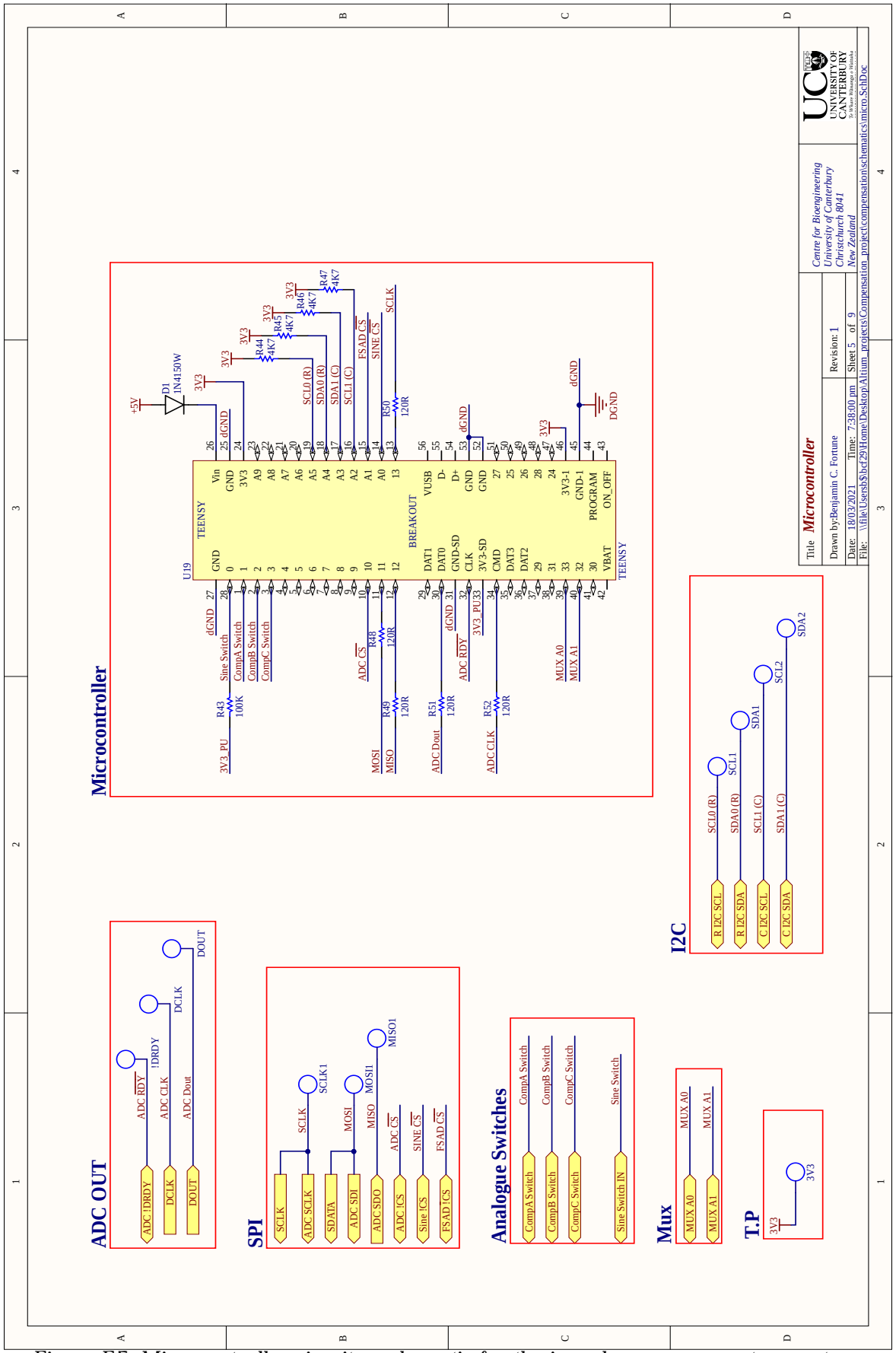

Figure F.5: Microcontroller circuitry schematic for the impedance compensatory system.

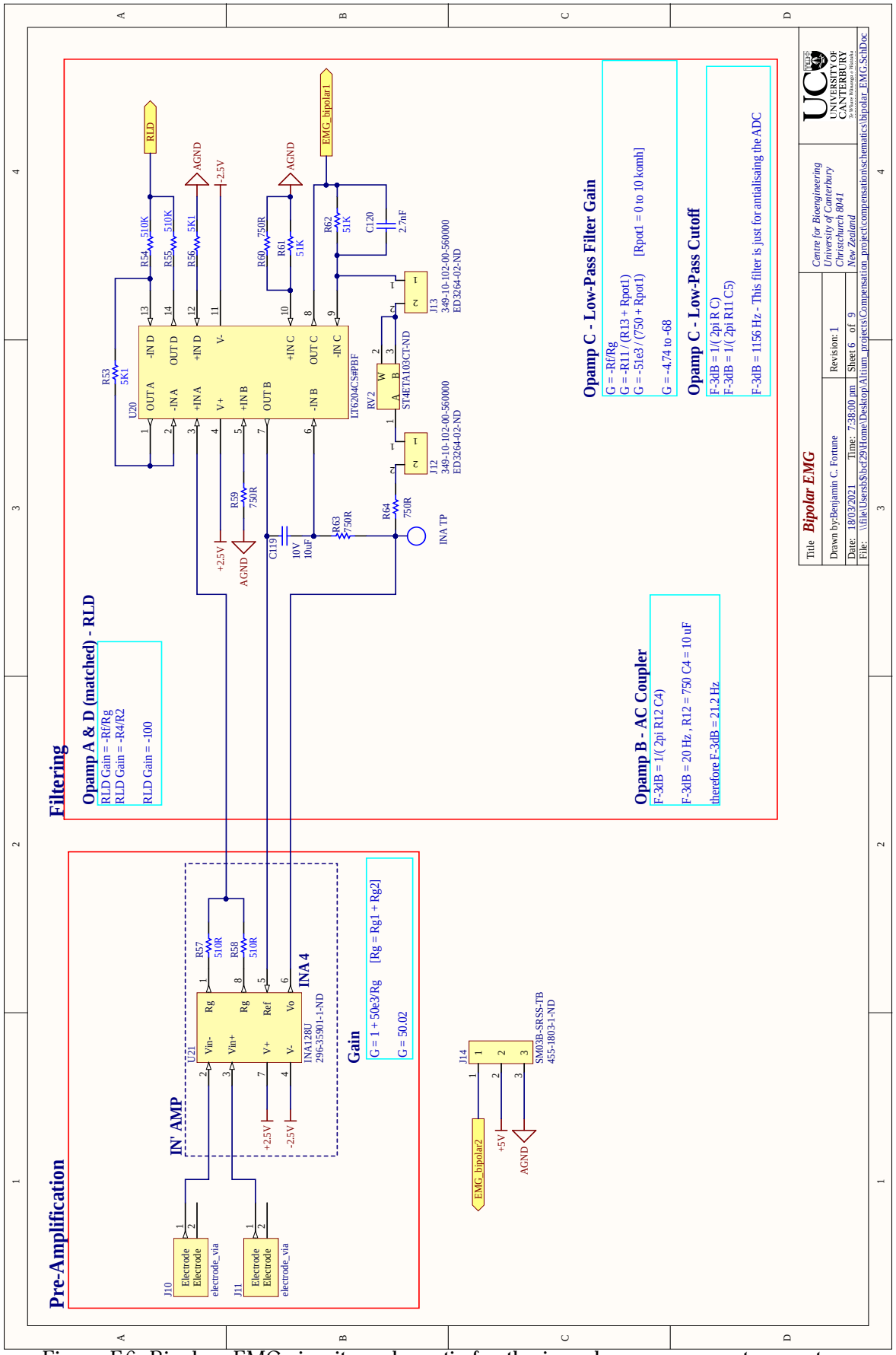

Figure F.6: Bipolar sEMG circuitry schematic for the impedance compensatory system.

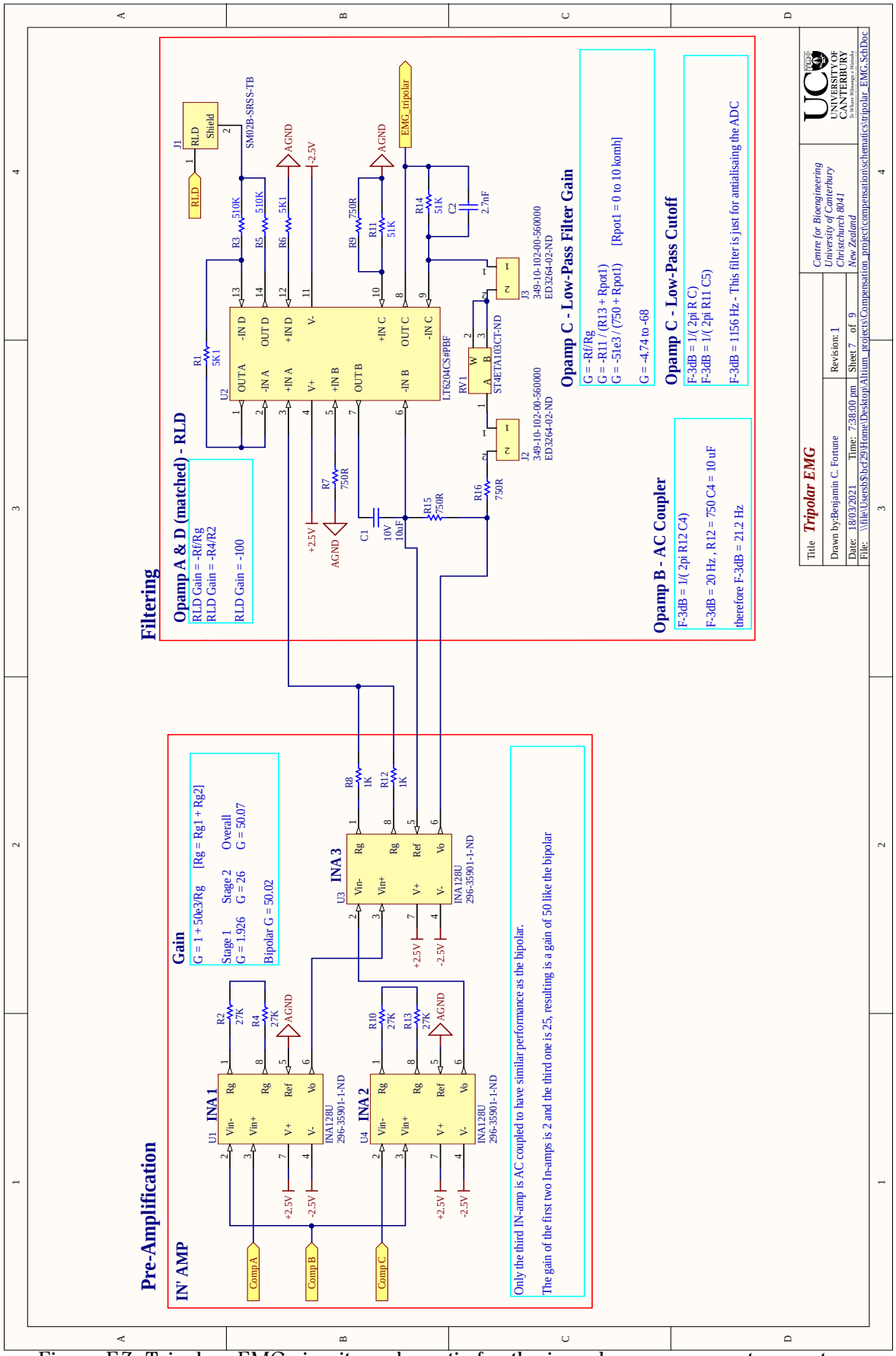

Figure F.7: Tripolar sEMG circuitry schematic for the impedance compensatory system.

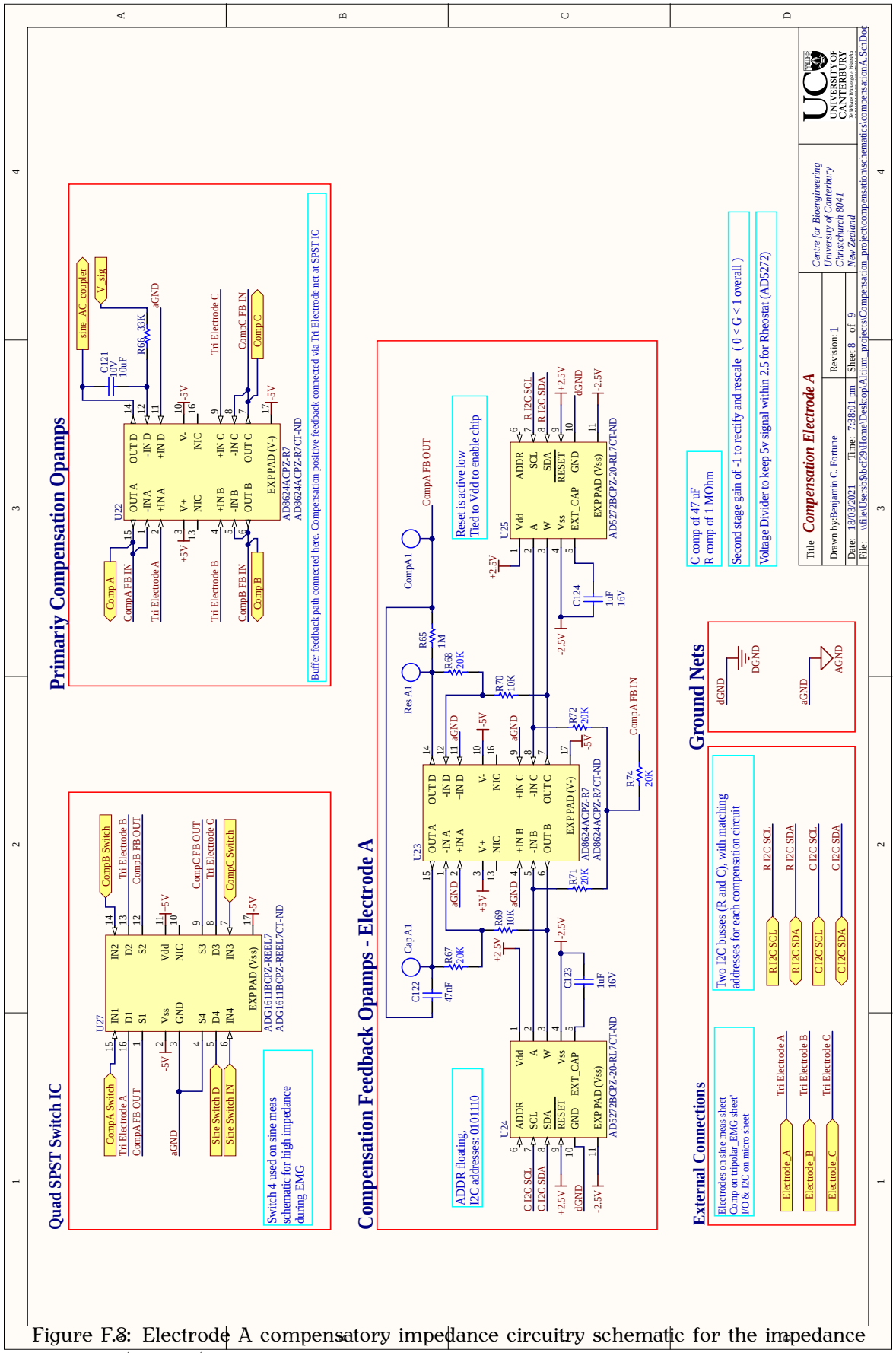

Figure F.8: Electrode A compensatory impedance circuitry schematic for the impedance compensatory system.

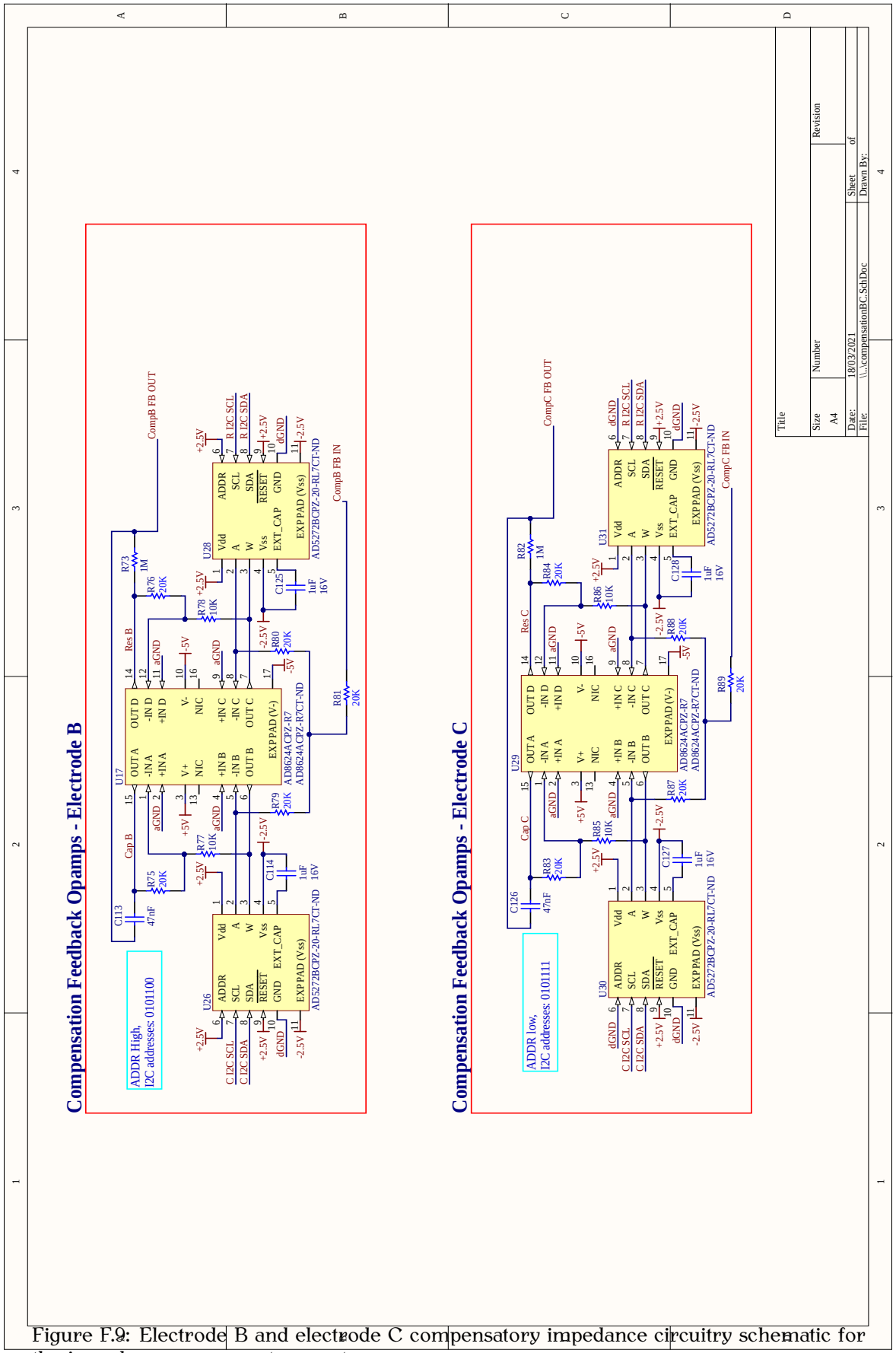

Figure F.9: Electrode B and electrode C compensatory impedance circuitry schematic for the impedance compensatory system.

APPENDIX G

Electrical Interference Pre- and Post-compensation

The accuracy of the resistive-capacitive model fit for the ten subjects over the three electrode-skin interfaces is outlined in Table G.1.

The error between the measured compensatory impedance and the modelled electrode-skin interface for the ten subjects using electrode A and electrode C is outlined in Table G.2.

The imbalance between the three simulated transfer functions for the ten subjects is outlined in Table G.3.

The error between the transfer function formed using the measured electrode-skin impedance data and the simulated compensatory impedance data, and the transfer function formed using the measured electrode-skin impedance data and the measured compensatory impedance data for the ten subjects using electrode A and electrode C is outlined in Table G.4.

Table G.1: The RMSE of the resistive-capacitive model fit for the ten subjects over the three electrode-skin interfaces.

Mains frequency (50 Hz)

Electrodes	**A**		**B**		**C**	
Subject	$\|Z\|$ (%)	ϕ (%)	$\|Z\|$ (%)	ϕ (%)	$\|Z\|$ (%)	ϕ (%)
1	9.7	7.6	14.9	11.3	9.3	13.8
2	13.4	0.6	9.6	0.6	10.4	1.0
3	16.9	1.0	17.9	3.8	18.7	2.0
4	9.4	7.6	10.4	1.5	9.2	10.0
5	7.3	6.4	10.3	4.1	16.2	3.2
6	6.5	2.9	9.9	0.4	6.8	5.3
7	21.0	15.8	18.6	21.4	17.5	4.6
8	16.4	1.5	12.1	4.7	15.7	2.7
9	10.1	2.5	14.1	1.4	3.0	0.7
10	7.8	5.7	14.9	3.1	0.8	0.8
MEAN (SD)	11.8 (4.8)	5.1 (4.6)	13.3 (3.3)	5.2 (6.5)	10.8 (6.2)	4.4 (4.3)

Whole range (20–500 Hz)

Electrodes	**A**		**B**		**C**	
Subject	$\|Z\|$ (%)	ϕ (%)	$\|Z\|$ (%)	ϕ (%)	$\|Z\|$ (%)	ϕ (%)
1	18.3	13.1	20.9	16.3	30.6	15.0
2	7.9	17.7	8.9	16.0	7.9	20.4
3	10.6	19.5	13.9	23.5	13.9	19.5
4	16.9	15.2	8.0	20.0	20.4	17.0
5	6.7	18.3	6.7	19.8	9.4	19.9
6	5.6	14.1	6.5	15.6	5.4	14.7
7	28.5	24.3	32.3	28.1	15.6	10.9
8	11.3	23.4	10.7	25.5	8.7	16.7
9	13.2	14.1	12.3	15.1	8.9	14.3
10	15.6	12.8	10.4	16.5	9.8	18.0
MEAN (SD)	13.5 (6.8)	17.2 (4.2)	13.1 (8.0)	19.7 (4.6)	13.0 (7.6)	16.6 (3.0)

Table G.2: The RMSE of the measured compensation impedance fit to the modelled fit for all three electrodes.

Mains frequency (50 Hz)

Electrodes	**A**		**C**	
Subject	$\|Z\|$ (%)	ϕ (%)	$\|Z\|$ (%)	ϕ (%)
1	1.7	2.0	1.3	3.3
2	1.0	0.1	4.9	9.3
3	15.8	0.7	14.6	0.3
4	6.7	0.9	11.6	0.9
5	7.5	1.4	10.9	1.5
6	6.0	0.2	7.9	16.1
7	5.6	1.3	1.8	19.8
8	11.1	2.2	7.0	2.3
9	4.7	0.3	1.8	2.9
10	3.6	0.6	4.8	8.0
MEAN (SD)	6.4 (4.4)	1.0 (0.7)	6.7 (4.6)	6.4 (6.8)

Whole range (20–500 Hz)

Electrodes	**A**		**C**	
Subject	$\|Z\|$ (%)	ϕ (%)	$\|Z\|$ (%)	ϕ (%)
1	3.6	1.5	4.8	2.3
2	2.1	0.9	4.5	6.9
3	16.1	1.4	17.1	1.4
4	7.9	0.7	14.0	2.0
5	5.8	1.7	8.4	2.0
6	5.5	0.3	5.5	12.3
7	10.6	0.8	1.3	16.5
8	12.4	1.3	8.9	2.1
9	4.9	0.6	4.2	3.2
10	3.8	0.3	5.4	7.6
MEAN (SD)	7.3 (4.5)	0.9 (0.5)	7.4 (4.9)	5.6 (5.2)

Table G.3: The imbalance between each simulated transfer function.

Whole range (20–500 Hz)

Electrodes	**A-B**		**A-C**		**B-C**	
Subject	$\|H\|$ (%)	$\phi\,(deg)$	$\|H\|$ (%)	$\phi\,(deg)$	$\|H\|$ (%)	$\phi\,(deg)$
1	6.4	1.2	12.5	1.6	13.1	1.2
2	12.3	0.5	5.0	1.2	13.4	1.1
3	6.9	1.2	6.8	0.7	9.6	1.4
4	12.8	2.6	5.1	0.5	17.0	2.7
5	3.4	0.6	13.9	0.8	10.9	0.4
6	3.5	0.7	2.6	0.8	4.0	1.1
7	4.1	1.7	17.3	5.0	20.8	6.4
8	3.3	1.0	9.3	2.6	11.4	3.4
9	5.2	0.4	6.7	0.7	9.7	0.6
10	9.8	1.7	9.5	2.2	8.9	0.6
MEAN (SD)	6.8 (3.7)	1.1 (0.7)	8.9 (4.6)	1.6 (1.4)	11.9 (4.6)	1.9 (1.8)

Table G.4: The RMSE between simulated and measured transfer functions, electrode A and C.

Whole range (20–500 Hz)				
Electrodes	**A**		**C**	
Subject	$\|H\|$ (%)	$\phi\,(deg)$	$\|H\|$ (%)	$\phi\,(deg)$
1	3.5	0.5	5.7	0.8
2	2.8	0.3	8.7	2.2
3	30.8	0.4	28.7	0.3
4	12.0	0.2	20.2	0.6
5	10.0	0.4	14.4	0.4
6	10.1	0.2	13.1	3.6
7	14.9	0.4	3.9	4.9
8	22.0	0.4	14.5	0.6
9	8.4	0.2	5.4	1.1
10	5.3	0.1	7.6	2.5
MEAN (SD)	12.0 (8.7)	0.3 (0.1)	12.2 (7.7)	1.7 (1.6)

The magnitude of electrical interference at the five frequencies of interest, 50 Hz, 100 Hz, 200 Hz, 300 Hz and 400 Hz, for the ten subjects during the resting period, for pre- and post-compensated bioelectrical signals are outlined in Tables G.5 and G.6, respectively.

Table G.5: Electrical interference pre-compensation at the 5 frequencies of interest

Pre-compensation					
Frequency (Hz)	50	100	200	300	400
Subject	$\|H\|\,(\mu V)$	$\|H\|\,(\mu V)$	$\|H\|\,(\mu V)$	$\|H\|\,(\mu V)$	$\|H\|\,(\mu V)$
1	37.5	171.0	279.6	107.2	156.2
2	12.9	129.7	158.7	45.5	71.7
3	124.9	278.7	335.0	104.5	137.2
4	73.4	135.9	261.7	123.1	105.0
5	15.1	44.7	51.0	40.6	31.6
6	15.4	51.1	61.1	45.9	37.1
7	63.0	218.8	265.2	182.7	155.9
8	132.8	41.7	122.9	46.8	53.7
9	140.5	71.3	220.3	91.2	103.8
10	50.5	43.5	57.5	22.0	21.7
MEAN (SD)	66.6 (50.1)	118.6 (83.4)	181.3 (104.9)	81.0 (49.7)	87.4 (51.4)

Table G.6: Electrical interference post-compensation at the 5 frequencies of interest

Post-compensation					
Frequency (Hz)	50	100	200	300	400
Subject	$\|H\|\,(\mu V)$	$\|H\|\,(\mu V)$	$\|H\|\,(\mu V)$	$\|H\|\,(\mu V)$	$\|H\|\,(\mu V)$
1	3.2	18.9	34.6	13.5	19.1
2	5.0	7.3	21.5	9.1	12.8
3	8.8	13.2	28.0	14.4	22.6
4	29.1	17.9	8.3	5.4	8.1
5	7.9	22.9	24.5	18.3	14.2
6	6.3	14.1	18.2	14.1	10.7
7	37.9	28.0	57.0	23.6	11.0
8	241.6	52.0	142.3	54.4	54.5
9	76.1	12.9	28.7	10.4	10.9
10	39.0	16.2	22.3	9.1	9.2
MEAN (SD)	45.5 (72.6)	20.3 (12.5)	38.5 (38.6)	17.2 (14.1)	17.3 (13.8)

APPENDIX H

Crosstalk Contamination Pre- and Post-compensation

The integration results for the bioelectrical signals recorded from the three sEMG devices during triceps brachii contractions from the ten subjects, pre- and post-compensation are outlined in Table H.1 and H.2, respectively.

Table H.1: Integration results of the three EMG devices for pre-compensation

Pre-compensation			
Subject	$\text{Bicep}_{SD}(\mu V)$	$\text{Tricep}_{SD}(\mu V)$	$\text{Tricep}_{DD}(\mu V)$
1	136	386	432
2	101	348	415
3	228	1,468	1,062
4	304	511	666
5	65	646	136
6	99	691	243
7	137	286	565
8	126	248	469
9	105	505	339
10	74	1,428	148
MEAN (SD)	138 (74)	652 (443)	447 (275)

Table H.2: Integration results of the three EMG devices for post-compensation

Post-compensation			
Subject	$\text{Bicep}_{SD}(\mu V)$	$\text{Tricep}_{SD}(\mu V)$	$\text{Tricep}_{DD}(\mu V)$
1	140	413	285
2	98	430	837
3	182	1,434	464
4	168	425	278
5	60	644	165
6	96	675	644
7	132	315	452
8	109	275	376
9	102	498	234
10	73	1,524	182
MEAN (SD)	116 (39)	663 (448)	392 (215)

APPENDIX I

Electrode-Skin Impedance Imbalance Measured in the Frequency Domain

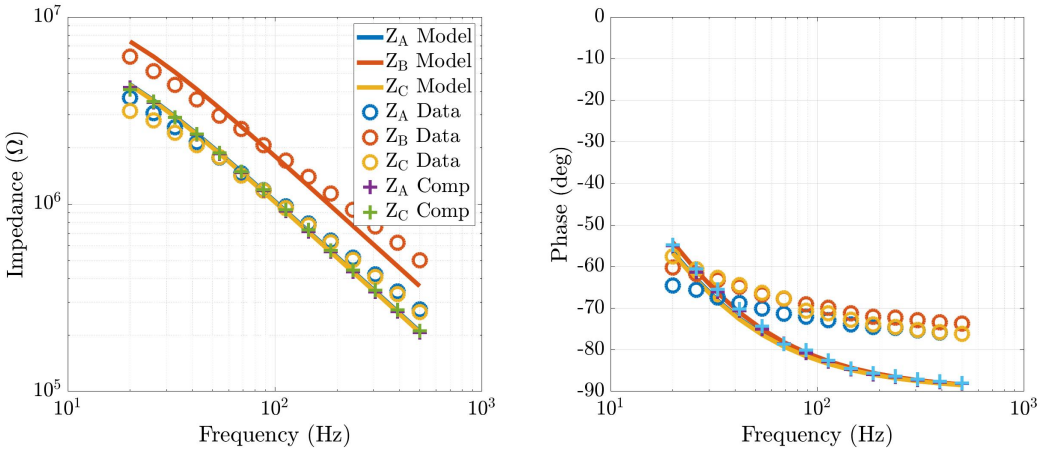

(a) Subject 1.

Figure I.1: Electrode-skin impedance, simulated compensatory impedance and measured compensatory impedance for all 10 subjects.

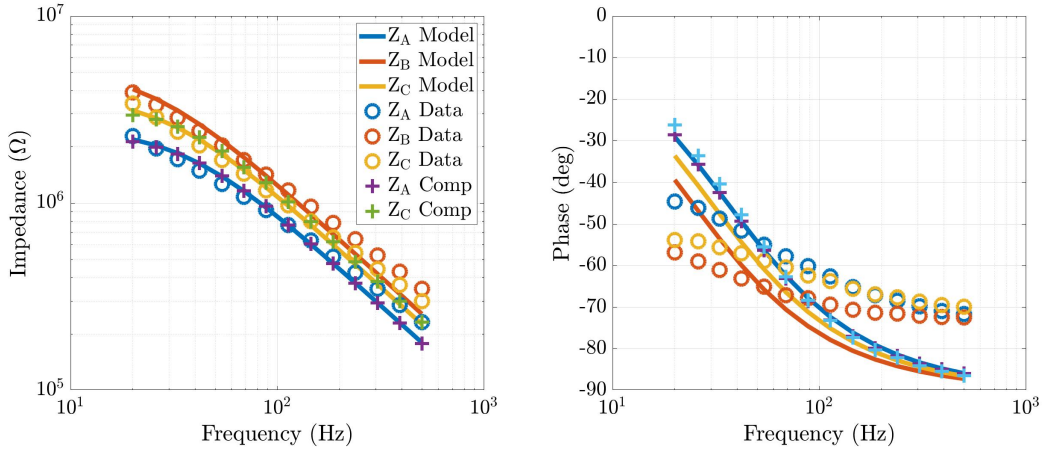

(b) Subject 2.

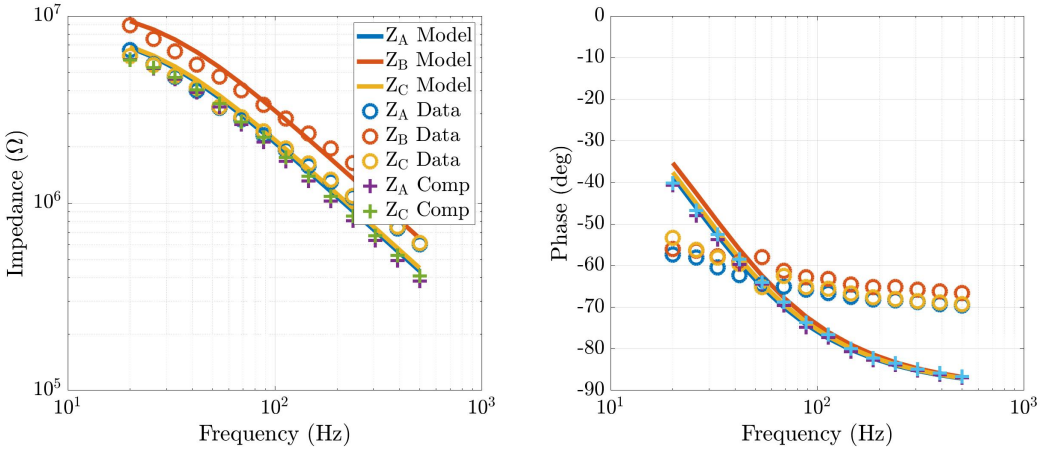

(c) Subject 3.

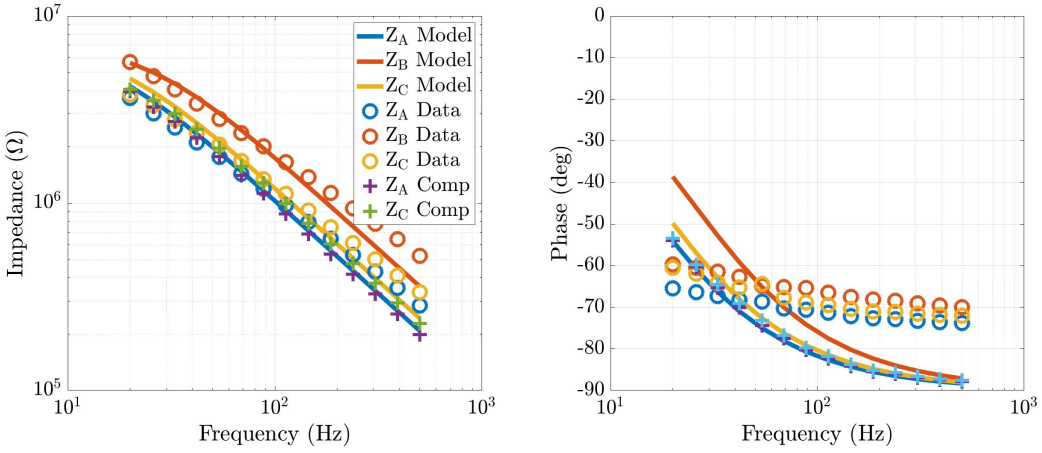

(d) Subject 4.

Figure I.1: Electrode-skin impedance, simulated compensatory impedance and measured compensatory impedance for all 10 subjects. (cont.).

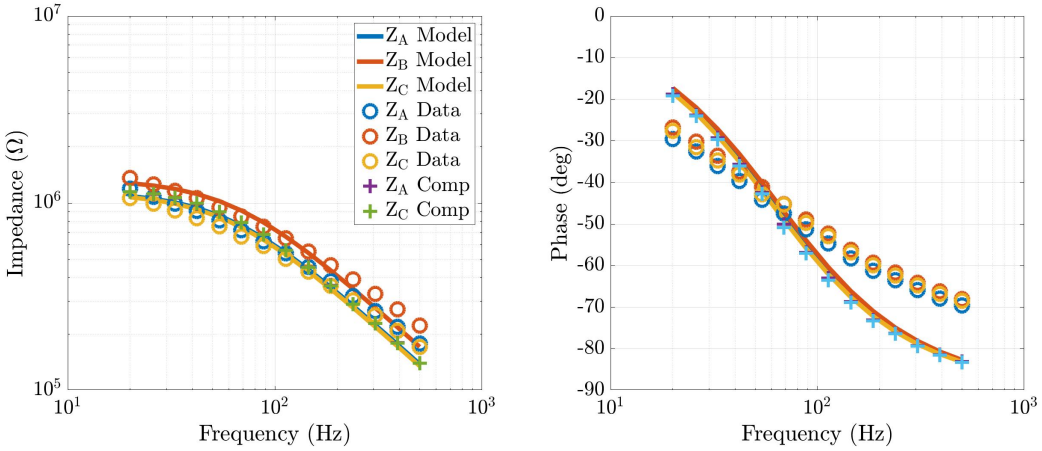

(e) Subject 5.

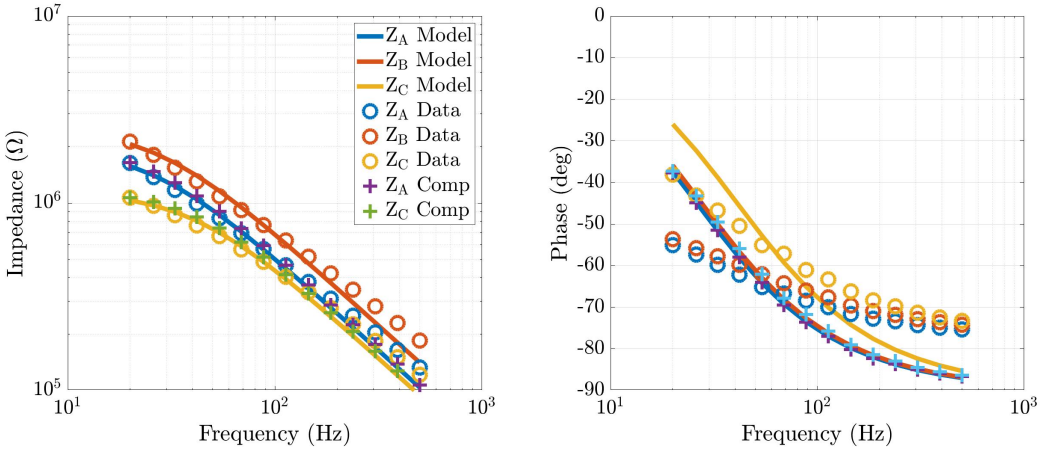

(f) Subject 6.

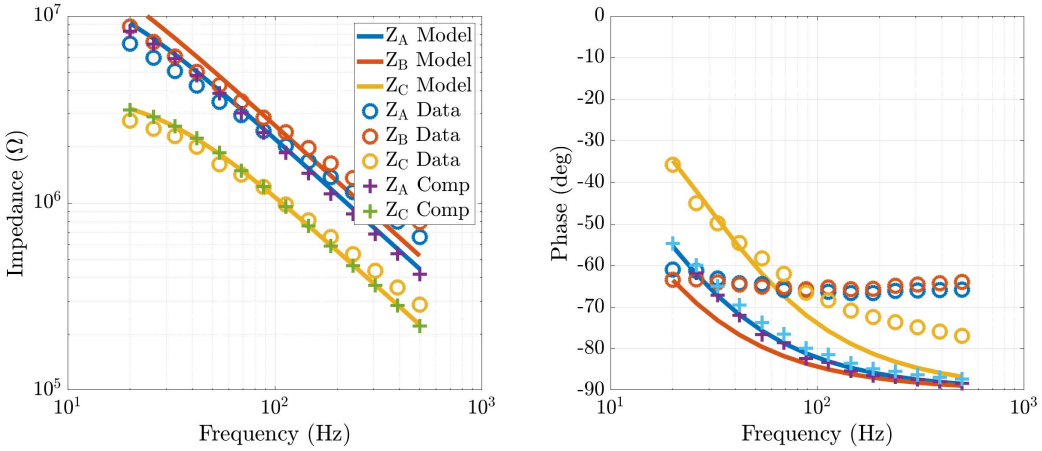

(g) Subject 7.

Figure I.1: Electrode-skin impedance, simulated compensatory impedance and measured compensatory impedance for all 10 subjects. (cont.).

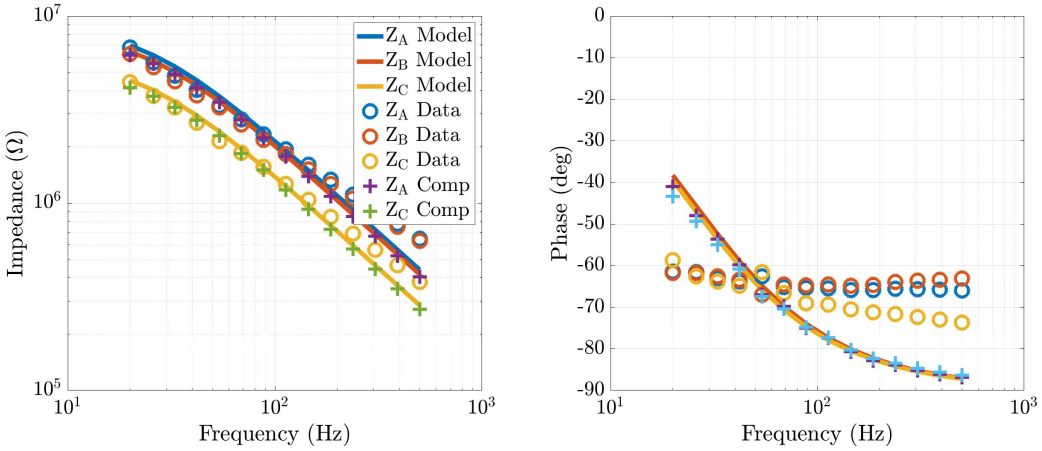

(h) Subject 8.

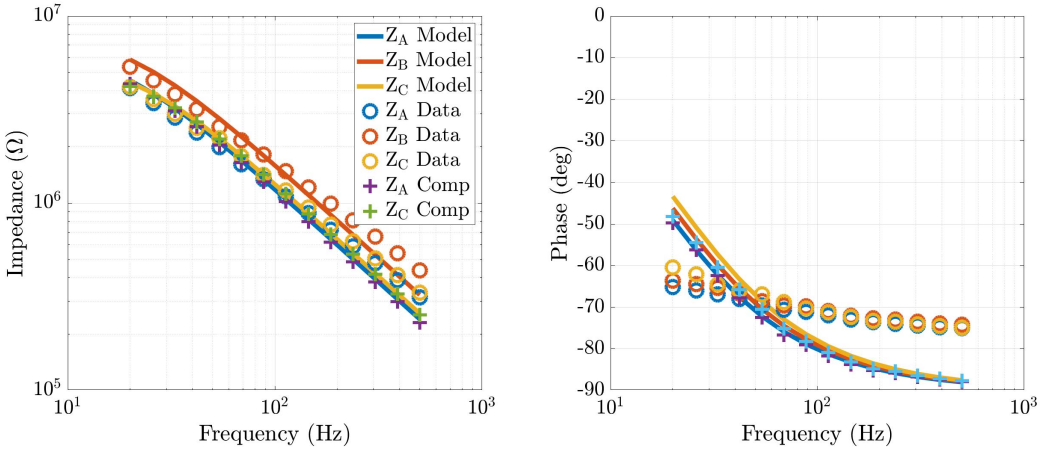

(i) Subject 9.

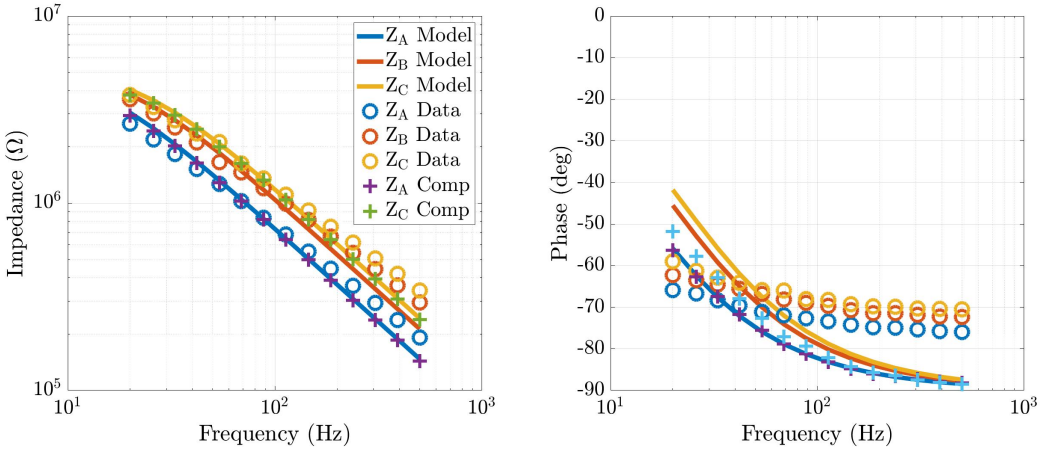

(j) Subject 10.

Figure I.1: Electrode-skin impedance, simulated compensatory impedance and measured compensatory impedance for all 10 subjects.. (cont.).

APPENDIX J

Electrode-skin Impedance Compensation Transfer Function

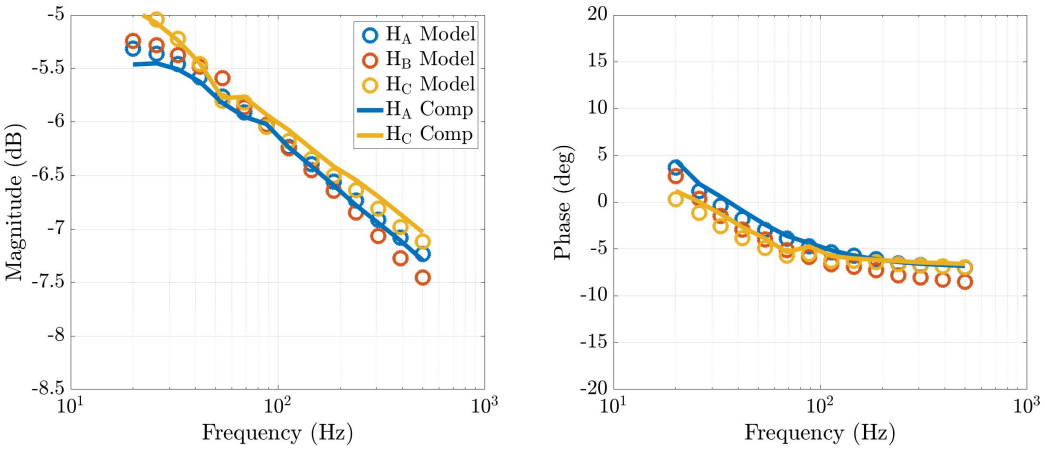

(a) Subject 1.

Figure J.1: Simulated and measured transfer functions for all 10 subjects.

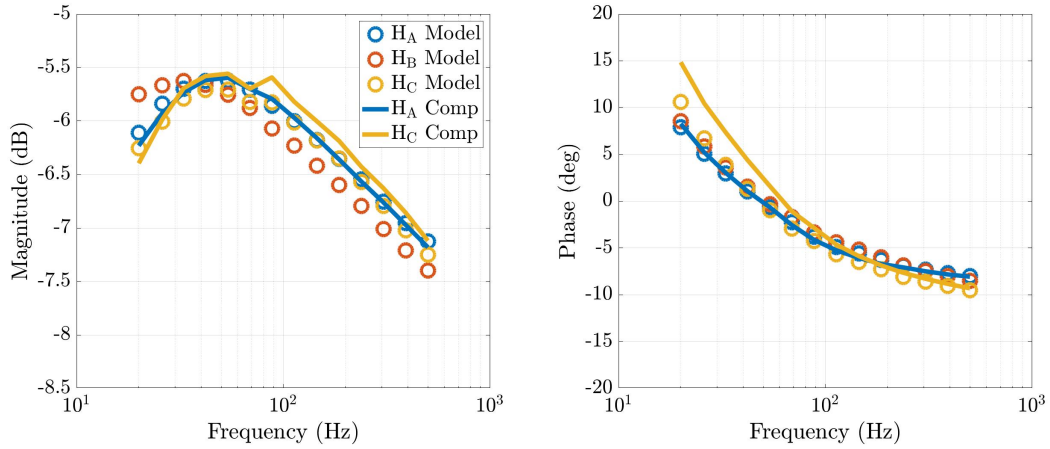

(b) Subject 2.

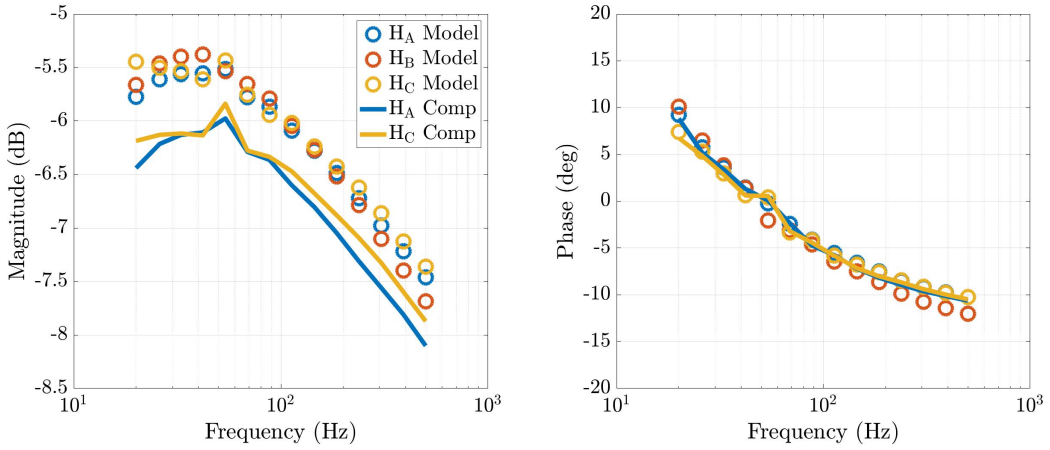

(c) Subject 3.

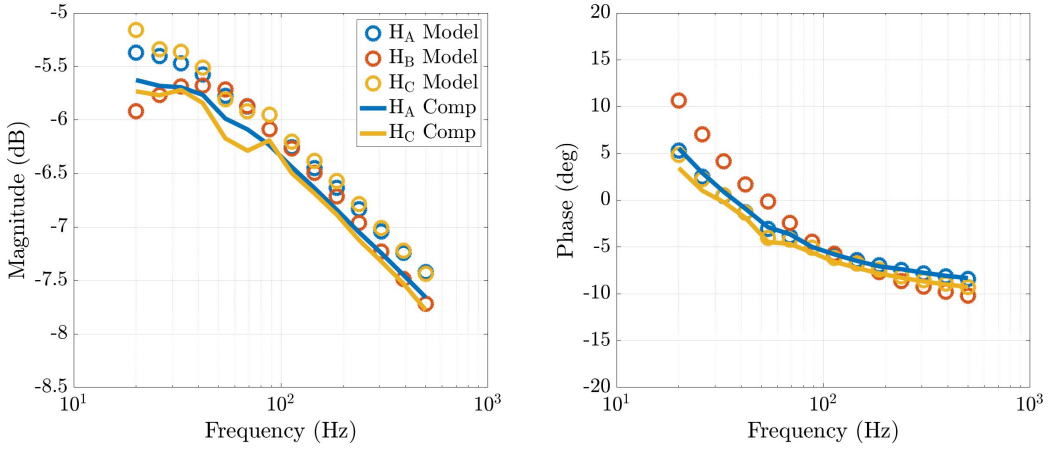

(d) Subject 4.

Figure J.1: Simulated and measured transfer functions for all 10 subjects. (cont.).

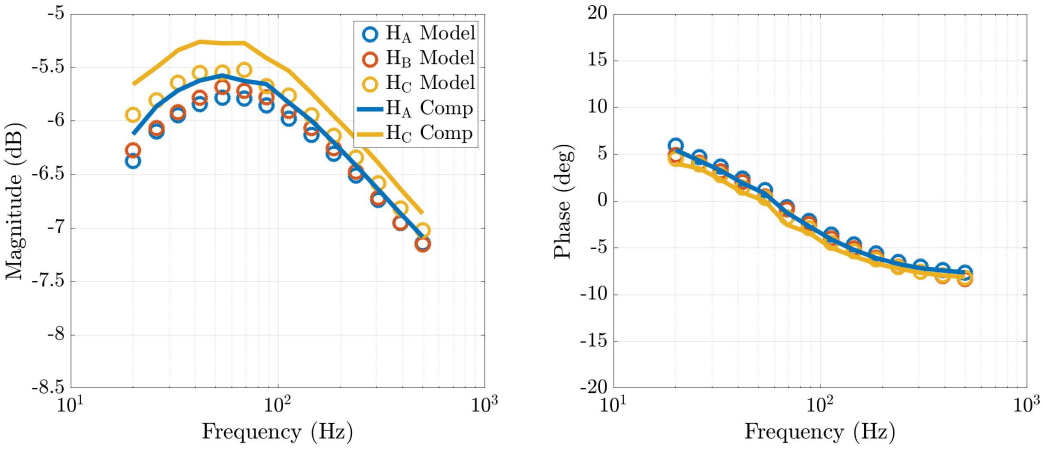

(e) Subject 5.

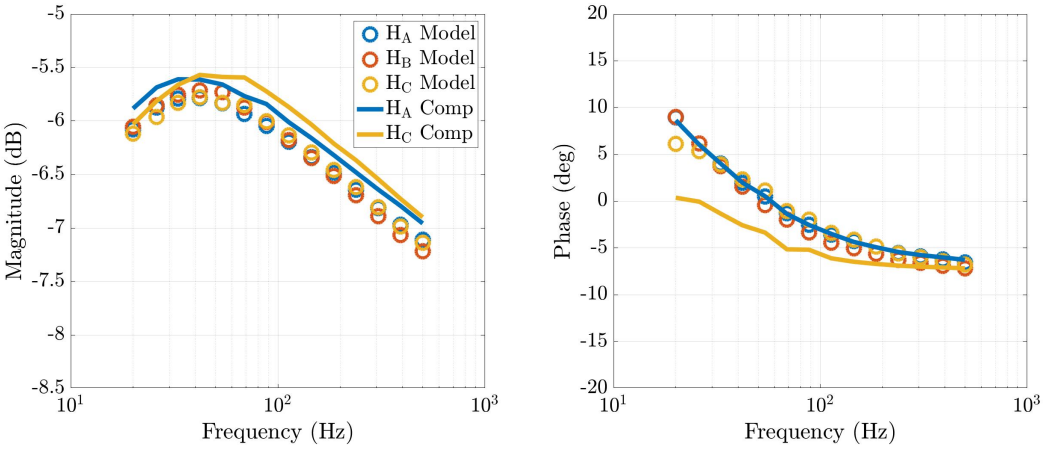

(f) Subject 6.

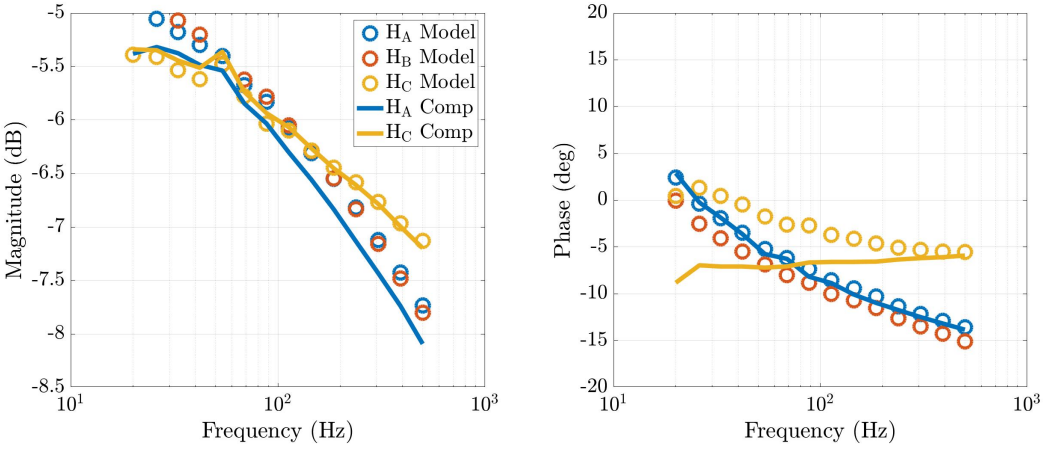

(g) Subject 7.

Figure J.1: Simulated and measured transfer functions for all 10 subjects. (cont.).

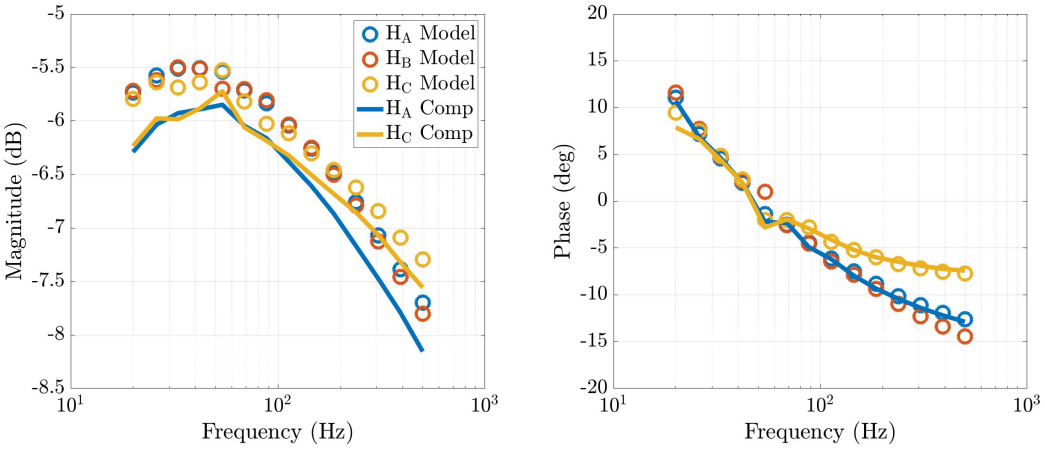

(h) Subject 8.

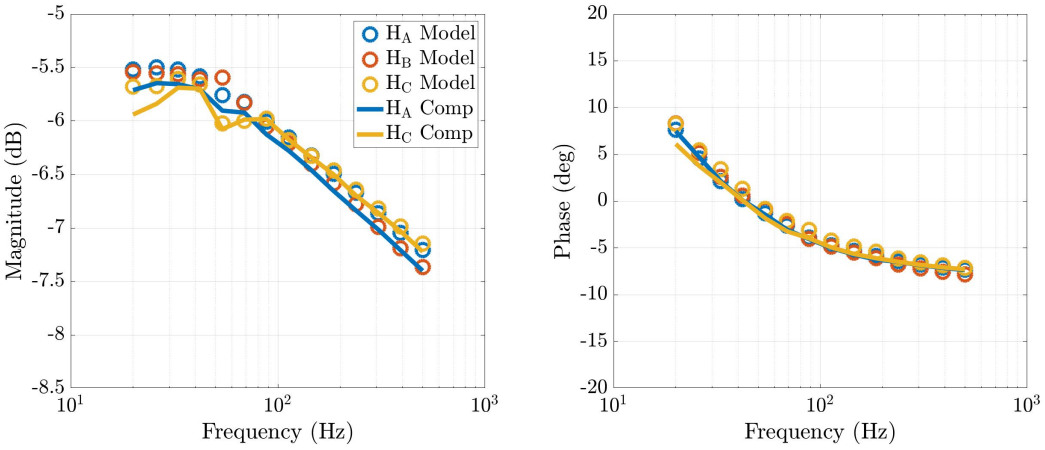

(i) Subject 9.

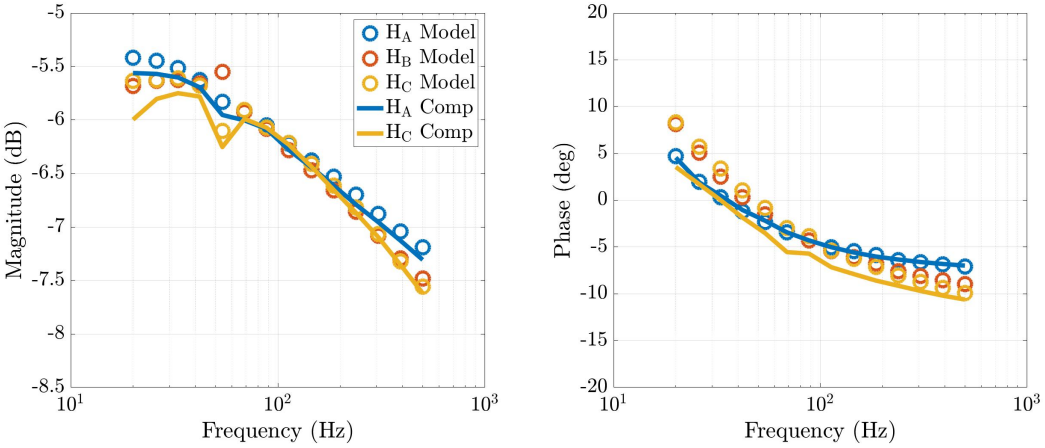

(j) Subject 10.

Figure J.1: Simulated and measured transfer functions for all 10 subjects. (cont.).

APPENDIX K

Electrical Interference Reduction due to Electrode-skin Impedance Compensation

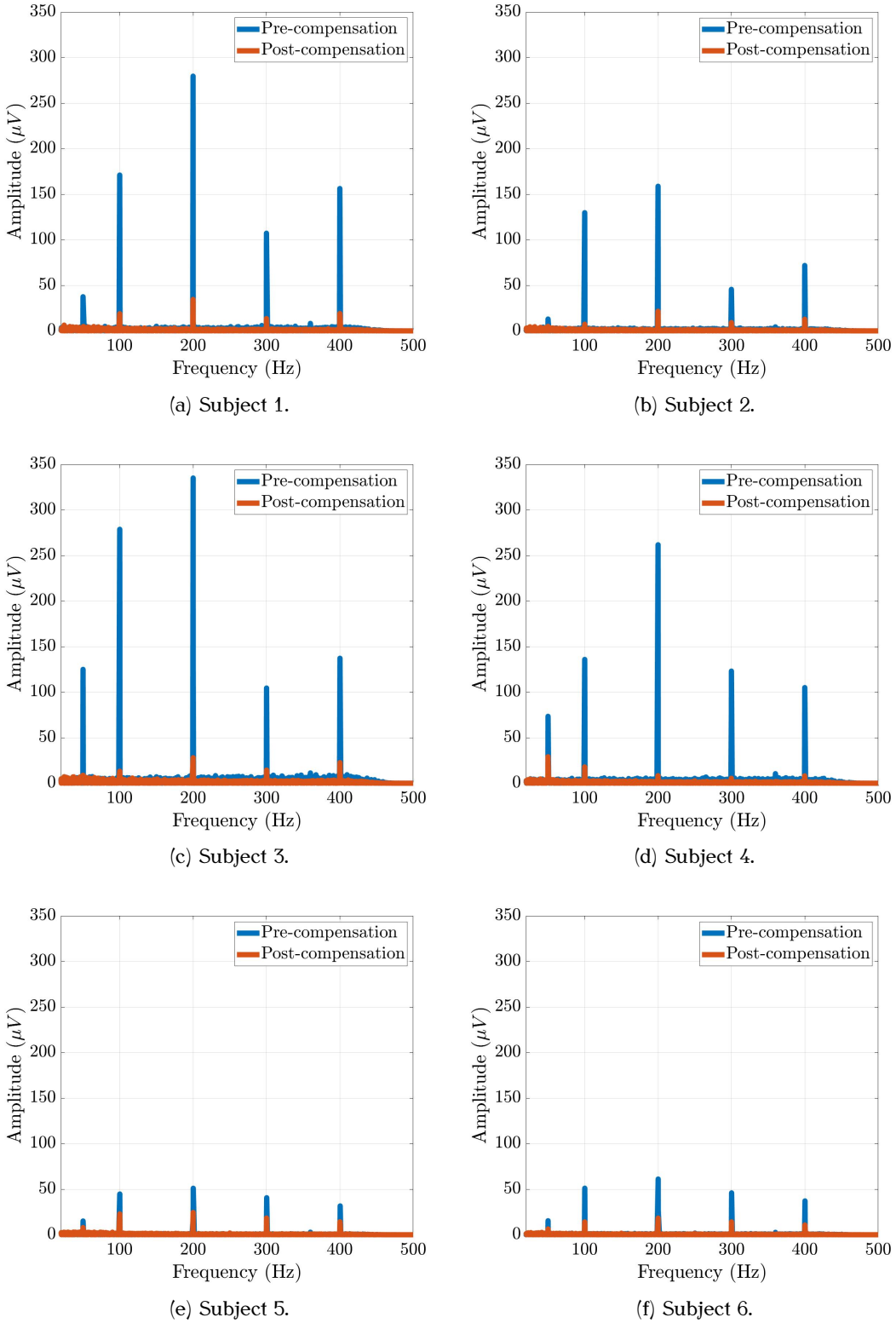

(a) Subject 1.

(b) Subject 2.

(c) Subject 3.

(d) Subject 4.

(e) Subject 5.

(f) Subject 6.

Figure K.1: FFT for pre- and post-compensated bioelectrical signals for all 10 subjects.

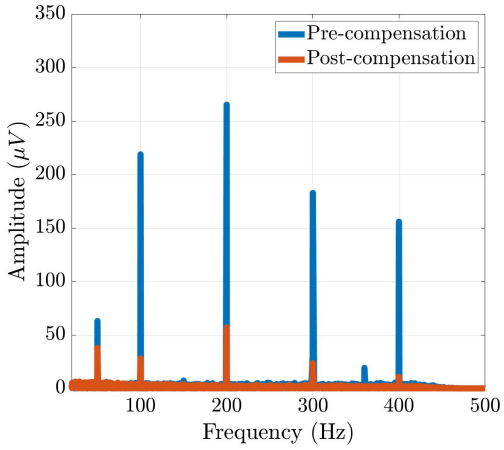

(g) Subject 7.

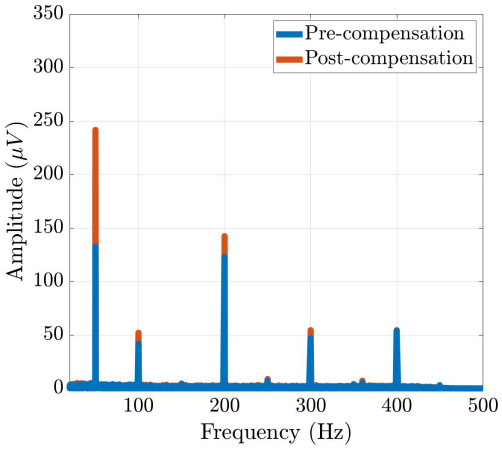

(h) Subject 8.

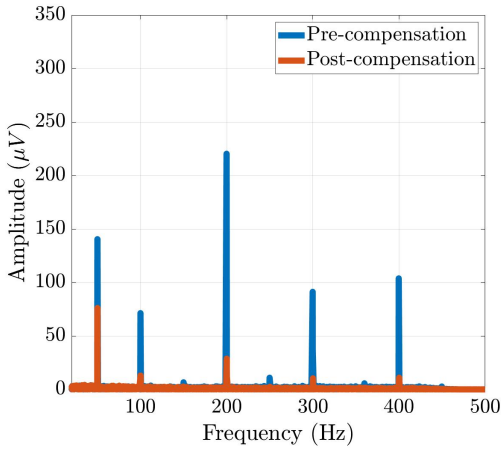

(i) Subject 9.

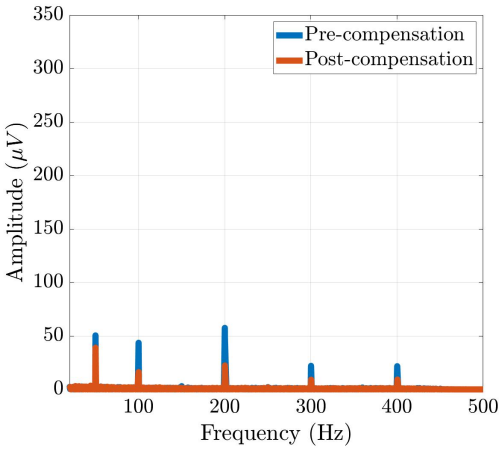

(j) Subject 10.

Figure K.1: FFT for pre- and post-compensated bioelectrical signals for all 10 subjects. (cont.).

APPENDIX L

EMG Contractions for Highlighting Crosstalk

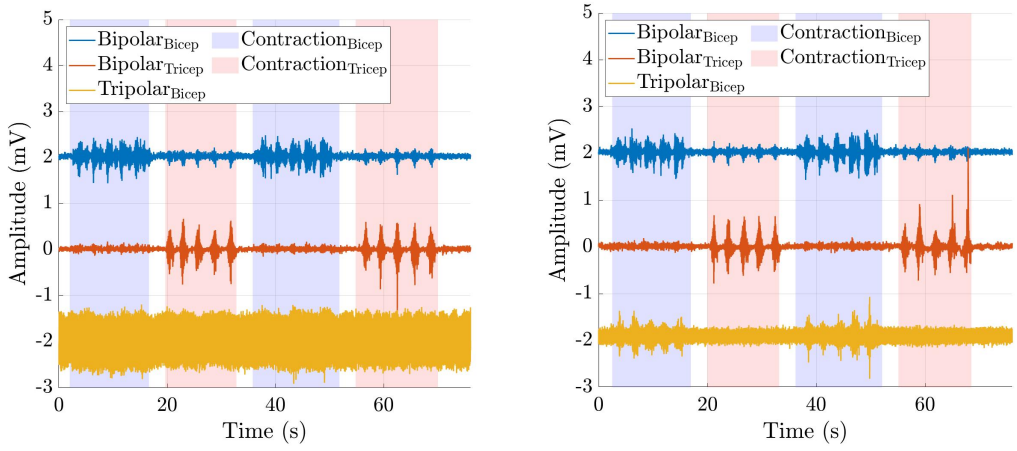

(a) Subject 1.

Figure L.1: Bioelectrical signals from the three sEMG devices, pre- and post-compensation for all 10 subjects.

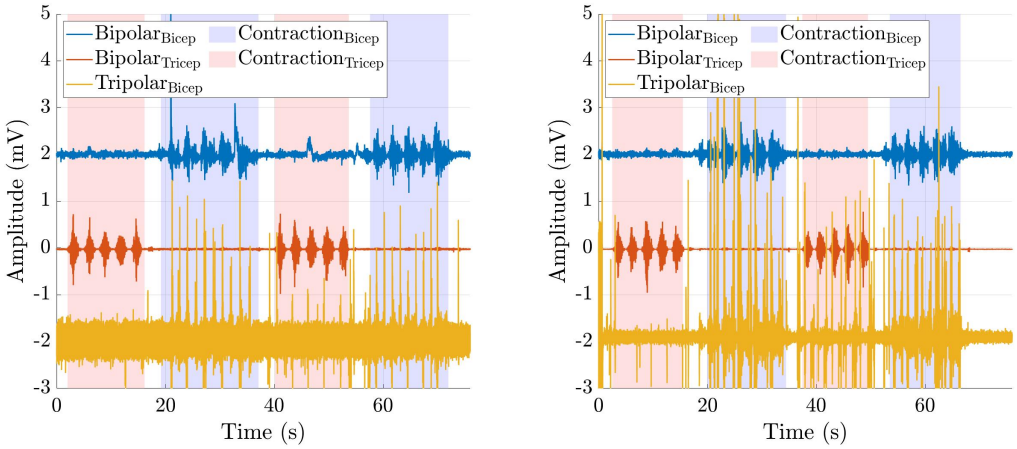

(b) Subject 2.

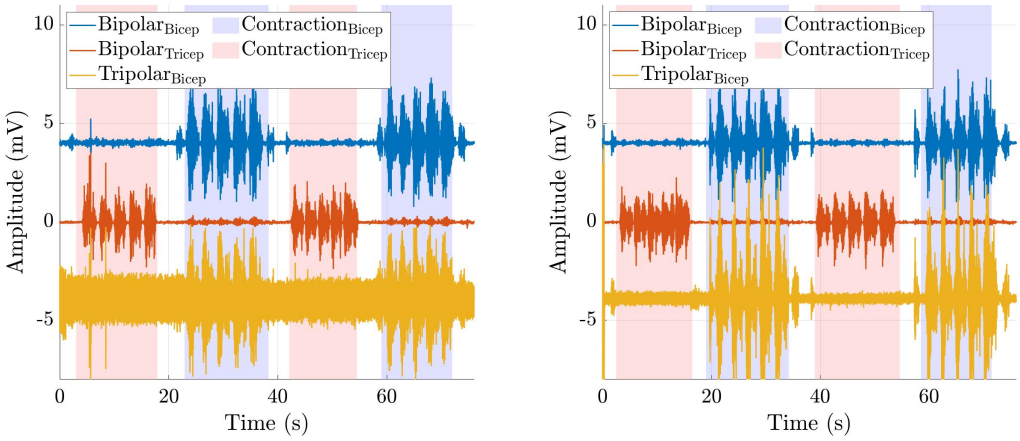

(c) Subject 3.

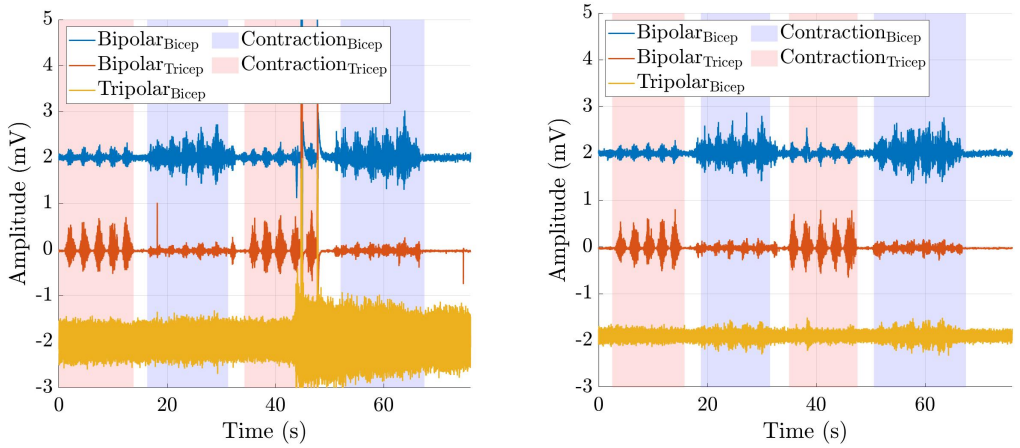

(d) Subject 4.

Figure L.1: Bioelectrical signals from the three sEMG devices, pre- and post-compensation for all 10 subjects. (cont.).

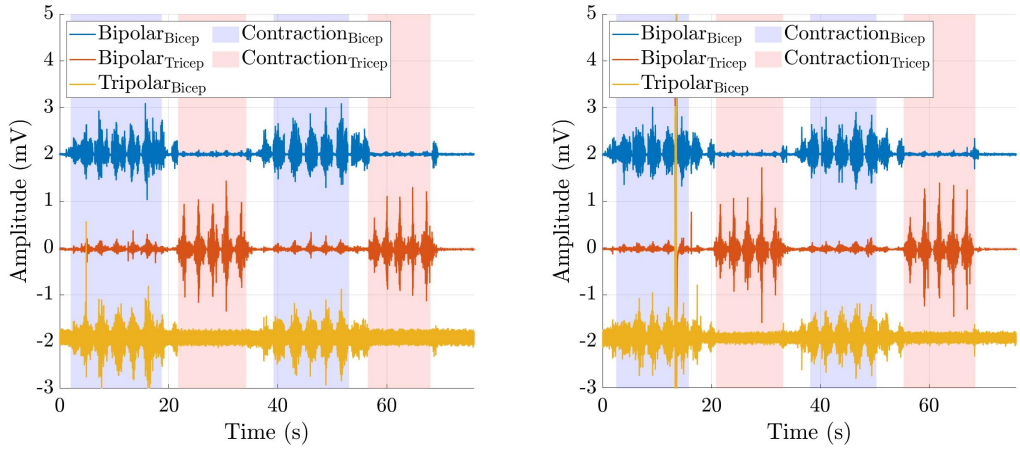

(e) Subject 5.

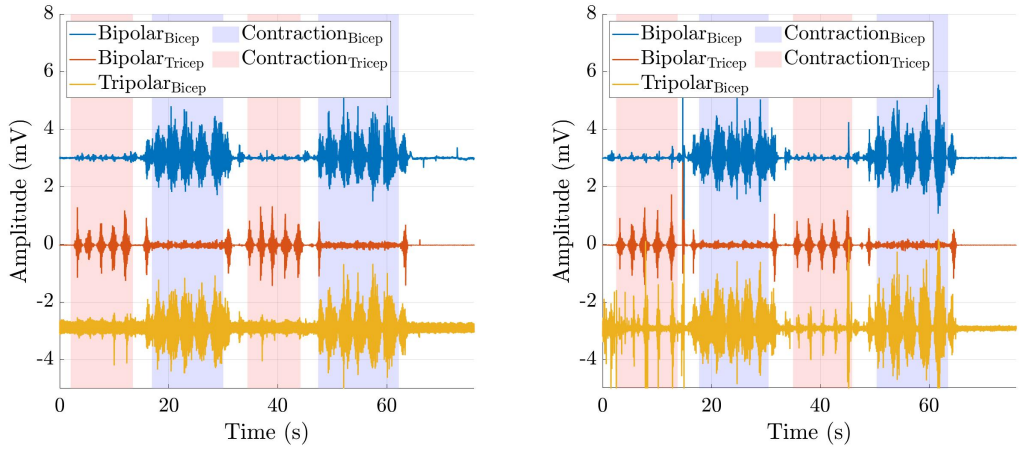

(f) Subject 6.

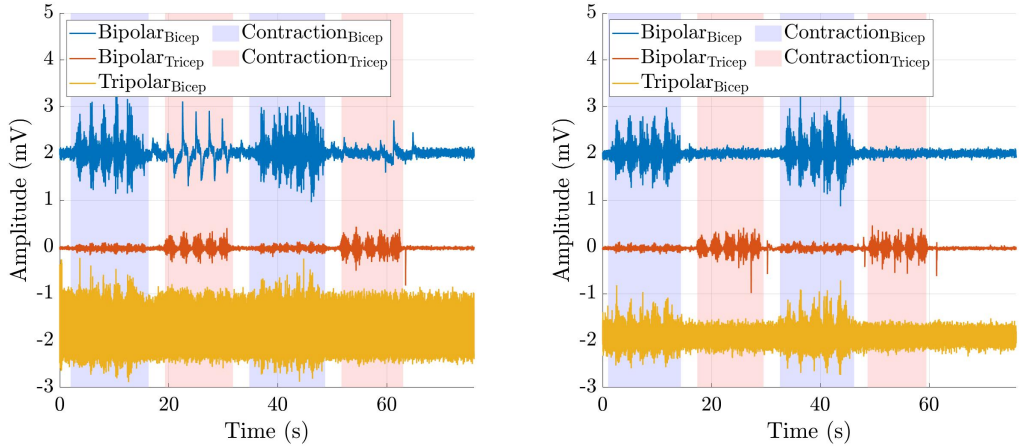

(g) Subject 7.

Figure L.1: Bioelectrical signals from the three sEMG devices, pre- and post-compensation for all 10 subjects. (cont.).

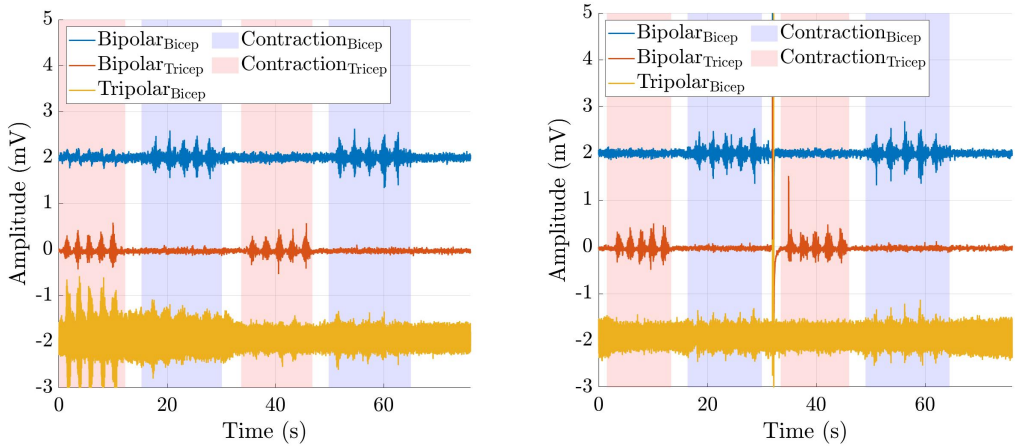

(h) Subject 8.

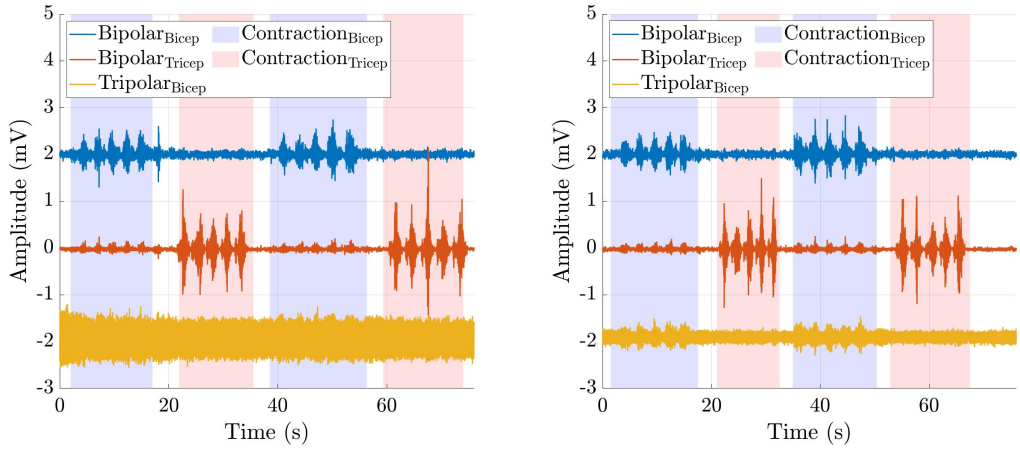

(i) Subject 9.

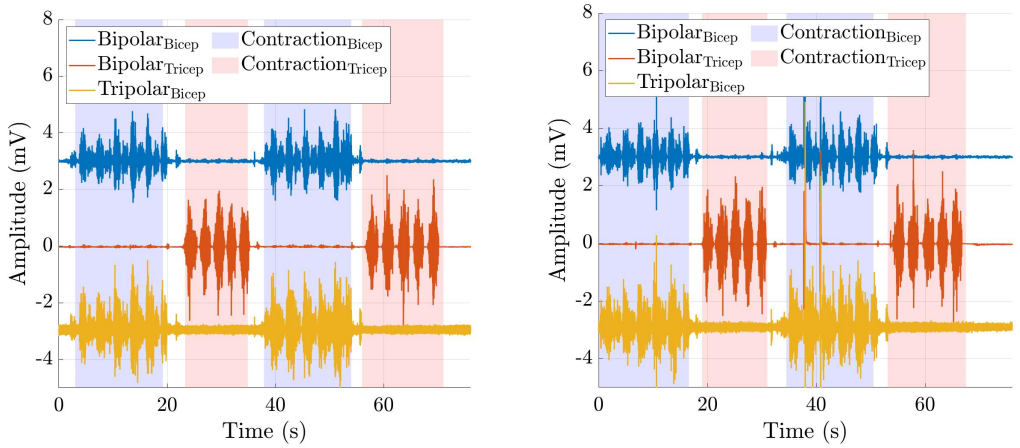

(j) Subject 10.

Figure L.1: Bioelectrical signals from the three sEMG devices, pre- and post-compensation for all 10 subjects. (cont.).

APPENDIX M

EMG FFT Contractions for Highlighting Crosstalk

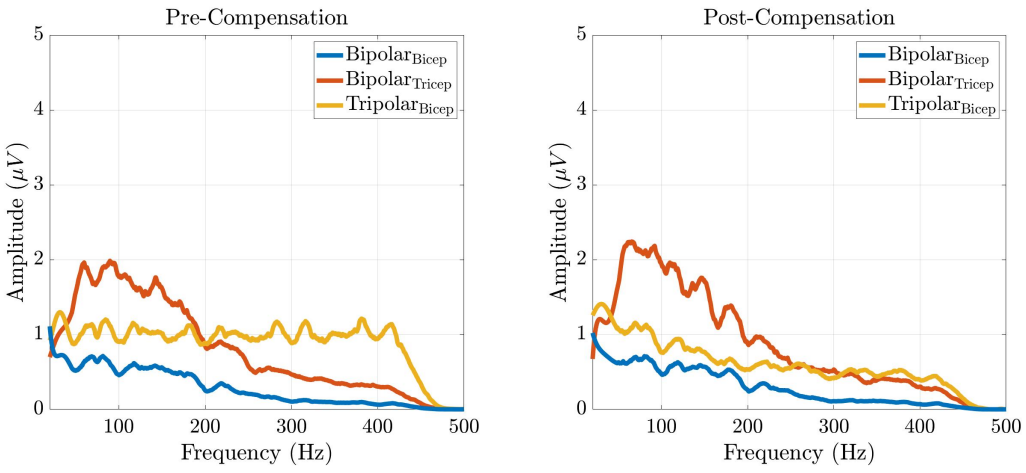

(a) Subject 1.

Figure M.1: FFT applied to the bioelectrical signals during contraction of the triceps, for all 10 subjects. A Savitzky-Golay finite impulse response filter was applied to increase visual ability.

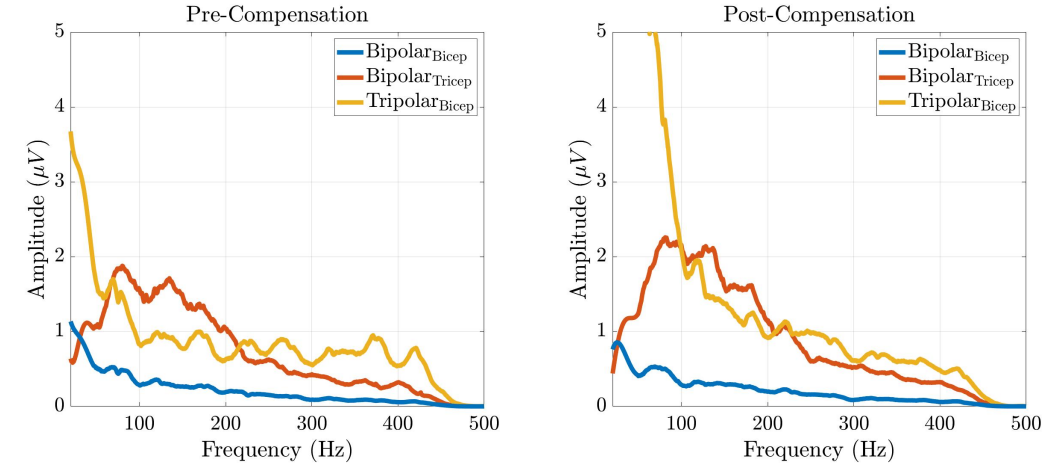

(b) Subject 2.

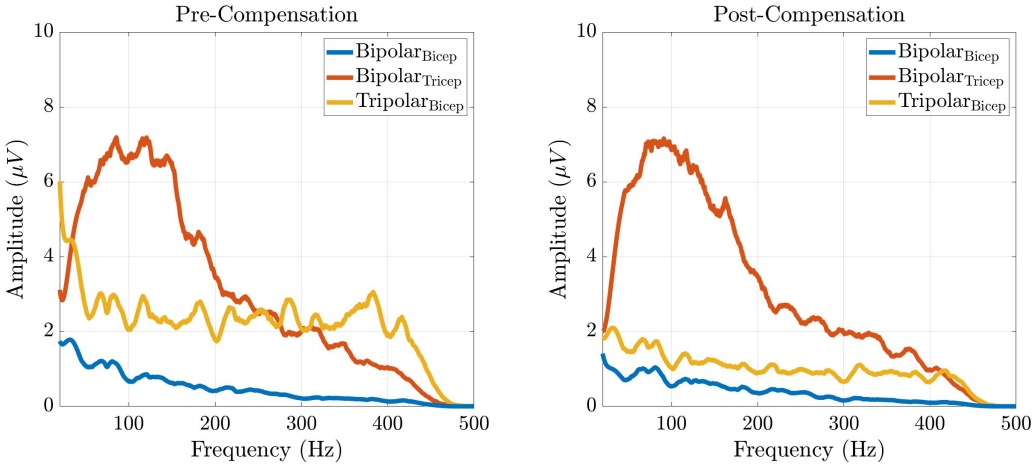

(c) Subject 3.

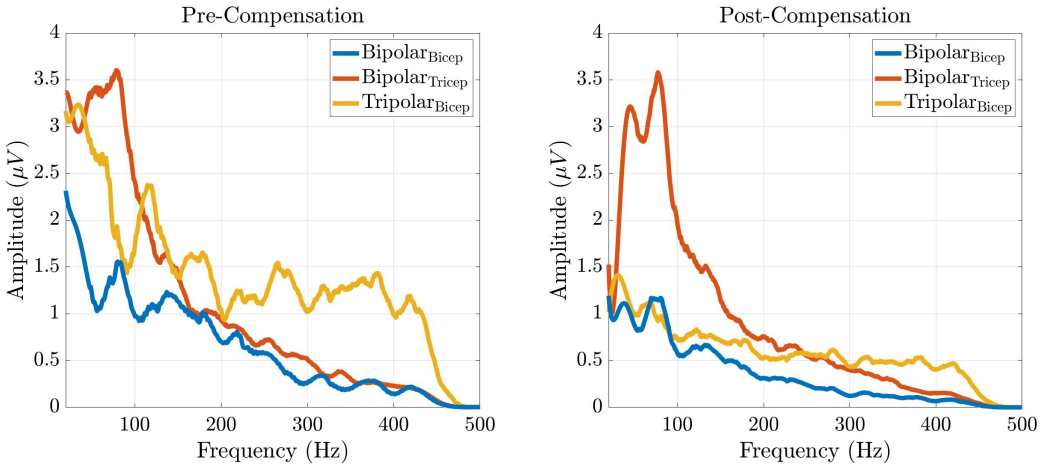

(d) Subject 4.

Figure M.1: FFT applied to the bioelectrical signals during contraction of the triceps, for all 10 subjects. A Savitzky-Golay finite impulse response filter was applied to increase visual ability. (cont.).

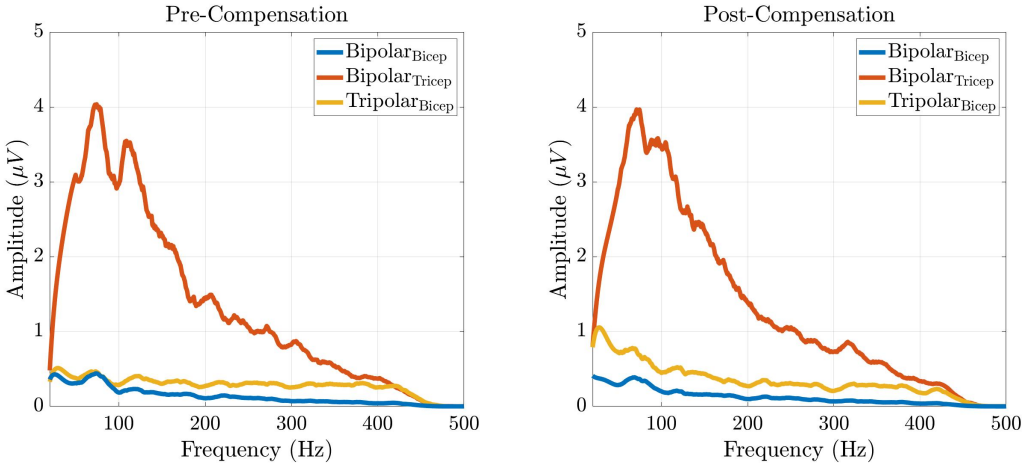

(e) Subject 5.

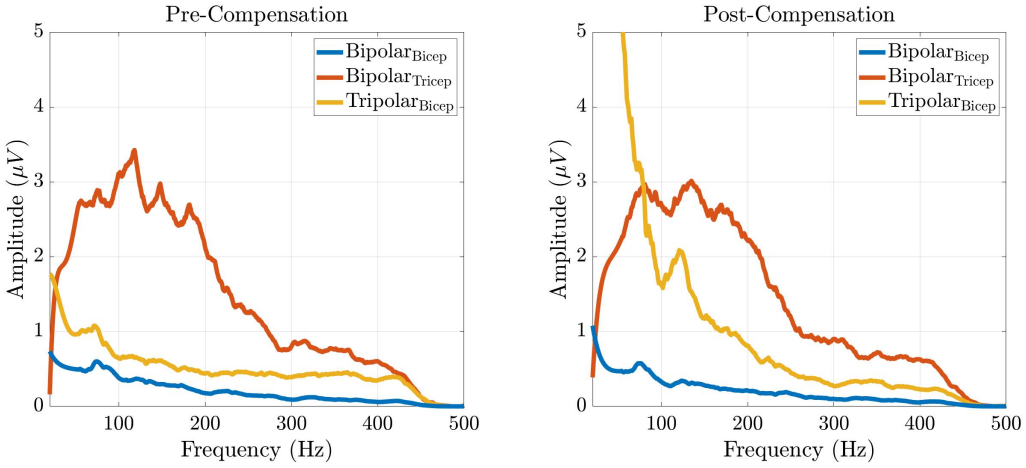

(f) Subject 6.

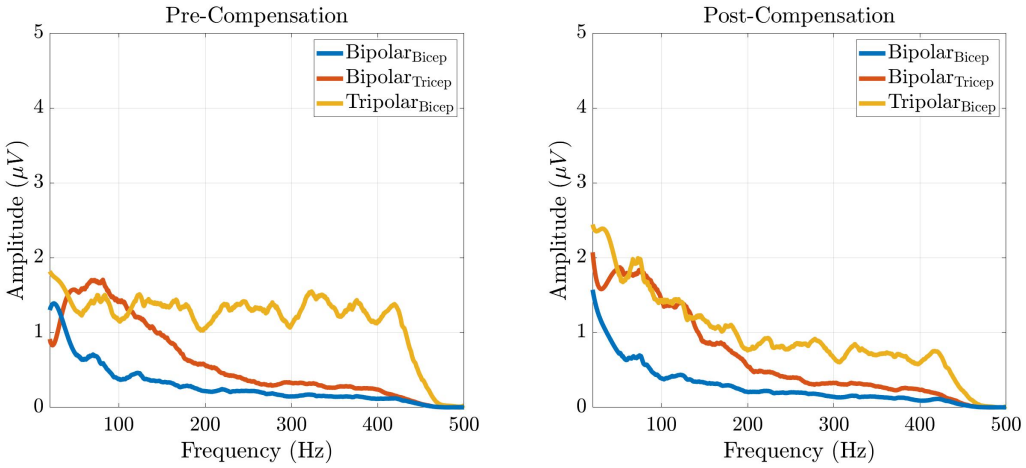

(g) Subject 7.

Figure M.1: FFT applied to the bioelectrical signals during contraction of the triceps, for all 10 subjects. A Savitzky-Golay finite impulse response filter was applied to increase visual ability. (cont.).

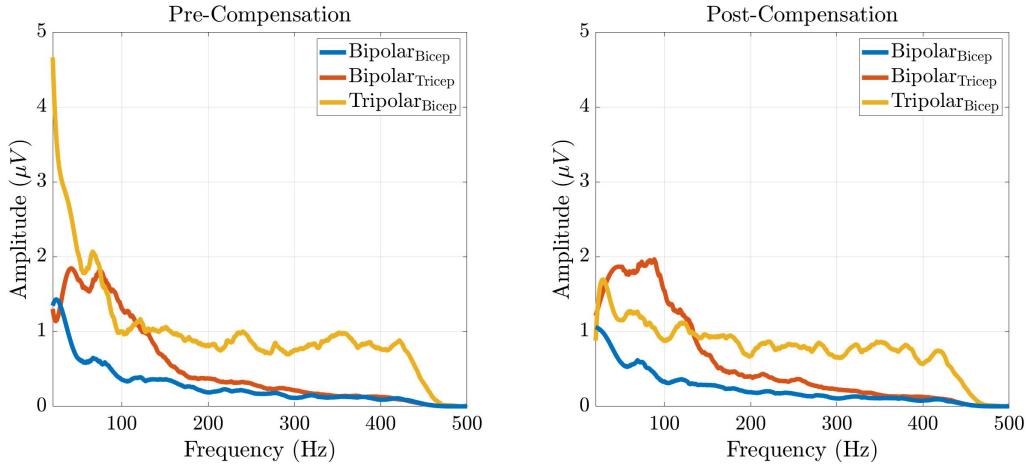

(h) Subject 8.

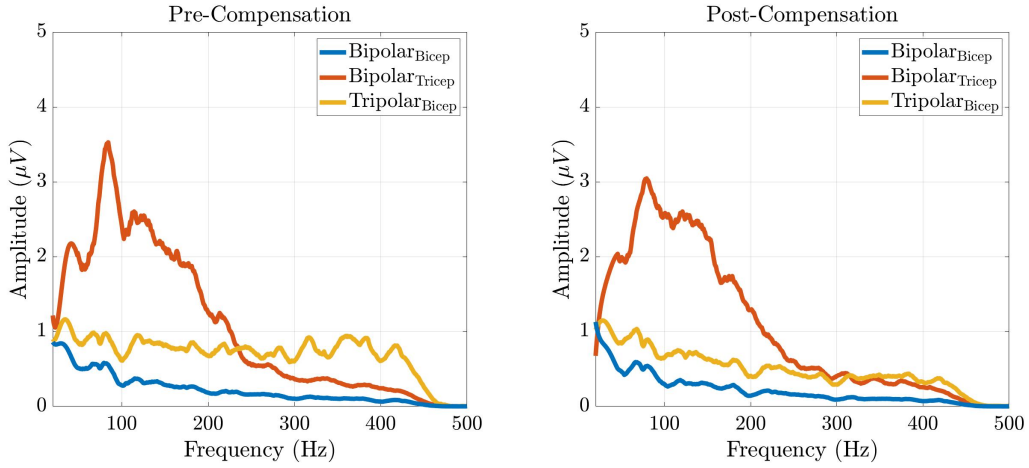

(i) Subject 9.

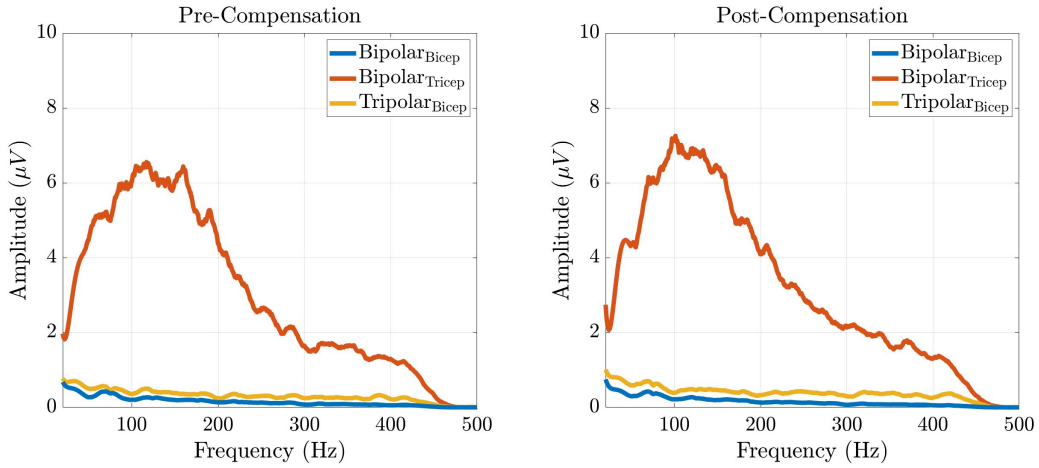

(j) Subject 10.

Figure M.1: FFT applied to the bioelectrical signals during contraction of the triceps, for all 10 subjects. A Savitzky-Golay finite impulse response filter was applied to increase visual ability. (cont.).

APPENDIX N

EMG FFT Integration for Highlighting Crosstalk

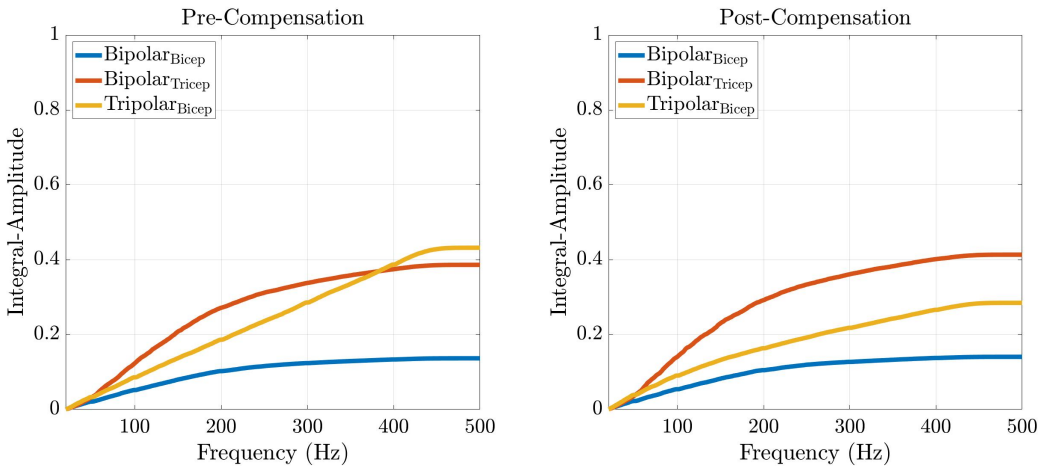

(a) Subject 1.

Figure N.1: Integrated FFT of the bioelectrical signals during tripolar contractions, for all 10 subjects.

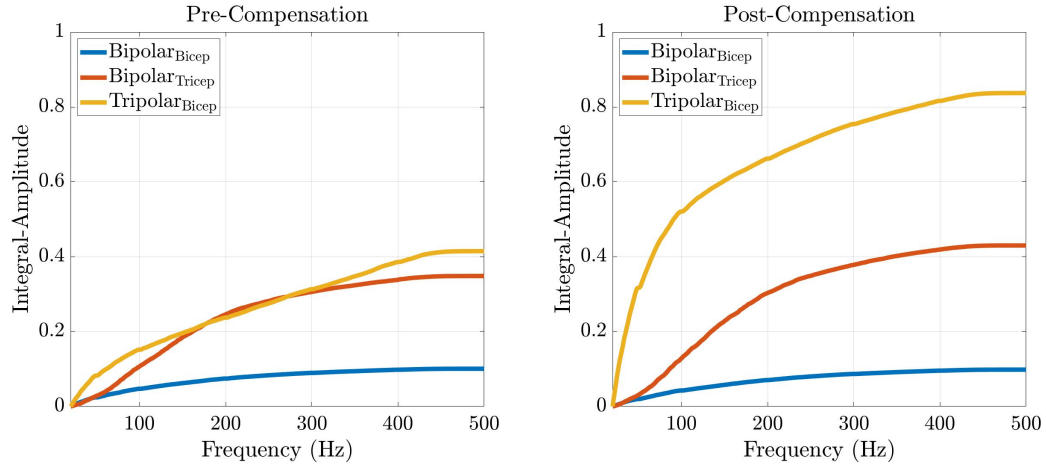

(b) Subject 2.

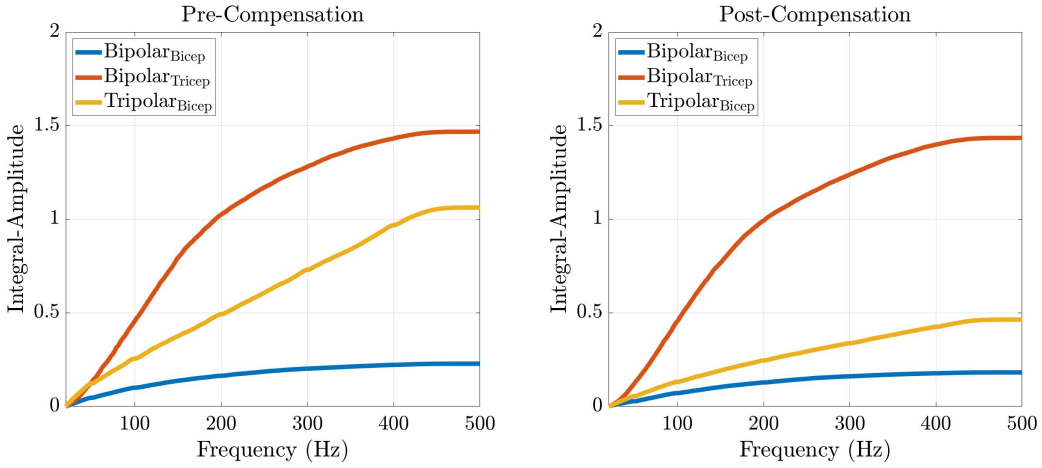

(c) Subject 3.

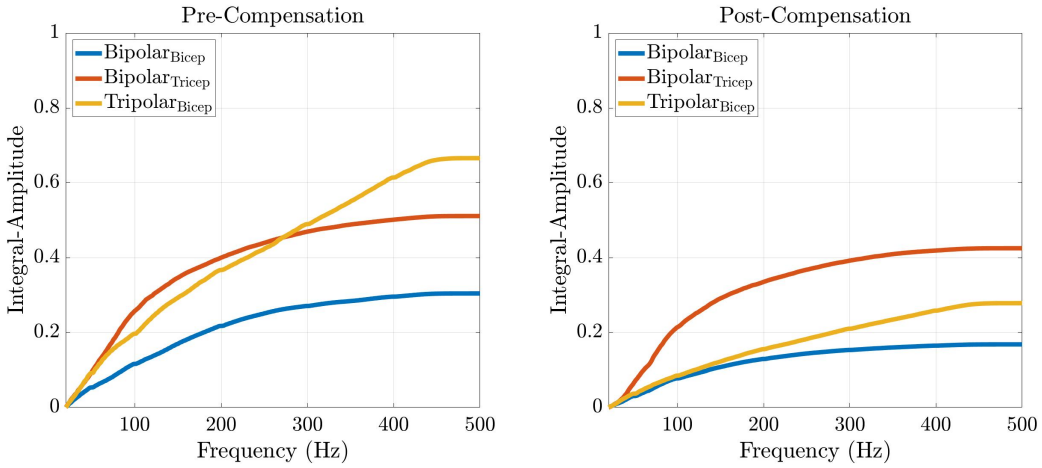

(d) Subject 4.

Figure N.1: Integrated FFT of the bioelectrical signals during tripolar contractions, for all 10 subjects. (cont.).

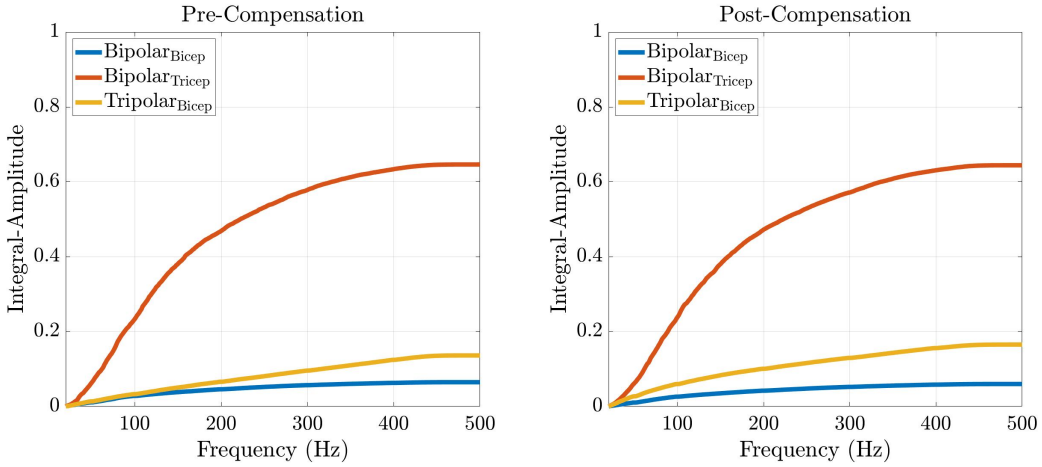

(e) Subject 5.

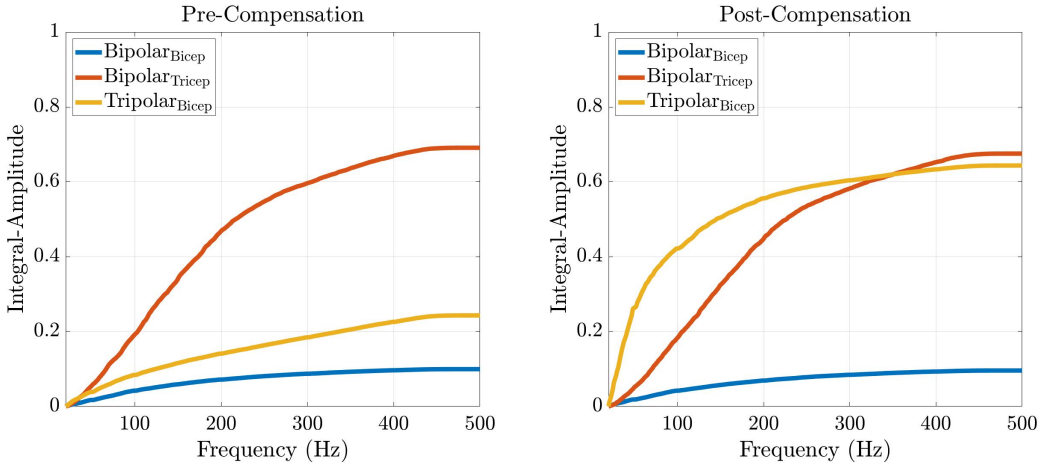

(f) Subject 6.

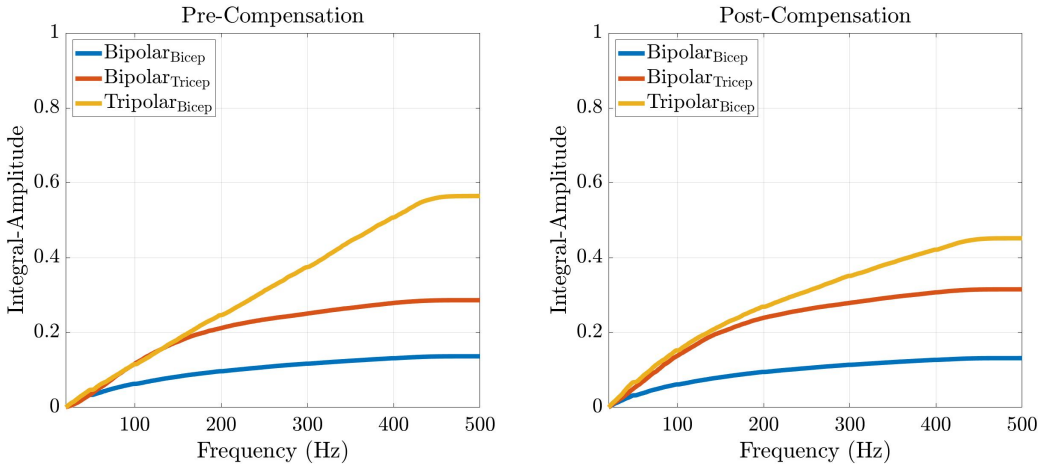

(g) Subject 7.

Figure N.1: Integrated FFT of the bioelectrical signals during tripolar contractions, for all 10 subjects. (cont.).

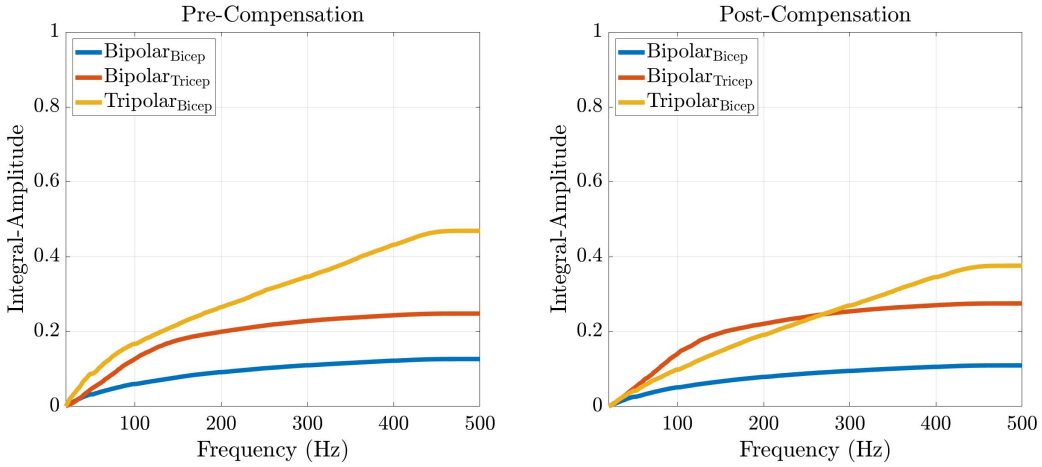

(h) Subject 8.

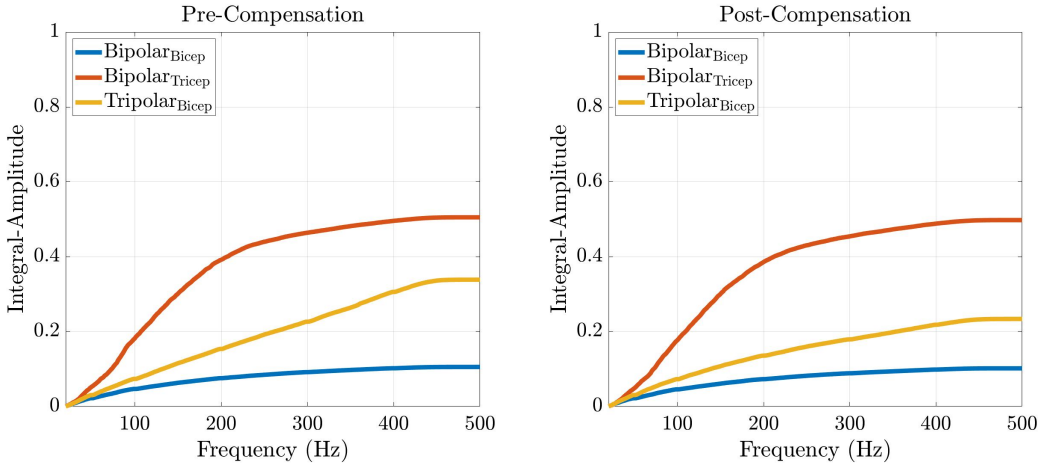

(i) Subject 9.

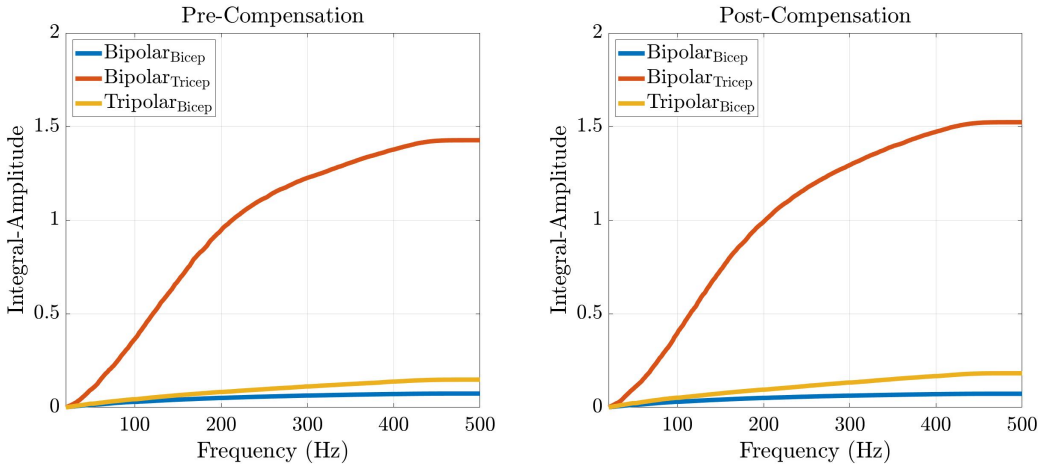

(j) Subject 10.

Figure N.1: Integrated FFT of the bioelectrical signals during tripolar contractions, for all 10 subjects. (cont.).

APPENDIX O

Co-Authorship Forms

The co-authorship forms are below.

Deputy Vice-Chancellor's Office
Postgraduate Office

UNIVERSITY OF CANTERBURY
Te Whare Wānanga o Waitaha
CHRISTCHURCH NEW ZEALAND

Co-Authorship Form

This form is to accompany the submission of any thesis that contains research reported in co-authored work that has been published, accepted for publication, or submitted for publication. A copy of this form should be included for each co-authored work that is included in the thesis. Completed forms should be included at the front (after the thesis abstract) of each copy of the thesis submitted for examination and library deposit.

Please indicate the chapter/section/pages of this thesis that are extracted from co-authored work and provide details of the publication or submission from the extract comes:

Section in Thesis: Chapter 6

Publication Type: Journal Paper

Publication: "Modelling the Impedance of Electrode-Skin Interfaces in a Bipolar Electrode Configuration" BioMedical Engineering Online

Please detail the nature and extent (%) of contribution by the candidate:

70%

The candidate processed the data, provided a major contribution to developing the modelling algorithm and wrote the manuscript.

Co-author contributions varied from contributing toward the development of the modelling algorithm, the analysis and interpretation of the findings, and revising the manuscript

Certification by Co-authors:

If there is more than one co-author then a single co-author can sign on behalf of all

The undersigned certifys that:

- The above statement correctly reflects the nature and extent of the PhD candidate's contribution to this co-authored work
- In cases where the candidate was the lead author of the co-authored work he or she wrote the text

Name: Chris Pretty Signature: Chris Pretty (on behalf of all co-authors) Date: *30 November 2020*

Deputy Vice-Chancellor's Office
Postgraduate Office

UNIVERSITY OF CANTERBURY
Te Whare Wānanga o Waitaha
CHRISTCHURCH NEW ZEALAND

Co-Authorship Form

This form is to accompany the submission of any thesis that contains research reported in co-authored work that has been published, accepted for publication, or submitted for publication. A copy of this form should be included for each co-authored work that is included in the thesis. Completed forms should be included at the front (after the thesis abstract) of each copy of the thesis submitted for examination and library deposit.

Please indicate the chapter/section/pages of this thesis that are extracted from co-authored work and provide details of the publication or submission from the extract comes:

Section in Thesis: Chapter 5

Publication Type: Journal Paper

Publication: "Electrode–skin impedance imbalance measured in the frequency domain." Biomedical Signal Processing and Control

Please detail the nature and extent (%) of contribution by the candidate:

90%

The candidate developed the hardware, processed the data, and wrote the manuscript.

Co-author contributions varied from providing hardware development, assisting with analysis, interpretation of the findings, and revising the manuscript

Certification by Co-authors:

If there is more than one co-author then a single co-author can sign on behalf of all

The undersigned certifys that:

- The above statement correctly reflects the nature and extent of the PhD candidate's contribution to this co-authored work
- In cases where the candidate was the lead author of the co-authored work he or she wrote the text

Name: Chris Pretty Signature: Chris Pretty (on behalf of all co-authors) Date: *30 November 2020*

Deputy Vice-Chancellor's Office
Postgraduate Office

UNIVERSITY OF CANTERBURY
Te Whare Wānanga o Waitaha
CHRISTCHURCH NEW ZEALAND

Co-Authorship Form

This form is to accompany the submission of any thesis that contains research reported in co-authored work that has been published, accepted for publication, or submitted for publication. A copy of this form should be included for each co-authored work that is included in the thesis. Completed forms should be included at the front (after the thesis abstract) of each copy of the thesis submitted for examination and library deposit.

Please indicate the chapter/section/pages of this thesis that are extracted from co-authored work and provide details of the publication or submission from the extract comes:

Section in Thesis: Chapter 3

Publication Type: Journal Paper

Publication: "Data captured using low-cost active electromyography." Data in Brief

Please detail the nature and extent (%) of contribution by the candidate:

90%

The candidate processed the data, and wrote the manuscript.

Co-author contributions varied from assistaning with analysis and revising the manuscript

Certification by Co-authors:

If there is more than one co-author then a single co-author can sign on behalf of all

The undersigned certifys that:

- The above statement correctly reflects the nature and extent of the PhD candidate's contribution to this co-authored work
- In cases where the candidate was the lead author of the co-authored work he or she wrote the text

Name: Chris Pretty Signature: Chris Pretty (on behalf of all co-authors) Date: *30 November 2020*

Deputy Vice-Chancellor's Office
Postgraduate Office

UNIVERSITY OF CANTERBURY
Te Whare Wānanga o Waitaha
CHRISTCHURCH NEW ZEALAND

Co-Authorship Form

This form is to accompany the submission of any thesis that contains research reported in co-authored work that has been published, accepted for publication, or submitted for publication. A copy of this form should be included for each co-authored work that is included in the thesis. Completed forms should be included at the front (after the thesis abstract) of each copy of the thesis submitted for examination and library deposit.

Please indicate the chapter/section/pages of this thesis that are extracted from co-authored work and provide details of the publication or submission from the extract comes:

Section in Thesis: Chapter 3

Publication Type: Journal Paper

Publication: "Low-cost active electromyography." HardwareX

Please detail the nature and extent (%) of contribution by the candidate:

90%

The candidate devloepd the hardware, processed the data, and wrote the manuscript.

Co-author contributions varied from providing hardware development, assistaning with analysis, interpretation of the findings, and revising the manuscript

Certification by Co-authors:

If there is more than one co-author then a single co-author can sign on behalf of all

The undersigned certifys that:

- The above statement correctly reflects the nature and extent of the PhD candidate's contribution to this co-authored work
- In cases where the candidate was the lead author of the co-authored work he or she wrote the text

Name: Chris Pretty Signature: Chris Pretty (on behalf of all co-authors) Date: *30 November 2020*

Deputy Vice-Chancellor's Office
Postgraduate Office

UNIVERSITY OF CANTERBURY
Te Whare Wānanga o Waitaha
CHRISTCHURCH NEW ZEALAND

Co-Authorship Form

This form is to accompany the submission of any thesis that contains research reported in co-authored work that has been published, accepted for publication, or submitted for publication. A copy of this form should be included for each co-authored work that is included in the thesis. Completed forms should be included at the front (after the thesis abstract) of each copy of the thesis submitted for examination and library deposit.

Please indicate the chapter/section/pages of this thesis that are extracted from co-authored work and provide details of the publication or submission from the extract comes:

Section in Thesis: Chapter 4

Publication Type: Conference Paper

Publication: "Electrode-Skin Impedance Component Estimation in the Time-domain". 15th ASME/IEEE International Conference on Mechatronic and Embedded Systems and Applications (MESA 2019).

Please detail the nature and extent (%) of contribution by the candidate:

90%

The candidate developed and conducted the algorithms for analysis, and wrote the paper.

Co-author contributions varied from providing assistance with analysis and interpretation of the results, and revising the paper.

Certification by Co-authors:

If there is more than one co-author then a single co-author can sign on behalf of all

The undersigned certifys that:

- The above statement correctly reflects the nature and extent of the PhD candidate's contribution to this co-authored work
- In cases where the candidate was the lead author of the co-authored work he or she wrote the text

Name: Chris Pretty Signature: Chris Pretty (on behalf of all co-authors) Date: *30 November 2020*

References

Adli, & Yamamoto, Y. (1998, May). Impedance balancing analysis for power-line interference elimination in ECG signal. In *IMTC/98 Conference Proceedings. IEEE Instrumentation and Measurement Technology Conference. Where Instrumentation is Going (Cat. No.98CH36222)* (Vol. 1, pp. 235–238 vol.1). (ISSN: 1091-5281) doi: 10.1109/IMTC.1998.679764

Almasi, J. J., & Schmitt, O. H. (1970). Systemic and Random Variations of Ecg Electrode System Impedance. *Annals of the New York Academy of Sciences*, *170*(2), 509–519. Retrieved 2019-11-26, from https://nyaspubs.onlinelibrary.wiley.com/doi/abs/10.1111/j.1749-6632.1970.tb17718.x doi: 10.1111/j.1749-6632.1970.tb17718.x

Analog Devices. (2018). *DC to 204 kHz, Dynamic Signal Analysis, Precision 24-Bit ADC with Power Scaling* (AD7768-1 Data Sheet, Rev. A). Retrieved 2019-05-27, from https://www.analog.com/media/en/technical-documentation/data-sheets/ad7768-1.pdf

Andersen, J. L., Schjerling, P., & Saltin, B. (2000). Genes. *Scientific American*, *283*(3), 48–55. Retrieved 2017-07-13, from http://www.patternsofbeing.com/downloads/pdf/muscle,.genes.and.athletic.performance--scientific.american.sept.2000.pdf

Assambo, C., Baba, A., Dozio, R., & Burke, M. J. (2007). Determination of the parameters of the skin-electrode impedance model for ECG measurement. In *Proceedings of*

the 6th WSEAS international conference on electronics, hardware, wireless and optical communications, Corfu Island, Greece (pp. 90–95).

Basmajian, J. V., & De Luca, C. J. (1979). *Muscles alive: their functions revealed by electromyography*. Williams & Wilkins.

Basmajian, J. V., & Szatmari, A. (1955). Effect of Largactil (Chlorpromazine) on Human Spasticity and Electromyogram: Preliminary Report. *AMA Archives of Neurology \& Psychiatry*, *73*(2), 224–231.

Benjamin, E. J., Blaha, M. J., Chiuve, S. E., Cushman, M., Das, S. R., Deo, R., … Muntner, P. (2017, March). Heart Disease and Stroke Statistics—2017 Update: A Report From the American Heart Association. *Circulation*, *135*(10), e146–e603. Retrieved 2017-08-21, from http://circ.ahajournals.org/content/135/10/e146 doi: 10.1161/CIR.0000000000000485

Betts, R. P., & Brown, B. H. (1976, May). Method for recording electrocardiograms with dry electrodes applied to unprepared skin. *Medical and biological engineering*, *14*(3), 313–315. Retrieved 2020-03-12, from https://doi.org/10.1007/BF02478127 doi: 10.1007/BF02478127

Brandstater, M., & Lambert, E. H. (1973). Motor Unit Anatomy. *Karger Publishers*, *1*, 14–22.

Broman, H., Bilotto, G., & Luca, C. J. D. (1985, May). A Note on the Noninvasive Estimation of Muscle Fiber Conduction Velocity. *IEEE Transactions on Biomedical Engineering*, *BME-32*(5), 341–344. doi: 10.1109/TBME.1985.325550

Buchthal, F., Erminio, F., & Rosenfalck, P. (1959). Motor unit territory in different human muscles. *Acta Physiologica*, *45*(1), 72–87.

Buchthal, F., & Schmalbruch, H. (1980, January). Motor unit of mammalian muscle. *Physiological Reviews*, *60*(1), 90–142. Retrieved 2020-07-17, from https://www.physiology.org/doi/10.1152/physrev.1980.60.1.90 doi: 10.1152/physrev.1980.60.1.90

Burns, R. C. (1950). Study of skin impedance. *Electronics*, *23*(4), 190–196.

Cardillo, T., Dresden, S., & Solem, J. (1998). *Crosstalk: Surface Versus Intramuscular*

Electrodes for the Peroneus Brevis and Peroneus Longus. Masters Theses.

Casal, L., & Mura, G. L. (2016, April). Skin-electrode impedance measurement during ECG acquisition: method's validation. *Journal of Physics: Conference Series*, *705*, 012006. Retrieved 2018-02-14, from http://stacks.iop.org/1742-6596/705/i=1/a=012006?key=crossref.eb304b23607bf6b6c1179a30e6c53829 doi: 10.1088/1742-6596/705/1/012006

Chan, D. C. B. (1997). *Blind signal separation* (Ph.D., University of Cambridge). Retrieved 2017-12-27, from http://ethos.bl.uk/OrderDetails.do?uin=uk.bl.ethos.597415

Chandrapal, M. (2012). *Intelligent Assistive Knee Orthotic Device Utilizing Pneumatic Artificial Muscles* (Doctoral dissertation). Retrieved 2017-01-17, from https://ir.canterbury.ac.nz/handle/10092/7475

Cram, J. R. (1998). *Introduction to surface electromyography*. Aspen Publishers.

Dam, M., Tonin, P., Casson, S., Ermani, M., Pizzolato, G., Iaia, V., & Battistin, L. (1993). The effects of long-term rehabilitation therapy on poststroke hemiplegic patients. *Stroke*, *24*(8), 1186–1191. Retrieved 2017-08-21, from http://stroke.ahajournals.org/content/24/8/1186.short

De Luca, C. J. (1997, May). The Use of Surface Electromyography in Biomechanics. *Journal of Applied Biomechanics*, *13*(2), 135–163. Retrieved from http://journals.humankinetics.com/doi/abs/10.1123/jab.13.2.135 doi: 10.1123/jab.13.2.135

De Luca, C. J. (2002). Surface electromyography: Detection and recording. *DelSys Incorporated*, *10*, 2011. Retrieved 2017-02-14, from https://www.delsys.com/Attachments_pdf/WP_SEMGintro.pdf

De Luca, C. J., Kuznetsov, M., Gilmore, L. D., & Roy, S. H. (2012, February). Inter-electrode spacing of surface EMG sensors: Reduction of crosstalk contamination during voluntary contractions. *Journal of Biomechanics*, *45*(3), 555–561. Retrieved 2017-10-16, from http://linkinghub.elsevier.com/retrieve/pii/S0021929011006920 doi: 10.1016/j.jbiomech.2011.11.010

De Luca, C. J., & Merletti, R. (1988, June). Surface myoelectric signal cross-talk among

muscles of the leg. *Electroencephalography and Clinical Neurophysiology*, *69*(6), 568–575. Retrieved from http://www.sciencedirect.com/science/article/pii/0013469488901691 doi: 10.1016/0013-4694(88)90169-1

Dobrev, D. P., & Neycheva, T. D. (2011). Bootstrapped Instrumentation Biosignal Amplifier. *Annual Journal of Electronics*, *5*(2), 76–79.

Díaz, I., Gil, J. J., & Sánchez, E. (2011). Lower-Limb Robotic Rehabilitation: Literature Review and Challenges. *Journal of Robotics*, *2011*, 1–11. Retrieved 2017-01-17, from http://www.hindawi.com/journals/jr/2011/759764/ doi: 10.1155/2011/759764

Farina, D., Merletti, R., Indino, B., Nazzaro, M., & Pozzo, M. (2002, November). Surface EMG crosstalk between knee extensor muscles: Experimental and model results. *Muscle & Nerve*, *26*(5), 681–695. Retrieved from http://onlinelibrary.wiley.com/doi/10.1002/mus.10256/abstract doi: 10.1002/mus.10256

Feigin, V. L., Forouzanfar, M. H., Krishnamurthi, R., Mensah, G. A., Connor, M., Bennett, D. A., … Murray, C. (2014, January). Global and regional burden of stroke during 1990–2010: findings from the Global Burden of Disease Study 2010. *The Lancet*, *383*(9913), 245–255. Retrieved from http://linkinghub.elsevier.com/retrieve/pii/S0140673613619534 doi: 10.1016/S0140-6736(13)61953-4

Fortune, B. C., Pretty, C. G., Chatfield, L. T., McKenzie, L. R., & Hayes, M. P. (2019, October). Low-cost active electromyography. *HardwareX*, *6*, e00085. Retrieved 2019-11-11, from http://www.sciencedirect.com/science/article/pii/S2468067219300501 doi: 10.1016/j.ohx.2019.e00085

Fortune, B. C., Pretty, C. G., Chatfield, L. T., McKenzie, L. R., & Hayes, M. P. (2020, April). Data captured using low-cost active electromyography. *Data in Brief*, *29*, 105239. Retrieved 2020-07-23, from http://www.sciencedirect.com/science/article/pii/S2352340920301335 doi: 10.1016/j.dib.2020.105239

Gelderblom, G. J., Wilt, M. D., Cremers, G., & Rensma, A. (2009, June). Rehabilitation robotics in robotics for healthcare; A roadmap study for the European Commission. In *2009 IEEE International Conference on Rehabilitation Robotics* (pp. 834–838).

doi: 10.1109/ICORR.2009.5209498

Grimnes, S. (1983). Impedance measurement of individual skin surface electrodes. *Medical and Biological Engineering and Computing*, *21*(6), 750–755.

Hardalaç, F., & Canal, R. (2004). EMG circuit design and AR analysis of EMG signs. *Journal of medical systems*, *28*(6), 633–642. Retrieved 2017-08-02, from http://www.springerlink.com/index/L1T6V27853674866.pdf

Hodgkin, A. L., & Huxley, A. F. (1952). A quantitative description of membrane current and its application to conduction and excitation in nerve. *The Journal of physiology*, *117*(4), 500–544. Retrieved 2017-07-20, from http://onlinelibrary.wiley.com/doi/10.1113/jphysiol.1952.sp004764/full

Huhta, J. C., & Webster, J. G. (1973, March). 60-Hz Interference in Electrocardiography. *IEEE Transactions on Biomedical Engineering*, *BME-20*(2), 91–101. doi: 10.1109/TBME.1973.324169

Huxley, A. F., & Niedergerke, R. (1954, May). Structural changes in muscle during contraction; interference microscopy of living muscle fibres. *Nature*, *173*(4412), 971–973.

Johnson, H., Johnson, H. W., & Graham, M. (2003). *High-speed Signal Propagation: Advanced Black Magic*. Prentice Hall Professional.

Kaczmarek, K. A., & Webster, J. G. (1989, November). Voltage-current characteristics of the electrotactile skin-electrode interface. In *Images of the Twenty-First Century. Proceedings of the Annual International Engineering in Medicine and Biology Society,* (pp. 1526–1527 vol.5). doi: 10.1109/IEMBS.1989.96322

Kawamoto, H., Lee, S., Kanbe, S., & Sankai, Y. (2003, October). Power assist method for HAL-3 using EMG-based feedback controller. In *IEEE International Conference on Systems, Man and Cybernetics, 2003* (Vol. 2, pp. 1648–1653 vol.2). doi: 10.1109/ICSMC.2003.1244649

Kawamoto, H., & Sankai, Y. (2002, July). Power Assist System HAL-3 for Gait Disorder Person. In *Computers Helping People with Special Needs* (pp. 196–203). Springer, Berlin, Heidelberg. Retrieved 2017-01-24, from http://link.springer.com/chapter/

10.1007/3-540-45491-8_43 doi: 10.1007/3-540-45491-8_43

Kilner, J. M., Baker, S. N., & Lemon, R. N. (2002, February). A novel algorithm to remove electrical cross-talk between surface EMG recordings and its application to the measurement of short-term synchronisation in humans. *The Journal of Physiology*, *538*(3), 919–930. Retrieved from http://onlinelibrary.wiley.com/doi/10.1113/jphysiol.2001.012950/abstract doi: 10.1113/jphysiol.2001.012950

Koh, T. J., & Grabiner, M. D. (1993). Evaluation of methods to minimize cross talk in surface electromyography. *Journal of biomechanics*, *26*, 151–157.

Kong, Y.-K., Hallbeck, M. S., & Jung, M.-C. (2010, December). Crosstalk effect on surface electromyogram of the forearm flexors during a static grip task. *Journal of Electromyography and Kinesiology*, *20*(6), 1223–1229. Retrieved from http://www.sciencedirect.com/science/article/pii/S1050641110001276 doi: 10.1016/j.jelekin.2010.08.001

Laszlo, S., Ruiz-Blondet, M., Khalifian, N., Chu, F., & Jin, Z. (2014, September). A direct comparison of active and passive amplification electrodes in the same amplifier system. *Journal of Neuroscience Methods*, *235*, 298–307. Retrieved 2020-07-17, from http://www.sciencedirect.com/science/article/pii/S0165027014001666 doi: 10.1016/j.jneumeth.2014.05.012

Loeb, G. E., & Gans, C. (1986). *Electromyography for experimentalists*. University of Chicago Press.

McKenzie, L. R., Fortune, B. C., Chatfield, L. T., Stewart, A. M., & Pretty, C. G. (2018, January). Same-Electrode Stimulation and Recording With Dynamic Hardware Artefact Suppression. *IFAC-PapersOnLine*, *51*(27), 56–61. Retrieved 2019-01-10, from http://www.sciencedirect.com/science/article/pii/S2405896318333184 doi: 10.1016/j.ifacol.2018.11.609

Metting van Rijn, A. C., Peper, A., & Grimbergen, C. (1990). High-quality recording of bioelectric events. *Springer*, *28*(5), 389–397. Retrieved 2019-11-14, from https://link.springer.com/content/pdf/10.1007%2FBF02441961.pdf

Mogk, J. P. M., & Keir, P. J. (2003, February). Crosstalk in surface electromyography of the proximal forearm during gripping tasks. *Journal of Electromyography and Kinesiology*, *13*(1), 63–71. Retrieved from http://www.sciencedirect.com/science/article/pii/S1050641102000718 doi: 10.1016/S1050-6411(02)00071-8

Nag, S., Sikdar, S. K., Thakor, N. V., Rao, V. R., & Sharma, D. (2015, July). Sensing of Stimulus Artifact Suppressed Signals From Electrode Interfaces. *IEEE Sensors Journal*, *15*(7), 3734–3742. doi: 10.1109/JSEN.2015.2399248

Olson, W. H., Schmincke, D. R., & Henley, B. L. (1979). Time and frequency dependence of disposable ECG electrode-skin impedance. *Medical instrumentation*, *13*(5), 269–272. Retrieved 2019-11-26, from http://europepmc.org/abstract/med/502923

Pacela, A. F. (1967). Collecting the body's signals. *Electronics*, *40*, 103–112.

Pallas-Areny, R., Colominas, J., & Rosell, J. (1989, April). An improved buffer for bioelectric signals. *IEEE Transactions on Biomedical Engineering*, *36*(4), 490–493. (Conference Name: IEEE Transactions on Biomedical Engineering) doi: 10.1109/10.18757

Pallás-Areny, R., & Webster, J. G. (1990, May). Composite instrumentation amplifier for biopotentials. *Annals of Biomedical Engineering*, *18*(3), 251–262. Retrieved 2020-03-19, from https://doi.org/10.1007/BF02368441 doi: 10.1007/BF02368441

Parente, F. R., Di Giovanni, S., Ferri, G., Stornelli, V., Pennazza, G., & Santonico, M. (2018, April). An Analog Bootstrapped Biosignal Read-Out Circuit With Common-Mode Impedance Two-Electrode Compensation. *IEEE Sensors Journal*, *18*(7), 2861–2869. (Conference Name: IEEE Sensors Journal) doi: 10.1109/JSEN.2018.2799849

Patton, K. T., & Thibodeau, G. A. (2010). *Anatomy and physiology*.

Reece, J. B., Urry, L. A., Cain, Michael L, Wasserman, Steven A, Minorsky, Peter V, & Jackson, Robert B. (2011). *Campbell biology*. Pearson Higher Ed.

Richardot, A., & McAdams, E. T. (2002, June). Harmonic analysis of low-frequency bioelectrode behavior. *IEEE Transactions on Medical Imaging*, *21*(6), 604–612. doi: 10.1109/TMI.2002.800576

Rosell, J., Colominas, J., Riu, P., Pallas-Areny, R., & Webster, J. G. (1988, August). Skin

impedance from 1 Hz to 1 MHz. *IEEE Transactions on Biomedical Engineering*, *35*(8), 649–651. doi: 10.1109/10.4599

Sankai, Y. (2010). HAL Hybrid Assistive Limb Based on Cybernics. In *Robotics Research* (pp. 25–34). Springer, Berlin, Heidelberg. Retrieved 2017-07-02, from https://link.springer.com/chapter/10.1007/978-3-642-14743-2_3 doi: 10.1007/978-3-642-14743-2_3

Schwan, H. P. (1968). Electrode Polarization Impedance and Measurements in Biological Materials. *Annals of the New York Academy of Sciences*, *148*(1), 191–209. Retrieved 2019-11-26, from https://nyaspubs.onlinelibrary.wiley.com/doi/abs/10.1111/j.1749-6632.1968.tb20349.x doi: 10.1111/j.1749-6632.1968.tb20349.x

Searle, A., & Kirkup, L. (2000, May). A direct comparison of wet, dry and insulating bioelectric recording electrodes. *Physiological Measurement*, *21*(2), 271–283. Retrieved 2020-07-13, from https://doi.org/10.1088%2F0967-3334%2F21%2F2%2F307 (Publisher: IOP Publishing) doi: 10.1088/0967-3334/21/2/307

Selvanayagam, V. S., Riek, S., & Carroll, T. J. (2012, January). A systematic method to quantify the presence of cross-talk in stimulus-evoked EMG responses: Implications for TMS studies. *Journal of Applied Physiology*, *112*(2), 259–265. Retrieved 2017-11-01, from http://jap.physiology.org/cgi/doi/10.1152/japplphysiol.00558.2011 doi: 10.1152/japplphysiol.00558.2011

Silva, I. S. S., Naviner, J. F., & Freire, R. C. S. (2006, April). Compensation of Mismatch Electrodes Impedances in Biopotential Measurement. In *IEEE International Workshop on Medical Measurement and Applications, 2006. MeMea 2006.* (pp. 33–36). doi: 10.1109/MEMEA.2006.1644454

Smith, D., Goldenberg, E, Ashburn, AE, Kinsella, G, Sheikh, K, Brennan, PJ, … Reeback, JS (1981). Remedial therapy after stroke: a randomised controlled trial. *British Medical Journal Publishing Group*, *282*(6263), 515–517. Retrieved 2017-08-21, from http://www.bmj.com/content/282/6263/515.abstract

Spinelli, E. M., Pallas-Areny, R., & Mayosky, M. A. (2003, March). AC-coupled front-end for

biopotential measurements. *IEEE Transactions on Biomedical Engineering*, *50*(3), 391–395. doi: 10.1109/TBME.2003.808826

Supuk, T. G., Skelin, A. K., & Cic, M. (2014, May). Design, Development and Testing of a Low-Cost sEMG System and Its Use in Recording Muscle Activity in Human Gait. *Sensors (Basel, Switzerland)*, *14*(5), 8235–8258. Retrieved from http://www.ncbi.nlm.nih.gov/pmc/articles/PMC4063015/ doi: 10.3390/s140508235

Texas Instruments. (2018, January). *INA128 Precision, Low-Power Instrumentation Amplifiers*. Retrieved 2020-07-14, from https://www.ti.com/product/INA128 (Revision E)

Thakor, N. V. (2015). Biopotentials and Electrophysiology Measurements. In *Telehealth and Mobile Health* (pp. 555–574). CRC Press. Retrieved 2017-04-14, from http://www.crcnetbase.com/doi/pdf/10.1201/b19147-32

Thakor, N. V., & Webster, J. G. (1980, December). Ground-Free ECG Recording with Two Electrodes. *IEEE Transactions on Biomedical Engineering*, *BME-27*(12), 699–704. (Conference Name: IEEE Transactions on Biomedical Engineering) doi: 10.1109/TBME.1980.326595

Van Vugt, J. P. P., & Van Dijk, J. G. (2001). A convenient method to reduce crosstalk in surface EMG. *Clinical Neurophysiology*, *112*(4), 583–592.

Webster, J. (2009). *Medical instrumentation: application and design*. John Wiley & Sons.

Winter, B. B., & Webster, J. G. (1983a, January). Driven-right-leg circuit design. *IEEE Transactions on Biomedical Engineering*, *BME-30*(1), 62–66. doi: 10.1109/TBME.1983.325168

Winter, B. B., & Webster, J. G. (1983b, January). Reduction of Interference Due to Common Mode Voltage in Biopotential Amplifiers. *IEEE Transactions on Biomedical Engineering*, *BME-30*(1), 58–62. doi: 10.1109/TBME.1983.325167

Yonce, D. J. (2005, September). *Automatic input impedance balancing for electrocardiogram (ECG) sensing applications* (No. US6950694B2). Retrieved 2020-03-04, from https://patents.google.com/patent/US6950694B2/en (Library Catalog: Google

Patents)

Youn, W., & Kim, J. (2009, August). Development of a compact-size and wireless surface EMG measurement system. In *2009 ICCAS-SICE* (pp. 1625–1628).